Inaugural-Dissertation presented for the Degree of
Doctor rerum naturalium (Dr. rer. nat., Ph.D.)

Interplay Between Bacterial Adhesion and Antibiotic Tolerance

Submitted by
Isabelle Wielert
from Cologne

Faculty of Mathematics and Natural Sciences
University of Cologne

Accepted for publication, Cologne, 2025

Abstract

Aggregation has been shown to play a key role when bacteria protect themselves from external stresses. *Neisseria gonorrhoeae*, a biofilm-forming pathogen, which is responsible for the second-most common sexually transmitted disease, gonorrhea, poses a critical public health concern due to its multidrug resistance. Tolerance, by means of prolonged survival times under high dose antibiotic treatment, promotes the emergence of resistance. However, the underlying mechanisms of tolerance remain unknown. Gonococci form aggregates by attractive interactions of single cells mediated by type IV pili (T4P). It is unclear how T4P control the physical properties of bacterial colonies and how these properties are linked to antibiotic tolerance.

In this thesis, we investigated the effect of antibiotics on T4P dynamics and cell-to-cell interactions. To this end, we developed a fluorescence-based method for direct visualisation of T4P, as well as a laser tweezers-based approach to characterise T4P-mediated interaction dynamics under external stress conditions. Using a self-developed semi-automated image analysis pipeline, we found that, without stress, pili are produced at an impressively high rate of approximately 200 pili per minute. The application of external stress, including antibiotic treatment, reduced both the production rate and the dynamics of T4P. Optical tweezers experiments further revealed that attractive interactions between cells are modulated by antibiotic treatment. Specifically, an increase in binding and retraction probabilities leads to reduced colony fluidity, whereas a decrease in these parameters results in increased fluidity. We conclude that T4P dynamics and production rates are strongly affected by external stress and influence cell-to-cell interactions.

The T4P filament is composed of subunits, the major pilin being PilE. The surface of the T4P is constantly varied as PilE undergoes antigenic variation, a mechanism also known to facilitate immune evasion. We investigated how antigenic variation of PilE affects bacterial lifestyle and antibiotic susceptibility. Image analysis of surface motility and transmission electron microscopy confirmed that all pilin variants support twitching motility and exhibit comparable levels of piliation. From structural predictions using *AlphaFold*, we predicted that different pilin variants have different stereochemistry, which affects cell-cell attraction. Indeed, double laser trap experiments confirmed that cell-to-cell interactions were altered. At the multicellular level, weakly interacting variants adopted a planktonic lifestyle, while strongly interacting variants formed aggregates. By analysing the survival fraction of bacteria when treated with antibiotics, we found that antibiotic tolerance to ceftriaxone and ciprofloxacin is significantly reduced for planktonic bacteria and that aggregating variants are protected from antibiotic treatment. In conclusion, the stereochemical properties of PilE modulate cell-cell interactions, thereby determining bacterial lifestyle and influencing antibiotic tolerance.

We aimed to identify the molecular mechanisms that contribute to aggregation-mediated tolerance and hypothesised that genes upregulated by aggregation would protect bacteria from antibiotic treatment. Transcriptome analysis revealed differential gene expression of pilin variants exhibiting either a planktonic or an aggregating lifestyle. We identified a prominent up-regulation of pro-phage genes and genes associated with a shift towards anaerobic respiration in aggregating strains, consistent with the reduced growth rate they exhibit compared to planktonic variants. To assess functional relevance in antibiotic tolerance, deletion of the most up-regulated genes was tested in relation to bacterial survival under antibiotic treatment with ceftriaxone and ciprofloxacin. By measuring the killing kinetics of the deletion strains in either a planktonic or an aggregating pilin variant background, five genes involved in antibiotic tolerance were identified. In summary, gonococcal aggregation leads to differential expression of genes involved in antibiotic tolerance.

Finally, we investigated the transition from microcolonies to mature biofilms of *N. gonorrhoeae*. Flow chamber experiments revealed that late-stage colonies undergo eversion, characterised by a directed outward flow of cells from the centre to the periphery, transporting live and dead cells to the surface. Based on the hypothesis that oxygen depletion at the colony centre reduces T4P density and thus cohesion, we propose that this local weakening of cohesion is the trigger for colony eversion. To test this, we analysed the spatio-temporal dynamics of single cells during colony maturation and found that eversion is initiated by the emergence of an expanding shell of hyper-motile cells originating from the centre. We conclude that eversion is triggered by reduced cohesion in the colony core as a result of oxygen depletion towards the centre of the colony.

To summarise, this study elucidates the interplay between T4P dynamics, antigenic variation and antibiotic treatment in shaping bacterial lifestyles and mechanical properties of *N. gonorrhoeae* colonies. In particular, it demonstrates that aggregation is a key determinant of antibiotic tolerance.

Zusammenfassung

Aggregation spielt nachweislich eine wichtige Rolle, wenn Bakterien sich vor äußeren Belastungen schützen. *Neisseria gonorrhoeae*, ein biofilmbildender Erreger, der für die zweithäufigste sexuell übertragbare Krankheit, Gonorrhö, verantwortlich ist, stellt aufgrund seiner Multiresistenz ein ernstes Problem für die öffentliche Gesundheit dar. Toleranz, die durch längere Überlebenszeiten unter hochdosierter Antibiotikabehandlung erreicht wird, fördert die Entstehung von Resistenzen. Die zugrunde liegenden Mechanismen der Toleranz sind jedoch noch unbekannt. Gonokokken bilden Aggregate durch attraktive Wechselwirkungen einzelner Zellen, die durch Typ-IV-Pili (T4P) vermittelt werden. Es ist noch unklar, wie T4P die physikalischen Eigenschaften von Bakterienkolonien steuern und wie diese Eigenschaften mit der Antibiotikaresistenz zusammenhängen.

Zunächst untersuchten wir, wie die T4P-Dynamik und die Zell-Zell-Interaktionen durch eine Antibiotikabehandlung beeinflusst werden. Zu diesem Zweck entwickelten wir eine fluoreszenzbasierte Methode zur direkten Visualisierung von T4P sowie einen laserpinzettenbasierten Ansatz zur Charakterisierung der T4P-vermittelten Interaktionsdynamik unter externen Stressbedingungen. Mithilfe einer selbst entwickelten halbautomatischen Bildanalyse-Pipeline konnten wir feststellen, dass Pili ohne Stress mit einer beeindruckend hohen Rate von etwa 200 Pili pro Minute produziert werden. Bei äußerem Stress, einschließlich einer Antibiotikabehandlung, wurden sowohl die Produktionsrate als auch die Dynamik von T4P reduziert. Optische Pinzettenexperimente zeigten außerdem, dass attraktive Interaktionen zwischen Zellen durch eine Antibiotikabehandlung moduliert werden. Insbesondere führt eine Erhöhung der Bindungs- und Rückzugswahrscheinlichkeit zu einer verringerten Fluidität der Kolonie, während eine Verringerung dieser Parameter zu einer erhöhten Fluidität führt. Daraus lässt sich schließen, dass die T4P-Dynamik und -Produktionsraten stark von externem Stress beeinflusst werden und einen Einfluss auf die Interaktionen zwischen den Zellen haben.

T4P setzen sich aus Untereinheiten zusammen, wobei das Hauptpilin PilE ist. Die Oberfläche von T4P wird ständig variiert, da PilE antigene Variationen erfährt, ein Mechanismus, von dem auch bekannt ist, dass er die Umgehung des Immunsystems erleichtert. Wir haben untersucht, wie sich die Antigenvariation von PilE auf die bakterielle Lebensweise und Antibiotikaempfindlichkeit auswirkt. Die Bildanalyse der Oberflächenmotilität und die Transmissionselektronenmikroskopie bestätigten, dass alle Pilin-Varianten die Zuckungsmotilität unterstützen und ein vergleichbares Niveau der Pilierung aufweisen. Anhand von Strukturvorhersagen mit *AlphaFold* sagten wir voraus, dass verschiedene Pilin-Varianten eine unterschiedliche Stereochemie

aufweisen, die die Zell-Zell-Attraktion beeinflusst. In der Tat bestätigten Doppellaserfallen-Experimente, dass die Zell-Zell-Interaktionen verändert waren. Auf der multizellulären Ebene nahmen schwach interagierende Varianten einen planktonischen Lebensstil an, während stark interagierende Varianten Aggregate bildeten. Durch die Analyse des Überlebensanteils der Bakterien bei der Behandlung mit Antibiotika haben wir festgestellt, dass die Antibiotikatoleranz gegenüber Ceftriaxon und Ciprofloxacin bei planktonischen Bakterien deutlich verringert ist und dass aggregierende Varianten vor einer Antibiotikabehandlung geschützt sind. Wir schließen daraus, dass die stereochemischen Eigenschaften von PilE die Zell-Zell-Interaktionen modulieren und somit die bakterielle Lebensweise und damit auch die Antibiotikatoleranz beeinflussen.

Wir wollten die molekularen Mechanismen identifizieren, die zur aggregationsvermittelten Toleranz beitragen, und stellten die Hypothese auf, dass Gene, die durch die Aggregation hochreguliert werden, Bakterien vor einer Antibiotikabehandlung schützen würden. Die Transkriptomanalyse ergab eine unterschiedliche Genexpression von Pilin-Varianten, die entweder eine planktonische oder eine aggregierende Lebensweise aufweisen. Wir stellten eine auffällige Hochregulierung von Pro-Phagen-Genen und Genen fest, die mit einer Verschiebung hin zur anaeroben Atmung in aggregierenden Stämmen verbunden sind, was mit der geringeren Wachstumsrate im Vergleich zu planktonischen Varianten übereinstimmt. Um die funktionelle Bedeutung für die Antibiotikatoleranz zu bewerten, wurde die Deletion der am stärksten hochregulierten Gene in Bezug auf das bakterielle Überleben unter antibiotischer Behandlung mit Ceftriaxon und Ciprofloxacin getestet. Durch Messung der Abtötungskinetik der Deletionsstämme entweder in einem planktonischen oder einem aggregierenden Pilin-Varianten-Hintergrund wurden fünf Gene identifiziert, die an der Antibiotikatoleranz beteiligt sind. Zusammenfassend lässt sich sagen, dass die Aggregation von Gonokokken zu einer unterschiedlichen Expression von Genen führt, die an der Antibiotikatoleranz beteiligt sind.

Schließlich haben wir den Übergang von Mikrokolonien zu reifen Biofilmen von *N. gonorrhoeae* untersucht. In Strömungskammerexperimenten zeigte sich, dass Kolonien im Spätstadium eine Eversion durchlaufen, die durch einen nach außen gerichteten Zellfluss vom Zentrum zur Peripherie gekennzeichnet ist und lebende und tote Zellen an die Oberfläche transportiert. Ausgehend von der Hypothese, dass die Sauerstoffverarmung im Koloniezentrum die T4P-Dichte und damit den Zusammenhalt verringert, wird die Annahme aufgestellt, dass diese lokale Schwächung des Zusammenhalts der Auslöser für die Kolonie-Eversion ist. Um dies zu überprüfen, analysierten wir die räumlich-zeitliche Dynamik einzelner Zellen während der Reifung der Kolonie und stellten fest, dass die Eversion mit der Bildung einer sich ausdehnenden Hülle aus hypermotilen Zellen einhergeht, die vom Zentrum ausgeht. Wir kommen zu dem Schluss, dass die Eversion durch einen verminderten Zusammenhalt im Kern der Kolonie ausgelöst wird, der durch eine Sauerstoffverarmung im Zentrum der Kolonie entsteht.

Zusammenfassend lässt sich sagen, dass diese Studie das Zusammenspiel zwischen der T4P-Dynamik, der Antigenvariation und der Antibiotikabehandlung bei der Gestaltung der bakteriellen Lebensweise und der mechanischen Eigenschaften von *N. gonorrhoeae*-Kolonien verdeutlicht. Insbesondere wird gezeigt, dass die Aggregation eine Schlüsseldeterminante für die Antibiotikatoleranz ist.

Contents

Abbreviations

AOD	acousto-optic deflector
BSA	bovine serum albumin
CFU	colony forming units
DNA	deoxyribonucleic acid
EU/EAA	european union/ european economic area
G4	guanine-quadruplex motif
gfp	green fluorescent protein
GUI	graphical user interface
IR	infrared
IVX	isovitalex
MDK	minimum duration for killing
MIC	minimal inhibitory concentration
MSD	mean squared displacement
OD	optical density
PIV	particle image velocimetry
Px	pixels
RNA	ribonucleic acid
ROI	region of interest
T4P	type IV pilus/pili
WHO	world health organisation
wt	wild-type

1 Introduction

Bacteria primarily exhibit two distinct lifestyles: the planktonic lifestyle, in which they are mobile and exist as individual entities, and the biofilm lifestyle, in which bacteria are sessile, living in microbial communities embedded in a self-produced matrix [1]. In nature, bacteria mostly reside within biofilms, which are found in diverse habitats, such as seawater, groundwater and soil [2]. The biofilm lifestyle offers protection from external stressors, triggered by changes in the cell physiology, including metabolically dormant states and the protective characteristics of the matrix [3, 4]. It has been observed that numerous pathogenic bacteria, including *Pseudomonas aeruginosa*, *Vibrio cholerae*, *Staphylococcus aureus* and *Neisseria meningitidis* often form biofilms, particularly in the context of persistent and chronic infections [5–7]. The dense packaging of the cellular communities facilitates the spread of resistance, leading to bacteria becoming multi-resistant, posing a major health threat [8, 9]. Among these, *Neisseria gonorrhoeae*, responsible for the second most common sexually transmitted disease, gonorrhea, is of particular concern [10]. The notification rate for gonorrhea in EU/EEA countries increased by 321% between 2014 and 2023 [11] and antimicrobial resistance increased rapidly, further reducing treatment options [12]. In addition to an increase in resistance, recent studies have identified tolerant strains [13]. These strains exhibit prolonged survival times under high doses of antibiotics that exceed the minimal inhibitory concentration (MIC). The underlying mechanisms of antibiotic tolerance in *N. gonorrhoeae* remain to be elucidated, yet they are of significant interest, as it has been demonstrated in other bacterial species, such as *Escherichia coli*, that antibiotic tolerance can promote the emergence of highly resistant strains [14].

N. gonorrhoeae is a gram-negative bacterium that can form biofilms *in vitro* and *in vivo* during infection [15]. Gonococci form colonies via attractive cell-to-cell interactions mediated via their type IV pili (T4P) [16]. It was found that modification of T4P alters single-cell interactions, which in turn affect the properties of the multicellular aggregates of *N. gonorrhoeae*. Colonies undergo a phase transitions from gas-like to fluid-like to more solid-like by fine-tuning the single-cell interactions [17]. In *P. aeruginosa*, a link between viscosity and antibiotic susceptibility of biofilms grown with and without shear stress was found [18]. Nahum et al. concluded that the difference of antibiotic susceptibility depends on the penetration depth into the biofilm which is likely limited by the dense extracellular matrix [18]. The matrix of *N. gonorrhoeae* mainly consists of extracellular DNA and T4P [19], which was also found to stabilise early gonococcal colonies [20]. However, little is known about the connection of biophysical properties of gonococcal biofilms and antibiotic susceptibility. Since the biofilm lifestyle promotes tolerance [14], it is important to understand the interplay between the properties of the T4P and cell-to-cell interaction, and how the latter affects the material properties of the biofilm.

Finally, understanding the link between the material properties of the biofilm and antibiotic tolerance can facilitate the development of novel strategies for more effective treatment of biofilm-forming pathogens.

1.1 The Type IV Pilus

In order to form bacterial aggregates, bacteria have evolved a variety of mechanisms to attach to surfaces and attractively interact. These mechanisms include the production of specific adhesins and surface proteins, such as the Esp protein produced by *Enterococcus faecium*, which is located on the surface of the bacterium to initiate bacterial aggregation and biofilm formation [21]. Furthermore, exopolysaccharides (long carbohydrate chains) contribute to bacterial aggregation by binding to surfaces and other bacteria. For instance, *P. aeruginosa* produces alginate when attached to a substrate, leading to biofilm formation and stabilising the maturing biofilm [22].

A prominent mechanism for aggregate formation is the active attractive interaction mediated by T4P. Many pathogenic bacteria, including *Acinetobacter baumannii*, *P. aeruginosa* and *N. gonorrhoeae* [23–25], possess T4P – highly dynamic cell appendages which are characterised by their versatility as bacterial tools. The T4P facilitates bacterial adherence, motility and active cell-to-cell interactions [26, 27], thereby contributing to the formation of bacterial aggregates. As already mentioned, in the case of *N. gonorrhoeae*, this is the major driving force for bacterial aggregation [28]. The T4P machinery functions as a bacterial motor, generating forces of up to 100 pN [29]. Furthermore, it plays a crucial role in pathogenicity, as it has been shown that in several pathogenic bacterial species, e.g. *V. cholerae* or pathogenic *E. coli*, T4P disruption leads to decreased virulence [30, 31]. Additionally, to avoid immune responses, the T4P-related genes are highly variable and undergo antigenic and phase variations [26], which highlights the importance of understanding the composition, structure and function of the pilus filament.

In this study, we investigated how T4P-mediated attractive forces between neighbouring bacteria are affected by antibiotics and explored the dynamics of T4P under external stress conditions of *N. gonorrhoeae*. We then investigated how pilin variation affects bacterial lifestyle and antibiotic tolerance beyond immune surveillance.

1.1.1 Structure and Antigenic Variation of the Type IV Pilus

The T4P is a highly dynamic surface-exposed fibre measuring several micrometers in length and a diameter of 5-8 nm [32, 33]. It is composed of subunits, with the major subunit being PilE [34]. The PilE protein has a ladle-shaped structure, which is then dynamically assembled and disassembled in a helical fashion to form the filamentous structure [35] (Fig. 1.2). In this way, the pilus filament forms a hydrophobic inner core and a functional surface. The functionality of the pilus fibre is dependent on its surface, which is specified by the incorporation of smaller pilins, such as ComP (important for DNA uptake) and PilC (important for adherence) [36, 37]. The fibre has a mechanically stable and flexible structure with helical symmetry [32, 33]. Subunit assembly relies on ATP hydrolysis leading to rapid polymerisation and depolymerisation from a pool of subunits located in the inner membrane. The two ATPases, PilF and PilT, are hexameric proteins that bind stochastically to the T4P machinery, leading to pilus fibre extension and retraction, respectively [33]. The T4P machinery consists of the pilus filament, a complex protein structure (PilMNOP) anchored to the inner membrane and a secretin pore (PilQ) in the outer membrane (Fig. 1.1). The PilMNOP complex, which consists of PilM, PilN, PilO and PilP, stabilises the pilus fibre in the periplasm [38, 39]. An integral membrane protein (PilG) anchors the fibre to the inner membrane and the secretin pore allows the fibre to polymerise in the extracellular space.

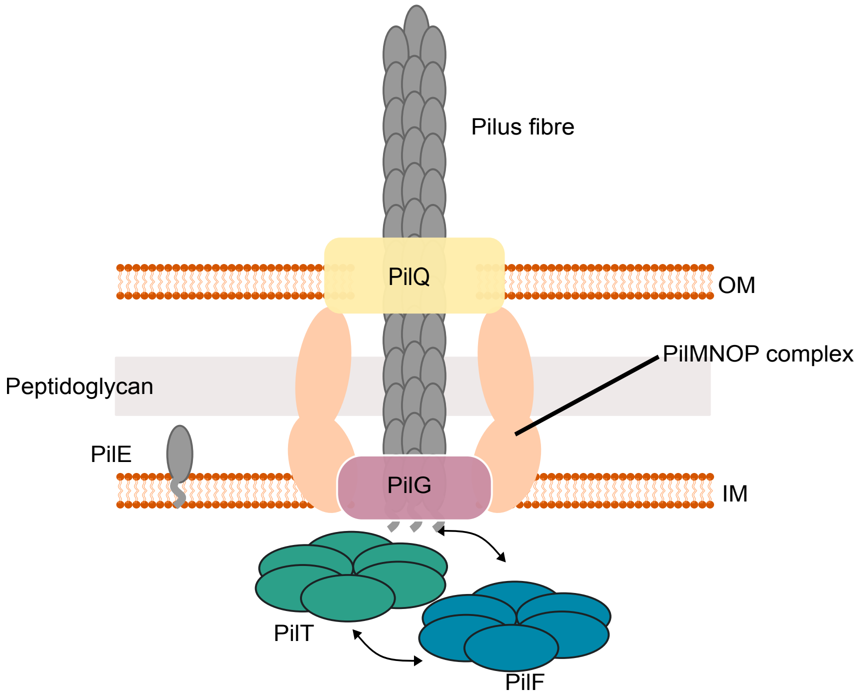

Figure 1.1: Schematic of T4P structure according to [35]. The pilus complex spans the inner (IM) and outer membrane (OM). It is anchored to the inner membrane via PilG and passes the outer membrane through a membrane pore PilQ. The PilMNOP complex stabilises the pilus in the periplasm. The two hexameric ATPases PilF and PilT fuel the polymerisation and depolymerisation, respectively.

The Major Pilin of the Type IV Pilus - PilE

PilE, the major subunit of the pilus fibre, has been the subject of a detailed cryo-electron microscopy study. The pilin of the MS11 *N. gonorrhoeae* strain revealed a ladder-shaped structure with an elongated size of (85 x 34 x 26 Å) [34]. The detailed structure showed an N-methylated N-terminus, a conserved hydrophobic N-terminal region and a C-terminal domain wrapped up by a four-stranded β-sheet, forming the globular head domain [33]. When a fibre is formed, the N-terminal regions form an α-helical spine which anchors to the head domains, providing the functionality of the pilus. This structural arrangement leads to a high degree of flexibility of the fibre [40]. The surface of the pilus fibre is governed by the β-sheet containing an α-helix with post-translational modifications at positions S63 and S68 and a disulphide bond, which forms a β-hairpin that contains a hypervariable loop also referred to as D-region (Fig. 1.2) [33].

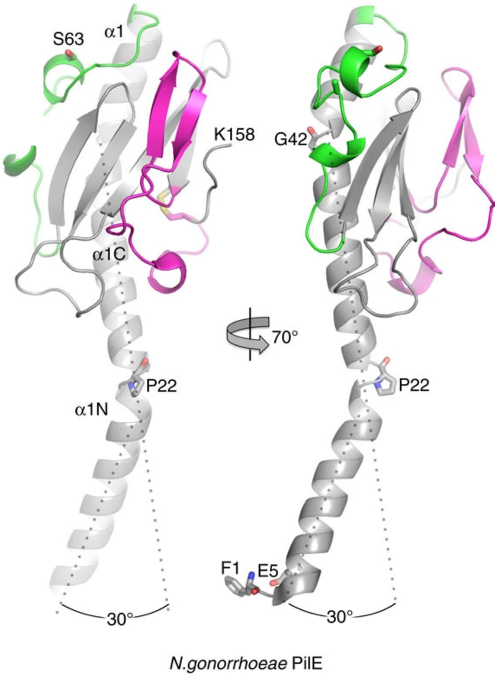

Figure 1.2: Predicted protein structure of PilE. The $\alpha\beta$-loop, also containing the serine S63 and S68 which are post-translationally modified, is shown in green and the hypervariable D-region in magenta. Adapted from [40] under CC-BY license.

Antigenic and Phase Variation

One of the most striking features of *N. gonorrhoeae* is its ability to modify surface-exposed structures to evade the host immune system, including PilE and opacity proteins [26, 41]. For *pilE*, two distinct mechanisms have been identified: antigenic variation, which leads to altered amino acid sequences of PilE, and phase variation, which leads to either piliated or non-piliated cells.

It has been determined that up to 18 distinguishable *pilS* sequences are present in the genome of *N. gonorrhoeae* [26]. The *pilS* genes share high sequence identities but lack a promoter and the N-terminal region of *pilE*. It has been believed that these regions are silent, however, it was shown that some of these loci are transcriptionally active and expressed as small RNAs but the function remains unknown [42]. These sequences recombine with *pilE* by replacing sequence sections of dozens of amino acids at a rate of $1.7 \cdot 10^{-3}$ events/cell/generation [43, 44]. This process is contingent on *recA* and the guanine-quadruplex motif (G4), upstream of *pilE*. Deletion of the G4 motif has been shown to impede antigenic variation [45]. The variability of *pilE* is heterogeneous and can be sub-divided into three variability regimes: a conserved region (the N-terminal and the disulphide bond formed by two cysteines), a semivariable region (the globular head domain) and a hypervariable region (the tail of *pilE*, also surface exposed and located in the head domain) [33] (Fig. 1.3a). In *N. meningitidis*, a functional map of the amino acid sequence of PilE was determined with regard to adhesion, biogenesis and aggregation. To this end, a deep mutational approach was used, by exchanging single amino acids with a coverage of 90%. These were further characterised considering their phenotypic functionality

[46]. The study revealed the presence of an electropositive cluster around the position K140 in the hypervariable region is necessary for attractive single-cell interactions. Adhesion was found to be associated with a region downstream of this aggregation region.
Next to antigenic variation, *pilE* can undergo phase variation. The *pilE* gene contains a poly C-stretch making it likely to undergo slipped strand mispairing during replication. This results in truncation or extension of the homopolymeric stretch, leading to the deactivation of the *pilE* gene and thus to non-piliated bacteria. Analogously, if a single base is added or truncated, the gene can be switched on again [26, 47] (Fig. 1.3b).

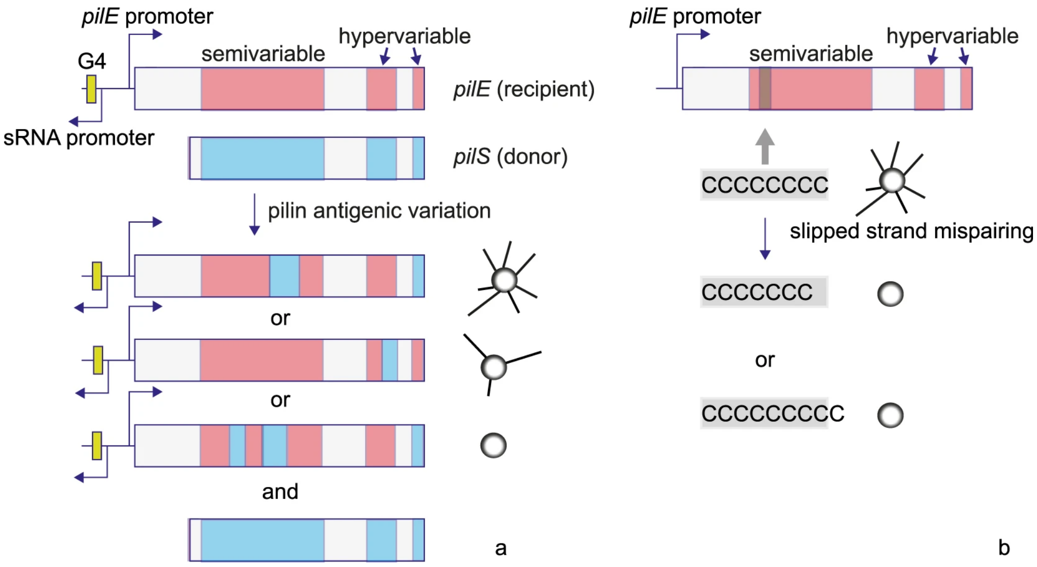

Figure 1.3: a) There are semi- and hypervariable regions in the gene encoding the major pilin PilE. *pilS*, can partially recombine into the *pilE* recipient, defined as antigenic variation. This process depends on the G4 motif, upstream of *pilE*, and *recA*. The pilin sequence of the resulting variant is modified and often non-functional, generating non-piliated variants [48]. b) Phase variation due to homopolymeric repeats is a process that can lead to non-piliated cells. Through slipped-strand mispairing during replication, the homopolymeric stretch is extended or truncated, which can switch the gene on or off. Adapted from [47] under CC-BY license.

1.1.2 The Type IV Pilus Motor

Directed movement is crucial for numerous cellular functions, including transport within the cell and cell division [49]. These processes necessitate energy, which is typically stored as chemical energy in high-energy covalent bonds and subsequently converted into mechanical energy. As previously discussed, T4P are highly dynamic surface-exposed structures. The motor is fueled by two ATPases which bind to the motor, leading to either retraction or elongation of the fibre by removing or adding sub-units [50, 51].

Characterisation of Type IV Pilus Mediated Forces

T4P dynamics have been studied with several techniques including optical tweezers, traction force microscopy and micropillars [52–55].

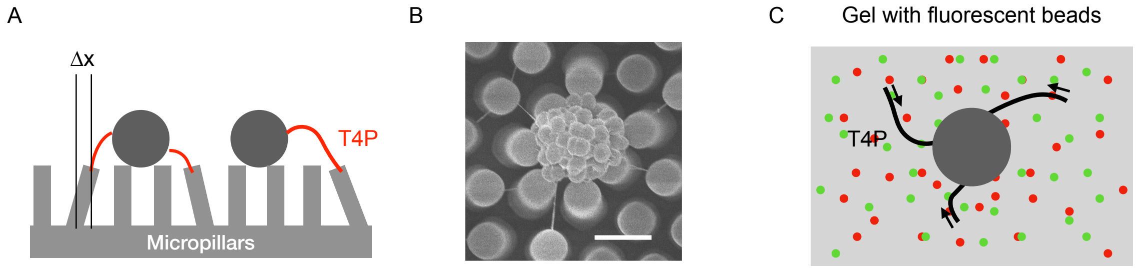

Figure 1.4: A) Schematic of the micropillar assay. The force can be determined via Hooke's law $F = -k \cdot \Delta x$ with k, the stiffness of the pillars and Δx the displacement of the pillar due to a force exerted by a retracting T4P. B) Scanning electron microscopy micrograph of a gonococcal colony with T4P (the pillars were molded in polymethylsiloxane to enable electron microscopy), adapted from [54] under CC-BY license. C) Schematic of the traction force microscopy technique. Red and green fluorescent beads are embedded in the gel (grey). If the bound T4P retract, the force is displayed by deformation of the gel which is tracked by displacements of the beads. The use of two colors increases the resolution during tracking [55].

The micropillar assay was utilised to investigate the forces of pili bundles on a substrate in *N. gonorrhoeae*. Here, the force sensor consists of pillars of an elastic hydrogel, which are displaced when a force is exerted. With this assays forces ranging from pN to nN could be determined, including single pili and pili bundles [54] (Fig. 1.4A, B). Via traction force microscopy the forces exerted during twitching motility of *Myxococcus xanthus* were investigated and showed average forces of about 55 pN [55]. For traction force microscopy cells are placed on an elastic gel with embedded fluorescent beads. During cell migration, the gel is deformed which can be tracked via the fluorescent beads [56] (Fig. 1.4C).

Both, the micropillar assay and the traction force microscopy are methods suitable to measure forces with a high cell throughput, but are less sensitive for lower forces [55, 57]. Optical tweezers are a powerful tool for investigating T4P dynamics and T4P mediated forces [29, 52] (Fig. 1.5). A particle or bacterium is trapped in a highly focused laser beam and gets displaced due to attractive interactions, here, mediated by T4P. The displacement of the trapped particle Δx is proportional to the force according to Hooke's law $F = -k \cdot \Delta x$ where k is the stiffness of the trap (Methods 2.2). Using single optical traps, T4P-mediated attractive interactions of *N. gonorrhoeae* were observed when single cells were brought into close proximity to a colony and subsequently pulled towards it [53]. Single optical traps also enable the study of bacterial interactions with abiotic or functionalised surfaces [53]. Interactions of gonococci with a trapped bead revealed that pilus retraction events depend on the ATPase PilT and that T4P are capable of generating forces of up to 100 pN [29]. Moreover, it was also shown that pilus elongation is force dependent [58]. In a similar experimental setup but in force clamp mode, it was found that the retraction velocities have a bimodal distribution and that the bimodality depends on the applied force and the concentration of PilT [52] (Fig. 1.5A). In the absence of PilT, it has been observed that the motor is able to retract, albeit with strongly diminished forces and velocities [59]. Further experiments, in which a bacterium was trapped in close proximity to a T4P-coated surface, demonstrated that pili-pili interactions are strongly reduced under anaerobic compared to aerobic conditions [60].

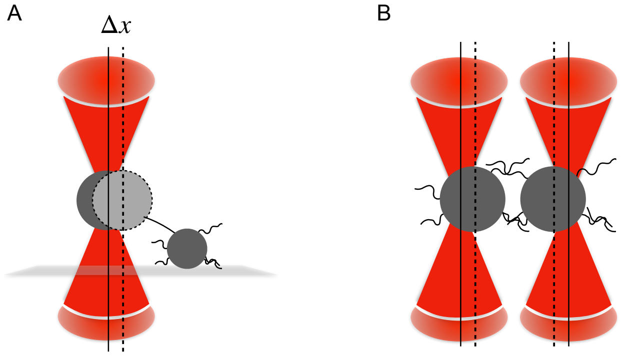

Figure 1.5: A) Single optical trap experiment. A carboxylated bovine serum albumin-treated latex bead is trapped and a bacterium, which is attached to the surface, is interacting with the bead. Experimental set-up according to [52]. B) Dual optical trap experiment according to [16]. The bacteria are trapped and displaced by T4P mediated attractive interactions between the bacteria. The equilibrium position is marked with a line and the displaced position is marked with a dashed line.

To analyse cell-to-cell interactions, a dual optical trap has been found to be a powerful tool for identifying the interaction states and their characteristics [16, 59, 61] (Fig. 1.5B). When two bacteria attractively interact while trapped in an optical trap, they are displaced from the centre of the traps during retraction of the pili until the bond breaks (Fig. 1.6). The characterisation of these single-cell interactions has revealed five distinct interaction states: retraction, elongation, bundling, pausing and rupture [16]. During retraction, the cells are displaced from their equilibrium positions. When the pili elongate while they are bound, the cells gradually return to their equilibrium positions. If retraction or elongation stops out of the equilibrium position, this interaction event is defined as pausing. A fourth cell-to-cell interaction state is the bundling state, which is defined by a previous retraction event of multiple pili (bundles), then a few bonds break but the force post-rupture is not zero, meaning not all pili ruptured, but single pili bonds remained. A rupture event is characterised by a bond breakage.
In *N. gonorrhoeae*, it was found that the average rupture force of the $\Delta G4$ MS11 strain is 50 pN and the average probability to be bound over the interaction periods was determined to be 0.15 [16]. Post-translational modifications of the major pilin have been shown to influence both the average rupture force and the probability to be bound [59, 62]. Furthermore, it was demonstrated that the interaction probabilities of the states are altered when non-functional PilT is introduced by means of increased elongation and decreased retraction probabilities [61].

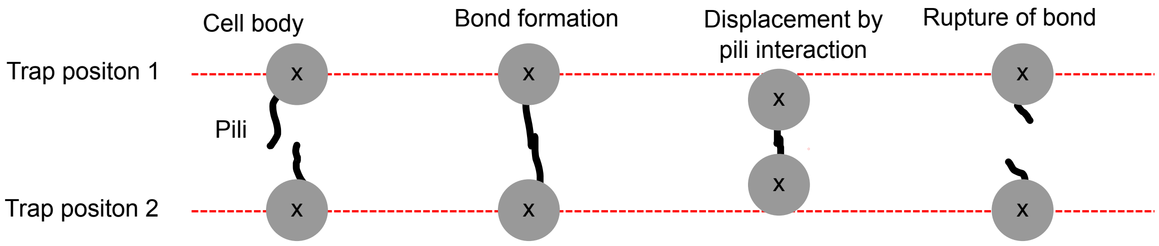

Figure 1.6: Sketch of bacterial cell-to-cell interactions when trapped in two time-shared optical tweezers. The bacteria are displaced from their equilibrium positions during pilus retraction until the bond ruptures.

1.1.3 Direct Visualisation of Type IV Pilus Dynamics

The precise mechanism of cell-to-cell interactions remains to be elucidated, as it is not known how pilus-pilus interaction takes place [27]. One approach addressing this questions is the direct visualisation of the T4P dynamics and interactions.

In *P. aeruginosa*, fluorescent labelling has been employed via a Cy3 amino-specific fluorescent dye [63]. Total internal reflection microscopy of the labelled pili revealed elongation and retraction velocities of 0.5 µm/s [63]. However, this protocol was not applicable for further studies [64].

Another approach to visualise the T4P of *P. aeruginosa* during twitching motility is based on label-free interferometric scattering [65]. The major advantage of this approach is that the pilus does not need to be modified or externally labelled, allowing the dynamics to be studied without external perturbation. However, the resolution was limited to pili with a length of 3 µm and labelling would be of interest if one wants to distinguish two interacting pili [65].

Recently, a protocol for fluorescent labelling based on maleimide chemistry has been developed. The introduction of a cysteine in the major pilin, which is surface-exposed and acts as target for the dye, resulted in fluorescently labelled pili [66]. This novel protocol has been successfully employed in several bacterial species, such as *Caulobacter crescentus*, *V. cholerae* and *P. aeruginosa* [64, 67, 68]. Image analysis of retraction and elongation of the T4P revealed stochastic and competitive binding of the motor ATPases [64] which is in good agreement with previous results from laser tweezers experiments [52]. In this study, we applied this visualisation approach to *N. gonorrhoeae* and investigated how the T4P dynamics change under external stress conditions.

1.1.4 Twitching Motility

It is well-documented that bacteria often attach to surfaces or host cells [2]. In such crowded environments, they are compelled to compete with other bacterial species for limited resources. In order to address this, bacteria have evolved motility mechanisms that facilitate exploration of their environment and the navigation of chemical gradients. A notable example of this is the bacterium *M. xanthus*, which has developed, next to twitching motility, a surface motility known as gliding. This mode of motility is driven by motor complexes that move in a helical path along the inner membrane. These motor complexes exert a propulsive force on the cell body, thereby generating the gliding motion [57, 69, 70]. *P. aeruginosa* and *N. gonorrhoeae* use their T4P to perform twitching motility, which is driven by the pilus cycling through elongation, retraction and attachment [24, 71, 72]. For gonococci, this motility mode follows a tug-of-war mechanism. When the bacterium attaches to a surface, usually, more than one pilus is bound to the surface (Fig. 1.7A) [71]. Subsequent, depolymerisation of the pili (retraction) leads to forces acting in different directions on the bacterial cell body. The bacterium then moves in the direction of the highest force (Fig. 1.7A). Linear movement of the bacterium is only given on the time scale of a single retraction event. Under the assumption of isotropic pilus production and a spherical shaped bacterium, as it is found for *N. gonorrhoeae* [71], the displacement track on larger time scales follows a random walk [49] (Fig. 1.7B).

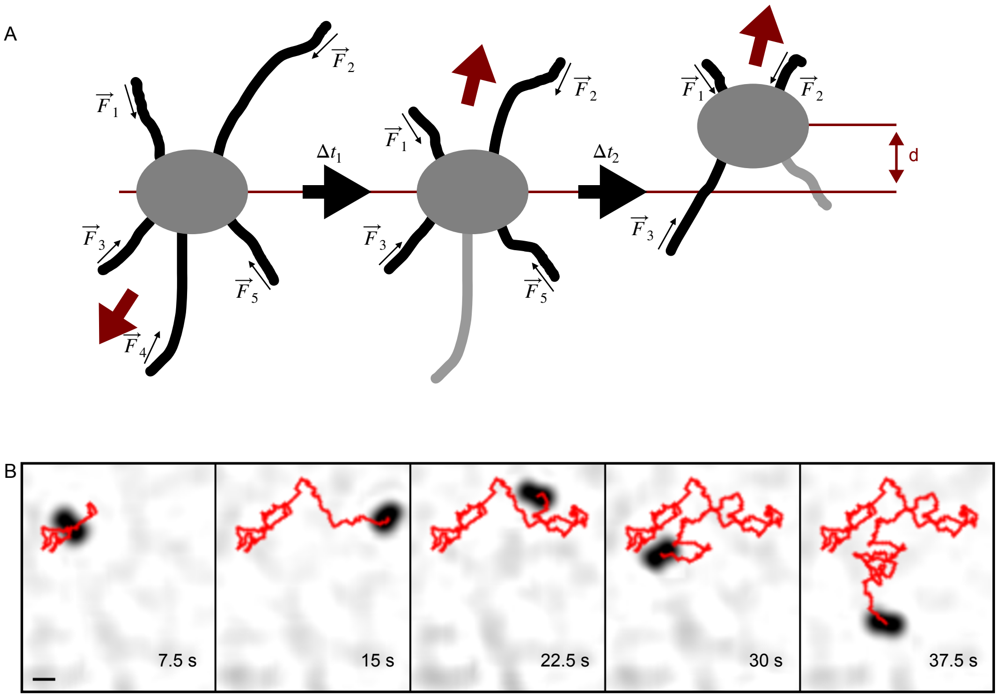

Figure 1.7: A) Tug-of-war mechanism underlying the twitching motility of *N. gonorrhoeae*. In the beginning, 5 pili are bound to the surface each exerting force on the cell body, the sum of the forces representing the net force (red arrow). After time Δt_1 pilus 4 detaches (shown in light grey) and the net force pointing in the opposite direction. When pilus 5 detaches after time Δt_2, the force is high enough to pull the bacterium in that direction with a displacement length d. B) Time-lapse of tracking a bacterium twitching on a BSA-coated surface over 37.5 s with the frame rate of the video of 10 Hz. The displacement track is shown in red. Scale bar = 0.5 µm.

A particle that moves along a two-dimensional surface with the same probability for every direction, the motion is described as diffusive with a mean squared displacement (MSD) over time of $\langle r(t)^2 \rangle = 4Dt$ with the diffusion constant D. However, for twitching motility, the steps are found to be correlated [73]. This is explained by a directional memory effect due to repeated polymerisation of stable pili complexes. Including the assumption of a correlation which decreases exponentially over time

$$\left\langle \vec{v}(t)\vec{v}(t+\tau) \right\rangle = v^2 exp(-\tau/\tau_c) \tag{1.1}$$

with the characteristic velocity v and the correlation time τ_c, the MSD of a correlated random walk is given by

$$\left\langle r(t)^2 \right\rangle = 2\tau_c v^2 (t - \tau_c(1 - \exp -t/\tau_c)) + A. \tag{1.2}$$

For *N. gonorrhoeae*, a typical correlation length of $l_c = v \cdot \tau_c = 2.2\,\mu\text{m}$ was found with a characteristic pilus length of 0.9 µm. From this, it was followed that 2.5 retraction events are necessary to show this persistence in movement [71]. Furthermore, it was found that the MSD correlates with the number of T4P [71]. During oxygen depletion, it has been observed that the twitching motility switches from a high speed mode of 1.5 µm/s to a low speed mode of 0.5 µm/s [74].

1.2 Multicellular Aggregation: Bacterial Biofilms

Biofilms represent the most abundant lifestyle of bacteria [2]. The formation of biofilms is initiated by adherent planktonic cells attaching to a surface, where bacteria attractively interact and grow, thereby forming small cellular aggregates, so called microcolonies. These bacteria start to produce an extracellular matrix comprising polymer substances, which reduces the motility of single cells. During the maturation of the biofilm, single cells can disperse again and generate a new biofilm [1, 75] (Fig. 1.8). Biofilm development is accompanied by changes in gene expression and local differentiation, resulting in phenotypic heterogeneity in bacterial communities [76].

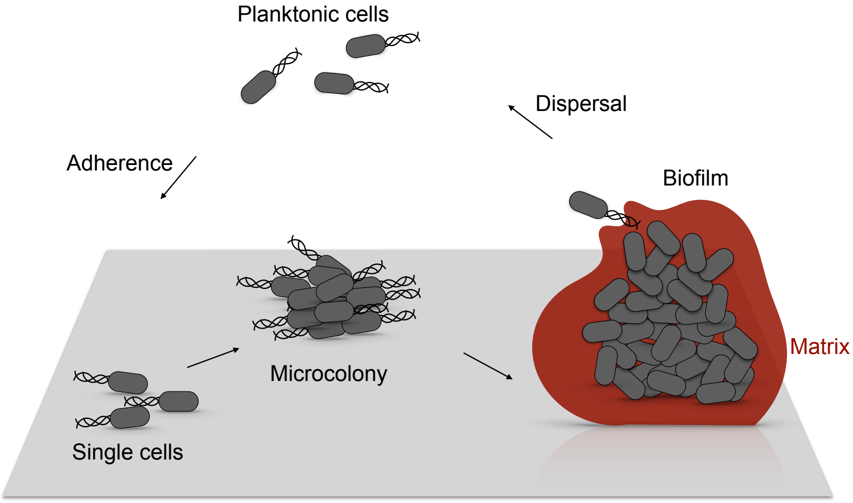

Figure 1.8: Life cycle of a biofilm according to [75]. Initially, single cells adhere to a surface and start forming small cellular aggregates. Then, cells produce extracellular matrix. In mature biofilms, cells are embedded in an extracellular matrix and single cells can disperse again, generating new biofilms.

In *P. aeruginosa* biofilms, it has been demonstrated that over 50% of the proteome is subject to differential regulation in comparison to the planktonic lifestyle [75]. Given the prominence of social interactions in circumstances where cells are in close proximity, the positioning and structure of cells are important parameters of the biofilm [1]. Furthermore, due to the three-dimensional structure of the bacterial aggregates, nutrient and oxygen gradients arise, leading to physiological changes and the cells adapting their metabolism. Cells located at the surface exhibit continued growth, while cells situated deeper within the biofilm have reduced access to nutrients and oxygen, resulting in the use of alternative metabolic pathways or the state of dormancy [77]. Transcriptome and proteome analysis of two-days old gonococcal colonies revealed a shift towards anaerobic respiration [78, 79], in particular AniA, a respiratory nitrite reductase, was observed to be upregulated in depth of the biofilm [80]. The extracellular matrix provides a protective barrier against external stresses, such as antimicrobials or immune responses during infection [81, 82]. For instance, it has been demonstrated that *curli* polymers within the extracellular matrix of *E. coli* impede the transportation of phages into the biofilm [83]. Moreover, the presence of these densely packed cellular communities has been observed to enhance horizontal gene transfer, thereby promoting the emergence of bacterial communities that are resistant to multiple antibiotics, a phenomenon that is of significant concern in medical contexts [84]. This highlights the importance of studying biofilm mechanics, structure and gene regulation.

1.2.1 The Physics of Aggregation

Bacterial biofilms have mechanical properties that are similar to eukaryotic tissue in various aspects. While the mechanical properties of tissue have been well characterised, biofilm mechanics is an emerging field [85]. At the molecular level, the mechanics are controlled by steric repulsion, bridging attraction, depletion attraction and osmotic pressure [17].

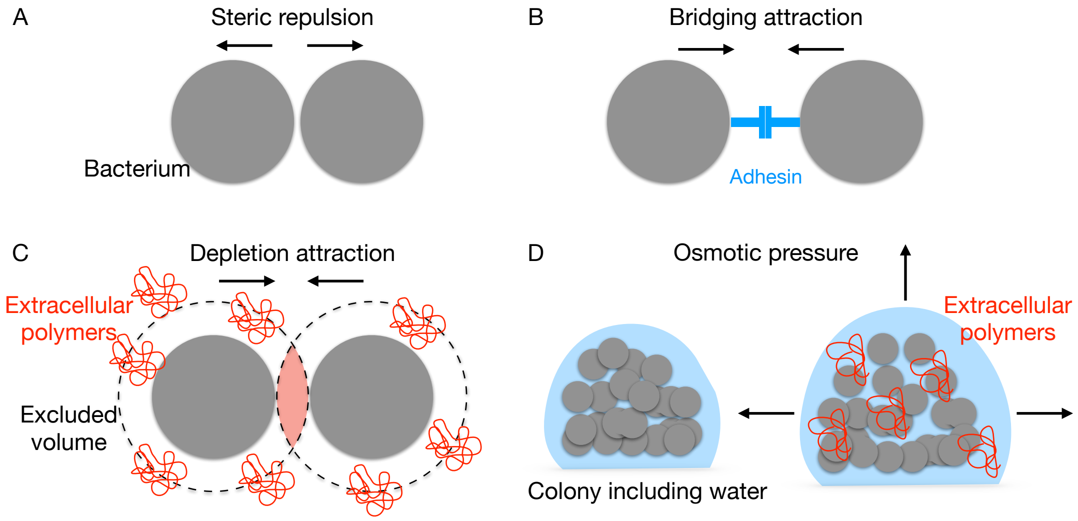

Figure 1.9: Physical interaction during aggregation according to [17]. A) Steric repulsion, B) bridging attraction, C) depletion attraction and D) osmotic pressure.

On the one hand, cells have a well-defined shape and size, which leads to steric repulsion between cells (Fig. 1.9A). On the other hand, they may possess bridging factors – adhesins on the cell surface – which lead to attractive interactions described by electrostatic interactions, polar attraction and hydrogen bonding (Fig. 1.9B). Examples of adhesins are matrix components, such as alginate in *P. aeruginosa* biofilms, RbmA in *V. cholerae* biofilms, but also surface-exposed protein fibres such as the T4P in *N. gonorrhoeae* [16, 22, 86, 87]. In colonies, cells are surrounded by extracellular polymers present in the matrix, leading to excluded volume effects. Entropy is maximised when bacteria cluster together to minimise the excluded volume (Fig. 1.9C). These matrix components can also lead to osmotic pressure, as the concentration in the biofilms is higher than the surrounding environment, leading to influx of medium and swelling of the biofilm (Fig. 1.9D). This has already been shown for *V. cholerae* and *Bacillus subtilis*, where osmotic swelling leads to biofilm expansion on surfaces [88, 89]. In addition, growth of inner cells pushes cells outwards, creating pressure on neighbouring cells.

1.2.2 Determinants of Colony Morphology Formed by Rod-Shaped Bacteria

Cellular ordering within multicellular communities depends on cell shapes and cellular interactions, for example mixing *E.coli* with different cell morphologies leads to cellular patterning in colonies [90]. In two dimensions, rod-shaped bacteria show patterns with nematic domains [91] (Fig. 1.10A). The size of the domain is determined by cell size and growth rate. The larger the aspect ratio of the cells, the larger the domains. An increased growth rate leads to smaller domain sizes [91]. For non-motile bacteria, verticalisation depends on the growth pressure which is needed to overcome the cell-surface interaction [92] (Fig. 1.10B). The transition from a two-dimensional layer to a three-dimensional colony occurs at a critical colony size, which depends on cell size and cell-surface interaction [92].

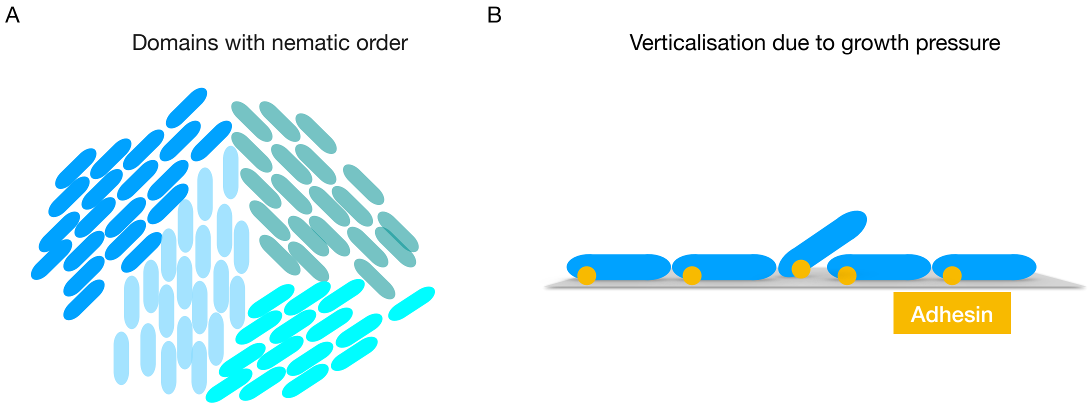

Figure 1.10: A) Domains of nematic order of rod-shaped bacteria in two dimensions. B) Transition from two-dimensional cell layers to three-dimensional colonies of rod-shaped bacteria.

An example for a rod-shaped, non-motile bacterium is *V. cholerae*, which initially expands in two dimensions during growth. At a cell number in the order of 20-100 cells, cells in the centre align vertically and cell division maintains this order, leading to nematic order and vertical growth [87, 93, 94]. The vertical orientation is dependent on the adhesion of the cells to the substrate, as reorientation was not observed in cells that were unable to adhere to the substrate [87]. Cellular ordering within these biofilms is promoted by growth, cell alignment and cell-to-cell interactions [94, 95]. In motile *M. xanthus*, which also forms two-dimensional cell layers with nematic order, new layers are formed independently of colony size. Because the bacteria are motile, they form an active nematic liquid crystal. As the bacteria migrate, they experience anisotropic friction along their orientations and topological defects induce the formation of new layers [96].

1.2.3 Determinants of Colony Morphology Formed by Spherical Bacteria

In colonies formed by attractively interacting cocci, liquid-like ordering has been observed [16, 97]. Effective surface tension, arising from attractive interactions between bacteria, leads to a minimisation of the aggregate's surface area. As in liquid systems, this energy minimisation results in the formation of a spherical shape of the bacterial colonies.

N. gonorrhoeae forms spherical shaped microcolonies within minutes mediated by attractive interactions via its T4P [60, 98]. Single-cell tracking of colony fusion events and analysis of the local order revealed liquid-like ordering of gonococcal colonies. By modifying single-cell interactions, colonies show phase transitions from fluid-like to solid-like [16]. In agreement, simulations of attractively interacting bacteria showed that single-cell interactions control motility and structure of colonies [98].

Sorting of gonococcal colonies, according to the differential strength of adhesion theory, was observed when cells showing differences in single-cell interactions via changes in piliation levels, post-translational modifications, or antigenic variation were mixed [47, 59, 62]. The differential adhesion theory [99, 100] states that segregation is caused by the active movement of cells in the direction where they can exert the highest force [17].

The within-colony motility is governed by a constant tug-of-war mechanism between neighbouring cells [17]. Gonococcal colonies show heterogeneous motility with a highly motile shell and a less motile inner core [98, 101]. For the motility of single cells embedded in colonies, it was observed that the motility, depending on the time scale analysed, transitions from a ballistic movement for very short time scales to a caging regime for time scales beyond the time scale of a single pilus retraction. In this caging regime, cells show diffusive behaviour [102].

Furthermore, analysis of the spatio-temporal dynamics of growth revealed reduced cell division in the centre of gonococcal colonies [103]. This is consistent with nutrient and oxygen gradients towards the centre of the colony [1, 104]. This assumption has been further supported by the recent observation of collective membrane polarisation of gonococcal colonies [105], which correlated with decreased oxygen and growth [103] in the centre of the colonies.

1.3 Antibiotic Treatment: Resistance and Tolerance

The discovery of the antibiotic penicillin by Sir Alexander Fleming in 1928 [106] revolutionised the treatment of infectious diseases. In the period between 1950 and 1970, many new classes of antibiotics, describing distinct targets and origins, were discovered [107]. As a result of misuse and overuse of antibiotics, bacteria evolved mechanisms towards resistance and tolerance, which displays a major global health concern [108, 109]. Resistance is defined by the minimum inhibitory concentration (MIC) of the specific antibiotic, which results in the loss of the bacterium's ability to replicate [110]. However, it was also found that bacterial populations survive antibiotic treatment with doses far beyond the MIC without acquiring resistance mechanisms [111]. These mechanisms are antibiotic tolerance and persistence [110]. Tolerance is defined by slower killing of the population and can be quantified by the minimum duration for killing (MDK) 99% of the population [112] (Fig. 1.11).

Persistence is defined by a subpopulation with higher tolerance than the rest of the population, resulting in biphasic killing curves [110]. Persistence and tolerance are only defined for bactericidal antibiotics, as bacteria are expected to survive a transient exposure to treatment with a bacteriostatic antibiotic [111]. Interestingly, it has been shown that for *E. coli* the prolonged survival due to tolerance promotes the emergence of higher levels of resistance compared to a resistance-evolved but previously less tolerant strain [113]. These findings highlight the importance of understanding the mechanisms of antibiotic resistance and tolerance in order to find new approaches to deal with them.

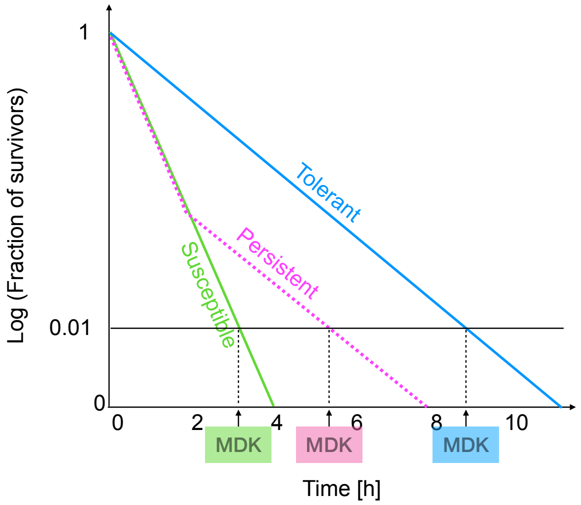

Figure 1.11: Typical killing kinetics of susceptible (green), persistent (pink) and tolerant (blue) bacterial populations during treatment with antibiotics above their MIC, according to [110, 111]. The slope of killing for the tolerant bacterial population is decreased when compared to the susceptible one. The persistent population is a more tolerant subpopulation.

Recently, several experimental protocols have been developed to determine the MDK and killing kinetics of planktonic bacteria. One such approach is assessing surviving bacteria after treatment by measuring the optical density (OD) of regrowth [110]. However, this method is not suitable for determining the killing kinetics of biofilm-forming bacteria, as optical density is an unreliable measure due to bacterial aggregation. To accurately count viable bacteria, biofilms must be disrupted, and the bacteria must be plated. The resulting colonies provide absolute numbers of treatment-surviving bacteria. Another protocol that may facilitate the study of planktonic bacteria is the tolerance disc assay. In this method, bacteria are plated in the presence of an antibiotic disc with a defined diffusion radius of the inhibition zone. If bacteria exhibit tolerance, they appear during regrowth at the edges of the death zone once the antibiotic has diffused away [114]. However, recently, it has been shown that antibiotics kill more efficiently when bacteria grow in rich medium [115]. It follows that counting colonies on plates is prone to error because plating on very rich nutrient sources can lead to cell death of previously viable bacteria as they lose viability after exposure to the nutrient-rich plates, as has been shown for fluoroquinolone-treated *E. coli* [115, 116]. One way to solve this problem is real-time single cell assays, which have been shown to be more accurate in distinguishing between susceptible, resistant and tolerant subpopulations in *Salmonella* [115].

1.3.1 Bacterial Survival Mechanisms under Antibiotic Treatment

At the single-cell level, bacteria have evolved resistance mechanisms. These mechanisms include enzymatic degradation, efflux pumps, reduced permeability or target-site modification [108] (Fig. 1.12). Genetic differences arise mostly due to *de novo* mutations or horizontal gene transfer [117]. Furthermore, at the level of individual cells, bacteria that survive antibiotic concentrations above the MIC can down-regulate their metabolism, which has been shown to increase tolerance [118] or being persisters in dormancy state [119]. For example, *E. coli* produces a protein, chaperone DnaJ, that is toxic to the cells. This inhibits growth and renders the bacteria highly tolerant to ampicillin and ciprofloxacin [120]. A similar mechanism is known for toxin-antitoxin systems to induce persistence of bacteria [121]. Tolerance mutations linked to dormancy have been found during laboratory evolution experiments. These include mutations that optimise the lag-time before regrowth in sequential antibiotic treatments [122]. Genes associated with increased tolerance have been linked to SOS response, oxidative stress response, ribosomal activity and biofilm formation [123].

The biofilm lifestyle provides many conditions that promote antibiotic tolerance. Due to nutrient and oxygen limitation in the centre of biofilms, bacteria show reduced metabolism which protects from antibiotic treatment. Furthermore, the biofilm matrix and the close packaging facilitates horizontal gene transfer and social interactions, leading to fast spread of resistance genes. It was also observed when comparing planktonic and biofilm forming populations, biofilms show higher numbers of persister cells [3, 8] (Fig. 1.12).

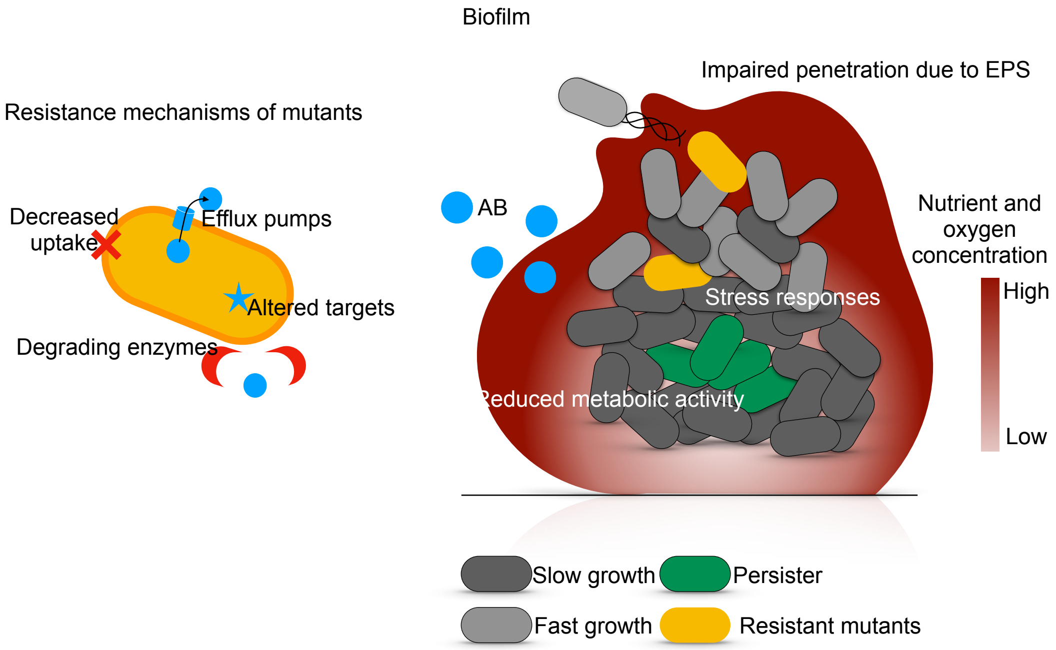

Figure 1.12: Survival mechanisms of bacteria against antibiotic treatment at the single-cell level (left) and the multicellular level (right), according to [124].

1.3.2 Antibiotic Treatment of Gonococcal Biofilms

N. gonorrhoeae has been observed to develop resistance to first-line and second-line empirical treatment as well as to several classes of antibiotics, including sulfonamides, penicillins, tetracyclines, fluoroquinolones, macrolides and cephalosporins [125, 126]. Resistance of *N. gonorrhoeae* is well understood and characterised genetically [127]. However, little is known about the mechanisms of tolerance. Recently, tolerant strains to ciprofloxacin, azithromycin and ceftriaxone of patients and WHO reference strains have been reported [13]. Using the disc test, it has been shown that tolerance to ceftriaxone can develop after only two cycles of sequential treatment [128].

Aggregation has been demonstrated to protect bacteria from ceftriaxone treatment [129]. Enolase, a glycolytic enzyme related to oxidative stress, has been identified as important for tolerance to ceftriaxone [130]. Moreover, collective membrane hyperpolarisation has also been observed in bacterial colonies, protecting cells from kanamycin treatment [105]. Reduced growth in the centre of gonococcal colonies [103] could lead to protection from antibiotics through reduced metabolism. However, it is still unclear which other mechanisms of biofilm formation are involved in antibiotic tolerance.

1.4 Aims and Goals of the Study

Biofilm formation is a key factor for antibiotic tolerance [8]. The human pathogen *N. gonorrhoeae* forms biofilms whose morphology is governed by the properties of the T4P. However, at the start of the project, it was unclear how T4P properties relate to antibiotic tolerance.

We approached this with the question how external stresses including antibiotic treatment affect T4P dynamics. Following a recently established approach for other bacterial species [66], we developed a method for directly visualising T4P dynamics of *N. gonorrhoeae*. In particular, we developed semi-automated image analysis tools for determining the T4P production rate as well as the T4P retraction and elongation velocities. We then compared these parameters under a variety of stress conditions, including antibiotics, with the control condition.

Then, we addressed the question how the altered T4P dynamics under stress affect the mechanical properties of gonococcal colonies. Using laser tweezers, we analysed the cell-to-cell interaction under antibiotic treatment. We determined interaction probabilities and could attribute these to changes of colony dynamics and structure.

T4P are major targets for the immune surveillance [26]. Through antigenic variation of the major pilin, *N. gonorrhoeae* constantly change their T4P and thus their cell surface, which helps them to evade the immune system. We hypothesised that variation of the pilin sequence affects other functions of T4P, including cell-to-cell attraction. We addressed this hypothesis in collaboration with Lisa Craig (Simon Fraser University, Canada) and Paul G. Higgins (University Hospital Cologne). The strategy was to replace the major pilin of the laboratory strain by pilins from clinical isolates and to characterise the effects of this replacement on structure, motility, attraction and aggregation. Finally, we assessed the question whether the strength of the attractive forces affects antibiotic tolerance and resistance.

Having established that the biofilm lifestyle offers protection against antibiotic tolerance in the previous project, we addressed the question how genes associated with the aggregation lifestyle affect antibiotic tolerance. Based on transcriptome analysis comparing planktonic and aggregating cells, we identified the 20 most upregulated genes in the biofilm. To investigate their roles in antibiotic tolerance, we individually deleted each gene and assessed the resulting killing kinetics under antibiotic treatment. By correlating these kinetics with genes associated with the bacterial lifestyles, we identified genes involved in antibiotic tolerance which are related to bacterial aggregation.

2 Materials and Methods

2.1 Microbiological Methods

2.1.1 *Neisseria* Strains

The main experimental procedures were performed with strains derived from the *N. gonorrhoeae* MS11 strain. Strain constructions were performed by Sebastian Kraus-Römer and are described in detail in the publications and listed in table 2.1.

Strain	Relevant genotype	Number	Reference
ΔG4, wt*, wt_{agg}	*VD300 G4::apraR*	Ng150	[47]
ΔpptA	*ΔG4 pptA::kanR*	Ng214	[59]
wt_{sfgfp}	*G4::aac, lctp:PpilE, sfgfp speR:aspC*	Ng194	[103]
wt_{gfp}	*G4::aac , igA::gfp:ermR* *ComE1-5'-UTR-apraR-pilE1*	Ng151	[16]
ΔpilE	*ΔG4 pptA::kanR*	Ng196	[131], this study
T126C	*G4::apraR* $pilE^{T126C}$	Ng226	[132], this study
N. gonorrhoeae NG32	Clinical isolate, piliated phenotype	Ngc001	[133], this study
N. gonorrhoeae NG17	Clinical isolate, piliated phenotype	Ngc004	[133], this study
N. gonorrhoeae NG24	Clinical isolate, piliated phenotype	Ngc007	[133], this study
wt_{pilE32}, wt_{plank2}	*G4::apraR,* $pilE_{clinicalisolateNG32}$	Ng230	[133], this study
wt_{pilE17}, wt_{plank}	*G4::apraR,* $pilE_{clinicalisolateNG17}$	Ng240	[133], this study
wt_{pilE24}, wt_{agg2}	*G4::apraR,* $pilE_{clinicalisolateNG24}$	Ng242	[133], this study
wt^{*}_{green}	*G4::apraR* $iga::P_{pilE}gfp\text{-}ermC$	Ng105	[62]]
wt^{*}_{red}	*G4::apraR* $lctp::P_{pilE}mcherry\ aadA::aspC$	Ng170	[47]
wt* ΔpglF	*G4::apraR* $pglF::P_{pilE}gfp\text{-}kanR$	Ng156	[62]
$\text{wt}_{pilE17green}$	*G4:: apraR* $pilE_{clinicalisolateNG17}$ $iga::P_{pilE}gfp\text{-}ermC$	Ng308	[133], this study
$\text{wt}_{pilE24green}$	*G4:: apraR* $pilE_{clinicalisolateNG24}$ $iga::P_{pilE}gfp\text{-}ermC$	Ng309	[133], this study

Strain	Relevant genotype	Number	Reference
wt$_{pilE32green}$	*G4:: apraR* $pilE_{clinicalisolateNG32}$ *iga::*P_{pilE}*gfp-ermC*	Ng310	[133], this study
wt$_{pilE17T136}$	*G4::apraR* ${pilE_{clinicalisolateNG17}}^{K137-E160}$ $::pilE_{wt}^{T136-K160}$	Ng293	[133], this study
wt$_{pilE32T136}$	*G4::apraR* ${pilE_{ClinicalIsolateNG32}}^{T135-P158}$ $::pilE_{wt}^{T136-K160}$	Ng295	[133], this study
wt$_{pilE17K155}$	*G4::apraR* ${pilE_{clinicalisolateNG17}}^{E156-P158}$ $::pilE_{wt}^{K155-K160}$	Ng305	[133], this study
wt$_{pilE32K155}$	*G4::apraR* ${pilE_{clinicalisolateNG32}}^{L157-P158}$ $::pilE_{wt}^{K155-K160}$	Ng307	[133], this study
ΔpilE$_{green}$	*pilE::gfp-kanR*	Ng081	[62]
wt$_{pilE17}$ Δ*pglF*	*pglF:*P_{pilE}*gfp-kanR*	Ng311	[133], this study
wt$_{pilE24}$ Δ*pglF*	*pglF:*P_{pilE}*gfp-kanR*	Ng312	[133], this study
wt$_{pilE32}$ Δ*pglF*	*pglF:*P_{pilE}*gfp-kanR*	Ng313	[133], this study
ΔpilE*	*pilE::kanR*	Ng253	[133], this study
ΔrecN$_{agg}$	*G4::apraR, recN::kanR*	Ng261	[134], this study
ΔNGFG_00826$_{agg}$	*G4::apraR, NGFG_00826::kanR*	Ng262	[134], this study
ΔNGFG_01491$_{agg}$	*G4::apraR, NGFG_01491::kanR*	Ng263	[134], this study
ΔNGFG_00584$_{agg}$	*G4::apraR, NGFG_00584::kanR*	Ng264	[134], this study
ΔNGFG_01283-84$_{agg}$	G4::apraR, NGFG_01283-1284::kanR	Ng269	[134], this study
ΔNGFG_01274-1275$_{agg}$	*G4::apraR, NGFG_01274-1275::kanR*	Ng270	[134], this study
ΔNGFG_01056-1059$_{agg}$	*G4::apraR, NGFG_01056-1059::kanR*	Ng271	[134], this study
ΔNGFG_00715$_{agg}$	*G4::apraR, NGFG_00715::kanR*	Ng272	[134], this study
ΔNGFG_01289-97$_{agg}$	*G4::apraR, NGFG_01289-1297::kanR*	Ng273	[134], this study
ΔrecN$_{plank}$	*wt*$_{pilE17}$ *recN::kanR*	Ng275	[134], this study
ΔNGFG_00826$_{plank}$	*wt*$_{pilE17}$*, NGFG_00826::kanR*	Ng276	[134], this study
ΔNGFG_01491$_{plank}$	*wt*$_{pilE17}$*, NGFG_01491::kanR*	Ng277	[134], this study
ΔNGFG_00584$_{plank}$	*wt*$_{pilE17}$*, NGFG_00584::kanR*	Ng278	[134], this study
ΔcysT$_{agg}$	*G4::apraR, cysT::kanR*	Ng279	[134], this study
ΔNGFG_01302$_{agg}$	*G4::apraR, NGFG_01302::kanR*	Ng280	[134], this study
ΔNGFG_01080$_{agg}$	*G4::apraR, NGFG_01080::kanR*	Ng281	[134], this study
ΔNGFG_00631$_{plank}$	*wt*$_{pilE17}$*, NGFG_00631::kanR*	Ng288	[134], this study
ΔNGFG_00631$_{agg}$	*G4::apraR, NGFG_00631::kanR*	Ng289	[134], this study
lctP::kanR:aspC$_{plank}$	*wt*$_{pilE17}$*, lctP::kanR:aspC*	Ng290	[134], this study

Strain	Relevant genotype	Number	Reference
lctP::kanR:aspC$_{agg}$	*G4::apraR, lctP::kanR:aspC*	Ng291	[134], this study
ΔNGFG_01284-83$_{plank}$	*wt*$_{pilE17}$, *NGFG_01284-1283::kanR*	Ng296	[134], this study
ΔNGFG_01274-75$_{plank}$	*wt*$_{pilE17}$, *NGFG_01274-1275::kanR*	Ng297	[134], this study
ΔNGFG_01056-59$_{plank}$	*wt*$_{pilE17}$, *NGFG_01056-1059::kanR*	Ng298	[134], this study
ΔNGFG_00715$_{plank}$	*wt*$_{pilE17}$, *NGFG_00715::kanR*	Ng299	[134], this study
ΔNGFG_01289-97$_{plank}$	*wt*$_{pilE17}$, *NGFG_01289-1297::kanR*	Ng300	[134], this study
ΔcysT$_{plank}$	*wt*$_{pilE17}$, *cysT::kanR*	Ng301	[134], this study
ΔNGFG_01302$_{plank}$	*wt*$_{pilE17}$, *NGFG_01302::kanR*	Ng302	[134], this study
ΔNGFG_01080$_{plank}$	*wt*$_{pilE17}$, *NGFG_01080::kanR*	Ng303	[134], this study
ΔNGFG_00826	*G4::apraR, NGFG_00826::kanR*	Ng321	[134], this study
ΔNGFG_01080 ΔrecN$_{agg}$	*ΔNGFG_01080 ΔrecN*		
ΔNGFG_01080	*G4::apraR, NGFG_01080::kanR*	Ng325	[134], this study
ΔNGFG_00826 ΔrecN$_{agg}$	ΔNGFG_00826 ΔrecN		

Table 2.1: List of strains used in this study. The clinical strains were gifts from Paul G. Higgins from the University Hospital Cologne.

2.1.2 Cultivation of *N. gonorrhoeae*

To cultivate *N. gonorrhoeae*, bacteria were streaked onto GC agar plates (Tab. 2.2). These plates were incubated at 37 °C and 5% CO_2 for a maximum of 14 h prior to the experiment. For experiments in liquid media, GC medium (Tab. 2.2) supplemented with isovitalex (IVX) (Tab. 2.3) was prepared and additionally filtered using filters designed for organic solvents (for small volumes up to 50 mL: Sterile Syringe Filter (*VWR*); for large volumes up to 500 mL: Filtropur BT50 (*Sarstedt*)) with a pore size of 0.2 µm. Then, bacteria from the plates were resuspended, and the OD was set. If additional supplements were needed for the experiments, this is described in the specific methods section. Bacterial stocks were prepared in GC freeze medium (10% milk powder (*Roth*) in MilliQ water). Bacteria from overnight GC agar plates were collected, resuspended in the liquid GC freeze medium, and placed in a 1 mL CryoFreeze tube. The tubes were frozen in liquid nitrogen to prevent cell damage, and the stock was stored at −80 °C.

Ingredient	Amount	Company
NaCl	5 g	*Roth*
K_2HPO_4	4 g	*Roth*
KH_2PO_4	1 g	*Roth*
Proteose Peptone No.3	15 g	*BD*
+ Soluble Starch	0.5 g	*Sigma Aldrich*
+ Bacto Agar	10 g	*BD*
Isovitalex	10 mL	Custom made
Ascorbic acid [88 mg/mL]	1 mL	Depending on experiment
MilliQ water	1 L	

Table 2.2: Ingredients for 1 L GC medium or agar (+ = agar). The medium was autoclaved and stored at 4 °C. IVX (Tab. 2.3) was added prior to use at a final concentration of 1%. For agar, IVX (Tab. 2.3) was added to a final concentration of 1% after agar was autoclaved and cooled down to at least 55 °C. Plates were poured under a sterile hood and left to dry for 1 day. For laser tweezers experiments the media was supplemented with ascorbic acid at a final concentration of 88 µg/mL to reduce cell damage by free radicals generated by the laser beam.

Ingredient	Concentration	Company
D(+)-Glucose	100 g/L	*Roth*
L-Glutamine	10 g/L	*Roth*
L-Cystein $\cdot HCl \cdot H_2O$	28.9 g/L	*Roth*
Cocarboxylase(Thiamine Pyrophosphate)	0.1 g/L	*Sigma Aldrich*
Ferric Nitrate ($Fe(No_3)_3 \cdot 9H_2O$)	0.02 g/L	*Sigma Aldrich*
Thiamine·HCl	0.003 g/L	*Roth*
4-Aminobenzoic Acid (PABA)	0.013 g/L	*Sigma Aldrich*
β-Nicotinamide Adenine Dinucleotide (NAD)	0.25 g/L	*Roth*
Cyanocobalamin (Vitamin B_{12})	0.01 g/L	*Sigma Aldrich*

Table 2.3: Ingredients for IVX, frozen in aliquots and stored at −20 °C.

2.1.3 Pellicle Formation and Establishment of Piliated Clinical Isolates of *N. gonorrhoeae*

For this study, piliated bacteria were investigated. The clinical isolates of *N. gonorrhoeae* used in the study *Pilin antigenic variants impact gonococcal lifestyle and antibiotic tolerance by modulating interbacterial forces* [133] (Chapter 5) were brought into a piliated state by following the protocol developed by Robert Zöllner [135]. First, bacteria from overnight agar plates were resuspended in 2 mL GC medium in a 24-well plate (*Greiner Bio One*). After 24 h of growth at 5% CO_2 and 37 °C, pellicle formation was checked. If pellicles were visible at the surface of the well, they were picked and plated on GC agar plates overnight. If no pellicles were observed, the solution with cells was further diluted (1:2) with fresh medium. Then, the procedure was repeated until pellicles arose. Finally, the ability of the bacteria to perform twitching motility was checked by imaging, and a monoculture was prepared to generate stocks.

2.1.4 Bacterial Growth Curves

To analyse the growth behaviour of the pilin variants in chapter 5, bacteria were treated as follows. First, bacteria from overnight GC agar plates were resuspended in liquid GC medium and the OD was set to 0.1 (corresponding to approximately $5 \cdot 10^7$ CFU/mL). Then, a 48-well plate (*Greiner Bio One*) with 1 mL liquid GC medium was inoculated with 10 µL of the bacterial suspension. The plates were incubated in a microplate reader (*TECAN* Infinite M200 plate reader) with a shaking period of 2 min per measurement cycle (OD was measured every 10 min) at 37 °C and 5% CO_2. Within a time span between 0 h and 19 h, the bacteria from a whole well were collected in a 1.5 mL tube, followed by centrifugation at 5000 g for 3 min, and the supernatant was discarded. Then, 500 µL fresh medium was added, and the tube was vortexed for 30 s. To make sure that the colonies were completely disrupted, 500 µL of MilliQ water was added, and the tube was vortexed for 2 min. To plate the colonies, a 1:10 dilution series was prepared, and 50 µL was used to plate with 6 glass beads (note: the number of beads affected the number of colonies) on three GC agar plates in a range of 1-100 colony-forming units (CFU). After incubation for 48 h at 37 °C and 5% CO_2, the colonies were counted, and for analysis, the plate with a colony number between 50 and 500 was used.

The growth rates were determined between the time points 2 h and 8 h from a linear regression fit via the *fitlm* function in *Matlab*, and the slope determines the growth rate. Statistical tests of the growth rate of different strains were conducted via a pairwise *ANOVA* test for linear regression models in *Matlab*. The scripts which were used can be found on the *GitHub* repository of this thesis [136].

2.1.5 Survival Assay

Survival assays were performed to determine the tolerance level of *N. gonorrhoeae* pilin variant strains (Chapter 5). Bacteria from GC agar plates were resuspended in liquid GC medium, and the OD was set to 0.1. Subsequently, 10 µL were added to 1 mL GC medium in a 48-well plate (*Greiner Bio One*). Bacteria were incubated for 10 h at 5% CO_2 and 37 °C in a microplate reader (*TECAN* Infinite M200 plate reader) with a shaking period of 2 min per measurement cycle (OD was measured every 10 min). Then, the antibiotics ceftriaxone, ciprofloxacin, and kanamycin were added to the wells, excluding the control wells. The final concentration of ceftriaxone was set to 300xMIC, 600xMIC, and 1200xMIC (2.4, 4.8, 9.6 µg/mL), for ciprofloxacin, the final concentration was 600xMIC (2.4 µg/mL). For kanamycin, the concentration was set to 15xMIC (240 µg/mL) as the solubility was too low to increase the concentration. The control wells, without antibiotic treatment, were collected after 10 h in an 1.5 mL tube, then centrifuged for 3 min at 5000 g, and the supernatant was discarded from the tube. Afterwards, 500 µL fresh medium was added, and the pellet was resuspended by vortexing for 30 s. To ensure that colonies were disrupted, 500 µL of MilliQ water was added, and again the bacterial suspension was vortexed for 2 min. Then, a dilution series of 1:10 was prepared, and 50 µL of the three dilution series in the range of 1-100 CFUs were plated with 6 glass beads by carefully shaking on GC agar plates. The number of beads was fixed, as the number influenced the CFU since bacteria also stick to the beads. After 3 h, 6 h, and 9 h, the treated wells were analogously plated. After 48 h of growth, CFUs were counted. For further analysis, the plate with a number between 50 and 500 was used. All experiments were repeated at least three times.

To statistically compare the killing kinetics of different strains, the trends of the normalised raw data to 10 h growth over time were statistically analysed via a combined p-values method for discrete data to depict if the trends of surviving bacteria of two strains during the killing period is significantly different [137]. Here, a method was implemented based on the Mann-Whitney U test to compare single time points, followed by combining p-values via the method of Mudholkar and George [138]. The scripts can also be found on the *GitHub* repository [136].

2.2 Optical Tweezers

Optical tweezers are a versatile tool to investigate interaction forces of bacteria and were used in this study to exploit the interaction forces under antibiotic stress (Chapter 4) and how pilin variation affects the single-cell interactions (Chapter 5).
The concept of utilising optical tweezers for the investigation of biological samples was pioneered by Arthur Ashkin [139].

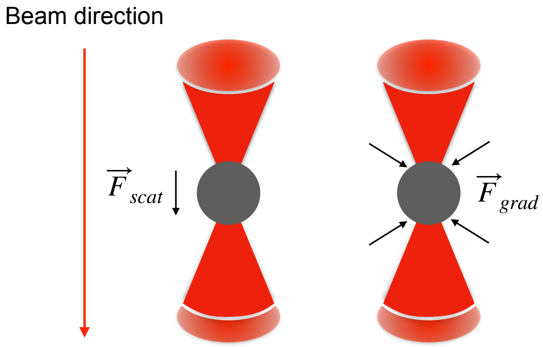

Figure 2.1: During optical trapping, the forces acting on a dielectric particle can be described by the scattering force $\vec{F}_{\text{scat}}$, which is pointing in the same direction as the incident light and the gradient force $\vec{F}_{\text{grad}}$ in the direction of the intensity gradient.

The process of optical trapping can be understood as the capture of dielectric particles by a high-intensity laser beam. The photons within the laser beam undergo refraction and scattering at the surface of the dielectric particle, thereby inducing a change in their momentum $\vec{P}$ over time. In accordance with the principle of conservation of momentum, this process also results in the exertion of a force on the particle

$$\vec{F} = \frac{d\vec{P}}{dt}. \tag{2.1}$$

The force can be divided into two components: a scattering force $\vec{F}_{\text{scat}}$, which is directed along the trajectory of the incident laser beam, and a gradient force $\vec{F}_{\text{grad}}$, which is directed along the direction of the light gradient [140] (Fig. 2.1). The total force is the sum of these two components. To successfully trap a particle in three dimensions, a highly focused laser beam is needed to maximise the gradient force, as it must exceed the scattering force $\left|\vec{F}_{\text{scat}}\right|<\left|\vec{F}_{\text{grad}}\right|$. The forces acting on a dielectric sphere can be described in two regimes depending on the wavelength λ and the diameter of the particle d: the Mie-regime with $d \gg \lambda$ and the Rayleigh-regime with $d \ll \lambda$. In the Mie-regime, the object acts as a lens and the optical trapping can be described in the geometrical optics. The light is decomposed into individual rays, resulting in the force components of

$$F_{\text{scat}} = \frac{nP}{c} \cdot \left(1 + R\cos 2\theta - \frac{T^2\left[\cos 2\theta - 2r + R\cos 2\theta\right]}{1 + R^2 + 2R\cos 2r}\right) \tag{2.2}$$

and

$$F_{\text{grad}} = \frac{nP}{c} \cdot \left(R \sin 2\theta - \frac{T^2 \left[\sin 2\theta - 2r + R \sin 2\theta \right]}{1 + R^2 + 2R \cos 2r} \right) \tag{2.3}$$

with θ and r, the angles of incident light and refraction, respectively. R and T are the Fresnel reflection and transmission coefficients and n is the corresponding refractive index of the surrounding medium. The prefactor nP/c, describes the momentum of an incident ray with power P [140].

In the Rayleigh-regime, the particle is considered as a point dipole, resulting in the force components of

$$\vec{F}_{\text{scat}} = \frac{8}{3}\pi(ka)^4 a^2 \left(\frac{m^2 - 1}{m^2 + 2} \right)^2 \left(\frac{n_1}{c} \right) I(\vec{r})\hat{\mathbf{e}}_z \tag{2.4}$$

and

$$\vec{F}_{\text{grad}} = \frac{2\pi n_1 a^3}{c} \left(\frac{m^2 - 1}{m^2 + 2} \right)^2 \nabla I(\vec{r}), \tag{2.5}$$

with $m = n_2/n_1$ as the relative refractive index of the particle, I is the intensity of the beam, a the radius of the particle and $\hat{\mathbf{e}}_z$ the direction of beam propagation [141]. It is important to note that the gradient force is dependent on the intensity gradient and the polarisability of the dielectric particle. These factors also influence the stiffness of the trap k, which must be determined experimentally through calibration of the trap. Approximating the potential of the trap with a harmonic potential, the force a particle experiences when displaced from the centre of the trap can be described using Hooke's law

$$F = -k \cdot d. \tag{2.6}$$

2.2.1 Setup

To build a laser trap three major building blocks are needed: the infrared (IR) laser, a microscope and a detection system. Here, the double laser trap setup, which was used to study interaction forces of bacteria, will be explained. This setup was first built by Dirk Opitz and modified by Robert Zöllner and myself [135, 142].

The optical trap setup was integrated into a confocal microscope (Eclipse TE2000-E C1, *Nikon*). The laser (J20I-BL-106C, *Newport Spectra Physics*) used in this study was a solid-state Nd:YVO$_4$ IR laser with a wavelength of 1064 nm. The laser beam could be manually stopped by a self-built beam shutter, which was controlled via a switch. First, the beam crossed L1 (−10 mm) and L2 (80 mm) (G052-303-329 and G063-046-329, *Qioptiq Photonics*) to broaden the beam. Next, it passed through a $\lambda/2$-plate P1 (G362-503-247, *Qioptiq Photonics*) and a polarising beam splitter P2 (G335-723-000, *Qioptiq Photonics*) to control the laser intensity. The beam was split via a two-axis controllable acousto-optic deflector (AOD) (DTD-274HD6 Collinear Deflector, *IntraAction Corp.*) via a signal generator (SDG 2042 X, *Siglent*) and a synthesizer. Then, the beam crossed a telescope L3 and L4 (125 mm and 125 mm) (LB1904-B, BK7 B coating, *Thorlabs*) and was directed via a mirror M1. A second beam expansion followed via the lenses L5 and L6 (60 mm and 175 mm) (LA1134-B, BK7 B coating and LA1229-B, BK7 B coating, *Thorlabs*) directed via a

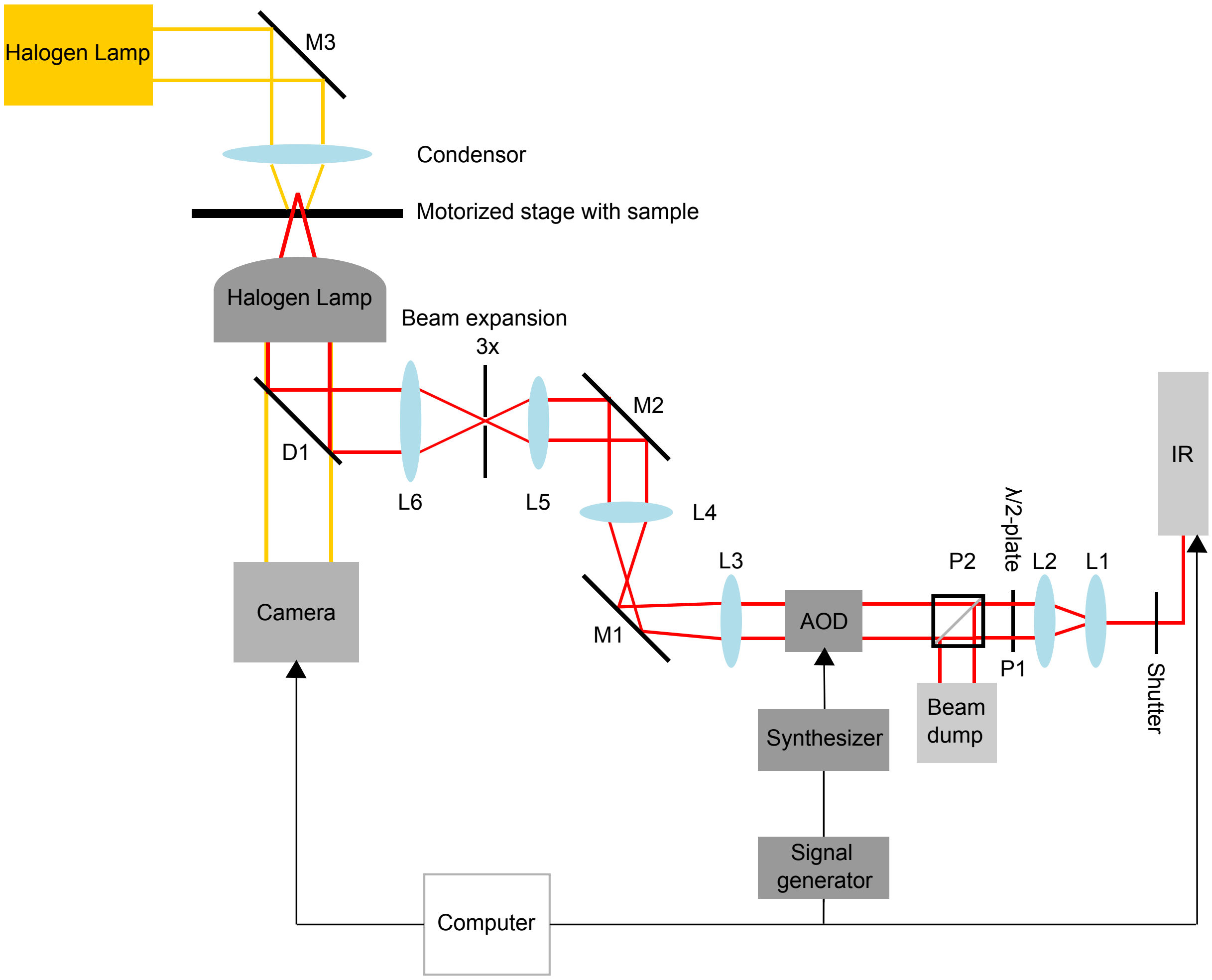

Figure 2.2: Schematic of the optical setup of the double laser trap.

second mirror M2. An aperture between these lenses selected the (1,1)-diffraction order of the beam. Finally, the beam was directed via a dichroic mirror D1 into the 60x objective onto the sample plane (PlanApochromate VC 60x water immersion, N.A. 1.20, W.D. 0.27 mm, *Nikon*). The objective and microscope were embedded inside a self-built thermobox. The illumination of the sample was provided by a halogen lamp. The stage and the height of the objective was controlled via a computer. Detection was based on image acquisition via a high-speed camera with 2.500 frames per second (EoSens 3CL, *Mikrotron*).

2.2.2 Control of the Trap

The goal of the setup was to be capable of trapping spherical-shaped objects and measuring inter-bacterial forces of *N. gonorrhoeae* up to 100 pN [29]. Therefore, the trap stiffness needed to be approximately 0.1 pN/nm.

The main element controlling the trap of the setup (Methods 2.2.1) presented the AOD. Using the AOD, two time-shared optical traps originating from one laser beam were created [141]. The concept of the AOD relies on two orthogonally aligned tellurium dioxide crystals that are actuated by a piezo element. By this an optical grating can be created when the signal generator excites the acousto-optical medium in x- and y-directions. The angular distance is defined by

$$\Theta = \frac{\lambda v}{\Lambda} = \frac{\lambda f}{v}. \tag{2.7}$$

λ is the wavelength of the laser, Λ is the acoustic wavelength, f is the acoustic frequency and v is the acoustic velocity in the acousto-optical medium (Fig. 2.3).

To generate two time-shared optical traps, a square wave was superimposed on the channels of the signal generator, which determined the vertical or horizontal alignment of the double trap. The frequency then switched between f_1=25 MHz and, e.g., f_2=23.6 MHz with a switching frequency of 100 kHz and two time-shared optical traps were created. It was important that the switching frequency was high enough to ensure that the trapped particle did not jump from one trap into the other. The distance was defined by the difference of the acoustic frequencies Δf (distances of traps for this study are mentioned in the results part, Chapter 4 and 5).

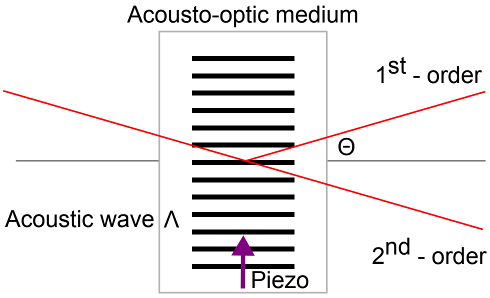

Figure 2.3: Principle of the AOD. The AOD in this scheme is operated with a single acoustic frequency and Θ can be adjusted by the frequency of the acoustic wave.

The laser intensity was controlled via a goniometer or by altering the current to generate the laser beam. Two custom-developed LabView programs, *LaserPowerGonio.vi* and *LaserControl.vi*, were used for this purpose. The first program adjusted the angle of the $\lambda/2$-plate, which regulated the light intensity passing through the beam splitter (Methods 2.2.1) while the second, controlled the current to generate the laser beam.

2.2.3 Image Acquisition, Tracking and Controlling the Microscope

To protect the camera from the IR laser, first, an IR filter was applied using the *TiControl* program (Ti Control. Ink, *Nikon*). The image acquisition of interacting bacteria was controlled via a custom-developed LabView program *FGCameraLinkFreeRunIW.vi* by Tom Cronenberg and adapted by myself. The high-speed camera can capture images at a maximum frame rate of 2.500 Hz [143]. For image acquisition the frequency was downsampled to 50 Hz as this was sufficient to track the bacterial movement. However, to calibrate the trap via the power spectral density (Methods 2.2.4) the frame rate was set to the maximum. The graphical user interface (GUI) of the image acquisition displayed the live images at 50 Hz of the microscope. Images were stored as .tif-files of 1710 x 1696 pixels (Px). Additionally, to increase resolution, an extra magnification lens of the microscope was added resulting in a resolution of 88.652 nm/Px.

Tracking of the trapped particles was performed using a custom *Matlab* tracking program based on a Circular Hough Grid Transform algorithm. This approach has been used in previous studies [135] and has been shown to provide robust tracking of spherically shaped particles [144].

Briefly, the raw images were pre-processed using Gaussian filtering, followed by the application of a two-dimensional digital filter. Subsequently, the Hough Grid Transform algorithm was applied. The programs *TrackingDoubleTrap.m* and *CircularHoughGrd.m* are available in a *GitHub* repository [136].

2.2.4 Calibration of the Double Laser Trap

The high-speed camera enabled calibration of the trap via the power spectral density, as described by Berg-Sørensen et al. [143].

The trapping potential of an optical trap can be approximated as a harmonic potential [141]. The power spectrum method uses the Brownian motion of a spherically shaped particle when trapped in an harmonic potential [141]. This motion can be described by the Einstein-Ornstein-Uhlenbeck theory, based on the stochastic description of the particle's position. This results in a Langevin equation [145]

$$m\ddot{x}(t) + \gamma_0\dot{x}(t) + kx(t) = (2k_B T\gamma_0)^{1/2}\eta(t), \tag{2.8}$$

where $x(t)$ is the trajectory of the Brownian particle, m is its mass, γ_0 is its friction coefficient, k is the stiffness of the trap. The term on the left site $(2k_B T\gamma_0)^{1/2}\eta(t)$ describes a random Gaussian process at temperature T with $\langle\eta(t)\rangle = 0$ and $\langle\eta(t)\eta(t')\rangle = \delta(t - t')$. Since the image acquisition was short we neglected the friction term in the following steps. By introducing the corner frequency

$$f_c \equiv \frac{k}{2\pi\gamma_0} \tag{2.9}$$

and the Einstein equation $D = k_B T/\gamma_0$, Fourier transformation of equation 2.8 from $-T_{record}/2$ to $T_{record}/2$ results in a function of noise. With respect to the Gaussian noise, the experimental values for the spectral density should follow the Lorentzian power spectrum

$$P_k = \frac{D}{2\pi^2(f_c^2 + f_k^2)}. \tag{2.10}$$

The corner frequency represents the frequency where the spectral power starts dropping, which means that at low frequencies for $f_c \gg f_k$ the particle is free to move and beyond the trap significantly restricts movement by restricting its free diffusion. The trap stiffness was determined for at least 10 pairs of bacteria for each laser power (2%, 5%, 7% and 10%) using the Δ*pilQ* strain, which is unable to build pili, preventing interactions. The acquisition time for each bacterial pair was 1 min, which was split into intervals of 20 s. The data were Fourier transformed and then averaged over the full time interval. Next, the Lorentzian function (Equ. 2.10) was fitted to the Fourier transformed data P_k against the frequencies f_k (Fig. 2.4). The stiffness was determined from the fitted parameter f_c using the friction coefficient γ_0, with

$$k = 2\pi\gamma_0 \cdot f_c. \tag{2.11}$$

Finally, we extrapolated the linear fit to the four different laser powers up to 100% laser power,

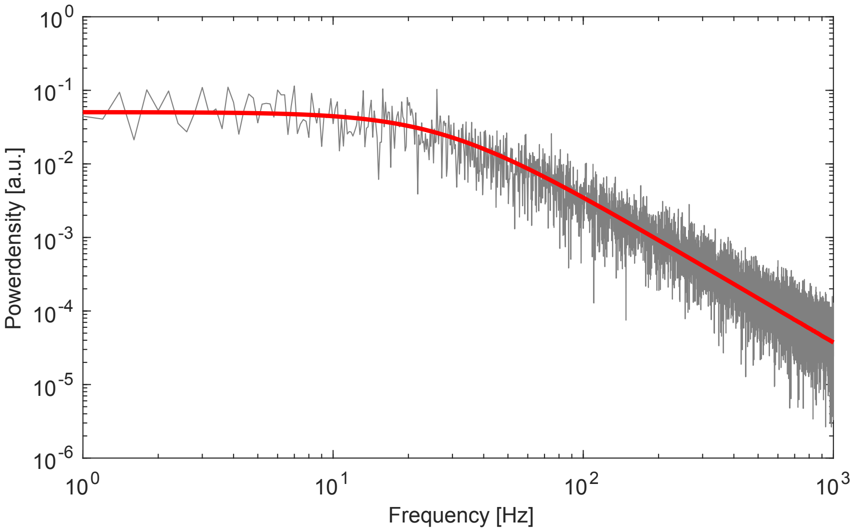

Figure 2.4: Power spectra of the $\Delta pilQ$ strain in an optical trap at 2% laser power (grey) with Lorentzian fit (red).

resulting in a trap stiffness of k=0.1 pN/nm for both traps. The linear regime ends at 80 pN and forces above are systematically overestimated [135].

2.2.5 Sample Preparation

In order to investigate the interaction forces of *N. gonorrhoeae* strains, dual laser tweezers experiments were performed. First, BSA (Bovine Serum Albumin, *Roth*)-coated cover glasses needed to be prepared. To coat a glass cover slip with BSA, the glass was etched by incubation in a 1 M KOH solution for 24 h. Then, the glasses were washed 10 times with MilliQ water to ensure that the KOH will not affect cell-to-cell interactions during the experiment. After drying, the glasses were coated homogeneously with a BSA solution (1 mg/mL in MilliQ water) and incubated for 30 min at 37 °C. Subsequently, the glasses were washed thrice with MilliQ water to prevent free BSA in the medium. To prepare the bacteria, a total of 10-30 colonies from overnight GC agar plates were collected and resuspended in GC medium that had been supplemented with 1% IVX and ascorbic acid at a final concentration of 88 µg/mL. The addition of ascorbic acid was crucial in reducing the amount of free radicals created during the experiment, thereby extending the duration of the measurement. Following a 2 min vortexing step, 60 µL of the bacterial solution was applied to a BSA coated coverslip. The coverslip was then attached to a microscopy slide and sealed with VALAP (Vaseline, Lanonlin and Paraffin wax (*Roth*) in a 1:1:1 mixture). Each sample was measured for a maximum of 15 min to ensure the maintenance of aerobic conditions, and the temperature was set to 33 °C during the experiments.

2.2.6 Characterisation of Interaction States

The output of the laser trap experiment is displacement as a function of time. The analysis of the displacement tracks was performed by a *Matlab* GUI, *Interactionstates.m*, which was developed during my Master's thesis and is available on the *GitHub* repository [136]. Initially, the displacement tracks of the two bacteria were summed to eliminate systematic errors, such as differences in the trap stiffnesses of Trap 1 and Trap 2. For a Brownian particle in a harmonic potential, Hooke's law applies [146]

$$F = -k \cdot x. \tag{2.12}$$

The interaction forces F are proportional to the trap stiffness k and the displacements x. The resulting interaction tracks were categorised into specific interaction states: elongation, retraction, pausing, bundling and rupture states (Fig. 2.5).

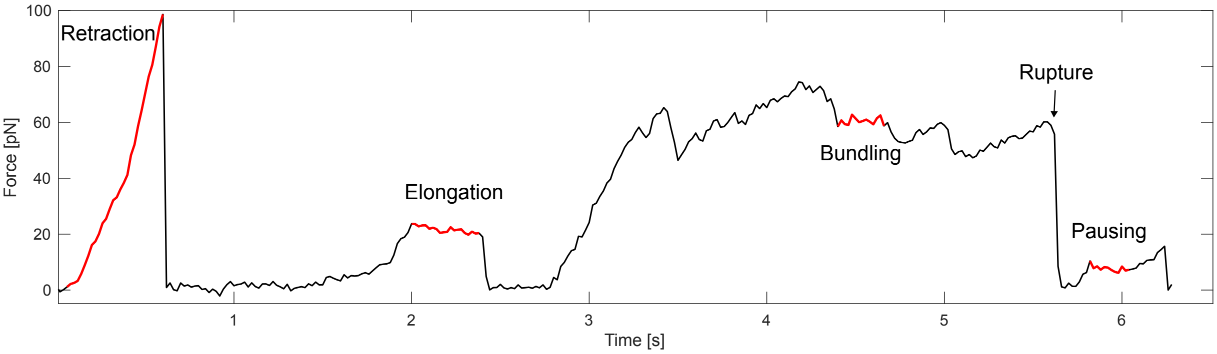

Figure 2.5: Typical force track of interacting bacteria showing the characteristic interaction states: retraction, elongation, pausing, bundling and rupture (marked in red).

During retraction of the pilus fibre the bacteria were displaced from their equilibrium positions, and the force tracks exhibited a positive slope, with velocities exceeding 110 nm/s for at least 0.15 s. In contrast, when the polymerisation of the T4P resumed, the bacteria moved back towards their equilibrium positions, resulting in a negative slope in the force tracks. This was defined as elongation state. The pausing state was characterised by a plateau in the force tracks following an elongation or retraction event. The tracks also exhibited sudden jumps to lower forces, attributed to rupture of individual pili of the interacting bacteria. A characteristic feature of the rupture events was a velocity larger than 500 nm/s. In instances where not all pili ruptured, but the force post-rupture exceeded 10 pN, this interaction state was designated as bundling state, under the assumption that multiple pili were responsible for the attractive forces exerted by the bacteria.

Through the analysis of the duration and frequency of these events, characteristic interaction patterns emerged for the bacteria. The forces were displayed in force histograms, which characterised the interaction strengths (Chapter 4 and 5). The probability to be bound was determined by summing all event durations and dividing by the total track time, which was defined as the period from the first detected event to the end of the last interaction state. The program *InteractionsEvaluation.m*, used for the data analysis, is also available on the *GitHub* repository of this thesis [136].

2.3 Image Analysis

2.3.1 Analysis of Type IV Pilus Dynamics

For the study of how *External stresses affect gonococcal type 4 pilus dynamics* [132] (Chapter 3) recorded videos of fluorescently labelled pili were analysed. Briefly, the laboratory strain $\Delta G4$ was engineered to contain a cysteine in *pilE* that allows binding to a maleimide-functionalised fluorescent dye, resulting in the *T126C* strain. The pili were fluorescently labelled, and single bacteria were immobilised under an agar pad to inhibit twitching motility.
Images were acquired using an inverted microscope (Ti-E, *Nikon*), equipped with a spinning disk confocal unit (CSU-X1, *Yokogawa*). The excitation wavelength was 488 nm and images were recorded for 20 s at a frame rate of 19.33 Hz.
To analyse the T4P dynamics the semi-automated program *T4P_dynamics.m* was developed in *Matlab* [136]. The first step in using the program was to select the cell to be analysed. This was followed by the selection of a smaller region of interest (ROI) (40 x 40 Px) around the cell, and a subsequent background subtraction (Fig. 2.6, Step I). Since the quality of the images varied and the cell body exhibited much higher intensities than the T4P (Supp. 9.1, Fig. S1), the next step involved optimising the image pre-processing parameters. This included (Fig. 2.6, Step II):

- the comparison of an ideal histogram for a fluorescently labelled bacterium to generalise the analysis
- the enhancement of contrast via the *imadjust.m* function in *Matlab*
- considering the implementation of a *Butterworth* filter (not used in publication but later demonstrated improved image quality).

The Butterworth filter suppresses either high or low-frequency components of an image by applying a Fourier transformation and multiplying the frequency spectrum with a smooth transfer function. By this the noise was strongly reduced (Fig. 2.6, Step II). This resulted in a pre-processed video that was then further analysed. The next step was to determine the centre of mass by binarising the image using the *binarize.m* function. In this step, the user could choose between manual determination of the centre or the program determined it automatically with the *regionprops.m Matlab* function since automised detection was difficult when the background was noisy or another bacterium was present in the chosen ROI. The position of the centre of mass was crucial for aligning the image with the pilus movement direction using *imrotate.m* (Fig. 2.6, Step III). The alignment angle was determined by drawing a reference line along the pilus. The two criteria that a pilus had to meet for analysis were that it had to point straight and radially away from the cell surface, and that the pilus had to be distinguishable from the cell envelope with a length greater than 0.7 µm.

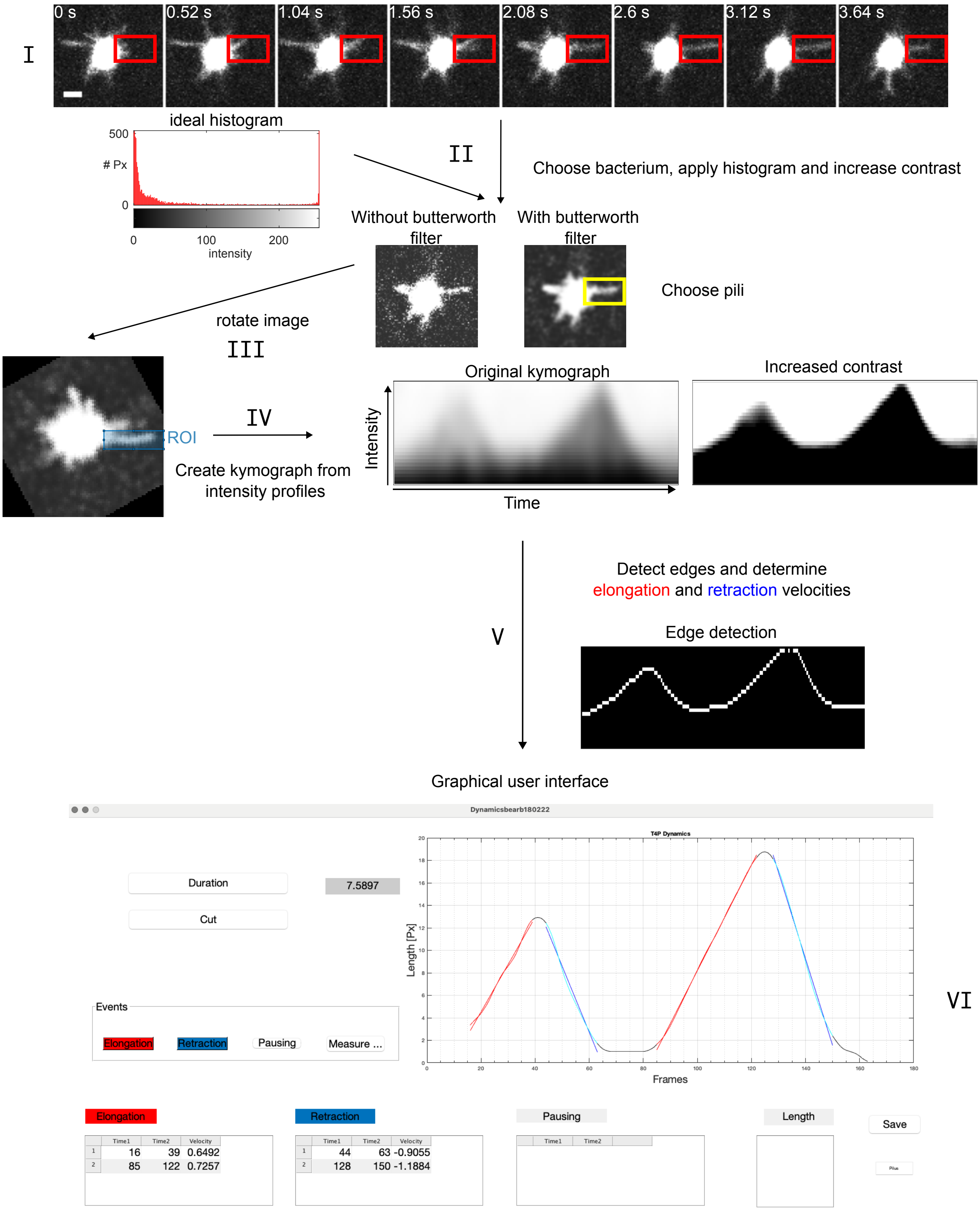

Elongation

	Time1	Time2	Velocity
1	16	39	0.6492
2	85	122	0.7257

Retraction

	Time1	Time2	Velocity
1	44	63	-0.9055
2	128	150	-1.1884

Pausing

	Time1	Time2	

Figure 2.6: Schematic to present the workflow of the image analysis to determine the T4P dynamics. Scale bar = 1 µm.

The rotated image then showed the pili horizontally, and a smaller ROI could be chosen around the pili. The next stage involved the selection of the surface of the bacterium where the pili originated, followed by the determination of an intensity profile across the entire ROI, with a width of 4 Px, for each frame. This process culminated in the creation of a kymograph of the pili, when the intensity profiles were plotted next to each other (Fig. 2.6, Step IV). The kymograph was processed using a Wiener filter and a Gaussian filter to ensure smoothness, followed by the application of the *imadjust.m* function to enhance contrast. This facilitated the identification of the edges via the *edge.m* function of the kymograph, which displayed the trajectory of the pilus over time (Fig. 2.6, Step V).

The analysis of this particular track was performed with a *Matlab* GUI. Within this framework, the segment of elongation, which pertains to the polymerisation of the pilus, and the segment of retraction, which corresponds to the depolymerisation of the pilus, was selected for examination. By ascertaining the slopes, via a linear fit, the velocities were determined (Fig. 2.6, Step VI). All analysis programs are available on the GitHub repository [136].

2.3.2 Analysis of Type IV Pilus Number and Production Rate

To study the effect of external stresses on T4P dynamics in *N. gonorrhoeae* [132] (Chapter 3), we also determined the T4P production rate. For this analysis, the same videos described in methods 2.3.1 were used. The *Matlab* program *T4P_Contour.m* was developed to facilitate the analysis, available on the GitHub repository of the thesis [136].

The methodology entailed the enumeration of the pili passages through a contour circumscribing the cell (Fig. 2.7). The first step included the pre-processing of the video by enhancing the contrast and applying a Gaussian filter (Fig. 2.7, Step I). The second step involved the delineation of the contour, which was accomplished by binarising the cell, excluding the T4P, and subsequently generating a mask of equivalent dimensions to the cell. This mask was then augmented by generating a disk-shaped structuring element via the *strel.m Matlab* function from the centre of mass of the binary mask of the cell. The dimensions of the disk are contingent on the original cell size and must be adapted for different conditions. The subtraction of the small mask and the large mask resulted in a mask delineating the contour of the cell with a width from 1-2 Px (Fig. 2.7, Step II). This method was sufficient to detect pili longer than 0.8 µm. To index this mask, a radial mask was created from the centre of mass of the cell with 80 sections, with each sector representing an angle of 4.5°. The subdivided mask was utilised to record the intensity profile surrounding the cell for each frame. Subsequently, the intensity profile was projected onto a line by averaging each over all pixels assigned to the same sector.

The kymograph of the intensity profiles around the cell was created by plotting these next to each other. The kymograph could be used to detect the location of the pili by observing filamentous structures over time. If a pilus was passing through the contour, it appeared as an intensity increase in the kymograph. In order to reduce noise and facilitate detection, the kymograph was Wiener filtered using the *Matlab* function *wiener2.m*. Furthermore, the *fibermetric.m Matlab* function was applied to enhance filamentous structures in the kymograph matrix. To detect the pili, the *findpeaks.m* function was applied, which detects the position of the pili for each frame along the sectors (Fig. 2.7, Step III). To prevent the erroneous detection of noise or the division of a pili into two, pili which were not longer detectable than 0.5 s were disregarded and detection events which showed breaks that lasted less than 0.5 s were connected. As pili fluctuations between sectors were observed, these were connected and counted as one (Fig. 2.7, Step IV).

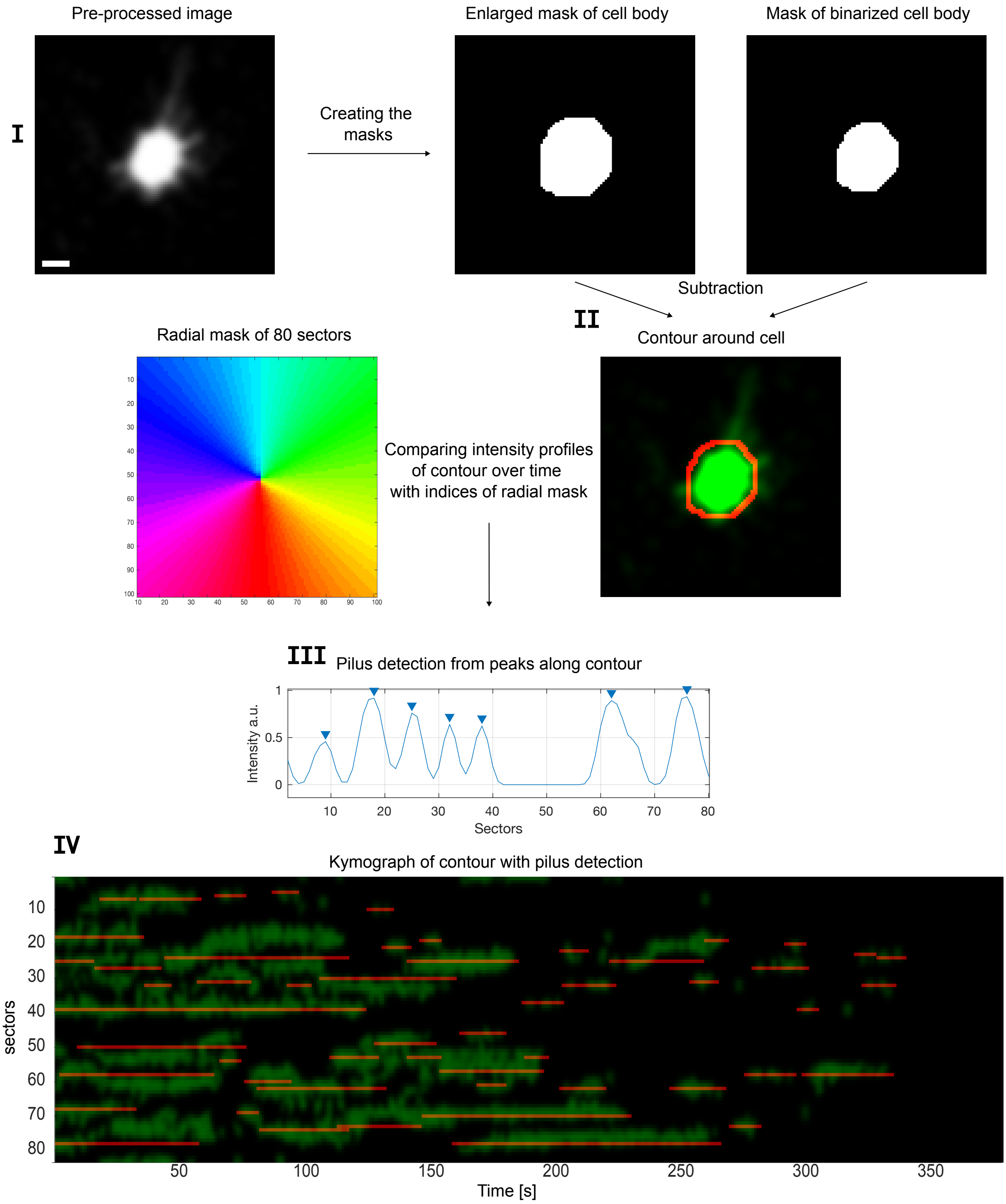

Figure 2.7: Schematic representation of the image analysis workflow used to determine the T4P production rate. Scale bar = 1 µm.

The pilus number, denoted by N_p, was determined by enumerating the pili in each sector during the first 7.5 s and then calculating the mean value across all analysed cells. The production rate, denoted by r_p, was determined by only counting the newly appearing pili during the first 7.5 s and then dividing by 7.5 s. This was also performed for multiple cells and averaged to obtain the mean r_p. A strong decrease in pilus number over time was observed, likely due to laser exposure and photobleaching (Supp. 9.1, Fig. S3). To mitigate this effect, the analysis was restricted to the first 7.5 s.

2.3.3 Analysis of Twitching Motility

In order to investigate the pilin variants in the work *Pilin antigenic variants impact gonococcal lifestyle and antibiotic tolerance by modulating interbacterial forces* [133] (Chapter 5), a first step was to verify the functionality of the T4P and their twitching behaviour on surfaces. To this end, an experiment was conducted, which has been employed in numerous studies to investigate the motility of *N. gonorrhoeae* [71, 73, 147].

Imaging of the Twitching Motility

Imaging was performed with a commercial microscope (Ti Microscope, *Nikon*) with a CMOS camera (C11440-36U ORCA-spark Digital CMOS camera, *Hamamatsu*). Furthermore, the microscope is equipped with a self-built heated thermal insulation box to keep the temperature during the experiment at 37 °C. An 100x objective (Plan Fluor 100x Oil Ph3cDLL, *Nikon*) was used to ensure single-cell resolution. The videos were taken at a frame rate of 10 Hz for 2 min. Bacteria were harvested from overnight agar plates (≈30 colonies) and resuspended in fresh GC medium. The sample was prepared as described in section 2.2.5. Each sample was only used for a maximum of 10 min to guarantee aerobic conditions.

Tracking of Single Cells and Analysis of Gonococcal Single-Cell Motility

The tracking was performed via a *Matlab* program *GC_tracking.m* developed by Rainer Kurre [147]. The program is based on the centroid tracking algorithm developed by J.C. Crocker and D. Grier originally written in *IDL* and further transferred to *Matlab* by D. Blair and E. Dufresne [148]. These programs can also be found on the *GitHub* repository [136]. Images were preprocessed in *Fiji* to enhance the contrast. After tracking, *.txt* files were saved and the MSD of the tracks, which quantifies the deviation of particles' position in time, could be determined from the displacements $\delta(\tau) = |r(t+\tau) - r(t)|$. The MSD is defined as

$$MSD(t) = \left\langle \left(\vec{r}_i(t+\tau) - \vec{r}_i(\tau)\right)^2 \right\rangle \tag{2.13}$$

$$= \frac{1}{N}\sum_{n=1}^{N}\frac{1}{T-t}\int_0^{T-t} d\tau \left|\vec{r}_i(t+\tau) - \vec{r}_i(\tau)\right|^2 \tag{2.14}$$

with the number of particles N and the length of the trajectory T of each particle n. $\vec{r}$ is the particles' position. For discrete time points M with a time step of Δt, this leads to

$$MSD(t) = \frac{1}{N}\sum_{n=1}^{N}\frac{1}{M-i}\sum_{j=0}^{M-i}\left|\vec{r}_n(t_i + \Delta t \cdot j) - \vec{r}_n(\Delta t \cdot j)\right|^2 . \tag{2.15}$$

To determine the correlation time τ_c and the velocities v the random-walk model

$$\left\langle \delta^2(\tau) \right\rangle = 2\tau_c v^2(\tau - \tau_c(1 - \exp(-\frac{\tau}{\tau_c}))) + A \tag{2.16}$$

was fitted to the MSDs for a time interval of 0.1 s<t<0.5 s for each cell. The variable A displays an overall shift of the MSD track and accounts for errors of the tracking. To determine the average correlation times and velocities we averaged over all cells which were analysed.

2.3.4 Analysis of Everting Gonococcal Colonies

We studied the maturation of single colonies of *N. gonorrhoeae*. As we could observe that colonies evert, we developed image analysis methods for tracking individual cells within colonies and methods to analyse the within-colony motility. Furthermore, particle image velocimetry (PIV) was used for the analysis of external DNA and dead cells during the eversion process. All image analysis programs used are available on the GitHub repository of the thesis [136].

Imaging of Colonies and Sample Preparation

The imaging of the colonies was performed under constant nutrient flow in a flow chamber (tissue culture treated µ-slides 0.8 I Luer, *Ibidi*) with a growth channel length of 50 mm, a width of 5 mm and a height of 0.8 mm. The flow chamber was connected via silicone tubes to a medium reservoir (120 mL). The outlet tube was connected to a peristaltic pump (Watson, *Marlow*) operating at 2.5 rpm, to generate a continuous flow through the chamber. Additionally, a self-built bubble-trap was connected to the slide to prevent air-bubbles from entering the flow chamber.

The bacteria were harvested from overnight agar plates and resuspended in liquid GC medium. Then, the OD was set to 0.05 and pre-incubated in a shaking incubator at 5% CO_2 and 37 °C for 30 min to form small aggregates prior to inoculating the flow chamber. The inoculation of 500 µL bacterial solution was performed via a syringe from the outlet side of the medium.

For image acquisition with single-cell resolution the wt_{gfp} strain was used with the inverted microscope (Ti-E, *Nikon*), equipped with a spinning disk confocal unit (CSU-X1, *Yokogawa*). The excitation wavelength was 488 nm and a 100x magnification (1.49 NA, oil immersion objective lens, *Nikon*) was used. Image sequences of 4 min with a frame rate of 15 frames/min were taken every 30 min.

For the analysis of the dead cells, external DNA and bright-field images, the wt* strain, was used. The medium was additionally supplemented with 1 µL SytoX (*Invitrogen*). We used a commercial microscope (Ti Microscope, *Nikon*) with a CMOS camera (C11440-36U ORCA-spark Digital CMOS camera, *Hamamatsu*) and a 20x objective (*Nikon*). Images of the colonies were acquired every 2.5 min for 10 h (unless stated otherwise). Both microscopes were equipped with a self-built heating box to ensure for an experimental temperature of 37 °C.

Tracking and Analysis of Within-Colony Motility

To determine the within-colony motility, we analysed the image sequences of the maturating colony prior to the eversion process. The videos were pre-processed in *Fiji* [149] by adjusting the contrast and applying the *Stackreg* plug-in [150] to exclude global motion of the colony from the movement of single cells. The tracking was performed with the *Fiji* plug-in *Trackmate* [151] (Fig. 2.8A). All tracks were saved as *.csv* data. To analyse the data, a self-developed *Matlab* program *RadialMSDwithoutshells.m* was used. The first step was to determine the centre of mass of the colony C_{colony}, depending on the colony size, this was done automatically by the program, using the *.tif* file of the colony image sequence. If the colony was too large to fit in the ROI or the analysis was not sufficient, the user could choose the centre of the colony by plotting the tracks from the *.csv* file. The automatic registration was based on the binarised image of the colony, and applying the *regionprops.m* Matlab function which determined the centroid of the colony area (Fig. 2.8B, C).

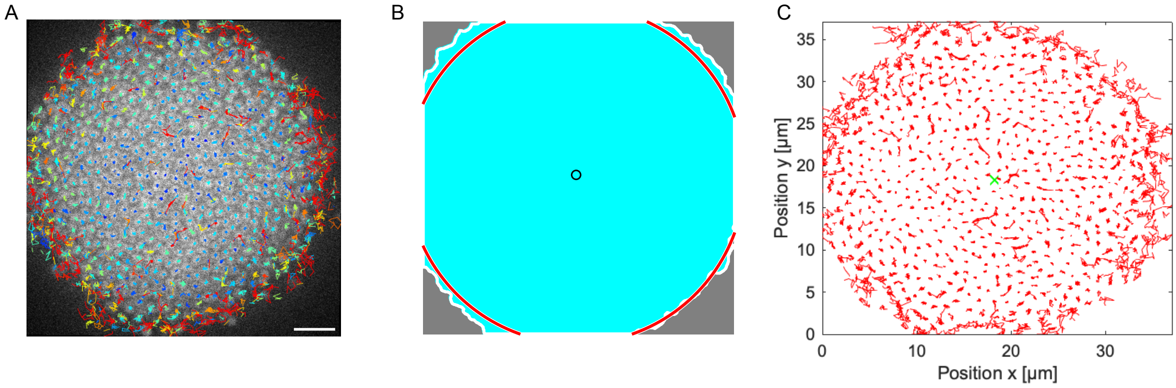

Figure 2.8: A) Fluorescent signal of cells in gonococcal colony with tracks from *Trackmate* in *Fiji*. Scale bar = 5 µm. B) Binarised colony and the centre of mass determined via the centroid of the colony. C) Displacement tracks of single cells with the determined centre of mass of the colony (green cross).

Only tracks with a duration longer than three frames were further processed. The time step was 4 s. Then, from these tracks the MSD (Section 2.3.3, Equ. 2.15) and the centre of mass of each track, C_{track}, were calculated. The centre of mass represents the location, from which the radial distance to the centre, C_{colony}, were determined. From the MSD, the diffusion constant D could be determined via the Einstein relation and a linear fit to the logarithmic MSD curves within the first 40 s (Fig. 2.9A)

$$D = \frac{MSD(t = 1s)}{4}. \tag{2.17}$$

The diffusion constant was plotted against the radial location of the tracks (Fig. 2.9B). To smooth the data, a moving average over 20% of the length of the data was applied via the *Matlab movmean.m* function (Fig. 2.9C).

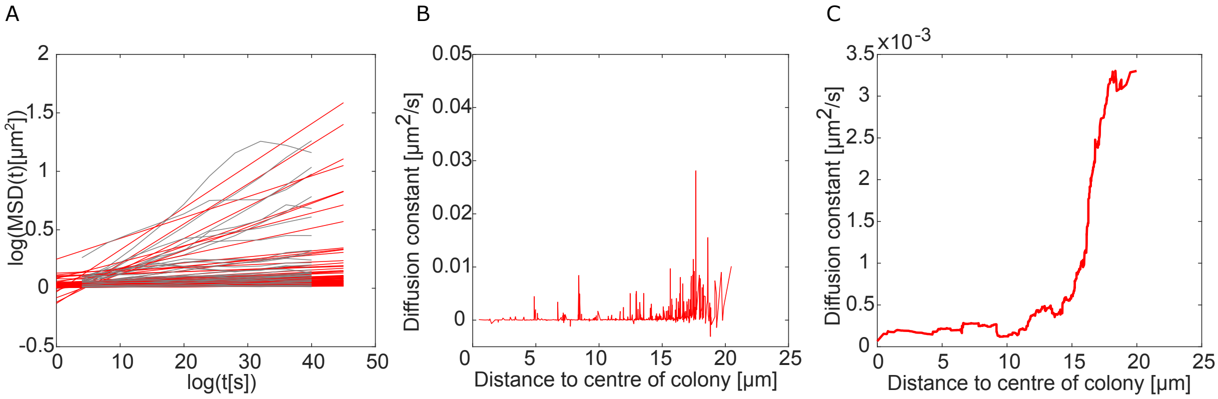

Figure 2.9: Example analysis of a colony 3 h before eversion. A) Logarithmically plotted MSD from raw data (grey) with linear fit (red). B) Determined diffusion constants of individual cells against the tracks' radial position. C) Moving average of the radial diffusion constants.

Radius of Highly Motile Shell

We determined the radius of the motile shell with the self-developed *Matlab* analysis program *MovingMeanRadialshell.m*. If a motile shell emerged (Fig. 2.10A), this was displayed as peak when the diffusion constants D were plotted against the radial position (Fig. 2.10B). Less motile regions were displayed as valleys. Inverting the plot, with $D_{max} - D$, resulted in the valleys displayed as peaks of the low motility regimes. We determined the peak position via the *findpeak.m Matlab* function of the low motility regime, also obtaining the information about the half width of the determined peak (Fig. 2.10C). The outer position of the half width, we defined as the boundary of the highly motile shell. We then subtracted the boundary position from the radius of the colony, which was defined by the maximal distance to centre of the colony. By this, we obtained the radius of the highly motile shell.

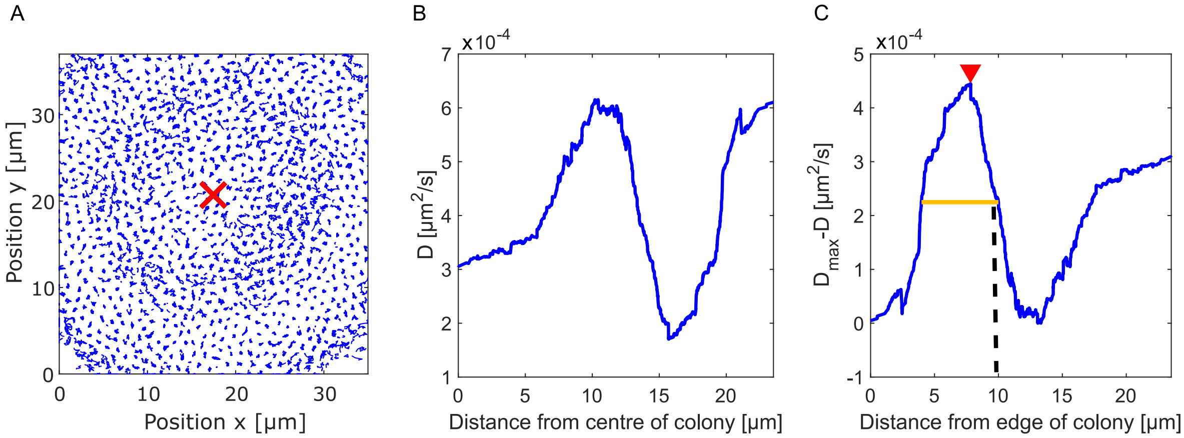

Figure 2.10: Methodology to determine the radius of the highly motile shell. A) Tracks of bacteria 30 min before eversion. The red cross indicates the centre of mass. B) The diffusion constant D was plotted against the radius starting from the centre. The motile shell appeared as peak. C) $D_{max} - D$ was plotted against the radial position from the edge of the colony towards the centre. The minimum valley of the motility was determined as peak using the *Matlab* function *findpeak.m* (marked as red triangle). The half width is marked in orange. The outer position of the half width (marked with dashed line) was used to determine the radius of the hyper-motile shell.

Motility Regimes

For the analysis of the motility regimes, we chose three time points per colony: during eversion, 30 min prior eversion and 2-3 h prior to eversion. For each time point, we chose a circular ROI and tracked the cell positions via *Trackmate* in *Fiji*, but did not apply the *Stackreg* plug-in. From the cell positions, we determined the MSD with the self-written *Matlab* program *DetermineMSDforEversion.m*. We averaged over all analysed colonies and fitted the logarithmic plotted MSD curves linearly within the interval of 50 s to 90 s and obtained the scaling behaviour of the motility regimes.

Analysis of the Dead Cells and External DNA during Eversion of Colonies

The PIV analysis was applied to investigate the flow of external DNA and dead cells during the eversion of late-stage gonococcal colonies.

First, the videos needed to be pre-processed using *Fiji*. The image processing tool *Enhance* *contrast* was applied by choosing a pixel saturation of 0.35% for each image in the time stack. These videos were saved as *.avi* files with the same pixel resolution and loaded into the PIV tool, which is provided as an app for *Matlab* [152, 153]. The algorithm for PIV used in this study was the *Multipass Fast Fourier Transform Window Deformation* method, which could be selected in the app. This algorithm cross-correlates signals in the frequency domain using the Discrete Fourier transform [154, 155]. Briefly, the images were represented as intensity matrices, where $I_1(x, y)$ and $I_2(x, y)$ denote the distribution of particles for two consecutive time points (in this case, the intensity signal of external DNA and dead cells). First, the images were subdivided into interrogation windows. For this analysis, we used four successive passes with decreasing window sizes: 64 x 64 Px (coarse estimation), 32 x 32 Px, 16 x 16 Px, and 8 x 8 Px. Then, a cross-correlation was applied between two consecutive images using the cross-correlation function $C(x, y)$ via Fast Fourier transformation [155]

$$C(x, y) = \mathcal{F}^{-1}\{\mathcal{F}[I_1] \cdot \mathcal{F}^*[I_2]\} \tag{2.18}$$

in which $\mathcal{F}$ is the Fourier transform, $\mathcal{F}^*$ is the complex conjugate of the Fourier transform and $\mathcal{F}^{-1}$ the inverse Fourier transform of the image. The shift between the two images was determined by the maximum of the cross-correlation matrix. To this end, the integer peak location

$$(\Delta x, \Delta y) = \arg\max_{(x,y)} C(x, y). \tag{2.19}$$

was determined and then a Gaussian distribution was fitted to obtain sub-pixel resolution. Next, the image was deformed according to the determined image displacement via a bilinear interpolation [154]. This was repeated for the successive interrogation windows with smaller window sizes which improved the alignment of the cross-correlation matrix. After each pass, the velocity components ($i = x, y$) could be determined, using the time interval of the images Δt [154]

$$v_i = \frac{\Delta(i)}{\Delta t}. \tag{2.20}$$

2.3.5 Negative Stain Transmission Electron Microscopy

For transmission electron microscopy (TEM), bacteria from overnight GC agar plates were resuspended in warm (37 °C) liquid GC medium and the OD was set to 0.1. Next, 10 µL were transferred onto a 100 mesh formvar-coated copper grid (*Science Services*). This drop was then incubated for 20 min to allow the bacteria to settle. To fixate the bacteria, the copper grid was turned upside down on a drop of 2% formaldehyde (*Science Services*) for 5 min. Then, the grid was washed five times in phosphate-buffered saline. This was followed by a drop of 1% glutaraldehyde (*Sigma*) for 5 min. Then the grid was washed 10 times with MilliQ water. To negative stain the bacteria, the grid was placed on 10 µL uranyl acetate for 4 min. Finally, the stain was removed by filter paper. Imaging was performed at the CECAD (Cologne) imaging facility with 6.000x magnification at room temperature. The images were then analysed using *Fiji* to count the pili. If a T4P bundle was visible, it was counted as one pilus.

3 External Stresses Affect Gonococcal Type IV Pilus Dynamics

3.1 Publication

This work was published in the journal *Frontiers in Microbiology* with the title *External stresses affect gonococcal type 4 pilus dynamics* in 2022 [132]. It is an open-access article under the term of the Creative Commons Attribution 4.0 International (CC-BY) license.

3.1.1 Contributions to the Publication

The work presented here was performed in close collaboration with two colleagues from our group, namely Sebastian Kraus-Römer and Isabel Rathmann.

Sebastian Kraus-Römer contributed in the experimental design of visualising the T4P fluorescently and conducted the experiments of pilus labelling under various stress conditions. I was also involved in setting up the experimental pipeline and the major part of my contribution was to build and develop the semi-automated analysis program in *Matlab* [136] to analyse the microscopy data. The analysis was sub-divided into two main parts: pilus dynamics and pilus production rate.

Another part of the project was to investigate the difference on the transcriptional level under the applied external stresses. The transcriptome analysis was performed by Isabel Rathmann and Sebastian Kraus-Römer with the help of Jan Grossmann (CECAD, Cologne).

Berenike Maier, Sebastian Kraus-Römer, Isabel Rathmann and I were contributing in the project design, writing the manuscript and creating the figures.

frontiers in Microbiology

ORIGINAL RESEARCH
published: 25 February 2022
doi: 10.3389/fmicb.2022.839711

External Stresses Affect Gonococcal Type 4 Pilus Dynamics

Sebastian Kraus-Römer[1]†, Isabelle Wielert[1]†, Isabel Rathmann[1], Jan Grossbach[2] and Berenike Maier[1,3]*

[1] Institute for Biological Physics, University of Cologne, Cologne, Germany, [2] Faculty of Mathematics and Natural Sciences, CECAD, University of Cologne, Cologne, Germany, [3] Center for Molecular Medicine Cologne, Cologne, Germany

Bacterial type 4 pili (T4P) are extracellular polymers that serve both as adhesins and molecular motors. Functionally, they are involved in adhesion, colony formation, twitching motility, and horizontal gene transfer. T4P of the human pathogen *Neisseria gonorrhoeae* have been shown to enhance survivability under treatment with antibiotics or hydrogen peroxide. However, little is known about the effect of external stresses on T4P production and motor properties. Here, we address this question by directly visualizing gonococcal T4P dynamics. We show that in the absence of stress gonococci produce T4P at a remarkably high rate of ∼200 T4P min^{-1}. T4P retraction succeeds elongation without detectable time delay. Treatment with azithromycin or ceftriaxone reduces the T4P production rate. RNA sequencing results suggest that reduced piliation is caused by combined downregulation of the complexes required for T4P extrusion from the cell envelope and cellular energy depletion. Various other stresses including inhibitors of cell wall synthesis and DNA replication, as well as hydrogen peroxide and lactic acid, inhibit T4P production. Moreover, hydrogen peroxide and acidic pH strongly affect pilus length and motor function. In summary, we show that gonococcal T4P are highly dynamic and diverse external stresses reduce piliation despite the protective effect of T4P against some of these stresses.

Keywords: type 4 pilus, antibiotics, reactive oxygen species, molecular motor, *Neisseria*, transcriptome

Edited by:
Daniel Pletzer,
University of Otago, New Zealand

Reviewed by:
Charlene Kahler,
University of Western Australia, Australia
Wenxia Song,
University of Maryland, College Park, United States
Olivera Francetic,
Institut Pasteur, France

***Correspondence:**
Berenike Maier
berenike.maier@uni-koeln.de

†These authors have contributed equally to this work

Specialty section:
This article was submitted to Infectious Agents and Disease, a section of the journal Frontiers in Microbiology

***Received:** 20 December 2021*
***Accepted:** 25 January 2022*
***Published:** 25 February 2022*

Citation:
Kraus-Römer S, Wielert I, Rathmann I, Grossbach J and Maier B (2022) External Stresses Affect Gonococcal Type 4 Pilus Dynamics. Front. Microbiol. 13:839711. doi: 10.3389/fmicb.2022.839711

INTRODUCTION

Type 4 pili (T4P) are polymeric cell appendages that are responsible for a remarkable variety of functions in the bacterial world. These functions include adhesion to host cells and other surfaces, microcolony formation, twitching motility, horizontal gene transfer, and surface sensing (Berry and Pelicic, 2015; Craig et al., 2019). In contrast to most other extracellular structures, their length is highly dynamic and T4P retraction generates mechanical force (Merz et al., 2000; Skerker and Berg, 2001; Maier et al., 2002). Dynamics and force generation are crucial for many T4P associated functions. Therefore, it is important to quantify T4P dynamics in different environmental conditions.

Bacterial aggregation causes tolerance against a large number of antibiotics (Hall and Mah, 2017). The potential mechanisms include hindered diffusion of the drug within the colony (Tseng et al., 2013; Singh et al., 2016), stress responses (Nguyen et al., 2011; Secor et al., 2018), and community-related differentiation (Yan and Bassler, 2019). In many bacterial species, aggregation is controlled by T4P and therefore, piliation and T4P dynamics likely affect stress tolerance.

For example, piliation increased the tolerance against the β-lactam antibiotic ceftriaxone (Stohl et al., 2013) and hydrogen peroxide (Wang et al., 2018) in the human pathogen *N. gonorrhoeae*. Susceptibility for this drug can be modulated by fine-tuning T4P-T4P interactions between neighboring cells within the colonies. In particular, posttranslational modification of the major pilin subunit PilE or variation of the activity of the T4P retraction motor PilT affect the strength of cell-to-cell attachment (Bonazzi et al., 2018; Welker et al., 2018). We have shown recently, that even small changes in T4P-T4P interaction cause order of magnitude changes in the viscosity of the bacterial colonies (Zollner et al., 2019; Maier, 2021). This change in viscosity correlates with bacterial survival under antibiotic treatment (Cronenberg et al., 2021); when the fluidity is increased, the survival rate under ceftriaxone treatment decays. Importantly, antibiotic treatment affects colony fluidity (Cronenberg et al., 2021). In particular, the macrolide azithromycin and the fluoroquinolone ciprofloxacin strongly enhance colony fluidity, suggesting that T4P dynamics may be altered by the action of the antibiotics.

The T4P fiber is composed of major and minor pilins which are stored in the inner membrane of bacteria. The fiber is extruded through a T4P complex that spans the inner membrane, the periplasm, and the outer membrane (Craig et al., 2019). This complex is stable in the absence of the T4P fiber (Friedrich et al., 2014; Chang et al., 2016). At the cytoplasmic site of the T4P complex either an elongation ATPase (PilF) or a retraction ATPase (PilT) bind, supporting T4P elongation or retraction, respectively (Freitag et al., 1995; Wolfgang et al., 1998). T4P dynamics have been studied by microscopic techniques involving laser tweezers (Merz et al., 2000; Clausen et al., 2009; Ribbe et al., 2017), micropillars (Biais et al., 2008), and fluorescence microscopy (Skerker and Berg, 2001; Koch et al., 2021). Laser tweezers and micropillars probe mechanical effects of T4P retraction and enable measurement of T4P generated force. Laser tweezers with force feedback allow for characterization of T4P retraction speed at high accuracy (Clausen et al., 2009) but they are insensitive to T4P elongation. Gonococcal T4P were shown to retract at a speed of 2 or 1 μm/s, respectively, depending on oxygen availability (Kurre and Maier, 2012). Early protocols for fluorescence imaging (Skerker and Berg, 2001; Eriksson et al., 2015) were recently improved using maleimide chemistry (Ellison et al., 2019) and proven useful for characterizing T4P elongation and retraction in various bacterial species (Ellison et al., 2017, 2018; Lam et al., 2021; Vesel and Blokesch, 2021). In particular, the fluorescence method was used for quantifying T4P dynamics in detail in *Pseudomonas aeruginosa* (Koch et al., 2021). The results strongly support a model of stochastic and competitive binding between the extension ATPase PilF and the retraction ATPase PilT in excellent agreement with cryo-electron microscopy studies (Koch et al., 2021) and laser tweezers studies (Clausen et al., 2009). In these rod-shaped *P. aeruginosa*, T4P were mainly formed at the active pole, where most of the membrane-standing T4P complexes resided (Koch et al., 2021).

Here, we employ the fluorescence microscopy technique for investigating the dynamics of all T4P in spherically shaped and peritrichously piliated *N. gonorrhoeae* and develop image analysis tools for characterizing T4P dynamics. At the level of the entire cell, we characterize the rate of T4P production and T4P density. At the level of single T4P, we measure the velocities of T4P elongation and retraction, the maximum length that a T4P reaches prior to the onset of retraction, and the T4P lifetime. Combining these tools with RNA sequencing, the effects of the two antibiotics whose application is currently recommended against gonorrhea, azithromycin and ceftriaxone (Prevention CfDCa, 2015), are investigated. We present evidence that application of both drugs reduces piliation by downregulating the membrane-standing T4P complex that extrudes the T4P fiber. Furthermore, we investigate effects of antibiotics affecting various targets, and of natural stressors of *N. gonorrhoeae*. By combining all data, we find evidence that external stresses reduce the rate of T4P production by reducing the density of T4P complexes. Since piliation has been shown to protect gonococci from diverse external stresses, the reduction of piliation is likely to amplify the damage caused by these stresses.

MATERIALS AND METHODS

Bacterial Strains and Growth Media

Neisseria gonorrhoeae was grown overnight at 37°C and 5% CO_2 on agar plates containing gonococcal base (GC) agar [10 g/l Bacto agar (BD Biosciences, Bedford, MA, United States), 5 g/l NaCl (Roth, Darmstadt, Germany), 4 g/l K_2HPO_4 (Roth), 1 g/l KH_2PO_4 (Roth), 15 g/l Proteose Peptone No. 3 (BD), 0.5 g/l soluble starch (Sigma-Aldrich, St. Louis, MO, United States)] supplemented with IsoVitaleX (IVX): 1 g/l D-Glucose (Roth), 0.1 g/l L-glutamine (Roth), 0.289 g/l L-cysteine-HCL × H_20 (Roth), 1 mg/l thiamine pyrophosphate (Sigma-Aldrich), 0.2 mg/l $Fe(NO_3)_3$ (Sigma-Aldrich), 0.03 mg/l thiamine HCl (Roth), 0.13 mg/l 4-aminobenzoic acid (Sigma-Aldrich), 2.5 mg/l β-nicotinamide adenine dinucleotide (Roth) and 0.1 mg/l vitamin B_{12} (Sigma-Aldrich). GC medium is identical to the base agar composition but lacks agar and starch.

E. coli was grown in LB (Lysogeny Broth, Roth) medium or on LB agar plates (15 g/l Bacto agar (BD Biosciences, Bedford, MA, United States) at 37°C.

For *N. gonorrhoeae* antibiotics were used at the following concentrations: 2.5–5 μg/ml erythromycin (Thermo-Fisher), 100 μg/ml streptomycin (Sigma-Aldrich), 10 μg/ml chloramphenicol (Sigma-Aldrich). For *E. coli* antibiotics were used at the following concentrations: 50 μg/mL kanamycin (Roth).

Construction of Strain Carrying Cys-Modification Within Major Pilin

First, a fragment containing the promoter of the major pilin, *pilE*, and the *pilE* gene, P_{pilE}*pilE,* were amplified from genomic DNA (ΔG4, Ng150, **Supplementary Data Sheet 2**) with primers sk5 and sk40 (**Supplementary Data Sheet 3**). The PCR product was digested with XhoI and AflII (New England Biolabs), as well as the *piga* vector. The digested products were ligated and subsequently transformed into *E. coli* DH5α. After selection on kanamycin, plasmid DNA of positive clones were isolated with the GenUP^{TM} Plasmid Kit (biotechrabbit GmbH, Berlin, Germany) according to the manufacturer's instructions.

Then, the threonine at position 126 was replaced by cysteine as follows. *Via* site-directed mutagenesis with the KAPA polymerase (Roche) and primer sk43 and sk44 threonine at position 126 was substituted by a cysteine resulting in *pilE*^{T126C}. Afterward, the PCR reaction was digested with DpnI (New England Biolabs) to reduce the amount of template DNA. Subsequently, the digested PCR product was transformed into *E. coli*. Plasmid DNA was purified with the GenUP^{TM} Plasmid Kit (biotechrabbit) according to the manufacturer's instructions and sequenced with primers sk9 and sk10.

Subsequently, the native *pilE* sequence was replaced by *pilE*^{T126C} with a "clean substitution." To this end, we used a two-step selection process with a *ermC/rpsL* cassette as described in Dillard (2011). Δ*G4* (Ng150) was transformed with the fusion PCR product 5′UTRpilE- pilE^{T126C}-ermC-rpsLs-3′UTRpilE and selected on erythromycin. Insertion was controlled *via* PCR with primers sk32 and sk45. 5′UTRpilE pilE^{T126C} was amplified using primer sk129 and sk147 from plasmid DNA piga::P_{pilE}*pilE*^{T126C}. Primer sk146 and sk135 were used to amplify the *ermC-rpsL*$_s$ construct. 3′UTR was amplified using primer sk143 and sk145. The PCR products were fused and then the PCR product was transformed into Δ*G4 (Ng150)* and selected on erythromycin resulting in strain Δ*G4 pilE*^{T126C} step1 (Ng225). To check for correct insertion, the transformants were controlled *via* screening PCR. Subsequently, Δ*G4 pilE*^{T126C} step1 was transformed with the fusion PCR product 5′UTR pilE- pilE^{T126C}- 3′UTRpilE and counter-selected on streptomycin. 5′UTR pilE- pilE^{T126C} was amplified from Δ*G4 pilE*^{T126C} step1 (Ng225) with primer sk129 and sk131. 3′UTR was amplified from Δ*G4 (Ng150)* using primer sk132 and sk158. The PCR products were fused and transformed into Δ*G4 pilE*^{T126C}step1 (Ng225). During a successful "clean substitution" the *ermC* resistance gene and the dominant streptomycin-sensitivity allele *rpsL*$_s$ are spliced out and the strain is again resistant to streptomycin. Insertion was controlled *via* PCR with primers sk32 and sk45 and subsequently checked *via* sequencing with primer sk129. After counter-selection, strain ΔG4 *pilE*^{T126C} (Ng226) is isogenic to ΔG4 (Ng150) besides the amino acid exchange within *pilE.*

To construct strain Ng250, strain ΔG4 *pilE*^{T126C} (Ng226) was transformed with genomic DNA containing *pilT::m-Tn3cm* (Aas et al., 2007) and selected on chloramphenicol.

T4P Fluorescence Labeling

In order to visualize gonococcal T4P the protocol of Ellison et al. (2018) was adapted. Strain Δ*G4 pilE*^{T126C} (Ng226) was used for pilus labeling. The OD600 was adjusted to 0.1 in 100 μL cysteine-free retraction assay medium (RAM) consisting of phenol red-free Dulbecco's Modified Eagle Medium (GIBCO, Grand Island, NY, United States), 4.5 g/l Glucose (GIBCO), 2 mM L-glutamine (Roth), 8 mM sodium pyruvate (GIBCO), and 30 mM HEPES (Roth). Subsequently, 62 μM AF488 Alexa Fluor 488 C5 Maleimide (Thermo-Fisher) was added and cells were incubated for approximately 1 h at 37°C and 250 rpm. Then cells were washed and resuspended in GC media. A droplet of the resuspended cells was transferred onto a glass slide attached to a sticky-Slide 8 well (ibidi GmBH, Germany). A GC agar pad was put on top of the droplet and cells were imaged after a short incubation time (37°C and 5% CO_2).

To investigate the effect of antibiotic treatment on T4P characteristics, we incubated the cells before (2h) and during labeling (1 h) with antibiotics at twofold MIC with the following antibiotics: 0.256 μg/ml azithromycin (hello bio, Dunshaughlin, Ireland), 0.016 μg/ml ceftriaxone (hello bio.), 0.008 μg/ml ciprofloxacin (Sigma-Aldrich) and 0.128 μg/ml streptonigrin (Sigma-Aldrich). Controls were treated with the same volume of either DMSO (Roth) or 0.1 M HCl.

Oxidative Stress was applied in form of hydrogen peroxide (Roth). Cells were treated after labeling for 15 min with 1 mM H_20_2, 2 mM H_20_2 or the same volume of water as control.

Furthermore, the effects of pH on T4P characteristics were analyzed. GC medium was supplemented with 100 mM lactic acid (Roth) and adjusted to a pH of 5.5, 6.3, 7.0, and 7.7 with 10 M NaOH (Roth). During the labeling process, the pH of RAM was adjusted to the respective pH. Subsequently, cells were incubated for 10 min in pH-adjusted GC media prior to imaging.

Confocal Microscopy

Images were acquired using an inverted microscope (Ti-E, Nikon) equipped with a spinning disc confocal unit (CSU-X1, Yokogawa) and a 100×, 1.49 NA, oil immersion objective lens. The excitation wavelength was 488 nm. For pilus dynamic analysis, movies were generally recorded for 20 s with an auto exposure of 50 ms, resulting in a frame-rate of 19.33 frames/s. We analyzed only individual and well separated gonococci.

Determination the Rate of T4P Production and Number of T4P

All image processing steps and the analysis explained in this section were performed with MATLAB 2021. A region of interest of 50 × 50 pixels was defined for one bacterium per recorded video. Only bacteria, that show dynamic T4P were analyzed and, therefore, dead or inactive cells are excluded from the analysis. The image of a single T4P is diffraction-limited and, therefore, has a diameter of 3 Px (0.25 μm). The labeling of the cell envelope poses problems with T4P analysis. **Supplementary Figure 1** shows that the fluorescence intensity of a single T4P is considerably weaker compared to the intensity of the contour. Thus, the contrast was adjusted and filters were applied to reduce the noise as explained in the following.

We determined the average number of present pili, N_p, as well as the T4P production rate, r_p, as follows. A contour encircling the cell body was generated following the shape of each bacterium including monococci and diplococci. First, two binary masks of the cell body were created by setting a threshold above the intensity of the T4P. One of the masks was then enlarged by creating a disk-shaped structuring element from the center of mass of the original binary mask of the cell. The magnification of this mask depends on the average radii of the bacteria for each condition, therefore the radius of the disk-shaped structuring element was adapted to the condition we analyzed (control, pH, H_2O_2: 9 Px; azithromycin treatment: 7 Px; ceftriaxone treatment: 13 Px). For the magnification the MATLAB function *imdilate* was used and the *strel* function was used to create the structuring element. Subsequently, the original mask was subtracted from the magnified mask, resulting in a contour with a width from 1 to 2 pixels (**Supplementary Figure 2A**).

If a new T4P elongates from the cell body and crosses the contour, the fluorescence intensity at the respective position along this contour increases step-wise. When a T4P is fully retracted, the fluorescence intensity decreases step-wise to the background level. To detect the crossing of the pili through the contour, the contour of the cell was subdivided in 80 sectors emanating from the center of mass of the cell body (**Supplementary Figure 2A**). Each sector represents an angular division of 4.5°. Then, for each frame (time point) the contour was projected onto a line by averaging over all pixels of the contour which were assigned to the same sector. A wiener filter *wiener2* (MATLAB) was applied to the kymograph. To reduce the noise and enhance filamentous structures, the *fibermetric* function of MATLAB [*fibermetric* enhances filamentous objects *via* a Hessian based multiscale filter (MATLAB)] was applied (**Supplementary Figure 2B**). Next, the peaks corresponding to T4P were detected *via* the *peak* function (MATLAB) for each frame along the sectors of the contour (**Supplementary Figure 2C**). To avoid that noise is detected as a T4P or cuts a single T4P into two T4P, peaks that lasted for less than 0.5 s were disregarded and two detection events were connected if the pausing in detection in one sector was below 0.5 s. Sometimes, T4P fluctuate between two sectors. Therefore, peaks detected in neighboring sectors were connected. The rate of pili production, r_p, is rate number of newly generated T4P per cell and unit time. The occurrence of a new T4P was detected as a stepwise increase in fluorescence intensity at the contour around the cell. For example, in **Supplementary Figure 2B** new T4P occur around sector 10 at 2, 3, 5, and 7 s. To obtain r_p, the number new T4P detected around the contour are summed over 7.5 s and divided by 7.5 s. To obtain the average rate of T4P production, all data were averaged over multiple bacteria. The number of T4P present at a specific time point, N_p, is determined as the number of peaks along the contour (**Supplementary Figure 2C**). To obtain the mean number of T4P, the data were averaged over 7.5 s for each cell, and over multiple cells. All data were acquired on at least 3 days.

There are several limitations to the methods described above. First, short T4P with a length shorter than $\sim 0.8\ \mu$m are not detectable. Please note that this minimum length is shorter for other types of analyses, e.g., the T4P length distribution or the dynamics of individual T4P. Second, the number of detectable T4P is strongly reduced while bacteria are illuminated with laser light (**Supplementary Figure 3**). This effect is likely to due to photobleaching. Additionally, illumination of the fluorescent dye is likely to stress the bacteria by production of radicals and thus reduce the rate of T4P production. For this reason, we analyzed only the initial 7.5 s.

Analysis of Single T4P Dynamics

The analysis of T4P dynamics was performed using MATLAB 2021. First, we chose a region of interest around the cell. Then, we applied a two-dimensional median filter to reduce noise. The last step was to apply a wiener filter *wiener2* (MATLAB) filter to reduce the noise which was amplified by adjusting the contrast. Subsequently, we chose the pili of the cell which were suitable to characterize and analyze. The criteria for analyzing the dynamics were as follows: (a) Pili point straight and radially away from the cell surface. (b) The pilus is clearly distinguishable from the noise of the cell body, which means, in general longer than about 0.7 μm.

In the next step, we rotated the video such that the pilus is directed in horizontal direction and a rectangular region of interest around one pilus was chosen (**Supplementary Figure 4A**). Then, a second region of interest with a width of five pixels was chosen as shown in **Supplementary Figure 4B**. The intensity profile within the region was averaged vertically. This procedure was repeated for every frame. To create the kymograph, all intensity profiles were plotted next to each other. The goal of the kymograph was to determine the elongation and retraction velocities. We edited the kymograph first by adjusting the contrast and then we detected the edges (**Supplementary Figure 4C**) which provided us with the track of the positions of the pilus tip. To obtain the velocity of T4P elongation and retraction, we determined the slope between the start and the end of each event (**Supplementary Figure 4D**). The procedure was repeated for each T4P of a gonococcus.

Analysis of T4P Length

We measured the maximum length of T4P, T_p, i.e., the length of each T4P at the time point where the pilus switched from elongation to retraction. All steps were performed with ImageJ (Fiji). We cropped a region of interest around a single gonococcus. Next, we summed all intensity values for the first hundred frames. Then, the contrast was adjusted and the image was sharpened (**Supplementary Figure 5**). From this image, we measured the length of every detectable pilus. As the noise of the cell body is still prominent, we decided that pili below a length of 0.5 μm were below the resolution of the measurement.

RNA Isolation, Sequencing, and Transcriptome Analysis

Strain Δ*G4* (Ng150) was grown in a 24 well plate (Greiner Bio-One) in 1 mL cultures inoculated with approximately 3×10^6 cells. Cells were grown for 6h at 37°C, 5% $C0_2$ in an Infinite M200 plate reader with a shaking period of 2 min per OD cycle (OD was measured every 10 min). After 6h growth, azithromycin or ceftriaxone were added at twofold MIC or an equal amount of DMSO as control. After 15 and 60 min samples were treated with RNA protect bacteria reagent (Qiagen, Hilden, Germany) according to the manufacturer's instructions. Pellets were stored in −80°C until total RNA was isolated by using the Qiagen RNeasy Protect Bacteria Mini Kit (Hilden, Germany) according to the manufacturer's instructions. RNA was isolated from each condition from three different days each representing one batch. RNA samples were sent to Cologne Genomic Center (Cologne, Germany) for next-generation sequencing (NGS) and depletion of ribosomal RNA. Sequencing was performed on an Illumina

HiSeq system with 100 bp paired reads and on average 10 million reads per sample. The RIN values of each sample were ≥ 9.9.

The reads from each library were trimmed and paired with Trimmomatic (version 0.36) (Bolger et al., 2014). The reads were then mapped against the reference genome of Neisseria gonorrhoeae MS11 (NCBI, CP003909.1) using STAR (2.5.3a) (Dobin et al., 2013). For calling read counts of all known genes of the reference, we used the program featureCounts from the subread package (version: 2.0.1) (Liao et al., 2014). We calculated the differential gene expression with the DESeq2 package implemented in R, controlling for batch differences between days. For each gene we then obtain the log2-fold change of the antibiotic treatment with respect to the DMSO-treated control, as well as the associated adjusted *p*-value. A gene is regarded as differentially regulated with if the (adjusted) *p*-value is ≤ 0.05 and the $|$ log2-fold change$| \geq 0.5$. The genes required for assembling the T4P core complex were annotated manually, the data can be found in **Supplementary Data Sheet 2**.

Genes with a copy number > 1 were excluded from the analysis, leaving 1,960 genes. For each gene, the ortholog in *N. gonorrhoeae* FA1090 (NC_002946.2) strain was determined *via* blastn (Camacho et al., 2008). Functional enrichment was performed for 17 functional categories, that were based on KEGG ontology (McClure et al., 2020) with the one-sided Fisher's exact test and Bonferroni correction. These categories were condensed such that each gene is associated with one category, as can be found in **Supplementary Data Sheet 3**.

RESULTS

Gonococci Generate T4P at a Remarkably High Rate

In the first step, we characterized gonococcal T4P dynamics in the absence of external stress. To this end, we adapted a T4P labeling protocol that was previously developed for *Caulobacter crescentus* and *Vibrio cholerae* (Ellison et al., 2019). A cysteine was introduced into the hypervariable region of the major pilin PilE enabling modification with the fluorescent dye Alexa Flour488 C_5 maleimide as described in the Methods. Fluorescently labeled gonococci were sandwiched between a cover glass and an agar pad and imaged using confocal microscopy. Wt gonococci showed impressively dynamic T4P (**Figure 1A** and **Supplementary Movie 1**). Typically, multiple T4P were present simultaneously at different stages of elongation and retraction. As expected, deletion of the retraction ATPase PilT inhibited T4P dynamics (**Supplementary Figure 6**), confirming that the observed dynamics depends on PilT.

The gonococcal cell envelope shows a strong fluorescent signal (**Figure 1A** and **Supplementary Figure 7**). Application of the dye to wt gonococci that do not carry the cysteine within the hypervariable loop of PilE, produces weakly fluorescent cells, indicating that the high density of PilE within the cell envelope is mostly responsible for the strong signal of the cell body. The strong signal of the cell envelope prohibits the detection and analysis of short T4P as explained in the Methods. Moreover, it was unclear how the signal-to-noise ratio affected T4P detection and whether the fluorescent label affects T4P assembly. To assess these potential problems, we counted the average number of T4P per cell. We averaged this number over time (7.5 s) and over multiple cells and found $\langle N_p \rangle = 5.9 \pm 0.1$ (mean ± se) (**Figure 1B**). We compared this result to the result previously obtained using transmission electron microscopy (TEM) of $N_p = 7.2 \pm 0.5$ (Holz et al., 2010). TEM detects T4P with length $\geq 0.2\ \mu\text{m}$, indicating that the shortest 20% of T4P are not detected by fluorescence microscopy. However, the difference is small and we conclude that most T4P are detectable by the new method. We note that using both methods we study a projection of T4P projected to 2D.

The number of T4P per cell, $N_p = r_p \tau_p$, is determined by the rate at which a cell produces new T4P, r_p, and the lifetime of a T4P, τ_p. The determination of τ_p will be described below. To determine r_p, newly formed T4P were detected as stepwise increases in fluorescence intensity in the cell contour as described in the Methods. We counted the number of new T4P around the cell contour during a time interval of 7.5 s. We found that the mean rate of T4P production was $\langle r_p \rangle = 196 \pm 3\ min^{-1}$ (**Figure 1C**), i.e., on average a single gonococcus produces 196 new T4P within 1 min. Furthermore, we characterized the distribution of maximum lengths, $l_p{}^{max}$, that T4P reached (**Figure 1D**). For each T4P, the length was measured at the time point of switching between elongation and retraction. The probability distribution of l_p agreed well with an exponential function $p\left(l_p\right) = p_0 exp\left(-l_p/l_p^c\right)$. A fit to this function yields a characteristic length of $l_p^c = (0.78 \pm 0.06)\ \mu m$. This exponential distribution was expected, assuming that the length of a T4P is determined by the rate of T4P elongation and the detachment rate of the elongation ATPase PilF. If PilF detaches at a constant rate, then its lifetime at the base of the T4P complex is exponentially distributed (Philips et al., 2013) and thus the distribution of T4P lengths is also exponential.

In summary, fluorescence labeling is a useful method for characterizing T4P in *N. gonorrhoeae*. We find that T4P are produced at a high rate of $\sim$200 T4P min^{-1}.

Elongation and Retraction of Single T4P Proceed Persistently

To further characterize T4P dynamics, we focused on individual T4P (**Figure 2** and **Supplementary Figure 4**). A single T4P was aligned (**Figures 2A,B**) and a kymograph of this pilus was generated (**Figure 2C**). We found that T4P elongation and retraction showed little pausing at a time resolution of 50 ms. Furthermore, there were no detectable pauses between T4P elongation and retraction, showing that retraction immediately succeeded elongation. As explained in the Methods part, the kymographs were used for determining the velocities of T4P elongation and retraction (**Figure 2D**). The elongation velocities were narrowly distributed around $v_{elo} = (0.86 \pm 0.02)\ \mu ms^{-1}$ (mean ± standard error) (**Figure 3C**). The retraction velocities were more broadly distributed around $v_{ret} = (-1.25 \pm 0.02)\ \mu ms^{-1}$. We note that the absolute speed measured in this work is lower compared to velocities of $v_{ret}^{lt} \approx 2 \mu ms^{-1}$ determined by laser tweezers

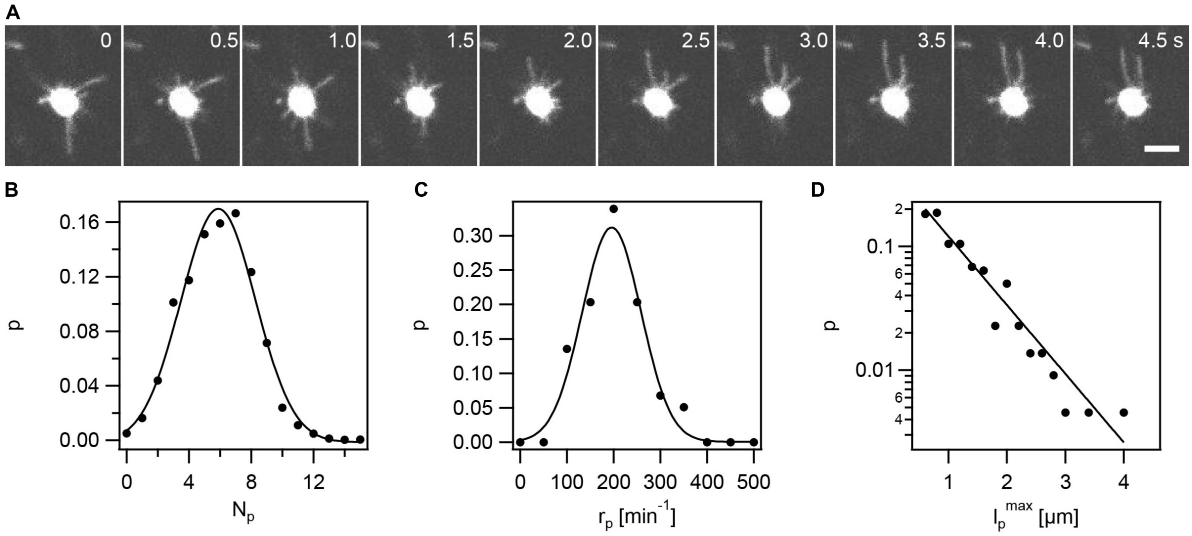

FIGURE 1 | Visualization of fluorescent T4P in *N. gonorrhoeae* (Ng226). **(A)** Time lapse of gonococcus with AF488-labeled T4P. Scale bar: 2 μm. **(B)** Circles: Probability (p) distribution of number of T4P per cell, N_p. Full line: Gaussian fit with $\langle N_p \rangle = 5.9 \pm 0.1$ (mean from 59 cells ± standard error). **(C)** Circles: Probability distribution of rates of T4P production per cell, r_p. Full line: Gaussian fit with $\langle r_p \rangle = (196 \pm 3)\ min^{-1}$ (mean of 59 cells ± standard error). **(D)** Circles: Probability distribution of T4P lengths l_p^{max} (derived from 220 T4P). l_p^{max} specifies the maximum length of a T4P, i.e., the length at the point in time where the T4P switches from elongation to retraction. Full line: exponential fit with characteristic length $l_p^c = (0.78 \pm 0.06)\ \mu m$.

(Kurre and Maier, 2012). This difference may be explained by different media used to probe T4P dynamics or by the fact that the fluorescent probe induces friction and thus reduces the retraction speed.

We conclude that in wt gonococci, no pausing is detectable between the end of T4P elongation and the start of T4P retraction. The rate of retraction is higher compared to the rate of elongation in agreement with recent results obtained for *P. aeruginosa* (Koch et al., 2021).

Treatment With Azithromycin or Ceftriaxone Reduces the Rate of T4P Production

Application of antibiotics may affect T4P production and dynamics and consequentially cellular attraction within colonies. Previously, we have shown that increased attraction enhances survivability under antibiotic treatment (Cronenberg et al., 2021). Here, we will assess the effects of azithromycin and ceftriaxone on T4P production and dynamics. Azithromycin inhibits translation and ceftriaxone inhibits cell wall synthesis.

Cells were incubated at twofold minimal inhibitory concentration (MIC, **Supplementary Table 3**) for 3 h with the antibiotics prior to imaging. Under these conditions, the pilus production rate was reduced ∼ twofold to $\left\langle r_p^{azi} \right\rangle = (121 \pm 8)\ \ min^{-1}$ under azithromycin treatment and to $\left\langle r_p^{cef} \right\rangle = (152 \pm 8)\ \ min^{-1}$ under ceftriaxone treatment (**Figures 3A–D**). This is consistent with early TEM studies showing reduced piliation in response to azithromycin treatment (Gorby and Mcgee, 1990).

At the level of single T4P, azithromycin significantly reduced the speed of T4P elongation to and of retraction to $v_{elo}^{azi} = (0.71 \pm 0.02)\ \mu ms^{-1}$ and $v_{ret}^{azi} = (-1.04 \pm 0.03)\ \mu ms^{-1}$, respectively (**Figures 3C,D** and **Supplementary Movie 2**). Moreover, the characteristic length of T4P was reduced under azithromycin treatment (**Figure 3E**). Ceftriaxone treatment did not affect the speed of T4P elongation and the length of T4P and slightly reduced the retraction speed (**Figures 3C–E** and **Supplementary Movie 3**).

We assessed whether other antibiotics showed similar effects on the T4P dynamics. Ciprofloxacin and streptonigrin are inhibitors of DNA replication. We applied both antibiotics at twofold their MICs. Both antibiotics strongly reduced the rate of T4P production (**Supplementary Figure 8**). Furthermore, their application reduced the speeds of T4P elongation and retraction slightly but significantly.

We conclude that treatment with antibiotics targeting translation, cell wall synthesis, and DNA replication strongly reduce piliation and interfere with T4P dynamics.

Treatment With Azithromycin Downregulates Expression of Genes Related to T4P Biogenesis

Since we found the azithromycin and ceftriaxone reduce the rate of T4P production, we addressed the question whether genes involved in T4P biogenesis were downregulated during antibiotic treatment. The transcriptome was sequenced and RNA levels under antibiotic treatment were compared to control samples that were treated with solvent only.

At the genome-wide level, azithromycin treatment caused differential regulation of a large fraction of genes. After 60 min

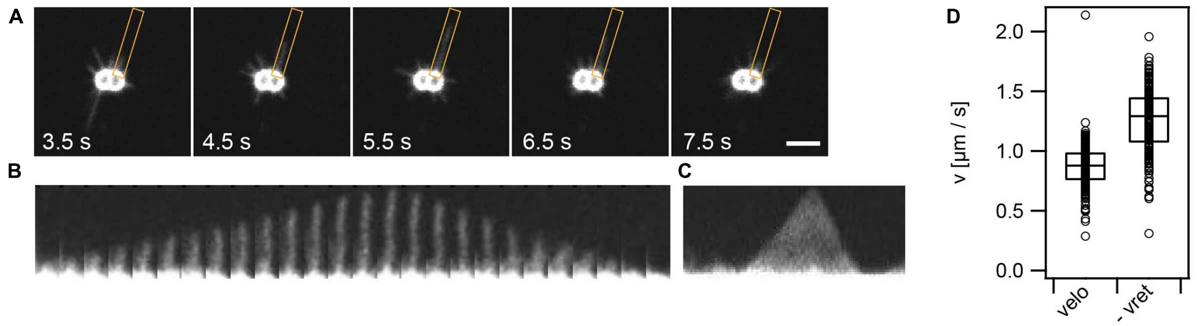

FIGURE 2 | T4P dynamics. **(A)** Time series of T4P dynamics. The orange box denotes the ROI used for analysis of one pilus. **(B)** For analysis, each pilus is aligned. Shown is a T4P that elongates and subsequently retracts. Time interval between two images: 0.1 s. **(C)** Kymograph of T4P shown in panel **(B)** as used for analysis of T4P elongation and retraction speed. **(D)** Velocities of T4P elongation, v_{elo}, and retraction, v_{ret}. Shown are circles: single T4P data, box: 25/75 percentiles, and median for 171 T4P.

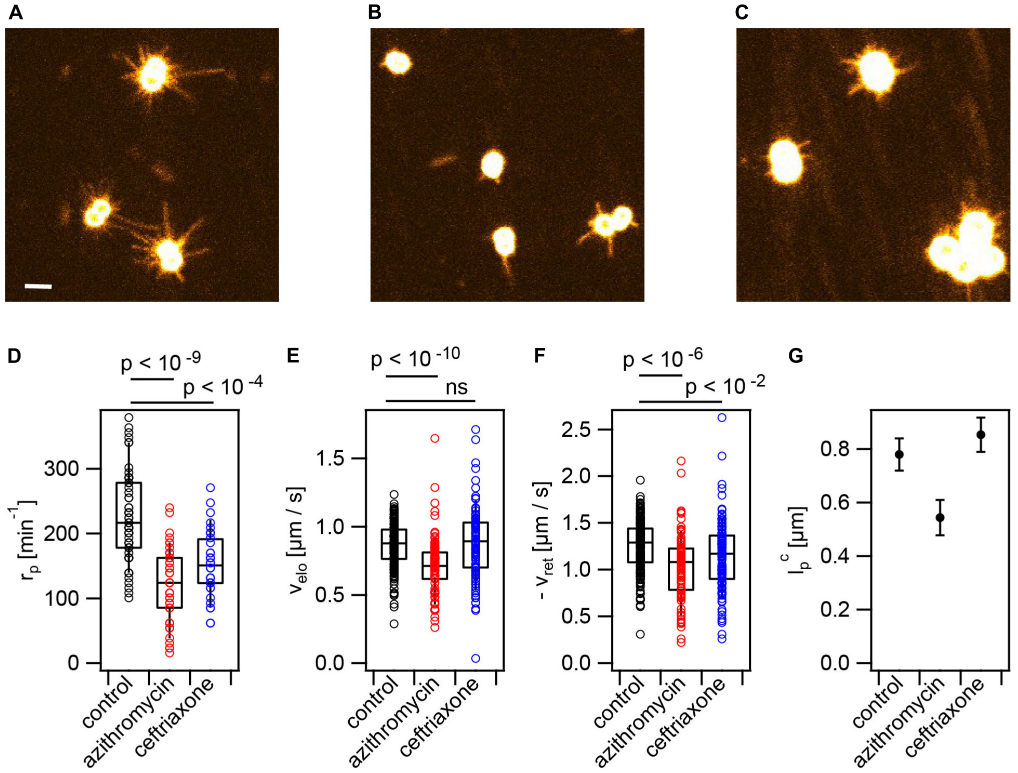

FIGURE 3 | Antibiotic treatment reduces T4P production rate. Cells (Ng226) were treated with azithromycin or ceftriaxone, respectively, at twofold MIC for 3 h. Typical images of fluorescent T4P **(A)** without treatment, **(B)** with azithromycin, **(C)** with ceftriaxone. Scale bar: 2 µm. **(D)** Rate of T4P production, r_p (>35 cells for each condition). **(E)** T4P elongation velocities, v_{elo} (>85 T4P for each condition). **(F)** T4P retraction velocities, v_{ret} (>96 T4P for each condition). Shown are circles: single T4P data, box: 25/75 percentiles, and median for 171 T4P. *p*-values obtained from KS test. **(G)** Characteristic maximum T4P lengths l_p^c and errors obtained from exponential fits to the length distributions.

of treatment, 12.9% were downregulated (at least −0.5 $\log_2$ fold or 0.7 fold change in mRNA levels, adjusted *p*-value of ≤ 0.05) and 14.3% were upregulated (at least 0.5 $\log_2$ fold or 1.4 fold change in mRNA levels, adjusted *p*-value of ≤ 0.05) (**Figure 4B**). Fewer genes were affected after 60 min of ceftriaxone treatment, with 1.6% downregulation and 2.6% upregulation (**Figure 4C**).

We investigated how azithromycin and ceftriaxone treatment affect mRNA levels of the 22 genes encoding for proteins that assemble the T4P core complex and the T4P fiber (**Figure 4A**). The genes considered as T4P assembly genes, listed in **Supplementary Data Sheet 2**, were annotated manually. After 60 min of azithromycin treatment, we find that 9 out of 22 genes were downregulated (**Supplementary Data Sheet 2** and **Figure 4B**) resulting in an enrichment of this group of genes (p = 0.001, one-sided Fisher's exact test). None of the T4P assembly genes were upregulated. Most prominently, the *pilMNOPQ* operon (with the exception of *pilP*) was downregulated (**Figures 4A,B**). This operon encodes for PilQ proteins forming the secretin for the extrusion of the pilus fiber and PilMNOP proteins assembling the periplasmic complex. Moreover, the gene encoding the platform protein, PilG, residing within the cytoplasmic membrane, is downregulated. Next to genes involved in core complex assembly, the expression of a gene affecting piliation, *pilW*, and the minor pilin *pilJ* is reduced. Finally, the retraction ATPases PilT2, and PilU are downregulated. Under ceftriaxone treatment, none of the T4P-related genes is differentially regulated under our criteria (adj. p-value $\leq$ 0.05 and $|$ log2-fold change$| \geq 0.5$). Yet multiple genes meet the adj. p-value $\leq$ 0.05 criterium, suggesting that they are weakly downregulated (**Figure 4C** and **Supplementary Data Sheet 2**).

To summarize, treatment with azithromycin downregulates T4P biogenesis genes in agreement with lower rates of T4P production observed by fluorescence microscopy.

Other External Stresses Reduce the Rate of T4P Production and T4P Dynamics

During their infection cycle, *N. gonorrhoeae* experiences various stresses. For example, lactobacilli produce H_2O_2 and lactic acid (Gong et al., 2016); macrophages produce reactive oxygen species including H_2O_2 (Quillin and Seifert, 2018). We assessed the effects of these stresses on T4P production and dynamics. Cells were pre-incubated with hydrogen peroxide for 15 min prior to imaging. Please note that the incubation time was shorter compared to the incubation time with antibiotics of 3 h. Therefore, the control values are slightly different from **Figures 1**, **3**. With 2 mM H_2O_2, the rate of T4P production was reduced to $(91 \pm 8)\ min^{-1}$ (**Figure 5A** and **Supplementary Movie 4**). The speeds of T4P elongation and retraction were reduced to $v_{elo}^{H2O2} = (0.68 \pm 0.02)\ \mu ms^{-1}$ and $v_{ret}^{H2O2} = (-0.78 \pm 0.02)\ \mu ms^{-1}$ (**Figures 5B,C**), respectively. H_2O_2 showed the strongest effect on the characteristic maximal length of T4P which was reduced from $l_p^c = (1.15 \pm 0.05)\ \mu m$ to $l_p^{c,\ H2O2} = (0.35 \pm 0.02)\ \mu m$ (**Figure 5D**).

Furthermore, we addressed the effects of lactic acid and external pH on T4P dynamics. During their infection cycle, gonococci experience pH ranging from pH 4–8 (Pettit et al., 1999). We supplemented the media with 100 mM lactic acid, since this acid is produced by lactobacilli known to counteract gonococcal infections (O'Hanlon et al., 2013). Prior to T4P fluorescence labeling, the pH of the solution was adjusted to different pH by titration of sodium hydroxide (NaOH). The same pH was maintained during imaging. So far, experiments were performed at pH 7.0. We found that increasing the pH to pH 7.7 showed little effect on T4P dynamics (**Figures 6D–F**). By contrast, decreasing the pH to pH 6.3 reduced the rate of T4P production, and the speeds of T4P elongation and retraction (**Figures 6D–F** and **Supplementary Movie 5**). At pH 5.5, we observed that the lengths of some T4P reached beyond 30 µm (**Figures 6A,B**). At this pH, T4P did not retract. The distribution of T4P lengths could not be described by a single exponential function like the distributions at higher pH. Instead, we fitted a double exponential function (**Figure 6B**) with one characteristic length of $l_{p1}^{c,\ pH5.5} = (0.8 \pm 0.2)\ \mu m$ that was comparable to

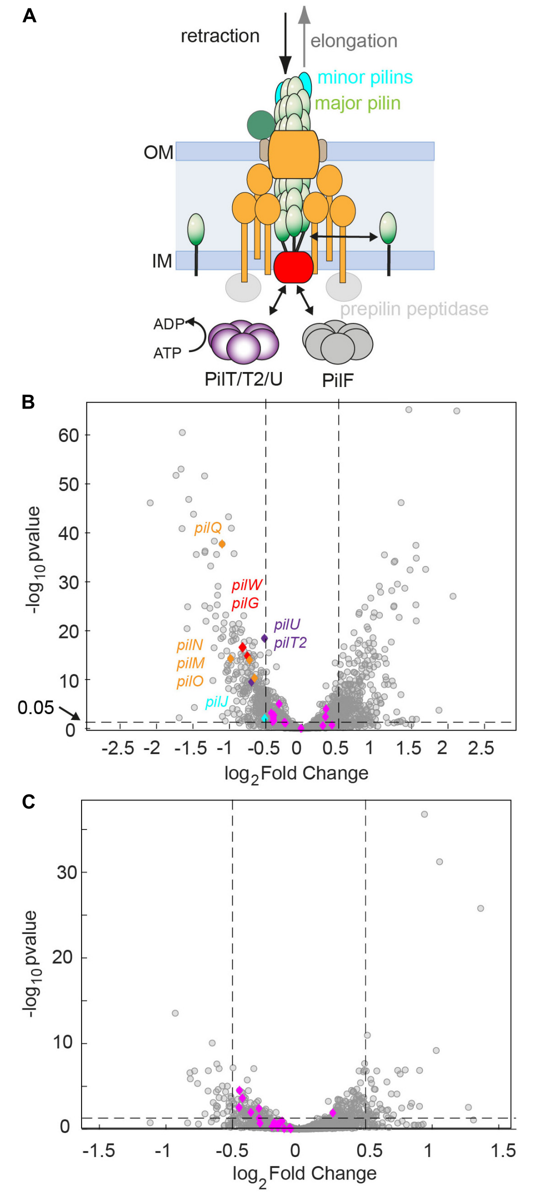

FIGURE 4 | Genes required for assembling the T4P core complex are downregulated after 60 min of antibiotic treatment at twofold MIC. **(A)** Sketch of the T4P assembly complex including the pilus fiber and the elongation and retraction ATPases. **(B,C)** Volcano plots showing adjusted p-values as a function of the $\log_2$fold changes of RNA levels relative to the DMSO-untreated control determined by RNA sequencing. Gray: all genes. Blue and other colors: genes involved in T4P assembly. Dotted lines: Genes are defined to be differentially regulated if adj. $p \leq 0.05$ and $|log_2 fold\ change| \leq 0.5$. **(B)** Treatment with azithromycin. 12.9% of genes are downregulated. 14.3% of genes are upregulated. **(C)** Treatment with ceftriaxone. 1.6% of genes are downregulated. 2.6% of genes are upregulated.

the length at higher pH and a second characteristic length of $l_{p2}^{c,\,pH5.5} = (5.5 \pm 0.6)\,\mu m$ (**Figure 6C**). This finding indicates that PilT is inactive or its binding to the T4P complex is inhibited at pH 5.5 while PilF is still functional. We suggest that consecutive PilF binding events generate the long T4P while the short T4P result from single binding events and, therefore, the lengths of the latter T4P are comparable to the length at higher pH.

Finally, we investigated how energy depletion affects T4P dynamics, in particular the effect of the proton motive force. We applied the uncoupler CCCP for 10 min and found that the T4P production rate as well as single T4P dynamics were strongly reduced (**Supplementary Figure 9**). This finding is consistent with earlier studies of T4P retraction, where we showed that depletion of pmf reduces the speed of T4P retraction (Kurre et al., 2013). Interestingly, the strong and rapid reduction of the T4P production rate can explain why gonococcal colonies disassemble under CCCP treatment (Dewenter et al., 2015).

Taken together, we found that various external stresses including hydrogen peroxide, uncouplers of the membrane potential, and low pH reduce the rate of T4P production and reduce the rates of T4P elongation and retraction. The only exception was application of low pH, where we found that T4P retraction was inhibited leading to elongated T4P.

The Rate of T4P Production Is Independent of T4P Lifetime but Correlates With T4P Density

We found that application of a variety of different stresses reduces the rate of T4P production r_p. This reduction may be caused either by increased lifetime of T4P τ_p, which would reduce the turn-over of T4P, but may not affect the number of T4P, N_p. On the other hand, if the production rate doesn't depend on the lifetime, then we expect that lower production rate results in a lower N_p.

To assess whether r_p correlates with τ_p, we determined the T4P lifetimes as $\tau_p = l_p/v_{elo} + l_p/v_{ret}$. Depending on the stress conditions, the lifetime varied between $\tau_p = (1.0 \pm 0.1)\ s$ and $\tau_p = (2.3 \pm 0.1)\ s$ (**Supplementary Figure 10**). The T4P production rate r_p and T4P lifetime τ_p showed no significant correlation (**Figure 7A** and **Supplementary Table 4**). Next, we determined the mean number of T4P per cell, N_p. This number is reduced under all stress conditions. In particular, N_p was reduced ~ threefold under azithromycin and CCCP treatment (**Supplementary Figure 10B**). We found strongly significant correlation between N_p and r_p (**Figure 7B** and **Supplementary Table 4**), indicating that the reduced rate of T4P production reduces the density of T4P.

It is also interesting to note that the velocities of T4P elongation and retraction show very strong correlation ($r = 0.9 \pm 0.2$, **Supplementary Table 4**). This indicates that reduction of the rates at which PilF and PilT work are similar under different stress conditions, possibly due to reduced energy levels.

We conclude that the lifetime of T4P is variable under different stress conditions and does not correlate with the rate of T4P production. Reduction of the T4P production rate results in reduced number of T4P in agreement with reduced expression of genes involved in the T4P complex under antibiotic treatment.

DISCUSSION

Putative Functions of Fast T4P Dynamics in *N. gonorrhoeae*

Dynamics of T4P have been characterized for different types of pilus systems in various species (under laboratory conditions) revealing a large dynamic range. For example, *P. aeruginosa* produces no more than ~8 T4P min^{-1} (Koch et al., 2021) and *V. cholerae* competence pili are produced at ~1 T4P min^{-1} (Ellison et al., 2018). Here we show that the rate of T4P production of ~200 T4P min^{-1} in *N. gonorrhoeae* is very high compared to these bacterial species. This rate is likely underestimated, because fluorescently labeled pilin in the membrane produce a strong signal and prohibit the characterization of short T4P.

Moreover, gonococcal T4P generate high force by retraction on the order of ~150 pN (Marathe et al., 2014) compared to ~40 pN of *P. aeruginosa* (Ribbe et al., 2017) and ~10 pN of *V. cholerae* (Ellison et al., 2018). We propose that high forces and fast T4P dynamics are required for the tug-of-war that enables twitching motility both at surfaces (Marathe et al., 2014) and within colonies (Bonazzi et al., 2018; Welker et al., 2018; Zollner et al., 2019) formed by *N. gonorrhoeae* and closely related *N. meningitidis*. In particular, within colonies, high force and fast dynamics enable fluid-like behavior of colonies. The fluid-like state is important for colonization of blood vessels (Bonazzi et al., 2018) and survivability within colonies (Cronenberg et al., 2021). Motor activity also enables gonococcal colonies to respond rapidly to environmental changes like oxygen limitation (Dewenter et al., 2015); when oxygen levels fluctuate close to a threshold concentration, T4P dynamics drive colony disassembly and re-assembly within seconds.

Taken together, we propose that fast T4P dynamics and high force generation support the lifestyle of *Neisseria*. A high density of T4P enables rapid colony formation, but the T4P-bonds are highly dynamic and thus keep colonies in a fluid-like state.

Downregulation of T4P-Related Genes Agrees With Reduction of T4P Production Rate Under Azithromycin Treatment

To better understand the effect of antibiotic treatment on T4P production, we characterized the transcriptional response of T4P-related genes to antibiotic treatment, focussing on two drugs that are currently used for treatment of gonorrhea, namely azithromycin and ceftriaxone. We found that genes required for building the membrane-standing T4P complex, are strongly downregulated under azithromycin treatment. The effect of downregulation was most severe (twofold) for *pilQ* and other members of the *pilMNOPQ* operon (Pelicic, 2008). Similarly, the expression of the gene encoding the platform protein PilG and a gene affecting piliation (*pilW*) (Carbonnelle et al., 2005;

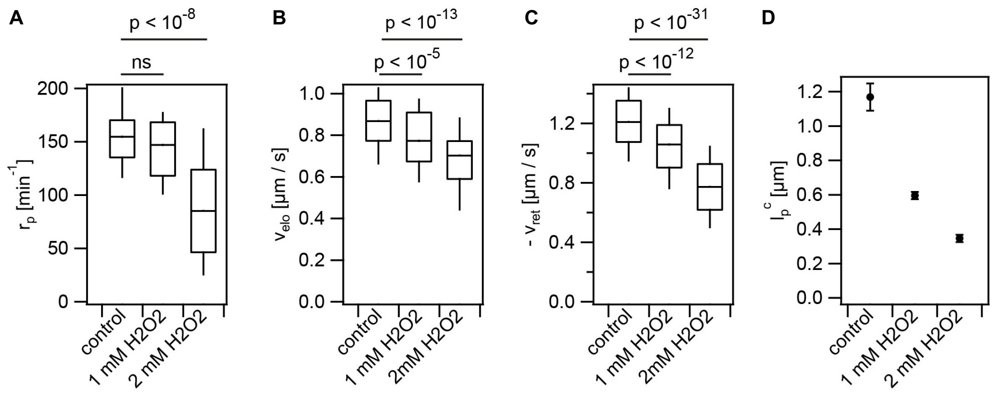

FIGURE 5 | Hydrogen peroxide reduces T4P production rate and T4P dynamics. Cells (Ng226) were treated with H_2O_2 for 15 min. **(A)** Rate of T4P production, r_p. (>40 cells for each condition) **(B)** T4P elongation velocities, v_{elo} (>97 T4P for each condition). **(C)** T4P retraction velocities, v_{ret} (>100 T4P for each condition). Shown are box: 25/75 percentiles, and median for 171 T4P. *p*-values obtained from KS test. **(D)** Characteristic maximal T4P length. (>340 T4P for each condition).

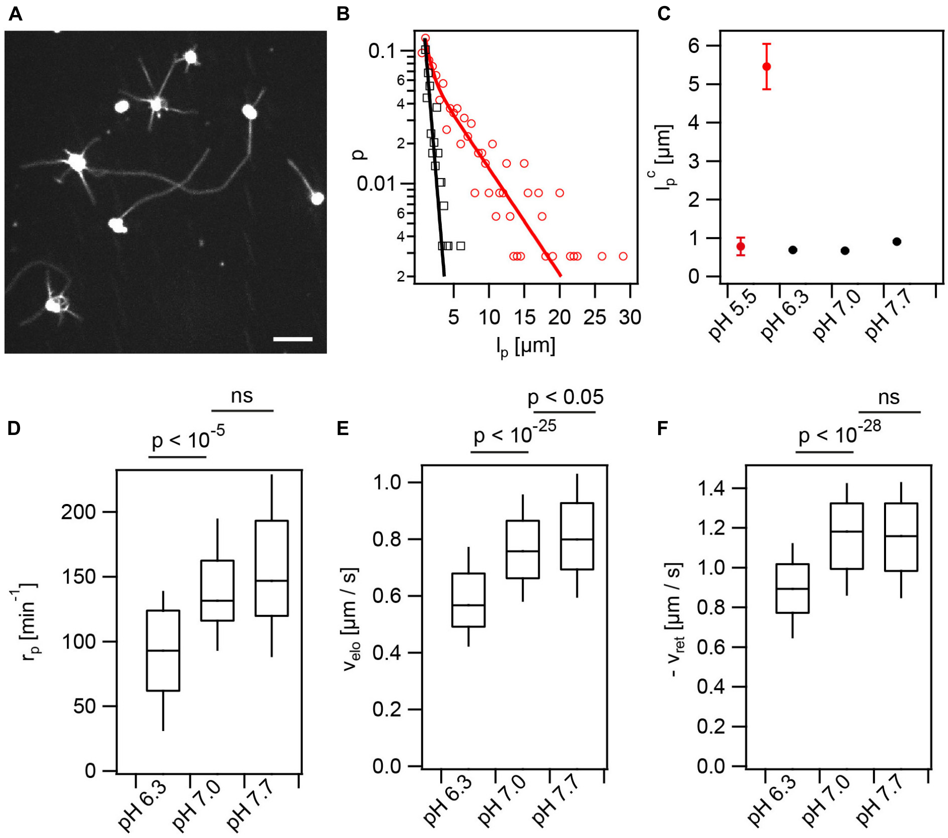

FIGURE 6 | Extracellular pH affects T4P dynamics. In the presence of lactic acid, the external pH was adjusted to different values. **(A)** At pH 5.5 T4P appear elongated. Scale bar: 5 µm. **(B)** Distribution of maximal T4P lengths at pH 5.5 with double exponential fit (red) and pH 7.0 with exponential fit (black). **(C)** Characteristic maximal T4P length at varying pH. The characteristic length was determined from an exponential fit for pH 6.3–7.7. At pH 5.5, the two characteristic lengths obtained from the double-exponential fit are shown. (>247 T4P for each condition) **(D)** Rate of T4P production, r_p (>32 cells for each condition). **(E)** T4P elongation velocities, v_{elo} (>87 T4P for each condition). **(F)** T4P retraction velocities, v_{ret} (>100 T4P for each condition).

Hu et al., 2020) are downregulated. Thus, the reduced expression of genes encoding for the membrane-standing T4P complex reduces the number of complexes from which T4P can extrude, explaining why the T4P density is reduced. Regulation of T4P related genes in *N. gonorrhoeae* is poorly understood. In the following, we will consider the potential roles of known

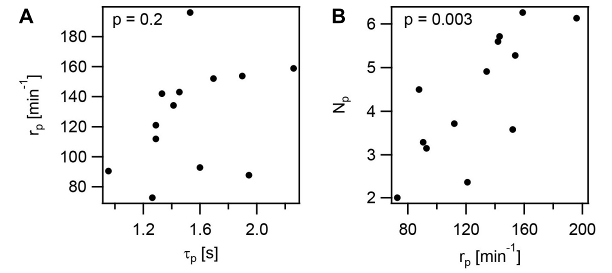

FIGURE 7 | Correlations in T4P dynamics and production rate. The data plotted are mean values from independent experiments at the different conditions investigated in this study. **(A)** Rate of T4P production as a function of the T4P lifetime. **(B)** Rate of T4P production as a function of the number of T4P per cell. *p*-values were obtained from 2-tailed test for the hypothesis that there is no correlation.

regulators whose expression is significantly changed in our study. Most interestingly, *misR*, a homologue of *E. coli cpxR*, is part of a two-component system involved in response to cell envelope stress (Kandler et al., 2016). Its deletion causes downregulation of genes involved in T4P production ($|\log_2$fold change$| \geq 0.5$, $p \leq 0.05$), including *pilQ*, *pilP*, *pilO*, *pilW*, *pilG*, *pilD*, *pilU*, *pilIJKL* (McClure et al., 2020). The differential expression similar to our results for azithromycin treatment. Therefore, we assessed the expression of *misR* (NGFG_00314) and found 0.7 fold downregulation. In another study, MtrR was shown to be a repressor of *pilM* (Folster et al., 2007). For this regulator, we find no significant change in its transcription under antibiotic treatment.

In summary, downregulation of T4P-related genes during antibiotic treatment explains why the rate of T4P production is reduced.

Putative Roles of Metabolic Changes in T4P Dynamics

The T4P elongation and retraction ATPases rely on ATP, and therefore, reduction of ATP levels will influence their activities. We have shown previously that depletion of ATP reduces the speed of gonococcal twitching motility (Kurre et al., 2013). The speed of twitching motility tightly correlates with the speed of T4P retraction (Marathe et al., 2014), indicating that reduced ATP levels reduce the speed of T4P retraction. Furthermore, the velocity of T4P retraction depends on proton motive force (Kurre et al., 2013). Here, we found that azithromycin and ceftriaxone treatment reduced the velocity of T4P retraction and azithromycin additionally reduces the velocity of T4P elongation.

We addressed the question whether antibiotic treatment affected metabolic pathways that govern the energy levels in gonococci. Analyzing the transcriptomes based on 17 categories from KEGG orthology (McClure et al., 2020), we found that carbohydrate metabolism was differentially regulated under azithromycin treatment (**Figure 8A**) ($p = 9 \times 10^{-6}$, one-sided Fisher's exact test with Bonferroni multiple testing correction). Most of these genes are downregulated (**Supplementary Data Sheet 3**). In particular, genes involved in ATP-producing glycolysis were expressed at lower levels. Under ceftriaxone treatment, energy metabolism was significantly affected (**Figure 8B**) ($p = 0.001$, one-sided Fisher's exact test with Bonferroni multiple testing correction). Again, most genes in this category were downregulated. This category involves oxidative phosphorylation which generates both ATP and proton motive force. Taken together, transcriptomic analysis suggests that the energy levels are reduced by treatment with azithromycin and ceftriaxone.

In this study, we also investigated whether depletion of proton motive force (using the uncoupler CCCP) phenotyped the application of stressors. We found that reduction of piliation can be achieved by depleting the proton motive force. Furthermore, reduced proton motive force and ATP levels would reduce the velocity of T4P retraction (Kurre and Maier, 2012; Kurre et al., 2013) in agreement with our results.

In summary, azithromycin and ceftriaxone treatments cause downregulation of different sets of metabolic genes that signify reduced energy levels. Depletion of proton motive force phenotypes the application of stressors. This strongly suggests that energy depletion caused by application of stressors is involved in reduction of T4P dynamics.

Gonococcal Piliation Is Reduced Under a Large Variety of Stresses Including Antibiotics With Different Targets, Hydrogen Peroxide, and Lactic Acid

Previously, it was shown that production of T4P enhances tolerance against hydrogen peroxide (Stohl et al., 2013) and ceftriaxone (Wang et al., 2018). Moreover, we showed that increasing the T4P-mediated attractive forces conferred higher survivability under ceftriaxone treatment (Cronenberg et al., 2021). Therefore, we expected that upregulation of pilus production can protect gonococci from antibiotic stress. To the contrary, we found that under all stress conditions tested in this study, the T4P production rate and T4P density were reduced. For *N. meningitidis,* further treatments have been shown to reduce piliation, providing additional examples for stress-induced reduction in T4P levels. Phenothiazines reduce piliation by interfering with the sodium motive force (Denis et al., 2019) and other therapeutic compounds reduce T4P formation by inhibiting the elongation ATPase (Aubey et al., 2019). It is tempting to speculate that the optimal rate of T4P production in the presence of external stress follows a trade-off between the protective effect of strong cell-to-cell attraction at high T4P density (Cronenberg et al., 2021) and the reduction of drug uptake rates by *pilQ* downregulation (Nandi et al., 2015). Interestingly, PilQ was reported to be involved in uptake of antibiotics (Chen et al., 2004; Nandi et al., 2015). Specific mutations in PilQ either enhanced (Chen et al., 2004) or decreased (Nandi et al., 2015) antibiotic susceptibility. Deletion of *pilQ* decreased antibiotic susceptibility, suggesting that PilQ plays a role in antibiotic permeation (Nandi et al., 2015). Downregulation of *pilQ* expression would therefore increase antibiotic tolerance and could be a gonococcal response to antibiotic treatment. Since *pilQ* is part of the *pilMNOPQ* operon it is conceivable that the entire membrane-spanning complex

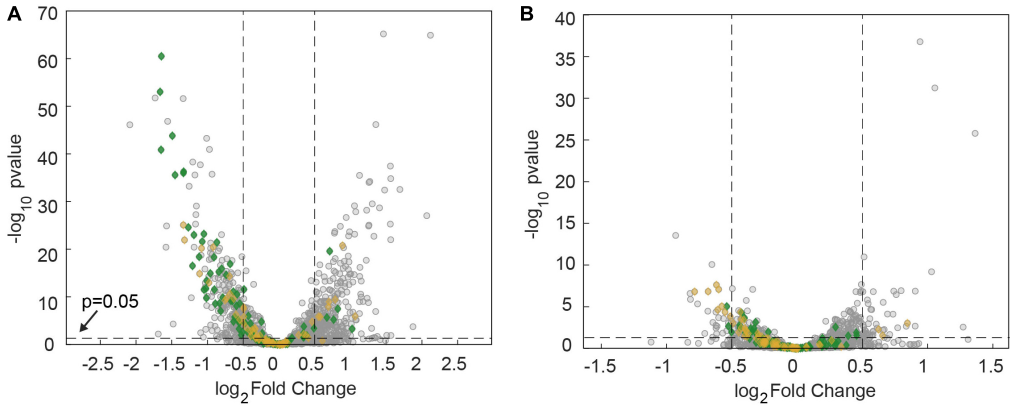

FIGURE 8 | Downregulation of metabolic genes after 60 min of antibiotic treatment at twofold MIC. Volcano plots showing adj. *p*-values as a function of the $\log_2$fold changes of RNA levels relative to the DMSO-untreated control determined by RNA sequencing. Gray: all genes. Green: genes involved in carbohydrate metabolism. Orange: Genes involved in energy metabolism. **(A)** Treatment with azithromycin. **(B)** Treatment with ceftriaxone.

built by the corresponding proteins are required for antibiotic permeation as well, although there is currently no evidence for their involvement (Nandi et al., 2015). On the other hand, it is unclear whether reduction of piliation results from a concerted stress response.

In general, reduction of T4P density reduces cell-to-cell attraction. The reduced piliation under azithromycin and ciprofloxacin treatment observed here is in excellent agreement with our previous finding that gonococcal colonies treated with these drugs become more fluid (Cronenberg et al., 2021). However, in that study we also showed that ceftriaxone enhances the attractive interaction and reduces the fluidity of colonies. Here, we observed that ceftriaxone treatment reduces piliation and downregulates genes involved in forming the T4P complex. Quantitatively, these effects are weaker compared to azithromycin treatment, yet their tendency is not in agreement with enhanced attractive force. We conclude therefore, that piliation is not the only factor determining colony fluidity. Instead, changes in surface-exposed structures or local order within the colony [as observed for ceftriaxone treatment (Cronenberg et al., 2021)] might counteract the effect of reduced piliation.

To summarize, piliation of *Neisseria* is reduced under a large variety of stresses, and it will be interesting to test whether a concerted stress response regulates this reduction.

CONCLUSION

T4P have been termed the bacterial "swiss army knife" because they are involved in many different functions (Berry and Pelicic, 2015). Here, we investigated the piliation response to a variety of different stresses that gonococci are likely to face. We reveal that under all conditions tested, the rate of T4P production and the number density of T4P are reduced. This suggests that external stress interferes with T4P functionality. In future studies it will be interested to find out whether downregulation of T4P is a general stress response.

DATA AVAILABILITY STATEMENT

The authors acknowledge that the data presented in this study must be deposited and made publicly available in an acceptable repository, prior to publication. Frontiers cannot accept a manuscript that does not adhere to our open data policies. The data presented in the study are deposited in the NCBI GEO repository, accession number GSE195465.

AUTHOR CONTRIBUTIONS

SK-R, IW, IR, JG, and BM designed research. SK-R and IW performed research. SK-R, IW, IR, and JG analyzed data. SK-R, IW, IR, and BM wrote the manuscript. All authors contributed to the article and approved the submitted version.

FUNDING

This work has been funded by the Deutsche Forschungsgemeinschaft through grants MA3898 and CRC1310, the IHRS BioSoft, and the Center for Molecular Medicine Cologne.

ACKNOWLEDGMENTS

We would like to thank Nicolas Biais for presenting the possible positions for cysteine substitution in the *pilE* sequence, and Hank Seifert, Paul Higgins, Tobias Bollenbach, and the Maier lab for stimulating discussions.

SUPPLEMENTARY MATERIAL

The Supplementary Material for this article can be found online at: https://www.frontiersin.org/articles/10.3389/fmicb.2022.839711/full#supplementary-material

REFERENCES

Aas, F. E., Winther-Larsen, H. C., Wolfgang, M., Frye, S., Løvold, C., Roos, N., et al. (2007). Substitutions in the N-terminal alpha helical spine of *Neisseria gonorrhoeae* pilin affect type IV pilus assembly, dynamics and associated functions. *Mol. Microbiol.* 63, 69–85. doi: 10.1111/j.1365-2958.2006.05482.x

Aubey, F., Corre, J. P., Kong, Y., Xu, X., Obino, D., Goussard, S., et al. (2019). Inhibitors of the *Neisseria meningitidis* PilF ATPase provoke type IV pilus disassembly. *Proc. Natl. Acad. Sci. U.S.A.* 116, 8481–8486. doi: 10.1073/pnas.1817757116

Berry, J. L., and Pelicic, V. (2015). Exceptionally widespread nanomachines composed of type IV pilins: the prokaryotic Swiss Army knives. *FEMS Microbiol. Rev.* 39, 134–154. doi: 10.1093/femsre/fuu001

Biais, N., Ladoux, B., Higashi, D., So, M., and Sheetz, M. (2008). Cooperative retraction of bundled type IV pili enables nanonewton force generation. *PLoS Biol.* 6:e87. doi: 10.1371/journal.pbio.0060087

Bolger, A. M., Lohse, M., and Usadel, B. (2014). Trimmomatic: a flexible trimmer for Illumina sequence data. *Bioinformatics* 30, 2114–2120. doi: 10.1093/bioinformatics/btu170

Bonazzi, D., Lo Schiavo, V., Machata, S., Djafer-Cherif, I., Nivoit, P., Manriquez, V., et al. (2018). Intermittent pili-mediated forces fluidize *Neisseria meningitidis* aggregates promoting vascular colonization. *Cell* 174:143–155.e16. doi: 10.1016/j.cell.2018.04.010

Camacho, C., Coulouris, G., Avagyan, V., Ma, N., Papadopoulos, J., Bealer, K., et al. (2008). BLAST+: architecture and applications. *BMC Bioinf.* 10:421. doi: 10.1186/1471-2105-10-421

Carbonnelle, E., Helaine, S., Prouvensier, L., Nassif, X., and Pelicic, V. (2005). Type IV pilus biogenesis in *Neisseria meningitidis*: PilW is involved in a step occurring after pilus assembly, essential for fibre stability and function. *Mol. Microbiol.* 55, 54–64. doi: 10.1111/j.1365-2958.2004.04364.x

Chang, Y. W., Rettberg, L. A., Treuner-Lange, A., Iwasa, J., Søgaard-Andersen, L., Jensen, G. J., et al. (2016). Architecture of the type IVa pilus machine. *Science* 351:aad2001.

Chen, C. J., Tobiason, D. M., Thomas, C. E., Shafer, W. M., Seifert, H. S., and Sparling, P. F. (2004). A mutant form of the *Neisseria gonorrhoeae* pilus secretin protein PilQ allows increased entry of heme and antimicrobial compounds. *J. Bacteriol.* 186, 730–739. doi: 10.1128/JB.186.3.730-739.2004

Clausen, M., Koomey, M., and Maier, B. (2009). Dynamics of type IV pili is controlled by switching between multiple states. *Biophys. J.* 96, 1169–1177. doi: 10.1016/j.bpj.2008.10.017

Craig, L., Forest, K. T., and Maier, B. (2019). Type IV pili: dynamics, biophysics and functional consequences. *Nat. Rev. Microbiol.* 17, 429–440. doi: 10.1038/s41579-019-0195-4

Cronenberg, T., Hennes, M., Wielert, I., and Maier, B. (2021). Antibiotics modulate attractive interactions in bacterial colonies affecting survivability under combined treatment. *PLoS Pathog.* 17:e1009251. doi: 10.1371/journal.ppat.1009251

Denis, K., Le Bris, M., Le Guennec, L., Barnier, J. P., Faure, C., Gouge, A., et al. (2019). Targeting Type IV pili as an antivirulence strategy against invasive meningococcal disease. *Nat. Microbiol.* 4, 972–984. doi: 10.1038/s41564-019-0395-8

Dewenter, L., Volkmann, T. E., and Maier, B. (2015). Oxygen governs gonococcal microcolony stability by enhancing the interaction force between type IV pili. *Integr. Biol. Uk* 7, 1161–1170. doi: 10.1039/c5ib00018a

Dillard, J. P. (2011). Genetic manipulation of *Neisseria gonorrhoeae*. *Curr. Protoc. Microbiol.* Chapter 4:Unit4A2.

Dobin, A., Davis, C. A., Schlesinger, F., Drenkow, J., Zaleski, C., Jha, S., et al. (2013). STAR: ultrafast universal RNA-seq aligner. *Bioinformatics* 29, 15–21. doi: 10.1093/bioinformatics/bts635

Ellison, C. K., Dalia, T. N., Dalia, A. B., and Brun, Y. V. (2019). Real-time microscopy and physical perturbation of bacterial pili using maleimide-conjugated molecules. *Nat. Protoc.* 14, 1803–1819. doi: 10.1038/s41596-019-0162-6

Ellison, C. K., Dalia, T. N., Vidal Ceballos, A., Wang, J. C., Biais, N., Brun, Y. V., et al. (2018). Retraction of DNA-bound type IV competence pili initiates DNA uptake during natural transformation in *Vibrio cholerae*. *Nat. Microbiol.* 3, 773–780. doi: 10.1038/s41564-018-0174-y

Ellison, C. K., Kan, J., Dillard, R. S., Kysela, D. T., Ducret, A., Berne, C., et al. (2017). Obstruction of pilus retraction stimulates bacterial surface sensing. *Science* 358, 535–538. doi: 10.1126/science.aan5706

Eriksson, J., Eriksson, O. S., Maudsdotter, L., Palm, O., Engman, J., Sarkissian, T., et al. (2015). Characterization of motility and piliation in pathogenic Neisseria. *BMC Microbiol.* 15:92. doi: 10.1186/s12866-015-0424-6

Folster, J. P., Dhulipala, V., Nicholas, R. A., and Shafer, W. M. (2007). Differential regulation of ponA and pilMNOPQ expression by the MtrR transcriptional regulatory protein in *Neisseria gonorrhoeae*. *J. Bacteriol.* 189, 4569–4577. doi: 10.1128/JB.00286-07

Freitag, N. E., Seifert, H. S., and Koomey, M. (1995). Characterization of the pilF-pilD pilus-assembly locus of *Neisseria gonorrhoeae*. *Mol. Microbiol.* 16, 575–586. doi: 10.1111/j.1365-2958.1995.tb02420.x

Friedrich, C., Bulyha, I., and Sogaard-Andersen, L. (2014). Outside-in assembly pathway of the type IV pilus system in *Myxococcus xanthus*. *J. Bacteriol.* 196, 378–390. doi: 10.1128/JB.01094-13

Gong, Z., Tang, M. M., Wu, X., Phillips, N., Galkowski, D., Jarvis, G. A., et al. (2016). Arginine- and polyamine-induced lactic acid resistance in *Neisseria gonorrhoeae*. *PLoS One* 11:e0147637. doi: 10.1371/journal.pone.0147637

Gorby, G. L., and Mcgee, Z. A. (1990). Antimicrobial interference with bacterial mechanisms of pathogenicity - effect of sub-mic azithromycin on gonococcal piliation and attachment to human epithelial-cells. *Antimicrob. Agents Ch.* 34, 2445–2448. doi: 10.1128/AAC.34.12.2445

Hall, C. W., and Mah, T. F. (2017). Molecular mechanisms of biofilm-based antibiotic resistance and tolerance in pathogenic bacteria. *FEMS Microbiol. Rev.* 41, 276–301. doi: 10.1093/femsre/fux010

Holz, C., Opitz, D., Greune, L., Kurre, R., Koomey, M., Schmidt, M. A., et al. (2010). Multiple pilus motors cooperate for persistent bacterial movement in two dimensions. *Phys. Rev. Lett.* 104, 178104. doi: 10.1103/PhysRevLett.104.178104

Hu, L. I., Yin, S., Ozer, E. A., Sewell, L., Rehman, S., Garnett, J. A., et al. (2020). Discovery of a New *Neisseria gonorrhoeae* Type IV pilus assembly factor, TfpC. *mBio* 11:e02528-20. doi: 10.1128/mBio.02528-20

Kandler, J. L., Holley, C. L., Reimche, J. L., Dhulipala, V., Balthazar, J. T., Muszyński, A., et al. (2016). The MisR response regulator is necessary for intrinsic cationic antimicrobial peptide and aminoglycoside resistance in *Neisseria gonorrhoeae*. *Antimicrob. Agents Ch.* 60, 4690–4700. doi: 10.1128/AAC.00823-16

Koch, M. D., Fei, C. Y., Wingreen, N. S., Shaevitz, J. W., and Gitai, Z. (2021). Competitive binding of independent extension and retraction motors explains the quantitative dynamics of type IV pili. *Proc. Natl. Acad. Sci. U.S.A.* 118:e2014926118. doi: 10.1073/pnas.2014926118

Kurre, R., and Maier, B. (2012). Oxygen depletion triggers switching between discrete speed modes of gonococcal type IV pili. *Biophys. J.* 102, 2556–2563. doi: 10.1016/j.bpj.2012.04.020

Kurre, R., Kouzel, N., Ramakrishnan, K., Oldewurtel, E. R., and Maier, B. (2013). Speed switching of gonococcal surface motility correlates with proton motive force. *PLoS One* 8:e67718. doi: 10.1371/journal.pone.0067718

Lam, T., Ellison, C. K., Eddington, D. T., Brun, Y. V., Dalia, A. B., Morrison, D. A., et al. (2021). Competence pili in *Streptococcus* pneumoniae are highly dynamic structures that retract to promote DNA uptake. *Mol. Microbiol.* 116, 381–396. doi: 10.1111/mmi.14718

Liao, Y., Smyth, G. K., and Shi, W. (2014). featureCounts: an efficient general purpose program for assigning sequence reads to genomic features. *Bioinformatics* 30, 923–930. doi: 10.1093/bioinformatics/btt656

Maier, B. (2021). How physical interactions shape bacterial biofilms. *Annu. Rev. Biophys.* 50, 401–417. doi: 10.1146/annurev-biophys-062920-063646

Maier, B., Potter, L., So, M., Long, C. D., Seifert, H. S., and Sheetz, M. P. (2002). Single pilus motor forces exceed 100 pN. *Proc. Natl. Acad. Sci. U.S.A.* 99, 16012–16017. doi: 10.1073/pnas.242523299

Marathe, R., Meel, C., Schmidt, N. C., Dewenter, L., Kurre, R., Greune, L., et al. (2014). Bacterial twitching motility is coordinated by a two-dimensional tug-of-war with directional memory. *Nat. Commun.* 5:3759. doi: 10.1038/ncomms4759

McClure, R., Sunkavalli, A., Balzano, P. M., Massari, P., Cho, C., Nauseef, W. M., et al. (2020). Global network analysis of *Neisseria gonorrhoeae* identifies coordination between pathways, processes, and regulators expressed during human infection. *Msystems* 5:e00729-19. doi: 10.1128/mSystems.00729-19

Merz, A. J., So, M., and Sheetz, M. P. (2000). Pilus retraction powers bacterial twitching motility. *Nature* 407, 98–102. doi: 10.1038/35024105

Nandi, S., Swanson, S., Tomberg, J., and Nicholas, R. A. (2015). Diffusion of antibiotics through the PilQ secretin in *Neisseria gonorrhoeae* occurs through the immature, sodium dodecyl sulfate-labile form. *J. Bacteriol.* 197, 1308–1321. doi: 10.1128/JB.02628-14

Nguyen, D., Joshi-Datar, A., Lepine, F., Bauerle, E., Olakanmi, O., Beer, K., et al. (2011). Active starvation responses mediate antibiotic tolerance in biofilms and nutrient-limited bacteria. *Science* 334, 982–986. doi: 10.1126/science.1211037

O'Hanlon, D. E., Moench, T. R., and Cone, R. A. (2013). Vaginal pH and microbicidal lactic acid when lactobacilli dominate the microbiota. *PLoS One* 8:e80074. doi: 10.1371/journal.pone.0080074

Pelicic, V. (2008). Type IV pili: e pluribus unum? *Mol. Microbiol.* 68, 827–837. doi: 10.1111/j.1365-2958.2008.06197.x

Pettit, R. K., McAllister, S. C., and Hamer, T. A. (1999). Response of gonococcal clinical isolates to acidic conditions. *J. Med. Microbiol.* 48, 149–156. doi: 10.1099/00222615-48-2-149

Philips, R., Kondev, J., Theriot, J., Gercia, H. G., and Orme, N. (2013). *Physical Biology of the Cell* (Garland Science). New York, NY: Taylor and Francis Group LLC.

Prevention CfDCa (2015). "Gonococcal infections in adolescents and adults," in *2015 Sexually Transmitted Diseases Treatment Guidelines*, ed. Sarah Kidd, Kimberly A. Workowski. 61, S785–S801. doi: 10.1093/cid/civ731

Quillin, S. J., and Seifert, H. S. (2018). *Neisseria gonorrhoeae* host adaptation and pathogenesis. *Nat. Rev. Microbiol.* 16, 226–240. doi: 10.1038/nrmicro.2017.169

Ribbe, J., Baker, A. E., Euler, S., O'Toole, G. A., and Maier, B. (2017). Role of cyclic Di-GMP and exopolysaccharide in type IV pilus dynamics. *J. Bacteriol.* 199:e00859-16. doi: 10.1128/JB.00859-16

Secor, P. R., Michaels, L. A., Ratjen, A., Jennings, L. K., and Singh, P. K. (2018). Entropically driven aggregation of bacteria by host polymers promotes antibiotic tolerance in *Pseudomonas aeruginosa*. *Proc. Natl. Acad. Sci. U.S.A.* 115, 10780–10785. doi: 10.1073/pnas.1806005115

Singh, R., Sahore, S., Kaur, P., Rani, A., and Ray, P. (2016). Penetration barrier contributes to bacterial biofilm-associated resistance against only select antibiotics, and exhibits genus-, strain- and antibiotic-specific differences. *Pathog. Dis.* 74:ftw056. doi: 10.1093/femspd/ftw056

Skerker, J. M., and Berg, H. C. (2001). Direct observation of extension and retraction of type IV pili. *Proc. Natl. Acad. Sci. U.S.A.* 98, 6901–6904. doi: 10.1073/pnas.121171698

Stohl, E. A., Dale, E. M., Criss, A. K., and Seifert, H. S. (2013). *Neisseria gonorrhoeae* Metalloprotease NGO1686 is required for full piliation, and piliation is required for resistance to H2O2- and neutrophil-mediated killing. *mBio* 4:e00399-13. doi: 10.1128/mBio.00399-13

Tseng, B. S., Zhang, W., Harrison, J. J., Quach, T. P., Song, J. L., Penterman, J., et al. (2013). The extracellular matrix protects *Pseudomonas aeruginosa* biofilms by limiting the penetration of tobramycin. *Environ. Microbiol.* 15, 2865–2878. doi: 10.1111/1462-2920.12155

Vesel, N., and Blokesch, M. (2021). Pilus production in *Acinetobacter baumannii* is growth phase dependent and essential for natural transformation. *J. Bacteriol.* 203:e00034-21. doi: 10.1128/JB.00034-21

Wang, L. C., Litwin, M., Sahiholnasab, Z., Song, W. X., and Stein, D. C. (2018). *Neisseria gonorrhoeae* aggregation reduces its ceftriaxone susceptibility. *Antibiotics-Basel* 7:48. doi: 10.3390/antibiotics7020048

Welker, A., Cronenberg, T., Zöllner, R., Meel, C., Siewering, K., Bender, N., et al. (2018). Molecular motors govern liquidlike ordering and fusion dynamics of bacterial colonies. *Phys. Rev. Lett.* 121:118102. doi: 10.1103/PhysRevLett.121.118102

Wolfgang, M., Lauer, P., Park, H. S., Brossay, L., Hébert, J., and Koomey, M. (1998). PilT mutations lead to simultaneous defects in competence for natural transformation and twitching motility in piliated *Neisseria gonorrhoeae*. *Mol. Microbiol.* 29, 321–330. doi: 10.1046/j.1365-2958.1998.00935.x

Yan, J., and Bassler, B. L. (2019). Surviving as a community: antibiotic tolerance and persistence in bacterial biofilms. *Cell Host Microbe* 26, 15–21. doi: 10.1016/j.chom.2019.06.002

Zollner, R., Cronenberg, T., Kouzel, N., Welker, A., Koomey, M., Maier, B., et al. (2019). Type IV pilin post-translational modifications modulate material properties of bacterial colonies. *Biophys. J.* 116, 938–947. doi: 10.1016/j.bpj.2019.01.020

Conflict of Interest: The authors declare that the research was conducted in the absence of any commercial or financial relationships that could be construed as a potential conflict of interest.

4 Antibiotics Modulate Attractive Interactions in Bacterial Colonies Affecting Survivability under Combined Treatment

4.1 Publication

The project *Antibiotics modulate attractive interactions in bacterial colonies affecting survivability under combined treatment* was published in *PLOS Pathogens* in 2021 applying the Creative Commons Attribution 4.0 International (CC-BY) license [131].

4.1.1 Contributions to the Publication

This publication constitutes a collaborative effort between Tom Cronenberg, Marc Hennes, myself and Berenike Maier. Tom Cronenberg was responsible for conducting and analysing the within-colony motility experiments, the structure of the treated gonococcal colonies and the experiments on the sequential antibiotic treatment in flow chamber experiments. He also determined the minimal inhibitory concentrations of the antibiotic treatment for the experiment. The subsequent analysis of these experiments was conducted by Marc Hennes and Tom Cronenberg, who employed a methodology involving the tracking of individual cells within the colony, the calculation of the radial distribution function and the analysis of colony motility. Furthermore, they analysed the live-dead staining of the colonies to investigate the survival under antibiotic treatment. My own contribution to this research was the analysis of the interaction forces of the treated bacteria by performing double laser tweezers experiments. In addition, I was responsible for determining the cell size via phase contrast microscopy.

Tom Cronenberg, Marc Hennes, myself and Berenike Maier were involved in the project design, writing the manuscript and creating the figures for the publication.

PLOS PATHOGENS

RESEARCH ARTICLE

Antibiotics modulate attractive interactions in bacterial colonies affecting survivability under combined treatment

Tom Cronenberg☯, **Marc Hennes**☯, **Isabelle Wielert**, **Berenike Maier***

Institute for Biological Physics, University of Cologne, Köln, Germany

☯ These authors contributed equally to this work.
* berenike.maier@uni-koeln.de

Citation: Cronenberg T, Hennes M, Wielert I, Maier B (2021) Antibiotics modulate attractive interactions in bacterial colonies affecting survivability under combined treatment. PLoS Pathog 17(2): e1009251. https://doi.org/10.1371/journal.ppat.1009251

Editor: Christoph Tang, University of Oxford, UNITED KINGDOM

Received: August 24, 2020

Accepted: December 21, 2020

Published: February 1, 2021

Data Availability Statement: All relevant data are within the manuscript and its Supporting Information files.

Funding: This work was supported by the University of Cologne (www.uni-koeln.de), the Deutsche Forschungsgmeinschaft (www.dfg.de) through grant MA3898 and the Center for Molecular Medicine Cologne (www.cmmc-uni-koeln.de) through grant B06 awarded to BM. IW was supported by the International Helmholtz Research School of Biophysics and Soft Matter

Abstract

Biofilm formation protects bacteria from antibiotics. Very little is known about the response of biofilm-dwelling bacteria to antibiotics at the single cell level. Here, we developed a cell-tracking approach to investigate how antibiotics affect structure and dynamics of colonies formed by the human pathogen *Neisseria gonorrhoeae*. Antibiotics targeting different cellular functions enlarge the cell volumes and modulate within-colony motility. Focusing on azithromycin and ceftriaxone, we identify changes in type 4 pilus (T4P) mediated cell-to-cell attraction as the molecular mechanism for different effects on motility. By using strongly attractive mutant strains, we reveal that the survivability under ceftriaxone treatment depends on motility. Combining our results, we find that sequential treatment with azithromycin and ceftriaxone is synergistic. Taken together, we demonstrate that antibiotics modulate T4P-mediated attractions and hence cell motility and colony fluidity.

Author summary

Aggregation into colonies and biofilms can enhance bacterial survivability under antibiotic treatment. Aggregation requires modulation of attractive forces between neighboring bacteria, yet the link between attraction and survivability is poorly characterized. Here, we quantify these attractive interactions and show that different antibiotics enhance or inhibit them. Live-cell tracking of single cells in spherical colonies enables us to correlate attractive interactions with single cell motility and colony fluidity. Even moderate changes in cell-to-cell attraction caused by antibiotics strongly impact on within-colony motility. Vice versa, we reveal that motility correlates with survivability under antibiotic treatment. In summary, we demonstrate a link between cellular attraction, colony fluidity, and survivability with the potential to optimize the treatment strategy of commonly used drug combinations.

Introduction

Aggregation has a strong potential for protecting bacteria from antibiotics. A multitude of different mechanisms has been shown to be responsible for protection [1]. They include

(http://www.ihrs-biosoft.de). The funders had no role in study design, data collection and analysis, decision to publish, or preparation of the manuscript.

Competing interests: The authors have declared that no competing interests exist.

inhibition of penetration of antibiotics into the biofilm [2,3] and activation of stress responses [4–6]. Reduction of growth rate, rate of protein synthesis, and proton motive force [1] often enhance tolerance against antibiotics [7,8] and increase the survival time during antibiotic treatment.

Some antibiotics cause structural rearrangements in biofilms. In particular, antibiotic treatment can induce biofilm formation [9,10]. Very little is known, however, about how antibiotics affect biofilm structure at the single cell level. Only recently it was shown that the local structure of *Vibrio cholerae* biofilms rearranges upon antibiotic treatment [11]. In particular, under treatment with proteins synthesis inhibitors the density of bacteria was reduced by a combined effect of increasing cell volume and decreasing amount of the matrix component that is responsible for cell-cell attraction in *V. cholerae* biofilms [11]. Lacking single cell resolution, this cell volume increase would have been observed as an increase in biofilm mass and likely interpreted as antibiotic-induced biofilm formation.

While first reports of biofilm structure at the single cell level are emerging, it is unclear how antibiotics affect biofilm dynamics. Many bacterial species use type 4 pili (T4P) for generating attractive forces between cells that initiate and stabilize biofilms [12]. Next to forming T4P-T4P bonds between neighboring cells, T4P function as strong molecular machines [13,14] that govern the viscosity or fluidity of colonies [15–17], i.e. early biofilms. T4P polymers grow, bind, and retract continuously [18], enabling a tug-of-war between bacteria in a colony [14,19]. For *Neisseria* species it was demonstrated that by modulating motor activity, T4P-T4P binding force, or T4P density, the dynamics of a colony transitions from gas-like to fluid-like to solid-like [15–17]. It is tempting to speculate that colony fluidity affects bacterial fitness. Indeed, it was shown that fluidity correlates with the ability to colonize narrow vessels [15]. It is also conceivable, that high motility of cells within colonies enables rearrangements of cells during growth and division and allows bacteria residing at the center of the colony to reproduce. Moreover, cell motility has been connected with enhanced diffusion of macromolecules into biofilms [20] supporting influx of both nutrients and antibiotics. Therefore, we address the question how bacterial motility affects survival under benign conditions and under antibiotic treatment.

Neisseria gonorrhoeae (gonococcus) is the causative agent of gonorrhea and conjunctivitis. Gonorrhea is currently the second most common sexually transmitted disease and the probability for failure of antibiotic treatment is rising rapidly [21]. Some aspects of antibiotic resistance are understood at the genetic level [22–25], but the effect of colony and biofilm formation, its structure, and its dynamics on the efficiency of treatment remain largely unexplored.

In this study, we employ a single cell approach to characterize effects of antibiotic treatment on colony structure and dynamics of *N. gonorrhoeae*. We show that antibiotics with different targets consistently affect cell volume and colony structure. Different antibiotics have varying effects on the cellular dynamics within the colonies. Focusing on the two currently recommended antibiotics for gonorrhea treatment, azithromycin and ceftriaxone [26], we correlate dynamics to T4P-T4P interactions by showing that antibiotic treatment can reduce or enhance T4P-mediated cell-to-cell attraction. Cellular dynamics itself impacts on the efficacy of antibiotic treatment. Motivated by the motility-enhancing effect of azithromycin, we study sequential treatment with azithromycin and ceftriaxone and find synergistic effects.

Results

Antibiotic treatment affects biofilm structure and cell size

To address how antibiotics affect the structure of gonococcal biofilms, we focused on early biofilms, namely (micro)colonies. Gonococci were allowed to assemble colonies within flow

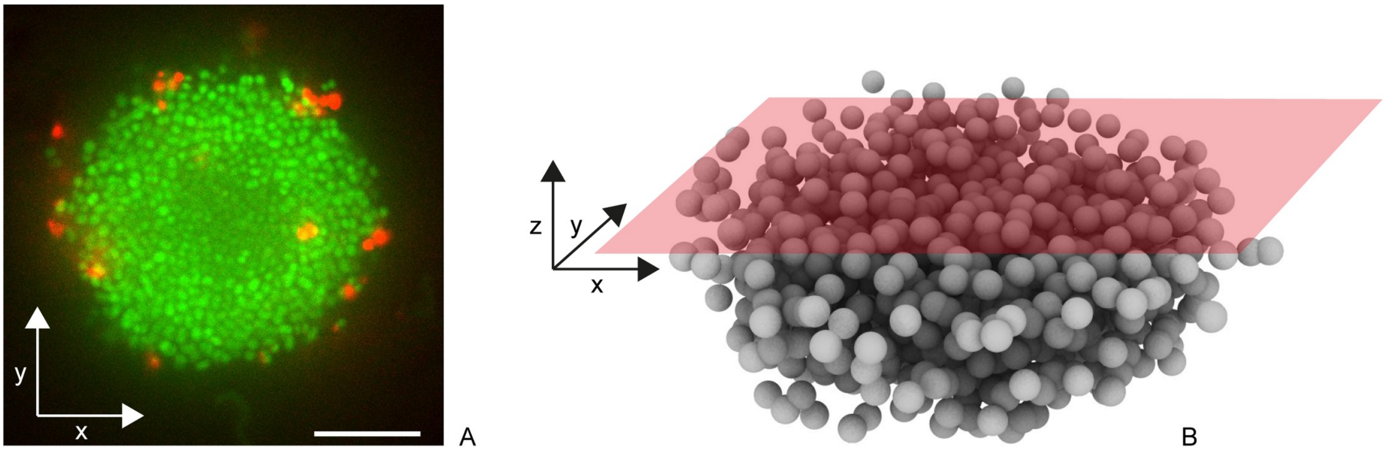

Fig 1. Determination of cell positions in three dimensions within spherical gonococcal colonies. a) Typical slice through Syto 9 (green)- and PI (red)-stained gonococcal colony. Scale bar: 10 μm. b) Confocal reconstruction of single cell positions.

https://doi.org/10.1371/journal.ppat.1009251.g001

chambers for one hour and subsequently treated with antibiotics. Constant supply of nutrients and antibiotics was ensured by applying continuous flow. Prior to data acquisition, bacteria were stained with Syto 9 to detect the position of individual cells and to determine the cell volume (Fig 1A). Moreover, propidium iodide (PI) enabled us to detect dead cells. Three-dimensional positions of single cells (Fig 1B) were detected as described in the Materials and Methods section. This protocol allows analysing effects of antibiotic treatment on preassembled gonococcal colonies at single cell resolution providing spatial information.

We investigated the effect of the translation inhibitor azithromycin and cell wall synthesis inhibitor ceftriaxone, on the structure of colonies. After 5 h exposure to azithromycin or ceftriaxone at 100x their minimal inhibitory concentrations (MICs) (S2 Table), the local structure changed considerably (Fig 2A). Colonies had swollen and holes became prominent. To quantify these structural changes, we measured the radial distribution functions *g(r)*. For each bacterium, we determined the probability *g(r)* of finding a bacterium at a distance *r* (Fig 2B). As previously shown [15,16], gonococcal colonies show liquid-like local order, i.e. *g(r)* shows distinct maxima and minima at short but not at long distances *r* as seen in Fig 2C for untreated and azithromycin-treated colonies. The position of the first maximum is the mean nearest neighbor distance r_0. By fitting *g(r)* with an analytical expression for colloidal systems [27], we determined r_0 (Fig 2C and 2D). In the presence of azithromycin, the nearest neighbor distance r_0 was strongly increased compared to the control (Fig 2D), i.e. the entire colony had swollen. Under ceftriaxone treatment, we found no clear maxima in *g(r)* (Fig 2C) indicating that liquid-like order was lost and the colony structure would be better characterized as gas-like. Independently, we measured the volumes of individual cells and found that for both antibiotics the volumes had increased by a factor of ~ 2.5 compared to the control cells (Figs 2E and S2). When the antibiotics were applied for a shorter period of time, we observed qualitatively similar effects on structure albeit less pronounced (S1 and S2 Figs).

To assess whether colony swelling was a general response of gonococci to antibiotics, we characterized the effects of antibiotics with different targets including translation (kanamycin), replication (ciprofloxacin), and folic acid metabolism (trimethoprim) as well as a producer of radicals (nitrofurantoin) on the structure of the colonies. These antibiotics were applied for 3 h at their respective MICs. All treatments increased the fractions of dead cells relative to the control (S3 Fig), however, most cells were still alive. Under these conditions, all colonies

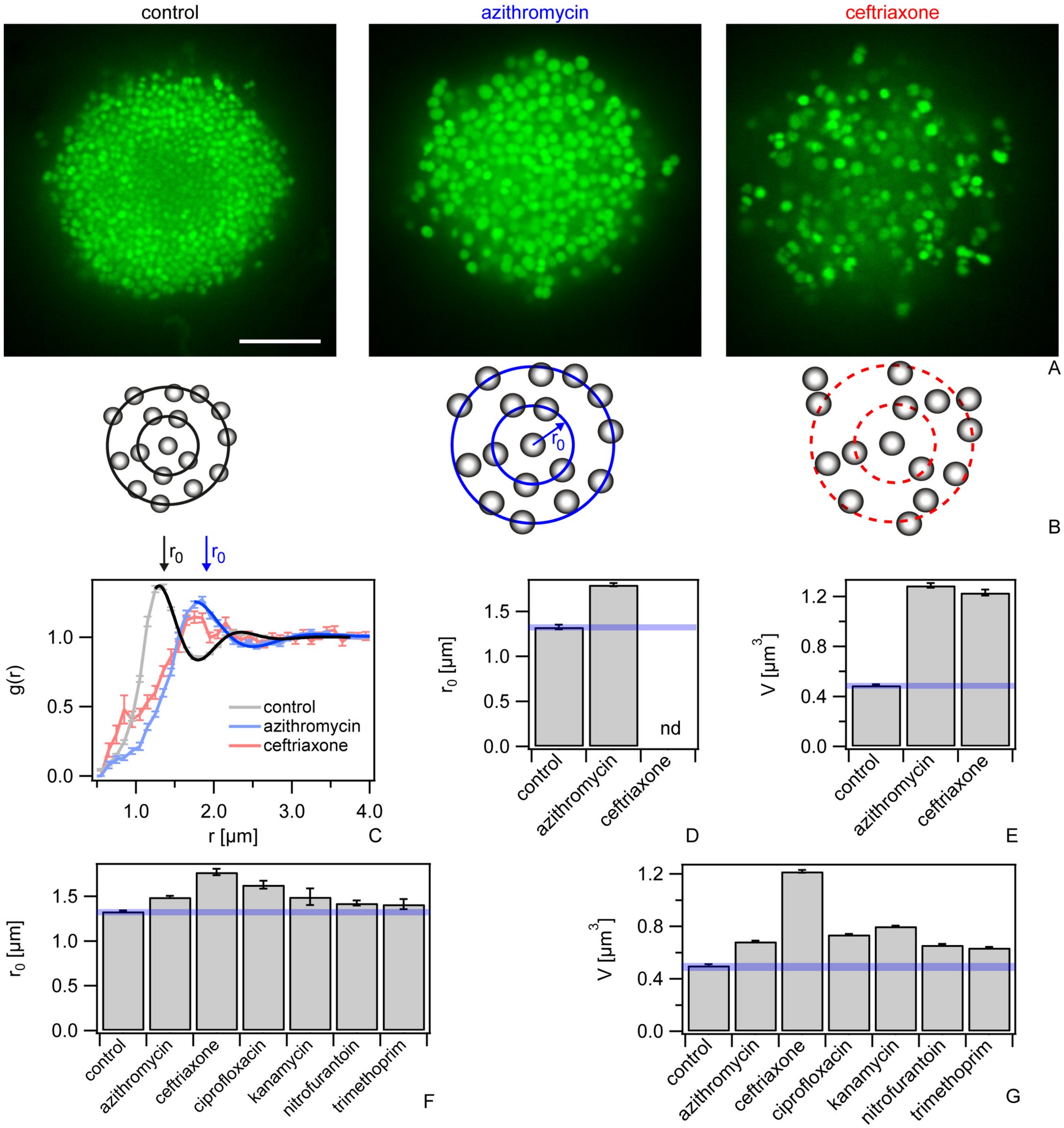

Fig 2. Antibiotics affect colony structure. Bacteria (wt*, Ng150) were inoculated into flow chambers and colonies were allowed to assemble for 1 h. Subsequently, they were treated with antibiotics at a-e) 100x MIC for 5 h, or f-g) 1x MIC for 3 h. a) Typical confocal slices. Scale bar: 10 μm. b) Scheme of local order. Left: Untreated cells show liquid-like order. The probability to find a nearest neighbor is highest at r_0. Middle: azithromycin-treated cells show liquid-like order with larger r_0. Right: ceftriaxone-treated cells show no local order. c) Radial distribution function *g(r)*. Error bars: standard error of the mean, N > 24 colonies. Full-line: Fit to Eq 1. d) Nearest neighbor distances r_0 determined from g(r) (S1 Fig). Error bars: errors from fit to Eq 1. e) Mean cell volume *V*. Error bars: errors from Gaussian fits to distributions (S2

Fig), N > 20000 cells. f) Nearest neighbor distances r_0 for 1x MIC determined from g(r) (S1 Fig). N > 24 colonies. Error bars: errors from fit to Eq 1. g) Mean cell volume V for 1x MIC. Error bars: errors from Gaussian fits to distributions (S2 Fig), N > 20000 cells. Blue transparent bars: uncertainties associated with mean values of controls.

https://doi.org/10.1371/journal.ppat.1009251.g002

showed liquid-like local structure (S1 Fig), but the mean distance to the nearest neighbor r_0 was shifted to higher values for all antibiotics tested (Fig 2F). In agreement with an increased nearest neighbor distance, the mean cell volumes were significantly increased for all antibiotics tested (Figs 2F and S4).

In summary, treatment with antibiotics with a large variety of targets increases the nearest neighbor distance in liquid-like colonies as well as the cell volumes.

Antibiotic treatment affects the within-colony motility

Driven by T4P retraction, gonococci show motility within colonies (Fig 3A and 3B and S1 Movie). Here, we found that motility increased strongly under azithromycin treatment (Fig 3

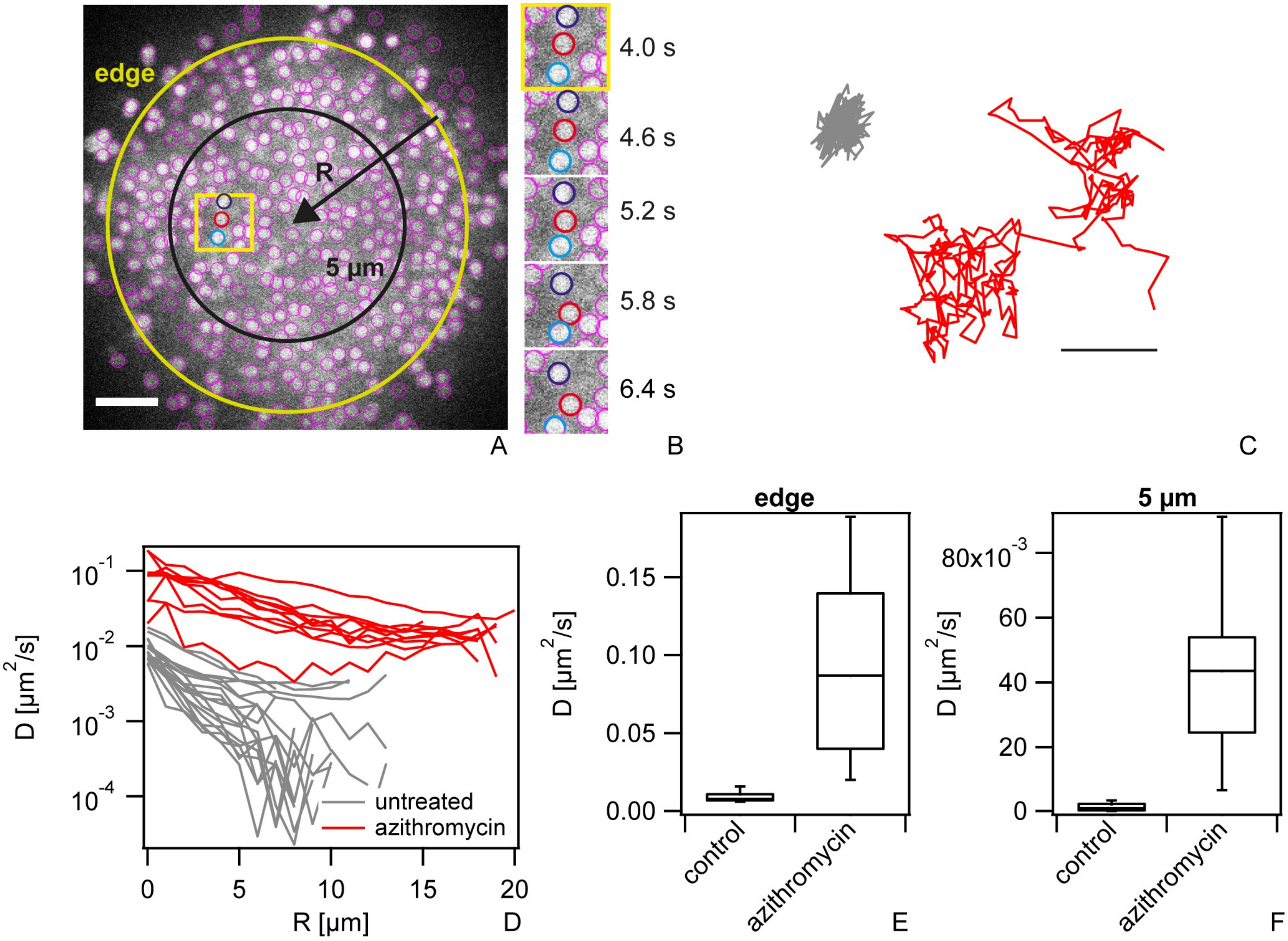

Fig 3. Within-colony motility increases during azithromycin treatment. wt* gonococci (Ng150) were inoculated into flow chambers and colonies were allowed to assemble for 1 h. Subsequently, they were treated with azithromycin (100x MIC) for 5 h. a) Typical confocal plane of wt* colony with Syto 9 staining. Purple circles: cells detected by tracking algorithm. Scale bar: 5 μm. b) Time lapse within region of interested depicted by yellow box in a). c) Typical traces of untreated (grey) and treated (red) single bacteria over 25 s. Scale bar: 0.5 μm. d) Effective diffusion constant as a function of penetration depth for untreated (grey) and treated cells (red), respectively. Effective diffusion constant D at e) the edge of the colony and f) within the colony at $R = 5$ μm. Box plot: median, 25/75 percentile, whiskers: 10/90 percentile. N = 10–18.

https://doi.org/10.1371/journal.ppat.1009251.g003

and S2 Movie). Single cell motility was characterized by tracking the positions of individual cells within a confocal plane. Fig 3B shows a typical example of rapid movement of three cells at a time scale of seconds. We quantified motility by calculating the effective diffusion constant D by $\langle x(t = 1s)^2 \rangle = 4D \cdot t$ from trajectories of single cells as shown in Fig 3C. The effective diffusion constant tends to decrease with increasing distance from the edge of the colony (Fig 3A, 3C and 3D) in agreement with previous reports [15,28,29]. Importantly, after 5 h of azithromycin treatment at 100x MIC, the effective diffusion constant was increased by a factor of ~ 10 at the edge (Fig 3E) and by a factor of ~ 25 at 5 μm inside the colony (Fig 3F).

We assessed whether treatment with lower concentrations or other antibiotics also affected the motility of gonococci within colonies (S5 Fig). After 3 h of azithromycin treatment at 1x MIC, the effective diffusion constant was increased by a factor of ~ 3. Interestingly, ceftriaxone treatment significantly reduced the effective diffusion constant compared to the control. Ciprofloxacin strongly enhanced motility whereas nitrofurantoin showed no effect. For kanamycin and trimethoprim, the effects were different at the edge and at the center of the colony (S5 Fig). Taken together, various antibiotics enhance or inhibit within-colony motility.

Azithromycin and ceftriaxone affect T4P-mediated attraction between neighboring cells

We hypothesized that reduced or enhanced T4P-T4P interactions govern the motility of cells within gonococcal colonies during antibiotic treatment. To assess this hypothesis, we characterized cell-to-cell interactions using a double laser trap. Again, we focused on azithromycin and ceftriaxone which show converse effects on motility. The laser traps were positioned at a distance of 2.8 μm and a single monococcus was trapped in each of the traps. When T4P of both cells attach to each other and at least one of them retracts, both cell bodies are pulled towards each other (Fig 4A). Eventually, the bond ruptures and both cell bodies move rapidly back towards the centers of the traps. During several events, the cell bodies did not move back the full distance to the centers of the traps but instead paused or started retracting again (Fig 4B). In this case, most likely multiple T4P-T4P bonds have formed simultaneously, and we detect only the shortest bond.

We compared cells that were incubated for 1 h in medium and subsequently for 2 h in medium containing either azithromycin or ceftriaxone at 100x MIC with control cells that were incubated in medium for 3 h. We found less motor activity for azithromycin-treated pairs compared to the control pairs (S6 Fig) with the individual retraction events being well separated (Fig 4B and 4C). By contrast, untreated pairs had a strong tendency towards multiple T4P-T4P bonds. Ceftriaxone treatment increased the frequency of T4P retractions and multiple T4P-T4P bond formation (Figs 4D and S6).

Attractive interactions between pairs of cells were quantified by measuring the probability that two cells are bound to each other via T4P p_{bound}. This probability was determined for each pair of bacteria by normalizing the total amount of time during which the bacteria are deflected from the trap centers by the total time elapsed between the first and the last retraction event. The mean probability to be bound was considerably lower for azithromycin-treated pairs with $p_{bound}^{azithromycin} = 0.30 \pm 0.02$ compared to the control pairs with $p_{bound}^{control} = 0.49 \pm 0.02$ (Fig 4E) and higher for ceftriaxone-treated pairs with $p_{bound}^{ceftriaxone} = 0.58 \pm 0.03$. We note that our protocol is different from the previously used protocol where cells were directly harvested from agar plates explaining the difference in p_{bound} [16] in the control samples.

We conclude that azithromycin treatment inhibits and ceftriaxone enhances T4P-mediated attractions between neighboring cells.

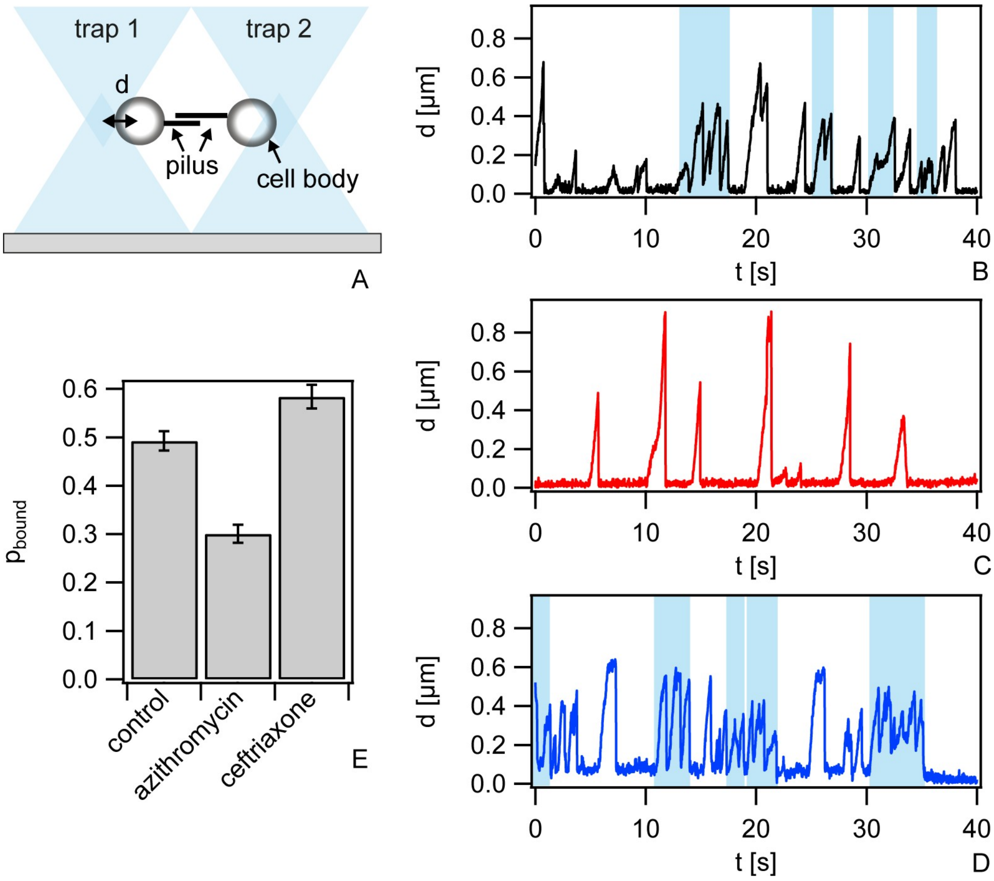

Fig 4. T4P-T4P interactions are reduced under azithromycin treatment and enhanced under ceftriaxone treatment. a) Sketch of the setup. A single bacterium is trapped in each of the traps. As T4P from different bacteria bind and retract, the cell bodies are deflected by the distances *d* from the centers of the traps. When the T4P-T4P bond ruptures, the cell bodies move rapidly back to *d* = *0*. Typical dynamics of deflections b) without treatment c) with 6.4 μg / ml azithromycin for (2–3) h, and d) with 0.4 μg / ml ceftriaxone for (2–3) h. Blue shaded boxes: multiple T4P pairs exist simultaneously (bundling). e) Probability that cells are bound via T4P-T4P bonds. N = (29–38) pairs, error bars: bootstrapping.

https://doi.org/10.1371/journal.ppat.1009251.g004

Within-colony motility correlates with survivability

Having observed that antibiotic treatment strongly influences cell motility, we asked—vice versa—how cell motility affected the efficacy of antibiotic treatment. Recently, it was shown that gonococcal aggregation by means of T4P protects bacteria from ceftriaxone treatment [30]. Therefore, we wondered whether colony dynamics impacts on survivability and used bacterial strains that form less fluid colonies as revealed by characterizing the relaxation dynamics of colonies. Fluidity of gonococcal colonies can be affected by the motor activity of the T4P or by the binding strength between T4P [16,17]. In particular, colony fluidity is strongly reduced in a strain expressing genes encoding for non-functional $pilT_{WB}$ T4P retraction ATPases in addition to the functional ones [16] (S1 Table). Here, we verified that lower fluidity at the colony scale correlates with lower motility at the level of single cells. The effective diffusion constants of untreated cells were significantly lower in the $pilT_{WB2}$ strain compared to the wt* strain (S7 Fig). To make sure that antibiotics-related effects are not merely caused by PilT functionality, we employed a second strain that reduces cell motility within colonies by a different mechanism. We used a strain lacking pilin phosphoform modification by deletion

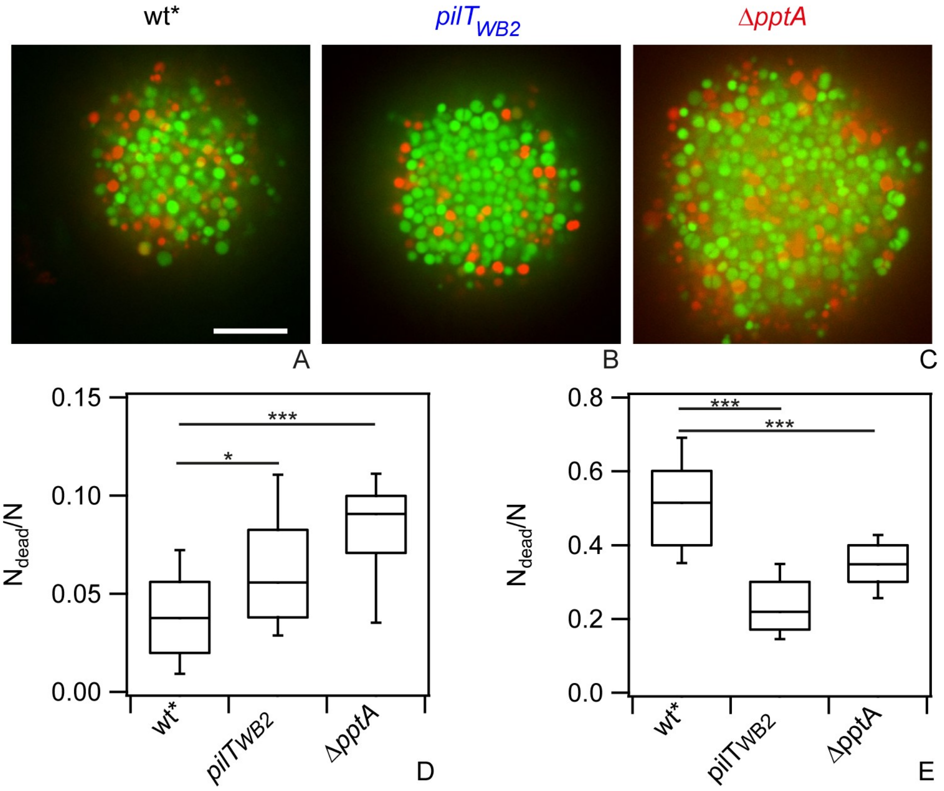

Fig 5. Fraction of dead cells in colonies with different fluidities. Bacteria were inoculated into flow chambers and colonies were allowed to assemble for 1 h. Subsequently, they were treated with 0.4 μg / ml ceftriaxone for 5 h. Typical confocal slices through ceftriaxone-treated colonies formed by a) wt* (Ng150), b) $pilT_{WB2}$ (Ng176), and c) *ΔpptA* (Ng142). Green: Syto 9, red: PI. Scale bar: 10 μm. Fraction of dead cells d) untreated and e) with ceftriaxone. N = 32–45 colonies. All statistical comparisons were made by two-sample KS-test: *P 0.05; ***P 0.001.

https://doi.org/10.1371/journal.ppat.1009251.g005

of *pptA* [31] resulting in reduction of colony fluidity [17]. Again, we found that single cell motility is reduced in strain *ΔpptA* compared to the wt* (S7 Fig).

First, we investigated the effect of cell motility on cell death in the absence of antibiotic treatment. The fraction of dead cells was determined by dividing the number of dead cells as detected by PI staining by the total number of cells detected by Syto 9 (Fig 5A). Under benign conditions, strains $pilT_{WB2}$ and *ΔpptA* showed a significantly higher fraction of dead cells compared to the wt*, suggesting that reduced motility was deleterious.

Subsequently, we addressed killing by ceftriaxone treatment. After 5 h of treatment at 100x MIC, a fraction of f_{dead} = 52% of the wt* cells within the colony were dead. Within the colonies formed by motility-inhibited cells, the fractions of dead cells were considerably lower with f_{dead} = 23% for $pilT_{WB2}$ and f_{dead} = 35% for *ΔpptA* (Fig 5E). At the edge of the colonies the fractions of dead cells of wt* and *ΔpptA* bacteria were comparable (S8 Fig), suggesting that bacteria are equally susceptible to antibiotic treatment when they are not surrounded by other bacteria. With increasing penetration depth R, f_{dead} decreased much more steeply for *ΔpptA* colonies compared to wt* colonies. This indicates that the less motile *ΔpptA* cells are better protected within the colony compared to the more motile wt* cells. At the edge of $pilT_{WB2}$ colonies, the fraction of dead cells was lower compared to the wt* colonies. This suggests that even in the absence of neighboring cells, the $pilT_{WB2}$ bacteria are less susceptible to ceftriaxone (S8A Fig). Importantly, when the fractions of dead cells were normalized to the values at the edges of the colonies, f_{dead} showed a very steep decrease for both motility-inhibited colonies, $pilT_{WB2}$ and $\Delta pptA$ (S8B Fig), showing that cell death was inhibited by colony formation. For very large depths $R > 15\ \mu m$, the f_{dead} became comparable between all three strains.

Taken together we found that T4P mutant strains that reduce colony fluidity and within-colony motility show reduced survivability under benign conditions but strongly enhanced survivability under antibiotic treatment.

Sequential treatment with azithromycin and ceftriaxone shows synergistic killing

So far, we found that treatment with various antibiotics including azithromycin enhances motility of bacteria within colonies. Also, our data strongly suggest that enhanced motility makes the bacteria more susceptible to ceftriaxone treatment. Therefore, we asked whether the killing efficiency of the drug combination azithromycin and ceftriaxone is additive. To address this question, we designed different treatment protocols all using 100x MIC with a total exposure time of 3 h azithromycin and 3 h ceftriaxone.

First, we treated colonies with pure azithromycin for 3 h, and subsequently with pure ceftriaxone for another 3 h. After a total treatment for 6 h, the fraction of dead cells was determined (Fig 6A). We found that the mean fraction of dead cells was $\langle f_{dead}^{azi\ 3h,cef\ 3h} \rangle = 0.37 \pm 0.02$. To find out whether the effect was additive, we measured $\langle f_{dead}^{azi\ 3h,med\ 3h} \rangle$ after 3 h of azithromycin treatment and 3 h of incubation in medium. Moreover, we determined $\langle f_{dead}^{cef\ 3h} \rangle$ after 3 h of ceftriaxone exposure. Then we determined $\langle \Delta f_{dead}^{azi\ 3h,cef\ 3h} \rangle = \langle f_{dead}^{azi\ 3h,cef\ 3h} \rangle - (\langle f_{dead}^{azi\ 3h,med\ 3h} \rangle + \langle f_{dead}^{cef\ 3h} \rangle)$. This is a measure of the fraction of dead cells arising from the interplay between both antibiotics. The first term on the right side describes the mean fraction of dead cells after combined treatment while the second term describes the sum of the mean fractions of dead cells after individual treatments. Interestingly, $\langle \Delta f_{dead}^{azi\ 3h,cef\ 3h} \rangle = 0.17 \pm 0.03 > 0$ (Fig 6D) indicates the sequential treatment with azithromycin and ceftriaxone is synergistic. Next, we inverted the order of the sequential treatment and found $\langle f_{dead}^{cef\ 3h,azi\ 3h} \rangle = 0.52 \pm 0.01$ and $\langle \Delta f_{dead}^{cef\ 3h,azi\ 3h} \rangle = \langle f_{dead}^{cef\ 3h,azi\ 3h} \rangle - (\langle f_{dead}^{cef\ 3h,med\ 3h} \rangle + \langle f_{dead}^{azi\ 3h} \rangle) = 0.10 \pm 0.02 > 0$ (Fig 6B–6D). Importantly, sequential treatment with both drugs shows synergistic effects regardless of the order of application. The total fraction of dead cells was higher when cells were treated first with ceftriaxone and then with azithromycin. However, the interpretation of this result is hampered by the fact that detection of cell death is delayed after ceftriaxone treatment (Fig 6A and 6B). The fraction of dead cells determined directly after 3 h treatment was three-fold lower compared to the fraction determined after 3 h treatment and 3 h growth in medium. Therefore, we compared the degree of synergism plotted in Fig 6D showing $\langle \Delta f_{dead}^{azi\ 3h,cef\ 3h} \rangle > \langle \Delta f_{dead}^{cef\ 3h,azi\ 3h} \rangle$.

Finally, we treated colonies simultaneously with azithromycin and ceftriaxone. We found $\langle f_{dead}^{(azi,cef)\ 3h} \rangle = 0.18 \pm 0.01$ and $\langle \Delta f_{dead}^{(azi+cef)\ 3h} \rangle = \langle f_{dead}^{(azi+cef)\ 3h} \rangle - (\langle f_{dead}^{azi\ 3h} \rangle + \langle f_{dead}^{cef\ 3h} \rangle) = 0.00 \pm 0.02$ (Fig 6C and 6D). This result indicates that the effects of azithromycin and ceftriaxone are additive during simultaneous treatment.

We conclude that sequential treatment with azithromycin and ceftriaxone (and vice versa) shows synergistic effects.

Discussion

We present a single-cell level study of antibiotic effects on gonococcal colonies and focus on the interplay between cell motility and antibiotic treatment. Our method opens up the possibility to characterize novel parameters as compared to classical assays such as the detection of the fraction of viable cells by colony counting. First, we can characterize spatial effects within

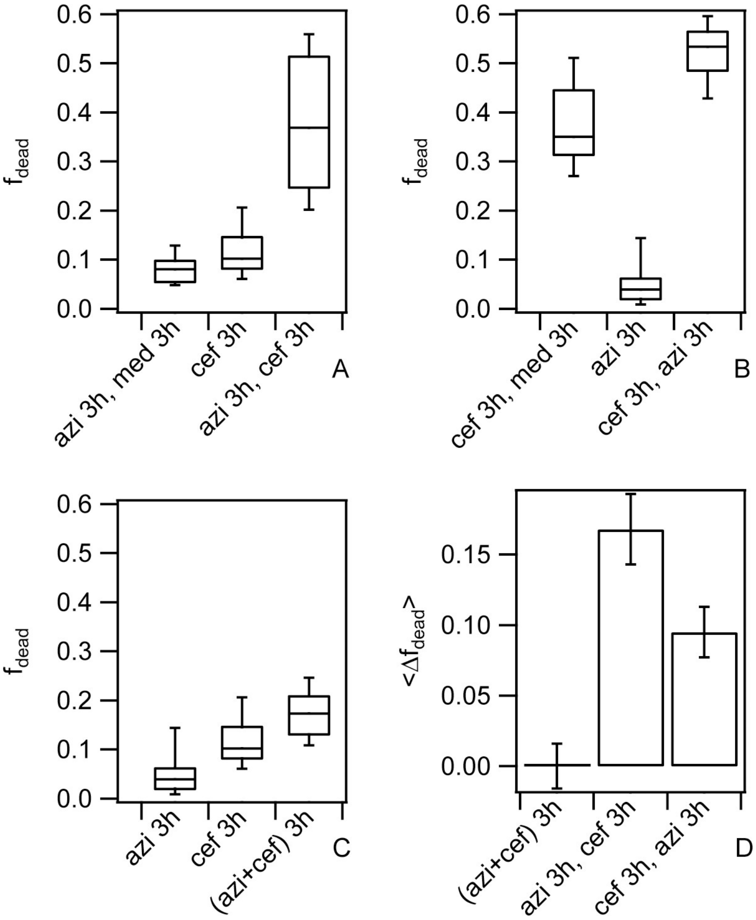

Fig 6. Sequence of drug application affects fraction of dead cells. Wt* bacteria (Ng150) were inoculated into flow chambers and colonies were allowed to assemble for 1 h. Subsequently, they were treated at 100x MIC with azithromycin or ceftriaxone, respectively, as indicated in the figure labels. a)—c) Fractions of dead cells f_{dead}. Figure labels explain the protocol. For example, *azi 3h*, *med 3h* indicates that colonies were treated with azithromycin for 3 h, subsequently incubated with medium for another 3 h, and f_{dead} was determined after 6 h in total; *cef 3h* indicates that colonies were treated with ceftriaxone for 3 h and f_{dead} was determined after 3 h. Box plots: median, 25/75 percentile, whiskers: 10/90 percentile. N = (30–61) colonies. d) Difference $<\Delta f_{dead}>$ between $<f_{dead}>$ of combined treatment and independent treatments was calculated as describe in the Results. Error bars: standard error of the mean.

https://doi.org/10.1371/journal.ppat.1009251.g006

colonies. Second, cell dynamics and biophysical properties are accessible. Third, we characterize the instantaneous state of bacteria within colonies. This is particularly relevant for studying drug combinations because we probe bacteria at the moment of drug application. Fourth, we exclusively probe gonococci within colonies. Gonococci continuously produce unpiliated cells by pilin phase- and antigenic variation [32]. These cells are sorted out of the colonies [19,33] and exist as planktonic cells. In plating assays, a mixture between colonie-associated and planktonic cells is probed. Despite these important benefits our method shows limitations compared to viable cell counting. One limitation associated with confocal microscopy is the penetration depth of several tens of micrometers which precludes the analysis of thick biofilms. Moreover, the determination of the fraction of dead cells is based on a fluorescence assay that probes membrane permeability. It is conceivable, that cells are unable to recover from antibiotic treatment even though their membrane is still intact at the time point of image acquisition.

In this case, we would correctly determine that the cell is still alive but it would not produce offspring. In a plating assay these cells would be counted as dead cells. Indeed, for ceftriaxone treatment, we found delayed killing (Fig 6) and this delayed killing would reduce colony counts. For azithromycin treatment, little cell death was observed even after 5 h treatment at 100x MIC. It is possible that while most of these cells have intact membranes after 5 h, they will never escape from their stressed state and resume cell growth. As a consequence, cells with an intact cell membrane but incapable of dividing would lead to lower counts in a plating assay. Characterizing both the short-term cellular response investigated in this study and long-term viability will provide a more complete picture of how antibiotics affect colony-bound gonococci.

Many bacterial species employ T4P for cell motility and aggregation [12]. In *Neisseria* species, T4P-T4P mediated attractive forces control the dynamics of bacteria within colonies [15–17,28]. Here, we show that treatment with the protein synthesis inhibitor azithromycin reduces T4P-dependent attraction and, conversely, ceftriaxone enhances the attraction. This result is consistent with the following picture (S9 Fig). A gonococcus continuously extends and retracts its pili. Extended pili bind to pili of multiple neighboring cells. When a pilus retracts, the cell moves. During movement force builds up, eventually leading to rupture of the pilus-pilus bond. Thus bacterial motility within colonies can be understood as a continuous tug-of-war between adjacent bacteria [12]. Azithromycin treatment reduces the probability that a pilus-pilus bond is formed or maintained. As a consequence, the restoring forces from neighboring bacteria are reduced and bacteria become more mobile. Ceftriaxone has the opposite effect of enhancing the probability that neighboring cells are bound via T4P thus reducing within-colony motility.

Increased single cell motility within colonies correlates with increased colony fluidity (or decreased viscosity) [15–17]. Fine-tuning T4P-T4P mediated attractive forces induces a transition between gas-like, liquid-like, and solid-like behavior of the colonies. For *N. meningiditis* fluidity was correlated with their success in colonizing narrow tubing [15]. In particular, it was shown that motile cells that form fluid-like colonies were more efficient in colonizing blood vessels than non-motile cells forming solid-like colonies. Here, we demonstrate that cell motility correlates with fitness in a different manner, namely by influencing survivability. Ceftriaxone treatment was less effective within motility-inhibited colonies compared to highly motile colonies. Different mechanisms could explain our result. First, motility could enhance the influx of macromolecules as was shown for *Bacillus subtilis* biofilms [20]. Under benign conditions, nutrient influx would be faster. Our experimental observation that survivability of motile cells is higher would agree with this hypothesis. In the presence of antibiotics, motility-inhibited colonies would slow down antibiotic penetration. Considering the fairly small size of our colonies, however, diffusion seems unlikely to be a limiting factor. Second, reproducing bacteria require space and bacteria residing at the center of the colony would be unable to grow unless the surrounding bacteria are motile enough to rearrange and create space. When motility is inhibited, central bacteria are likely to respond to growth inhibition by switching into the stationary state. In the growth-inhibited state, dead bacteria would accumulate explaining why the fraction of dead cells is high for motility-inhibited cells in the absence of antibiotics. In the presence of antibiotics, growth inhibition prior to the application of antibiotics is likely to confer tolerance and protect central bacteria from killing. Thus, we consider stress response due to limited space in the center of motility-inhibited colonies as likely explanation for reduced killing in these colonies. Taken together, our study together with the study of Bonazzi et al [15] demonstrates that within-colony motility confers strong fitness effects. High motility enhances survivability and the ability to colonize vessel-like confinements. However, it reduces survivability during antibiotic treatment.

Here we found that azithromycin treatment enhances cell motility and that increased cell motility makes colony-bound bacteria more susceptible to ceftriaxone treatment. This would suggest that treatment by a combination of both drugs was synergistic. Indeed, we found evidence for synergism with sequential treatment but not with simultaneous treatment. The synergistic effect was highest when colonies were first treated with azithromycin and subsequently with ceftriaxone. This result is consistent with azithromycin increasing cell motility, thus boosting the killing efficiency of ceftriaxone. Further studies will be required to find out why the reversed order of drug application also shows synergism.

For planktonic rod-shaped bacteria it is well-known that the cell morphology changes when bacteria are treated with certain antibiotics [34,35]. When *Escherichia coli* is treated with β-lactams or fluoroquinolones, it strongly increases its cell length [34,36]. By contrast, treatment with protein synthesis inhibitors has only minor effects on cell volume [34,37]. In biofilm-dwelling rod-shaped *V. cholerae*, antibiotics inhibiting protein synthesis were shown to enlarge the cell volume considerably [11]. While protein synthesis (and consequentially cell division) was inhibited, metabolism was still active causing the cell volume to increase. Curiously, we are unaware of any study investigating the effects of antibiotics on the cell volume of spherical bacteria (cocci). In line with filamentation of rod-shaped cells [34,35], we found that the cell volume of gonococci increases strongly (2.5 fold) when treated with the β-lactam antibiotics ceftriaxone at its MIC. When we applied high doses of the protein synthesis inhibitor azithromycin for extended periods of time, the cell volume approached the volume of ceftriaxone-treated bacteria, in agreement with the reports on *V. cholerae* [11]. Additionally, we found that also the folic acid inhibitor trimethoprim and the radical producing nitrofurantoin increased the cell volume. The fact that antibiotics from five different classes with four different targets induce an increase in cell volume when applied at the MIC suggests that cell size increase might be a result of general stress response. Inhibition of cell division is observed in response to various stresses [38] and could explain why cells grow larger. An increase in cell volume has been implicated with increased antibiotic tolerance enabling cells to extend their survival time during antibiotic treatment [39]. We conclude that spherically shaped gonococci increase their cell volume in response to treatment with different classes of antibiotics.

In conclusion, we demonstrate that antibiotics do not only affect biofilm structure but also its dynamics and identify T4P-mediated cell-to-cell attractions as the underlying mechanism. Since many biofilm-forming species form T4P [12], this finding likely has implications beyond the *Neisseria* field. Decreased cell-to-cell attractions enhanced the efficiency of antibiotic killing within colonies. In future studies it will be interesting to find out whether this holds true also for bridging attractions other than T4P.

Materials and methods

Growth conditions

Gonococcal base agar was made from 10 g/l dehydrated agar (BD Biosciences, Bedford, MA), 5 g/l NaCl (Roth, Darmstadt, Germany), 4 g/l K_2HPO_4 (Roth), 1 g/l KH_2PO_4 (Roth), 15 g/l Proteose Peptone No. 3 (BD Biosciences), 0.5 g/l soluble starch (Sigma-Aldrich, St. Louis, MO), and supplemented with 1% IsoVitaleX (IVX): 1 g/l D-glucose (Roth), 0.1 g/l L-glutamine (Roth), 0.289 g/l L-cysteine-HCL x H_2O (Roth), 1 mg/l thiamine pyrophosphate (Sigma-Aldrich), 0.2 mg/l $Fe(NO_3)_3$ (Sigma-Aldrich), 0.03 mg/l thiamine HCl (Roth), 0.13 mg/l 4-aminobenzoic acid (Sigma-Aldrich), 2.5 mg/l β-nicotinamide adenine dinucleotide (Roth), and 0.1 mg/l vitamin B12 (Sigma-Aldrich). GC medium is identical to the base agar composition but lacks agar and starch.

Bacterial colony formation and flow chambers

Bacterial colonies were grown in ibidi sticky-Slides $I^{0.8}$ Luer flow chambers with a glass bottom at a constant nutrient flow of 3 ml/h by using a peristaltic pump. Bacteria were harvested from overnight plates and resuspended in GC medium to an optical density at 600 nm (OD600) of 0.05, 300 μl of the cell suspension was inoculated into the chambers. The flow chambers were incubated at 37˚C. Antibiotics were added by changing the medium at the inlet.

Measurement of minimal inhibitory concentrations

The MICs were measured in 48 well plates (Greiner Bio-One) by measuring the OD600 using a plate reader (Infinite M200, Tecan). Each well was inoculated with 5×10^5 CFU/ml and antibiotics were added. The well plate was incubated for 24 h at 37˚C and 5% CO_2. The lowest concentration that did not lead to a change in OD600 over 24 h was determined to be the MIC (S2 Table). To avoid effects of colony formation, MICs were determined for strain *ΔpilE* (Ng196) that does not generate T4P and therefore colony formation is severely suppressed for this strain [19]. For comparison, we measured the MICs of the colony-forming wt* strain for azithromycin and ceftriaxone. As expected, they were higher compared to the MICs measured with the aggregation-inhibited strain.

Confocal microscopy

Prior to image acquisition, colonies were stained using 500 μl of GC medium containing 3 μmol/l Syto 9 (Thermo Fisher Scientific) and 4.5 μmol/l propidium iodide (PI) (Thermo Fisher Scientific). Images were acquired using an inverted microscope (Ti-E, Nikon) equipped with a spinning disc confocal unit (CSU-X1, Yokogawa) and a 100x, 1.49 NA, oil immersion objective lens. The excitation wave lengths were 488 and 561 nm.

Determination of bacterial positions in three dimensions

Single cell positions were determined in three dimensions using a method described in [16]. In short, confocal image stacks were filtered using a spatial bandpass filter. In the resulting image, local maxima were determined yielding the bacterial coordinates with pixel accuracy. Subpixel positions were determined by calculating the centroid of spherical masks around the local maxima.

Determination of radial distribution function

The radial distribution function $g(r)$ is defined so that $N/V\, g(r) r^2 dr$ is the probability that the center of a bacterium will be found in the range dr at a distance r from the center of another bacterium, where N/V is the number density of bacteria. To calculate $g(r)$, we calculated the distribution of distances between cells $n(r)$ by determining the distances between all pairs of cells and sorting them into bins with width dr. The distribution $n(r)$ was then smoothed using a moving average filter to generate the distribution $N(r)$. $N(r)$ is an approximation of the distribution of distances of a system with the same density as for $n(r)$ but with random distances between the particles. The radial distribution function was then calculated via the relation $g(r) = n(r)/N(r)$.

As described previously [16], the shapes of $g(r)$ show good qualitative agreement with the radial distribution functions found in colloidal systems with Lennard-Jones-like interactions.

We used the formula proposed by Matteoli and Mansoori [27]

$$g(r > r_0) = 1 + y^{-m}[g(r_0) - 1 - \lambda] + \left(\frac{y - 1 + \lambda}{y}\right) exp[-\alpha(y - 1)]cos[\beta(y - 1)] \qquad \text{(Eq 1)}$$

where r_0 is the nearest neighbor distance, $y = r/r_0$ and m, λ, α, and β are adjustable parameters.

Determination of fraction of dead cells

The fraction of dead cells was computed by dividing the number of dead cells by the total number of cells found within a colony. The number of dead cells within a colony was determined by counting the cells found in the PI channel. The total number of cells was measured by determining the sum of cells found in the PI and Syto 9 channel. In addition to the total fraction of dead cells per colony, the fraction of dead cells in dependence of the distance to the colony contour was measured. A binary mask of the colony was generated using an intensity threshold. The contour of the mask was extracted representing the colony contour. The closest point of the contour was determined for each cell and the distance was calculated. The cells were sorted into bins according to their distance to the contour and the fraction was determined as described above.

Determination of cell volume

The volume detection was based on an algorithm presented by [40]. A Laplacian of Gaussian filter was used to highlight the cell boundary. Masks representing the cellular objects were generated by filling the boundary and Watershedding was applied to separate falsely connected objects and diplococci. Then, the volume of the masks was determined yielding the volume of the cells.

To verify that the observed cell volume increase was not merely an effect of chromosome rearrangements, we imaged single cells in phase contrast. Overnight cultures were resuspended in GC medium plus Isovitalex and incubated for at least 1 h in liquid medium (37˚C, 5% CO_2) with a starting optical density of $OD_{600} = 0.05$. Subsequently, antibiotics were added at the appropriate concentration. After 2 h of treatment, bacteria were diluted 1:10 in phosphate buffered saline (PBS), put onto coverslips sealed with VALEP and subsequently imaged using phase contrast microscopy. The size of a bacterium was determined by analysing the intensity profiles of individual cocci using *ImageJ*. In agreement with the fluorescence data, cells treated with azithromycin were larger than control cells (S4 Fig). We note that the total volume estimated from this experiment is expected to be different from the volume measured using confocal microscopy because it depends on the exact definition of the edge of the cell. The diffraction pattern of the phase contrast image introduces an uncertainty of the absolute value. However, we are only interested in relative changes in radii under antibiotic treatment.

Time-resolved single cell tracking in two dimensions

Trajectories of single cells in time were obtained using the Fiji Plugin TrackMate in the following manner: Spinning Disc Confocal Microscopy time series at mid-height were loaded into Fiji, regularized using the Plugin StackReg (Rigid body regularization), then divided by a Gaussian smoothed version with smoothing radius 9 px (corresponding to ~ 1 cell diameter). In TrackMate, the threshold intensity and apparent cell diameter *d* was set to adequately capture the cells, but not any noise (we generally set *d* to 1 mum for normal sized cells, and *d* to 1.3 mum for enlarged cells). Further, the maximal displacement in the algorithm allowed for cells between two time frames was set to 0.4 mum. The resulting tracks were then saved as a CSV table.

Measurement of effective diffusion constant

From the two dimensional tracking data obtained in Fiji, the effective diffusion coefficients were determined as following: From the trajectories, the cell positions and velocities, as well as the center of mass of all cells, were corrected for global colony translation and rotation in Matlab by subtracting the average translational and angular velocity from the velocity of each cell. From here, $D(r)$ is obtained as the mean-square displacement at $t = 1s$ divided by 4. of all tracked cells with track length larger than 3 time steps (frame rate 50 Hz).

Static errors in the determination of particle positions (due to a noisy intensity signal) were obtained and corrected by calculating the velocity auto-correlation function $VACF(t, r)$. The latter showed clear decorrelation of single cell dynamics for $t>dt$, and we thus assumed that $VACF(dt, r) = -E/2dt^2$, with E equal the error of the MSD which we then substracted.

Characterization of T4P-mediated cell-to-cell attraction

In order to determine the interactions on the single-cell level we used a dual laser trap setup that was slightly modified from [16]. The trapping laser (20I-BL-106C, 1064 nm, 5.4 W; Spectra Physics, Santa Clara, CA) was directed into a water-immersion objective (Nikon Plan Apochromate VC 60× NA 1.20; Nikon). Manipulation of the trap position was done with a two-axis acousto-optical deflector (DTD-274HD6 Collinear Deflector; IntraAction, Bellwood, IL). The incoming signal for the AOD was generated using a signal generator (SDG 2042 X Function/Arbitrary Waveform Generator, Siglent, Germany) and reinforced by a synthesizer. The distance between the centers of the two traps was adjusted to be 2.84 μm, corresponding to 1.6 MHz in our setup. The beam was focused onto the sample plane via an 60x-objective (Plan Apochromate VC 60x water immersion, N.A. 1.20, W.D. 0.27mm, Nikon, Japan). Bacterial dynamics was recorded with a high-speed camera (EoSens 3CL, Mikrotron, Germany) with a framerate of 50 frames per second. The position of each bacterium for every point in time was calculated using the Hough transformation and MATLAB, described in detail in [16]. From the displacement tracks, durations and frequencies of retraction, elongation, pausing and bundling states were determined.

The samples were prepared by selection of single piliated colonies from overnight GC-plates and resuspended in GC medium plus Isovitalex. After 3h of incubation (37˚C, 5% CO_2) in liquid medium in a well with a starting optical density of $OD_{600} = 0.05$, the bacteria were diluted 1:10 in GC medium plus Isovitalex and ascorbic acid (500 mM). Prior the addition of antibiotics, bacteria were grown at least for 1 h in liquid media liquid in a well. Then antibiotics were added with the appropriate concentration. After 2 h of treatment, bacteria were prepared like the control strain.

Supporting information

S1 Fig. Radial distribution functions. Bacteria (wt*, Ng150) were inoculated into flow chambers and colonies were allowed to assemble for 1 h. Subsequently, they were treated with antibiotics for 3 h at A) 100x MIC, or B, C) 1x MIC. The values for r_0 shown in Fig 2D–2F are obtained from fits to Eq 1 to these distributions.
(TIF)

S2 Fig. Distributions of cell volumes. Bacteria (wt*, Ng150) were inoculated into flow chambers and colonies were allowed to assemble for 1 h. Subsequently, they were treated with

antibiotics for A, B) 5 h at 100x MIC, C) 3 h at 100x MIC, D—E) 3 h at 1x MIC. The mean values shown in Fig 2E–2G are obtained from Gaussian fits to these distributions. B) Markers: data points, full lines: fits to Gaussian function.
(TIF)

S3 Fig. Fractions of dead cells $f_{dead} = N_{dead}/N$ after 3 h of treatment at 1x MIC. Numbers: p-values from two sample KS-test against the control.
(TIF)

S4 Fig. Control for cell radius increase under azithromycin treatment. Wt* cells (Ng150) were incubated for 1 h in liquid medium and subsequently treated with azithromycin at 100x MIC for 2 h. Radii of individual cells were determined using phase contrast microscopy. Mean ± standard error of radii of N = 75 cells. $p < 10^{-16}$ (KS test).
(TIF)

S5 Fig. Antibiotic treatment strongly affects bacterial motility within colonies. wt* gonococci (Ng150) were inoculated into flow chambers and colonies were allowed to assemble for 1 h. Subsequently, they were treated with different antibiotics at their respective MICs for 3 h (0.064 μg / ml azithromycin, 0.004 μg / ml ceftriaxone, 0.002 μg / ml ciprofloxacin, 20 μg / ml kanamycin, 0.48 μg / ml nitrofurantoin, 32 μg / ml trimethoprim). Effective diffusion constant was measured at A) the edge and B) at R = 5 μm into the colony. N = 12–20 colonies. Numbers are p-values from two sample KS-test against the respective controls.
(TIF)

S6 Fig. Frequencies of T4P retraction, elongation, pausing, and multiple T4P-T4P bonds. Grey: control, red: with 6.4 μg / ml azithromycin for (2–3) h, blue: with 0.4 μg / ml ceftriaxone for (2–3) h. Error bars: bootstrapping.
(TIF)

S7 Fig. Mean effective diffusion constant D of untreated cells at A) the edge of the colony and B) within the colony at R = 5 μm after 6 h of growth for strains *ΔpptA* (Ng142), $pilT_{WB2}$ (Ng176), and wt* (Ng150). Box: 25/75 percentile, whiskers: 10/90 percentile. N = 13–20. All statistical comparisons were made by two-sample KS-test: *P 0.05; ***P 0.001.
(TIF)

S8 Fig. Fraction of dead cells $f_{dead} = N_{dead}/N$ in colonies as a function of distance from the edge of the colony at R = 0. Bacteria were inoculated into flow chambers and colonies were allowed to assemble for 1 h. Subsequently, they were treated with with 0.4 μg / ml ceftriaxone for 5 h. A) Fractions of dead cells. B) Fractions of dead cells normalized to fraction at the edge. Grey: wt* (Ng150), blue: $pilT_{WB2}$ (Ng176), red: *ΔpptA* (Ng142). Error bars: standard error of the mean. N = (9–46) colonies per data point.
(TIF)

S9 Fig. Tug-of-war model for motility within colony. In the absence of azithromycin, a bacterium within the colony simultaneously forms multiple bonds with adjacent bacteria (top). When a T4P retracts, movement of the cell body is hindered by T4P-T4P bonds at the opposite side of the retracting pilus. In the presence of azithromycin, the probability that a T4P-T4P bond is formed is reduced (bottom). Thus, the probability that a retracting T4P has opposing T4P-T4P bonds is lower. As a consequence, the bacterium is more motile.
(TIF)

S1 Table. Bacterial strains used in this study.
(DOCX)

S2 Table. Minimal inhibitory concentrations (MICs) of antibiotics. MICs were determined from bacteria that cannot form colonies (*ΔpilE*, Ng196) and from colony-forming *wt** (Ng150) by testing for the ability to grow overnight.
(DOCX)

S3 Table. Raw data. All data required for plotting the Figures are provided in S3 Table.
(XLSX)

S1 Movie. Typical movie of a single confocal plane of untreated wt* cells. Purple circles denote the positions of individual cells. When individual circles disappear transiently, the tracking algorithm has lost the position this bacterium. Scale bar: 10 μm, Δt = 0.03 s.
(AVI)

S2 Movie. Typical movie of a single confocal plane of azithromycin-treated wt* cells (100 MIC, 5 h). Purple circles denote the positions of individual cells. When individual circles disappear transiently, the tracking algorithm has lost the position this bacterium. Scale bar: 10 μm, Δt = 0.03 s.
(AVI)

Acknowledgments

We thank Knut Drescher and Anton Welker for suggestions about single cell detection, Tobias Bollenbach for critical reading of the manuscript, and Paul Higgins and the Maier lab for helpful discussions.

Author Contributions

Conceptualization: Tom Cronenberg, Marc Hennes, Berenike Maier.

Data curation: Tom Cronenberg, Marc Hennes, Isabelle Wielert.

Formal analysis: Tom Cronenberg, Marc Hennes, Isabelle Wielert.

Funding acquisition: Berenike Maier.

Investigation: Tom Cronenberg, Marc Hennes, Isabelle Wielert.

Methodology: Tom Cronenberg, Marc Hennes, Isabelle Wielert.

Project administration: Berenike Maier.

Software: Tom Cronenberg, Marc Hennes, Isabelle Wielert.

Supervision: Berenike Maier.

Validation: Tom Cronenberg, Marc Hennes, Isabelle Wielert, Berenike Maier.

Visualization: Tom Cronenberg, Marc Hennes, Berenike Maier.

Writing – original draft: Berenike Maier.

Writing – review & editing: Tom Cronenberg, Marc Hennes, Isabelle Wielert, Berenike Maier.

References

1. Hall CW, Mah TF. Molecular mechanisms of biofilm-based antibiotic resistance and tolerance in pathogenic bacteria. FEMS Microbiol Rev. 2017; 41(3):276–301. https://doi.org/10.1093/femsre/fux010 PMID: 28369412.

2. Tseng BS, Zhang W, Harrison JJ, Quach TP, Song JL, Penterman J, et al. The extracellular matrix protects Pseudomonas aeruginosa biofilms by limiting the penetration of tobramycin. Environ Microbiol. 2013; 15(10):2865–78. https://doi.org/10.1111/1462-2920.12155 WOS:000325367200018. PMID: 23751003
3. Singh R, Sahore S, Kaur P, Rani A, Ray P. Penetration barrier contributes to bacterial biofilm-associated resistance against only select antibiotics, and exhibits genus-, strain- and antibiotic-specific differences. Pathog Dis. 2016; 74(6). ARTN ftw056 https://doi.org/10.1093/femspd/ftw056 WOS:000385019700004. PMID: 27402781
4. Secor PR, Michaels LA, Ratjen A, Jennings LK, Singh PK. Entropically driven aggregation of bacteria by host polymers promotes antibiotic tolerance in Pseudomonas aeruginosa. P Natl Acad Sci USA. 2018; 115(42):10780–5. https://doi.org/10.1073/pnas.1806005115 WOS:000447491300072. PMID: 30275316
5. Nguyen D, Joshi-Datar A, Lepine F, Bauerle E, Olakanmi O, Beer K, et al. Active starvation responses mediate antibiotic tolerance in biofilms and nutrient-limited bacteria. Science. 2011; 334(6058):982–6. https://doi.org/10.1126/science.1211037 PMID: 22096200; PubMed Central PMCID: PMC4046891.
6. Bernier SP, Lebeaux D, DeFrancesco AS, Valomon A, Soubigou G, Coppee JY, et al. Starvation, together with the SOS response, mediates high biofilm-specific tolerance to the fluoroquinolone ofloxacin. PLoS Genet. 2013; 9(1):e1003144. https://doi.org/10.1371/journal.pgen.1003144 PMID: 23300476; PubMed Central PMCID: PMC3536669.
7. Yan J, Bassler BL. Surviving as a Community: Antibiotic Tolerance and Persistence in Bacterial Biofilms. Cell Host Microbe. 2019; 26(1):15–21. https://doi.org/10.1016/j.chom.2019.06.002 WOS:000474689300006. PMID: 31295420
8. Balaban NQ, Helaine S, Lewis K, Ackermann M, Aldridge B, Andersson DI, et al. Definitions and guidelines for research on antibiotic persistence. Nat Rev Microbiol. 2019. https://doi.org/10.1038/s41579-019-0196-3 PMID: 30980069.
9. Hoffman LR, D'Argenio DA, MacCoss MJ, Zhang ZY, Jones RA, Miller SI. Aminoglycoside antibiotics induce bacterial biofilm formation. Nature. 2005; 436(7054):1171–5. https://doi.org/10.1038/nature03912 WOS:000231416600049. PMID: 16121184
10. Kaplan JB, Izano EA, Gopal P, Karwacki MT, Kim S, Bose JL, et al. Low Levels of beta-Lactam Antibiotics Induce Extracellular DNA Release and Biofilm Formation in Staphylococcus aureus. Mbio. 2012; 3 (4). ARTN e00198-12 https://doi.org/10.1128/mBio.00198-12 WOS:000308588800026. PMID: 22851659
11. Diaz-Pascual F, Hartmann R, Lempp M, Vidakovic L, Song B, Jeckel H, et al. Breakdown of Vibrio cholerae biofilm architecture induced by antibiotics disrupts community barrier function. Nat Microbiol. 2019; 4(12):2136–+. https://doi.org/10.1038/s41564-019-0579-2 WOS:000499071100017. PMID: 31659297
12. Craig L, Forest KT, Maier B. Type IV pili: dynamics, biophysics and functional consequences. Nat Rev Microbiol. 2019; 17(7):429–40. https://doi.org/10.1038/s41579-019-0195-4 PMID: 30988511.
13. Merz AJ, So M, Sheetz MP. Pilus retraction powers bacterial twitching motility. Nature. 2000; 407 (6800):98–102. https://doi.org/10.1038/35024105 PMID: 10993081.
14. Marathe R, Meel C, Schmidt NC, Dewenter L, Kurre R, Greune L, et al. Bacterial twitching motility is coordinated by a two-dimensional tug-of-war with directional memory. Nat Commun. 2014; 5. ARTN 3759 https://doi.org/10.1038/ncomms4759 WOS:000337369100001. PMID: 24806757
15. Bonazzi D, Lo Schiavo V, Machata S, Djafer-Cherif I, Nivoit P, Manriquez V, et al. Intermittent Pili-Mediated Forces Fluidize Neisseria meningitidis Aggregates Promoting Vascular Colonization. Cell. 2018; 174(1):143–55 e16. https://doi.org/10.1016/j.cell.2018.04.010 PMID: 29779947.
16. Welker A, Cronenberg T, Zollner R, Meel C, Siewering K, Bender N, et al. Molecular Motors Govern Liquidlike Ordering and Fusion Dynamics of Bacterial Colonies. Phys Rev Lett. 2018; 121(11):118102. https://doi.org/10.1103/PhysRevLett.121.118102 PMID: 30265121.
17. Zollner R, Cronenberg T, Kouzel N, Welker A, Koomey M, Maier B. Type IV Pilin Post-Translational Modifications Modulate Material Properties of Bacterial Colonies. Biophys J. 2019; 116(5):938–47. https://doi.org/10.1016/j.bpj.2019.01.020 PMID: 30739725; PubMed Central PMCID: PMC6400827.
18. Skerker JM, Berg HC. Direct observation of extension and retraction of type IV pili. Proc Natl Acad Sci U S A. 2001; 98(12):6901–4. https://doi.org/10.1073/pnas.121171698 PMID: 11381130; PubMed Central PMCID: PMC34450.
19. Oldewurtel ER, Kouzel N, Dewenter L, Henseler K, Maier B. Differential interaction forces govern bacterial sorting in early biofilms. Elife. 2015; 4. https://doi.org/10.7554/eLife.10811 PMID: 26402455; PubMed Central PMCID: PMC4625442.

20. Houry A, Gohar M, Deschamps J, Tischenko E, Aymerich S, Gruss A, et al. Bacterial swimmers that infiltrate and take over the biofilm matrix. P Natl Acad Sci USA. 2012; 109(32):13088–93. https://doi.org/10.1073/pnas.1200791109 WOS:000307551700053. PMID: 22773813

21. Kirkcaldy RD, Harvey A, Papp JR, Del Rio C, Soge OO, Holmes KK, et al. Neisseria gonorrhoeae Antimicrobial Susceptibility Surveillance—The Gonococcal Isolate Surveillance Project, 27 Sites, United States, 2014. MMWR Surveill Summ. 2016; 65(7):1–19. https://doi.org/10.15585/mmwr.ss6507a1 PMID: 27414503.

22. Grad YH, Harris SR, Kirkcaldy RD, Green AG, Marks DS, Bentley SD, et al. Genomic Epidemiology of Gonococcal Resistance to Extended-Spectrum Cephalosporins, Macrolides, and Fluoroquinolones in the United States, 2000–2013. J Infect Dis. 2016; 214(10):1579–87. https://doi.org/10.1093/infdis/jiw420 PMID: 27638945; PubMed Central PMCID: PMC5091375.

23. Wadsworth CB, Arnold BJ, Sater MRA, Grad YH. Azithromycin Resistance through Interspecific Acquisition of an Epistasis-Dependent Efflux Pump Component and Transcriptional Regulator in Neisseria gonorrhoeae. Mbio. 2018; 9(4). ARTN e01419-18 https://doi.org/10.1128/mBio.01419-18 WOS:000443884300078. PMID: 30087172

24. Rouquette-Loughlin CE, Reimche JL, Balthazar JT, Dhulipala V, Gernert KM, Kersh EN, et al. Mechanistic Basis for Decreased Antimicrobial Susceptibility in a Clinical Isolate of Neisseria gonorrhoeae Possessing a Mosaic-Like mtr Efflux Pump Locus. Mbio. 2018; 9(6). ARTN e02281-18 https://doi.org/10.1128/mBio.02281-18 WOS:000454730100068. PMID: 30482834

25. Vincent LR, Kerr SR, Tan Y, Tomberg J, Raterman EL, Hotopp JCD, et al. In Vivo-Selected Compensatory Mutations Restore the Fitness Cost of Mosaic penA Alleles That Confer Ceftriaxone Resistance in Neisseria gonorrhoeae. Mbio. 2018; 9(2). ARTN e01905-17 https://doi.org/10.1128/mBio.01905-17 WOS:000431279600057. PMID: 29615507

26. Gonococcal Infections in Adolescents and Adults [Internet]. 2015.

27. Matteoli E, Mansoori GA. A Simple Expression for Radial-Distribution Functions of Pure Fluids and Mixtures. J Chem Phys. 1995; 103(11):4672–7. https://doi.org/10.1063/1.470654 WOS: A1995RU11000029.

28. Ponisch W, Weber CA, Juckeland G, Biais N, Zaburdaev V. Multiscale modeling of bacterial colonies: how pili mediate the dynamics of single cells and cellular aggregates. New J Phys. 2017; 19. ARTN 015003 https://doi.org/10.1088/1367-2630/aa5483 WOS:000393787400001.

29. Ponisch W, Eckenrode KB, Alzurqa K, Nasrollahi H, Weber C, Zaburdaev V, et al. Pili mediated intercellular forces shape heterogeneous bacterial microcolonies prior to multicellular differentiation. Sci Rep-Uk. 2018; 8. ARTN 16567 https://doi.org/10.1038/s41598-018-34754-4 WOS:000449499500056. PMID: 30410109

30. Wang LC, Litwin M, Sahiholnasab Z, Song W, Stein DC. Neisseria gonorrhoeae Aggregation Reduces Its Ceftriaxone Susceptibility. Antibiotics (Basel). 2018; 7(2). https://doi.org/10.3390/antibiotics7020048 PMID: 29914058; PubMed Central PMCID: PMC6022932.

31. Naessan CL, Egge-Jacobsen W, Heiniger RW, Wolfgang MC, Aas FE, Rohr A, et al. Genetic and functional analyses of PptA, a phospho-form transferase targeting type IV pili in Neisseria gonorrhoeae. J Bacteriol. 2008; 190(1):387–400. https://doi.org/10.1128/JB.00765-07 PMID: 17951381; PubMed Central PMCID: PMC2223744.

32. Rotman E, Seifert HS. The genetics of Neisseria species. Annu Rev Genet. 2014; 48:405–31. Epub 2014/09/25. https://doi.org/10.1146/annurev-genet-120213-092007 PMID: 25251852.

33. Zollner R, Oldewurtel ER, Kouzel N, Maier B. Phase and antigenic variation govern competition dynamics through positioning in bacterial colonies. Sci Rep. 2017; 7(1):12151. Epub 2017/09/25. https://doi.org/10.1038/s41598-017-12472-7 PMID: 28939833; PubMed Central PMCID: PMC5610331.

34. Nonejuie P, Burkart M, Pogliano K, Pogliano J. Bacterial cytological profiling rapidly identifies the cellular pathways targeted by antibacterial molecules. Proc Natl Acad Sci U S A. 2013; 110(40):16169–74. https://doi.org/10.1073/pnas.1311066110 PMID: 24046367; PubMed Central PMCID: PMC3791758.

35. Ojkic N, Serbanescu D, Banerjee S. Surface-to-volume scaling and aspect ratio preservation in rod-shaped bacteria. Elife. 2019; 8. ARTN e47033 https://doi.org/10.7554/eLife.47033 WOS:000487669700001. PMID: 31456563

36. Windels EM, Ben Meriem Z, Zahir T, Verstrepen KJ, Hersen P, Van den Bergh B, et al. Enrichment of persisters enabled by a beta-lactam-induced filamentation method reveals their stochastic single-cell awakening. Commun Biol. 2019; 2. UNSP 426 https://doi.org/10.1038/s42003-019-0672-3 WOS:000500305800001. PMID: 31815194

37. Basan M, Zhu ML, Dai XF, Warren M, Sevin D, Wang YP, et al. Inflating bacterial cells by increased protein synthesis. Mol Syst Biol. 2015; 11(10). ARTN 836 https://doi.org/10.15252/msb.20156178 WOS:000364315500008. PMID: 26519362

38. Jonas K. To divide or not to divide: control of the bacterial cell cycle by environmental cues. Curr Opin Microbiol. 2014; 18:54–60. https://doi.org/10.1016/j.mib.2014.02.006 WOS:000337018200009. PMID: 24631929

39. Zahir T, Wilmaerts D, Franke S, Weytjens B, Camacho R, Marchal K, et al. Image-Based Dynamic Phenotyping Reveals Genetic Determinants of Filamentation-Mediated beta-Lactam Tolerance. Front Microbiol. 2020; 11. ARTN 37410.3389/fmicb.2020.00374. WOS:000525711900001. https://doi.org/10.3389/fmicb.2020.00374 PMID: 32231648

40. Hartmann R, Singh PK, Pearce P, Mok R, Song B, Diaz-Pascual F, et al. Emergence of three-dimensional order and structure in growing biofilms. Nat Phys. 2019; 15(3):251–+. https://doi.org/10.1038/s41567-018-0356-9 WOS:000460166500021. PMID: 31156716

5 Pilin Antigenic Variants Impact Gonococcal Lifestyle and Antibiotic Tolerance by Modulating Interbacterial Forces

5.1 Publication

The following work was published in PLOS Biology under the title *Pilin antigenic variants impact gonococcal lifestyle and antibiotic tolerance by modulating interbacterial forces* in January 2025 applying the Creative Commons Attribution 4.0 International (CC-BY) license [133].

5.1.1 Contributions to the Publication

This work is based on close collaborations with Paul G. Higgins (University Hospital Cologne) and Lisa Craig (Simon Fraser University, Canada) and two colleagues from our group Sebastian Kraus-Römer and Thorsten Volkmann. Paul G. Higgins provided us with the clinical isolates the study is based on, which were brought into the piliated state by me. Lisa Craig performed and interpreted the analysis of PilE structures via *AlphaFold* [156] and generated the electrostatic potential of the pilus filaments using the APBS tool of PyMol [157]. From our group, Sebastian Kraus-Römer created the pilin variants and determined the minimal inhibitory concentrations for the antibiotic treatment. Furthermore, he analysed the sequences of *pilE* and *pilS* and performed the strain mixing experiments. My contribution to this work included determining the attractive forces of the pilin variants via the double laser trap and characterising the twitching performance. Furthermore, I performed the TEM of the pilin variants at the CECAD and analysed the images. Additionally, I measured the growth kinetics and developed the protocol for the survival assay and analysed the resulting data. The survival assays were performed in close collaboration between Sebastian Kraus-Römer, Thorsten Volkmann and myself.

Berenike Maier, Lisa Craig, Sebastian Kraus-Römer, and I contributed to the project design, writing the manuscript and creating the figures.

PLOS BIOLOGY

RESEARCH ARTICLE

Pilin antigenic variants impact gonococcal lifestyle and antibiotic tolerance by modulating interbacterial forces

Isabelle Wielert[1,2☯], Sebastian Kraus-Römer[1,2☯], Thorsten E. Volkmann[1,2], Lisa Craig[3], Paul G. Higgins[2,4,5], Berenike Maier[1,2*]

1 Institute for Biological Physics, University of Cologne, Cologne, Germany, **2** Center for Molecular Medicine Cologne, Cologne, Germany, **3** Department of Molecular Biology and Biochemistry, Simon Fraser University, Burnaby, British Columbia, Canada, **4** Institute for Medical Microbiology, Immunology and Hygiene, Faculty of Medicine and University Hospital Cologne, University of Cologne, Cologne, Germany, **5** German Centre for Infection Research, Partner site Bonn-Cologne, Cologne, Germany

☯ These authors contributed equally to this work.
* berenike.maier@uni-koeln.de

Abstract

Type 4 pili (T4P) are multifunctional filaments involved in adhesion, surface motility, biofilm formation, and horizontal gene transfer. These extracellular polymers are surface-exposed and, therefore, act as antigens. The human pathogen *Neisseria gonorrhoeae* uses pilin antigenic variation to escape immune surveillance, yet it is unclear how antigenic variation impacts most other functions of T4P. Here, we addressed this question by replacing the major pilin of a laboratory strain with pilins from clinical isolates. We reveal that the resulting strains vary substantially in their attractive forces. Strongly interacting bacteria form microcolonies while weakly interacting bacteria retain a planktonic lifestyle. In mixed microcolonies, different variant strains segregate in agreement with the differential strength of adhesion hypothesis. By combining structural predictions and laser tweezers experiments, we show that the C-terminal region of the pilin is crucial for attraction. Lifestyle affects growth kinetics and antibiotic tolerance. In the presence of ceftriaxone or ciprofloxacin, the killing kinetics indicate strongly increased tolerance of aggregating strains. We propose that pilin antigenic variation produces a mixed population containing variants optimized for growth, colonization, or survivability under external stress. Different environments select different variants, ensuring the survival and reproduction of the population as a whole.

OPEN ACCESS

Citation: Wielert I, Kraus-Römer S, Volkmann TE, Craig L, Higgins PG, Maier B (2025) Pilin antigenic variants impact gonococcal lifestyle and antibiotic tolerance by modulating interbacterial forces. PLoS Biol 23(1): e3003022. https://doi.org/10.1371/journal.pbio.3003022

Academic Editor: Victor Sourjik, Max Planck Institute for Terrestrial Microbiology: Max-Planck-Institut fur terrestrische Mikrobiologie, GERMANY

Received: October 10, 2024

Accepted: January 16, 2025

Published: January 30, 2025

Data Availability Statement: All relevant data are within the paper and its Supporting Information files.

Funding: This work has been supported by the Center for Molecular Medicine Cologne (B08 to BM & PH), the Deutsche Forschungsgemeinschaft (MA3898 to BM & CRC1310 A5 to BM), and the Helmholtz Gesellschaft (IHRS BioSoft stipend to IW). The funders had no role in study design, data

Introduction

Type 4 pili (T4P) are filamentous cell appendages generated by a variety of pathogenic bacteria including the *Neisseria* species, *Pseudomonas aeruginosa*, *Vibrio cholerae*, and *Acinetobacter baumannii*. They support functions such as adhesion, motility, aggregation, and horizontal gene transfer, which are crucial for survival, colonization, and virulence [1,2]. In pathogenic *Neisseria*, the amino acid sequence of the T4P major pilin, PilE, continually changes as a result

collection and analysis, decision to publish, or preparation of the manuscript.

Competing interests: The authors have declared that no competing interests exist.

Abbreviations: CFU, colony forming unit; MIC, minimal inhibitory concentration; T4P, Type 4 pili; TEM, transmission electron microscopy.

of antigenic variation [3,4]. This role of PilE variability in immune escape is well-established [5–7] and it has been shown that it can affect adhesion to host cells [8]. Currently, its implications in other pilus-mediated functions and how these influence gonococcal planktonic versus biofilm lifestyle are not well understood.

T4P are polymers of the major pilin, with multiple low-abundance minor pilins [2]. For gram-negative bacteria, they protrude from a complex that spans the inner and outer membrane [2]. Driven by cytosolic ATPases, the pilus filament elongates by polymerization and retracts by depolymerization. In *N. gonorrhoeae*, the gene encoding the major pilin PilE is hypermutable by antigenic variation. Pilin antigenic variation was originally discovered by the observation that the morphology of gonococcal colonies on agar plates is related to piliation [3,6,7]. Piliated *N. gonorrhoeae* produce convex colonies, whereas non-piliated variants produce flat colonies. A nonpiliated phenotype is mainly caused by an antigenic variation that generates a truncated PilE, e.g., by a frameshift mutation [9,10]. In general, the macroscopic phenotype can be linked to the strength of interactions generated by the T4P of neighboring cells [11]. Antigenic variation occurs at a rate of $1.7 \cdot 10^{-3}$ events/cell/generation for the gonococcal lab strain MS11 [12]. Segments of one of the up to 18 different *pilS* sequences [13,14] recombine with *pilE* and replace extended stretches of the *pilE* sequence. The variability along the *pilE* sequence is heterogeneous and can be subdivided into conserved, semi-variable and hyper-variable regions [15]. Pilin antigenic variation relies on a G4 motif upstream of *pilE*; deletion of this motif abolishes antigenic variation [16]. Using a mutational screen of the 3′ region of the gonococcal *pilE* coding sequence, it was shown that various point mutations caused loss of piliation [10]. For closely related *N. meningitidis* T4P, mutational analysis of *pilE* was used to generate a functional map of the major pilin [17]. In that study, a specific major pilin variant was used as a reference structure and single amino acid changes in different regions were associated with different T4P functions including biogenesis, adhesion, and aggregation [17]. However, it remains elusive how naturally occurring antigenic variations, which extend along dozens of amino acid residues throughout the PilE sequence, affect T4P functionality.

In this study, we focus on the following T4P-related functions: twitching motility, generation of attractive forces between cells, microcolony formation, and antibiotic tolerance. Twitching motility is a mode of surface motility driven by cycles of T4P elongation, surface attachment, and retraction [2,18,19]. *N. gonorrhoeae* uses a tug-of-war mechanism for twitching motility [20,21] and, as a consequence, gonococcal motility can be described as a correlated random walk. While T4P surface attachment mediates motility, pilus:pilus binding between adjacent cells causes attraction between gonococci [22]. In liquid media, this attraction causes rapid aggregation of *Neisseria* species into spherical (micro)colonies comprising thousands of cells [22–24]. The strength of the attractive force determines whether the colonies behave as liquids or solids [22,25,26], which impacts tolerance to antibiotics [27]. Attractive forces are reduced by the posttranslational surface modification of the T4P [25]. If gonococcal strains generating different levels of attractive force are mixed, they can form colonies comprising both strains. The bacteria segregate [11,25] in agreement with the differential strength of adhesion hypothesis that states that the most strongly interacting cells accumulate at the centre of the colony [28]. So far it is unclear whether the PilE sequence and thus the pilus surface stereochemistry also affect the attractive forces and colony morphology. Here, we investigate how different variants of PilE impact the gonococcal lifestyle, i.e., whether they live as planktonic cells or within aggregates including microcolonies or biofilms.

The emergence of resistance to several classes of antibiotics has made *N. gonorrhoeae* a multidrug-resistant pathogen [29]. While the mechanisms conferring gonococcal drug resistance are fairly well understood [30,31], very little is known about antibiotic tolerance of this pathogen. Tolerance describes the ability of bacteria to survive antibiotic treatment for extended periods of time [32]. This extended survival time is problematic for eradication of the pathogen and often precedes antibiotic resistance [33]. The mechanisms driving tolerance are multifaceted including reduced permeability to antibiotics, reduction of growth rate and metabolic activity, membrane polarization, as well as the activation of stress responses [34]. A major tolerance mechanism is aggregation and biofilm formation [35]. Gonococcal aggregation enhances tolerance to ceftriaxone, a β-lactam antibiotic that targets cell wall synthesis [36] with the physical properties of the microcolony impacting the degree of tolerance [27]. Ceftriaxone is currently recommended for gonorrhea treatment. Since pilin antigenic variation potentially affects gonococcal aggregation and the physical properties of the colonies, it likely impacts antibiotic tolerance.

In this study, we investigate how variation of the pilin sequence affects gonococcal properties, behavior, and lifestyle. Based on the PilE sequences, we predict structural changes to the surface of the T4P filament that likely impact gonococcal aggregation. Using laser tweezers, we confirm that pilin variation strongly affects the attractive force between pairs of cells. We show that all *pilE* variants in this study produce functional T4P but cluster into 2 distinct phenotypic lifestyles; planktonic and aggregating, depending on the T4P-mediated attractive force. Structural predictions suggest that complementarity between knobs and cavities in adjacent pili influences cell-to-cell attraction. We confirm this prediction experimentally by generating strains expressing *pilE* hybrids between different variants. We show that pilus attractive forces and gonococcal aggregation, growth and survival under antibiotic treatment strongly depend on the pilin variant. Taken together, we reveal that some pilin antigenic variants generate aggregative T4P while others assemble into non-aggregative T4P with phenotypic consequences that optimize bacterial proliferation and survival under a variety of conditions including antibiotic treatment.

Results

Pilin antigenic variants show different stereochemistries of key interaction sites on T4P

We sought to understand how pilin antigenic variation affects the pilus-mediated interactions between bacteria and to characterize the phenotypic changes including growth, antibiotic resistance, and antibiotic tolerance that result from altering these interactions. In the first step, we cloned the *pilE* genes from the *N. gonorrhoeae* clinical isolates Ng24, Ng17, and Ng32 into the background strain, wt*, in place of the native *pilE* gene. wt* is *N. gonorrhoeae* MS11 with the G4 motif deleted to prevent further antigenic variation of *pilE* [37]. The *pilS* sequences of the clinical isolates are similar to the respective sequences of the wt* strain (Fig i in S1 Text, S1 Data). Specific *pilS* sequences can be mapped nearly contiguously to the *pilE* sequences (Fig ii in S1 Text), indicating that the *pilE* variants of the clinical isolates have arisen by pilin antigenic variation. To understand the implications of differences in *pilE* sequences among variants, we examined their pilin sequences and predicted monomeric pilin structures and T4P filament structures. The amino acid sequences of the pilin variants were compared to that of the wt* strain (Fig 1A). Secondary structure and features were assigned based on alignment with the *N. gonorrhoeae* C30 PilE crystal structure [38], which is 90% identical in sequence to wt* PilE and 99% identical in the first 120 amino acids. The sequence of the N-terminal α-helix, α1, is identical for all pilins, with the exception of a glycine instead of glutamate at position 49 of Ng17 PilE (PilE$_{17}$). PilE$_{wt}$ and PilE$_{24}$ share a serine at position 63, which is posttranslationally modified with a glycan in *N. gonorrhoeae* MS11 and C30 [38]. PilE$_{32}$ and PilE$_{17}$ have charged residues at this position. Some sequence variation is observed in the αβ-loop, which lies

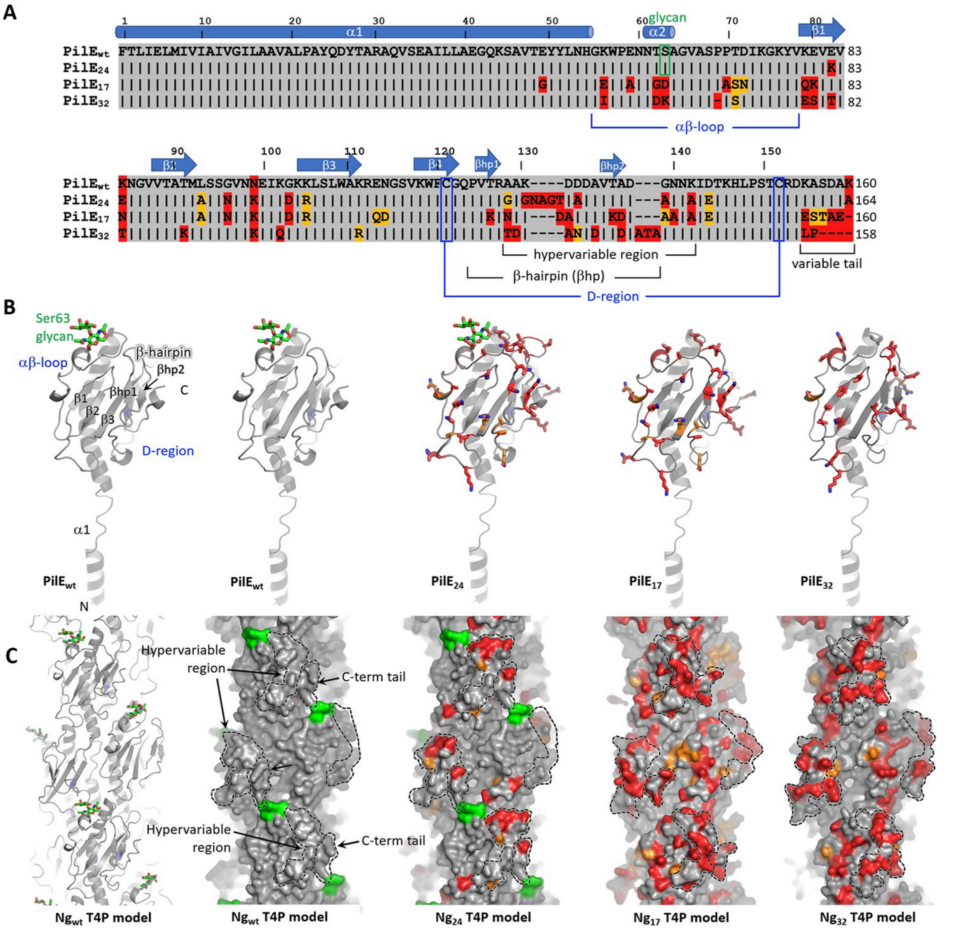

Fig 1. Sequence alignment and structure predictions for PilE variants and pilus filaments. (A) PilE amino acid sequence alignment for wt* and variant strains. Amino acids of the PilE variants that are identical to those in PilE$_{wt}$ are shown as black bars with gray shading, conservative amino acid changes are indicated with orange shading and non-conserved residues have red shading. The secondary structure and other hallmark features of *Neisseria* Type 4 pilins are indicated based on alignment of PilE$_{wt}$ with C30 PilE (Protein Data Bank ID 2HI2). (B) Pilin models were generated using AlphaFold [39,67]. Residues that differ from those in PilE$_{wt}$ are shown in stick representation, with carbon colored as in Fig 1A, nitrogen in blue and oxygen in red. Glycan carbons are green. The conserved disulfide-bonded cysteines that delineate the D-region are blue. Variable residues are located on the face of the C-terminal globular domain. (C) Filament models were generated by superimposing the pilin predictions on the *N. gonorrhoeae* T4P structure (EMD-8739) and applying its symmetry parameters. The wt* T4P model is shown on the left in cartoon representation and all models are shown in surface representation, colored as in Fig 1B. The hypervariable β-hairpin and C-terminal tail together form a protruding "knob" on each subunit (dashed lines) and deep cavities or "holes" lie at the interface between subunits.

https://doi.org/10.1371/journal.pbio.3003022.g001

between α1 and strand β1 of the β-sheet, in β1 and in the β1-β2 loop. The most variable region is the hypervariable β-hairpin that follows the β-sheet and the C-terminal tail, which have amino acid changes but also insertions and deletions. We determined the overall pilin sequence identities of the variant to that of MS11 (Table ii in S1 Text). PilE$_{24}$ is 90% identical to PilE$_{wt}$, whereas PilE$_{32}$ is 86.6% identical and PilE$_{17}$ is 80.6% identical.

Pilin models for each variant were generated using AlphaFold [39]. The continuous N-terminal α-helix, α1, seen in the crystal structure of PilE [38] and in the AlphaFold predictions was replaced with the partially melted α-helix seen in the cryo-electron microscopy reconstruction of the intact pilus [40] (Fig 1B). All variable residues are located on the face of the

PilE globular domain that is exposed in the pilus filament, as expected for antigenic variation. PilE_{17} shows the greatest degree of variability, particularly in the protruding β-hairpin and C-terminal tail.

Pilus filament models were generated by superimposing each pilin model onto a single subunit in the cryoEM structure of the *N. gonorrhoeae* T4P and applying its symmetry parameters (Fig 1C). Filament models are shown in Fig 1C. The T4P surface is undulating: the β-hairpin and the C-terminal tail regions, which show the highest sequence variability, together form protruding "knobs"; and deep cavities or grooves lie between the globular domains, lined with the variable C-terminal tail on one side and the αβ-loop and β1-β2 loop on the other. Accordingly, the conformation of both the knobs and the cavities/grooves ("holes") vary considerably among the variants, with wt* and Ng24 T4P being most similar. The electrostatic surface potential also differs substantially from one pilus variant to the next (Fig iii in S1 Text), with positively charged residues framing the holes of PilE_{wt} and PilE_{24} and negatively charged residues lining the edges of the PilE_{17} and PilE_{32} holes. The knobs of each pilin differ in their distribution of charged residues, with PilE_{32} having the most negatively charged knob. Pilus:pilus interactions likely require both structural and chemical complementarity between these surface features to allow the knobs in one filament to fit into the holes in another. Thus, these marked differences in stereochemistry among the pilus variants could impact pilus:pilus interactions and bacterial aggregation.

All PilE variants support twitching motility and high pilus densities

Pilin antigenic variation can lead to loss of T4P function, in particular to reduced levels of piliation [9,10]. To test for piliation, we assessed the density of T4P for each strain using negative-stain transmission electron microscopy (TEM). All 4 strains show high levels of piliation (Fig 2A). Quantitatively, wt_{pilE32} has elevated number of pili per cell compared to the other strains which have comparable piliation levels (Fig iv in S1 Text).

We next compared T4P dynamics among the variants. T4P dynamics correlates quantitatively with twitching motility; the faster T4P retract the faster gonococci move on BSA-coated glass [20,21]. To find out whether variations in the PilE sequence affect T4P dynamics, we compared the trajectories of gonococci moving at the glass surface. All variants exhibit twitching motility on BSA-coated glass surfaces. A representative track for each *pilE* variant is shown in Fig 3B. A detailed analysis of the trajectories using a correlated random walk model [21] (described in Methods, Fig vi in S1 Text) showed that strain wt_{pilE17} is the most motile; both the velocity v_{corr} and the correlation time τ were significantly higher than for the wt* strain (Fig v in S1 Text). The correlation time is a measure of how long the bacterium moves without changing direction. We conclude that all PilE variants have comparable or even higher levels of pili and generate dynamic T4P.

Replacing the native pilin in the laboratory strain with antigenic variants affects bacterial attractive forces and consequently aggregation and segregation

We examined the effects of the variations in pilus surface stereochemistry on pilus:pilus interaction and aggregation. In this study, the term pilus:pilus interaction is used to describe the interaction between T4P of adjacent gonococci. Using a dual laser tweezers assay, we investigated the attractive forces generated by the pilin variants. For each strain, we trapped pairs of bacteria and measured the T4P-mediated interaction forces between them (Fig 3A). When bacteria in different traps interact via their T4P, and at least one T4P retracts, the cell bodies approach each other. Bacteria are deflected by a distance *d* from the centers of the traps. As the

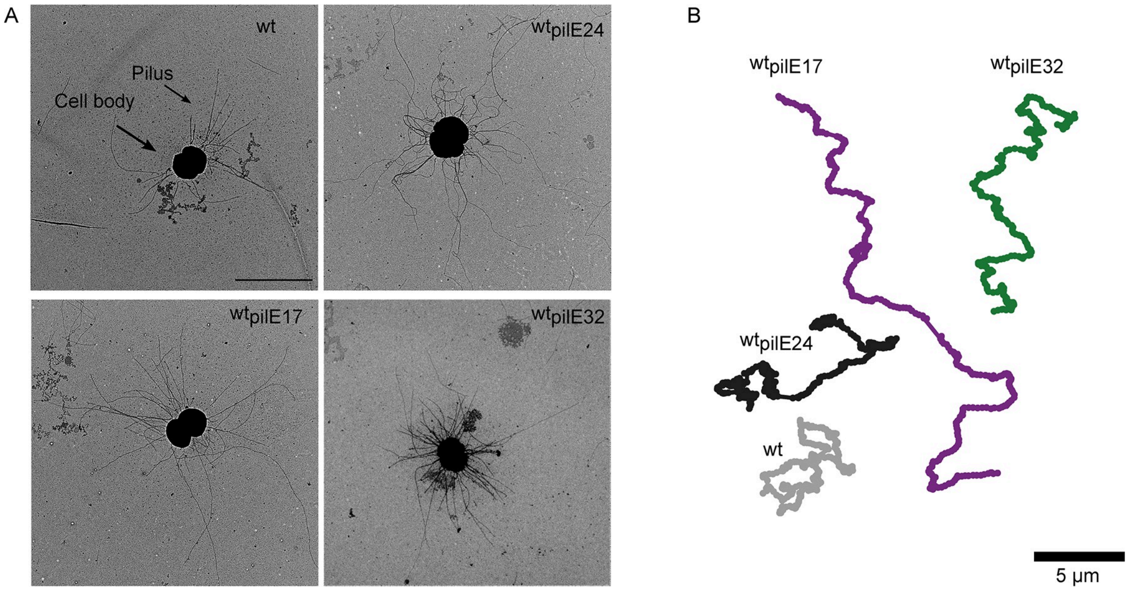

Fig 2. Replacing the native *pilE* sequence by antigenic variants does not reduce T4P density and maintains twitching motility. (A) Representative TEM images of pilin variants. Scale bar: 2 μm. (B) Trajectories of motile bacteria. Representative trajectories of pilin variants over 30 seconds (tracks made via Trackmate Image J [68]) (gray: wt* (Ng150), dark gray: wt_{pilE24} (Ng242), purple: wt_{pilE17} (Ng240), green: wt_{pilE32} (Ng230)). Scale bar: 5 μm.

https://doi.org/10.1371/journal.pbio.3003022.g002

deflection increases, the restoring force of the laser traps increases as well leading to a rupture event when the optical force exceeds the (rupture) force that the pilus:pilus bond can sustain.

The force at which a pilus:pilus bond ruptures was used as a measure of the attractive force between gonococci. $F_{rupture}$ is defined as the maximal force attained before the bond breaks and the bacteria move back to their equilibrium positions. We did not observe significant differences between wt* and wt_{pilE24} (Kolmogorow–Smirnow test), where the mean rupture forces with standard errors were $F^{wt}_{rupture}$ = 40.9 ± 0.9 pN and $F^{pilE24}_{rupture}$ = 38.3 ± 1.0 pN, respectively (Fig 3B). The deviation from previously published results for the wt* [27] most likely results from a different distance of the traps. Interestingly, the wt_{pilE17} and wt_{pilE32} variants exhibit much lower rupture forces of $F^{pilE17}_{rupture} = 3.8 \pm 0.1$ pN and $F^{pilE32}_{rupture} = 6.1 \pm 0.3$ pN, respectively. Moreover, the probability that a pair of bacteria shows attractive interactions is lower for all *pilE* variant strains compared to wt* (Fig ix in S1 Text).

The attractive force between bacteria initiates aggregation into microcolonies. In this study, the term "microcolony" describes spherical aggregates formed by gonococci in liquid or at the interface between the surface and liquid (Fig 3C). By the combined action of twitching motility, pilus:pilus attraction, and microcolony-fusion, wt* gonococci self-assemble within several minutes into spherical colonies comprising thousands of cells [22,24,41]. We investigated whether the different *pilE* variants support microcolony formation in this time frame. In agreement with the dual laser tweezers experiments, we found that only the strains that mediate the stronger attractive forces, wt* and wt_{pilE24}, are capable of microcolony formation (Fig 3C). After 1 h of incubation, colonies are mostly spherical (S1 Data) with a broad distribution of colony sizes (Fig viiA in S1 Text). While many colonies are small, more than 90% of the cells reside within colonies exceeding 1,000 cells (Fig viiB in S1 Text). We note that the colony size distribution is highly dynamic because colonies are motile and can fuse [22]. By contrast, the strains wt_{pilE17} and wt_{pilE32} remain planktonic (Fig 3D and S1 Data). Since the number of pili

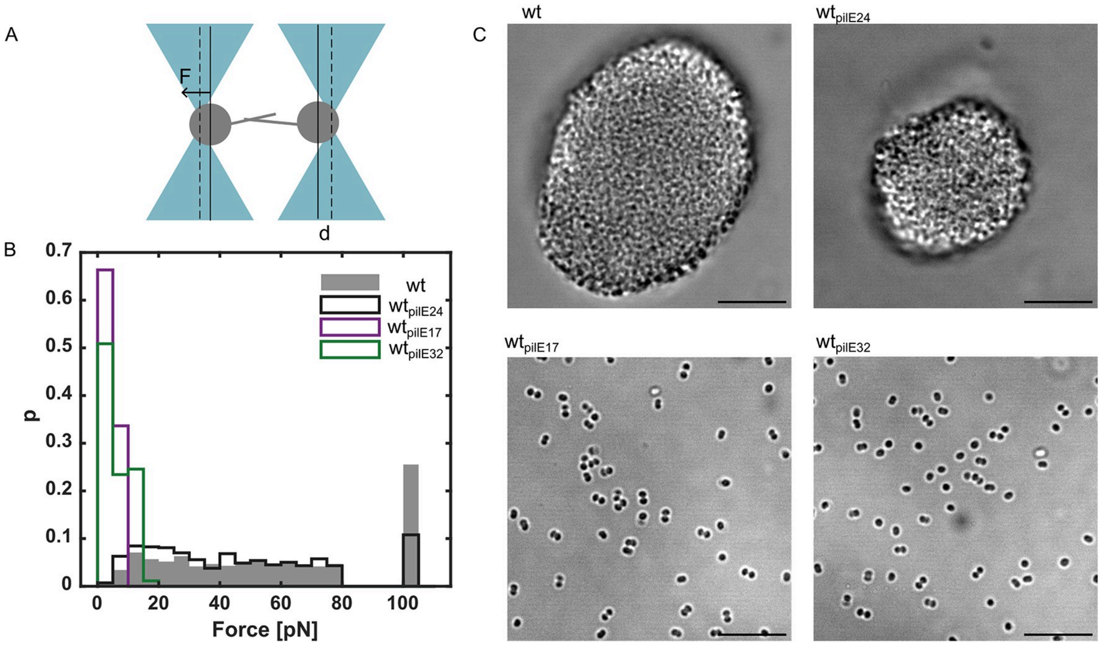

Fig 3. Attractive force between pairs of bacteria depends on the pilin sequence. (A) Sketch of dual laser tweezers setup. (B) Probability distribution of rupture forces (number of interacting cell pairs: $N_{wt} = 71$, $N_{wtpilE24} = 59$, $N_{wtpilE17} = 30$, $N_{wtpilE32} = 54$). The linearity of the laser trap is limited to 80 pN. All rupture events exceeding this force were grouped into a single bin shown at 100 pN. The data underlying this figure can be found in S1 Data. (C) Representative brightfield images of gonococci in liquid culture show aggregated microcolonies for wt and wt$_{pilE24}$ and planktonic cells for wt$_{pilE17}$ and wt$_{pilE32.}$ Scale bar: 10 μm.

https://doi.org/10.1371/journal.pbio.3003022.g003

per cell of the planktonic strains is not lower than the density of the aggregating strains (Fig iv in S1 Text), we attribute the different interaction properties to T4P stereochemistry.

We next addressed the question whether wt* cells and strains expressing pilin variants self-assembled into mixed microcolonies. To this end, we mixed *mcherry*-expressing wt* cells (wt*$_{red}$) with *gfp*-expressing pilin variant strains. The 2 aggregating strains wt*$_{red}$ and wt$_{pilE24\ green}$ formed colonies in which both strains segregate (Fig 4A). The most common pattern is one where each strain occupies one half of the colony. According to the differential strength of adhesion hypothesis, this phenotype is indicative of strong intrastrain interactions and weaker inter-strain interactions [28,11]. Strains wt$_{pilE17\ green}$ (Fig 4B) and wt$_{pilE32\ green}$ (Fig 4C) show comparable colony pattern when mixed with wt*$_{red}$ cells. Both form a shell around the wt*$_{red}$ colony made up from a single-celled layer. This morphology indicates that wt* T4P attract wt$_{pilE17}$ and wt$_{pilE32}$ pili, but less strongly than they attract wt*. By contrast, wt*$_{red}$ colonies do not attract unpiliated *ΔpilE*$_{green}$ bacteria (Fig 4D). These results show that while the planktonic piliated strains cannot form colonies by themselves, they can attach to existing colonies.

Taken together, these results demonstrate that different antigenic variants of the T4P have different attractive force between pairs of cells. Strongly interacting strains form colonies while weakly interacting strains remain planktonic but can associate with colonies formed by strongly interacting cells.

The C-terminal sequence of the pilin determines the attractive force between T4P

We investigated which region of the pilin governs pilus:pilus interaction. The pilin structure models show high variability between the knobs and the cavities of the different pilin variants

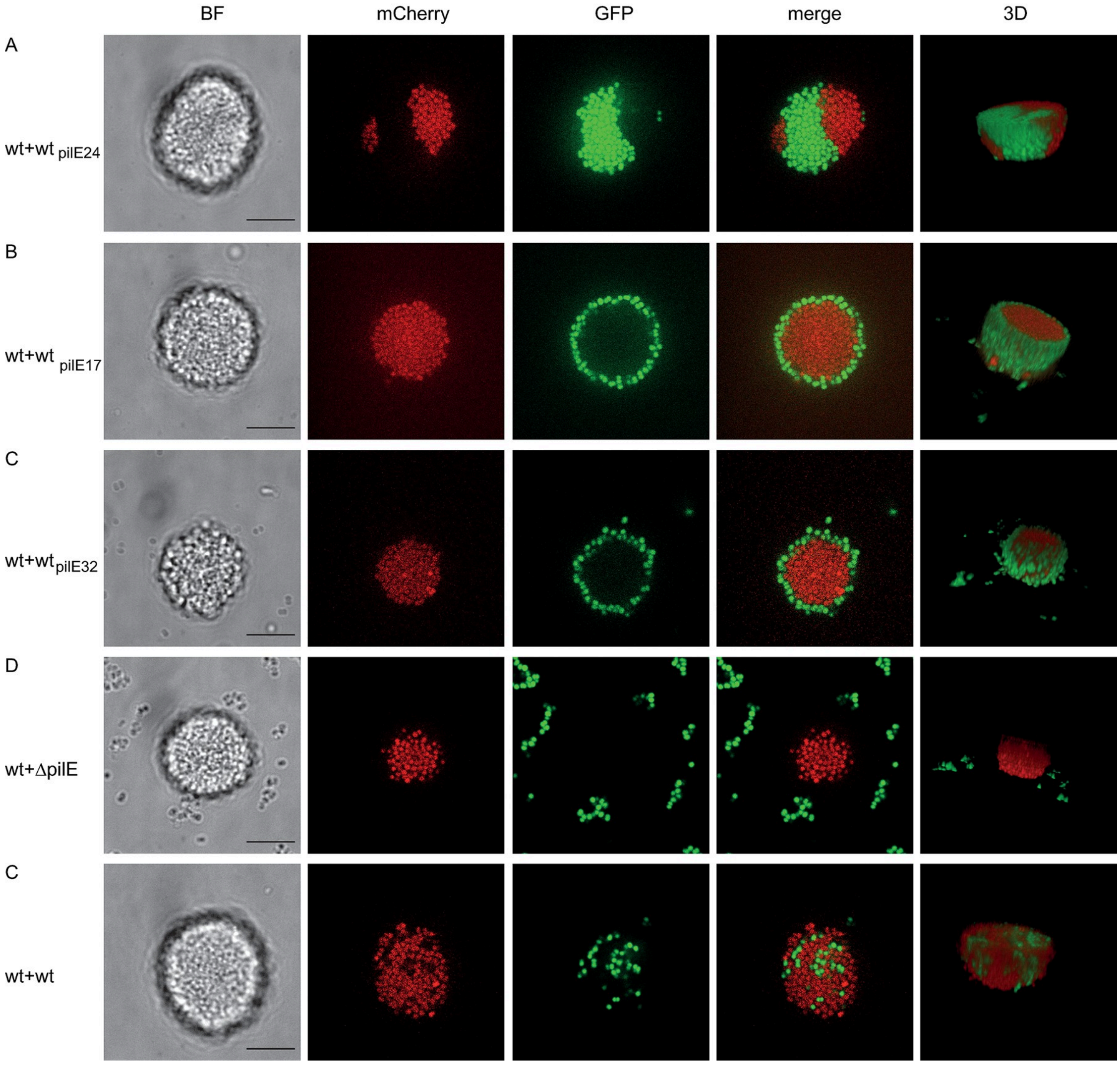

Fig 4. Pilin variants segregated in mixed microcolonies. wt$^*_{red}$ (Ng170) were mixed at a 1:1 ratio with (A) wt$_{pilE24\ green}$ (Ng309), (B) wt$_{pilE17\ green}$ (Ng308), (C) wt$_{pilE32\ green}$ (Ng310), (D) $\Delta pilE_{green}$ (Ng081), (E) wt$^*_{green}$ (Ng105). Scale bar: 10 μm. Additional biological culture replicates can be found in S1 Data.

https://doi.org/10.1371/journal.pbio.3003022.g004

(Fig 1). We predicted that swapping the C-terminal sequence of wt$_{pilE17}$ and wt$_{pilE32}$, which aggregate poorly, with the corresponding sequence of wt*, which aggregates well, could restore strong interactions and aggregation to these variants. The variable knob of wt* PilE is defined approximately by residues T136 to the C-terminus, thus this segment, designated "T136", was used to replace the corresponding C-terminal segments in the wt$_{pilE17}$ and wt$_{pilE32}$ PilE proteins (Fig 5A). These hybrid pilins were predicted by AlphaFold to have very similar folds to that of wt PilE (Fig viii in S1 Text). The hybrid pilins were used to generate filament models that closely resemble the model for the wt T4P (Fig 5B). The hybrid strains were strongly piliated, although the mean T4P number was slightly lower compared to the wt* strain (Fig iv in S1 Text). Rupture forces were determined for the hybrid strains wt$_{pilE17\_T136}$ and wt$_{pilE32\_T136}$ and found to be comparable to the wt* strain (Fig 5C and 5D). Furthermore, these strains aggregate and form spherical colonies (Fig 5E and S1 Data), consistent with the C-

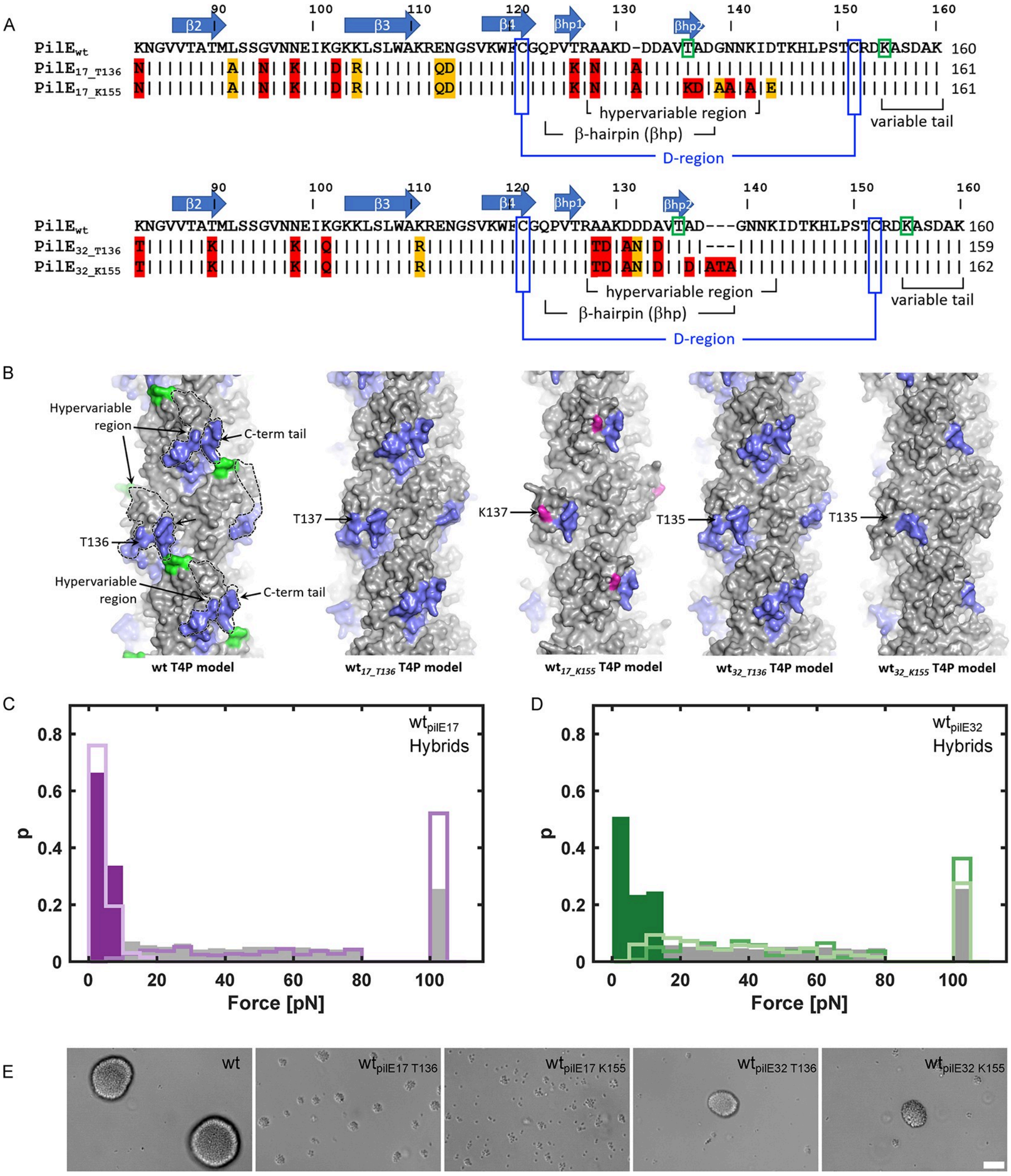

Fig 5. Swapping the C-terminal pilin region restores aggregation. (A) Sequences of the hybrid strains. (B) Alphafold 3 predictions of pilin monomers were used to generate filament models. The regions of PilE$_{wt}$ that were inserted into PilE$_{17}$ and PilE$_{32}$, T136-160 (T136) or K155-160 (K155) are shown in blue. K137 in PilE$_{17\text{-}K155}$ is colored magenta; the corresponding threonines in the other models are indicated. Probability distribution of rupture forces (C), gray: wt* (Ng150), dark purple: wt$_{pilE17}$ (Ng240), purple: wt$_{pilE17\_T136}$ (Ng293), light purple: wt$_{pilE17\_T155}$ (Ng305), and (D) gray: wt* (Ng150), dark green: wt$_{pilE32}$ (Ng230), green: wt$_{pilE32\_T136}$ (Ng295), light green: wt$_{pilE32\_T155}$ (Ng307). (Number of interacting cell pairs: $N_{wt} = 71$, $N_{wtpilE17\_T136} = 45$, $N_{wtpilE17\_K155} = 54$, $N_{wtpilE32\_T136} = 33$, $N_{wtpilE32\_K155} = 42$.) The data underlying this figure can be found in S1 Data. The linearity of the laser trap is limited to 80 pN. All rupture events exceeding this force were grouped into a single bin shown at 100 pN. (E) Typical brightfield images of gonococci in liquid culture. Scale bar: 15 μm. Additional biological culture replicates can be found in S1 Data.

https://doi.org/10.1371/journal.pbio.3003022.g005

terminal segment of PilE defining the strength of pilus:pilus interactions. We note, however, that these colonies had a different size distribution compared to wt* (Fig vii in S1 Text).

Though there is considerable amino acid sequence variability in the C-terminal region of PilE, the C-terminal tail following the conserved disulfide bond is particularly disparate between the aggregating and planktonic strains. While only the last amino acid of the C-terminal tail is different between the aggregating strains wt* and wt_{pilE24}, the tails of wt_{pilE24} and wt_{pilE32} are shorter by several residues and bear no sequence identity to each other or to PilE_{wt} or PilE_{24} (Fig 1A). To determine whether this difference affects pilus:pilus interactions, we generated the *pilE* hybrid strains wt_{pilE17_K155} and wt_{pilE32_K155}, each with their C-terminal residues replaced with residues K155-K160 of PilE_{wt} (Fig 5A and 5B). This replacement did not significantly affect the number of T4P per cell (Fig iv in S1 Text). We tested their pilus rupture forces and aggregative abilities. Whereas the *pilE* hybrid strain wt_{pilE32_K155} showed strong pilus:pilus interactions comparable to wt*, interactions for wt_{pilE17_K155} are considerably weaker (Fig 5C and 5D). wt_{pilE17_K155} showed a stronger tendency to aggregate than wt_{pilE17}, but the contours of the aggregates were not well defined (Fig 5E, S1 Data). wt_{pilE32_K155} formed spherical aggregates whose size distribution was shifted towards intermediate size colonies comprising (100 to 1,000) cells (Fig vii in S1 Text). To understand why the rupture forces of wt_{pilE17_K155} and wt_{pilE17} are comparable, but wt_{pilE17_K155} forms small aggregates, we addressed the question whether wt_{pilE17_K155} interacted more frequently in the double laser trap. We found that the fraction of randomly picked pairs of cells that exhibited pilus:pilus interaction was indeed higher for strain wt_{pilE17_K155} (Fig ix in S1 Text). These results show that the variable tail plays an important role in pilus:pilus interaction and aggregation, but this is not sufficient for restoring aggregation in all pilin variants.

We have previously shown that pilin posttranslational modification can affect pilus:pilus interaction [11,25]. The glycan attached to Ser63 in PilE_{wt}, and likely PilE_{24}, is positioned to impact the size and chemistry of the holes that govern the aggregative property of the T4P. PilE_{17} and PilE_{32} lack the Ser63. Therefore, we addressed the question whether loss of pilin glycosylation inhibits colony formation. To this end, we deleted the gene *pglF* encoding the flippase required for pilin glycosylation [42] and found that the colony phenotype was unchanged in all strains (Fig x in S1 Text). This finding shows that the loss of posttranslational modification at Ser63 is not the reason for loss of interaction of strains wt_{pilE17} and wt_{pilE32}.

In summary, we find that the C-terminal region of the aggregating strain wt*, which defines the knob-hole structure, restores aggregation to both non-aggregating strains wt_{pilE17} and wt_{pilE32}, whereas the hypervariable tail of wt* restores aggregation in only wt_{pilE32}.

Gonococci generating different pilin variants show different growth kinetics

We tested whether the 2 distinct phenotypes, aggregating and planktonic, correlate with bacterial growth. First, we imaged the cells at different time points during growth. The wt* strain formed spherical colonies whose size increased with time due to growth and fusion (Fig 6B). Over time, the wt* colonies formed networks while strain wt_{pilE17} remained planktonic (Fig 6C). We characterized the growth kinetics by determining the colony forming units (CFUs) as a function of time for strains wt* and wt_{pilE17} (Fig 6A). The aggregating strain shows a detectable lag phase, whereas the planktonic strain resumes growth immediately after inoculation. After 2 h, both the planktonic and the aggregating strains exhibit exponential growth. After approximately 10 h, the planktonic strain enters into the stationary phase, while the aggregating strain continued to grow up to 19 h. The growth kinetics of wt_{pilE24} was comparable to wt* and the kinetics of wt_{pilE32} was reminiscent of wt_{pilE17} (Fig xi in S1 Text). To evaluate whether

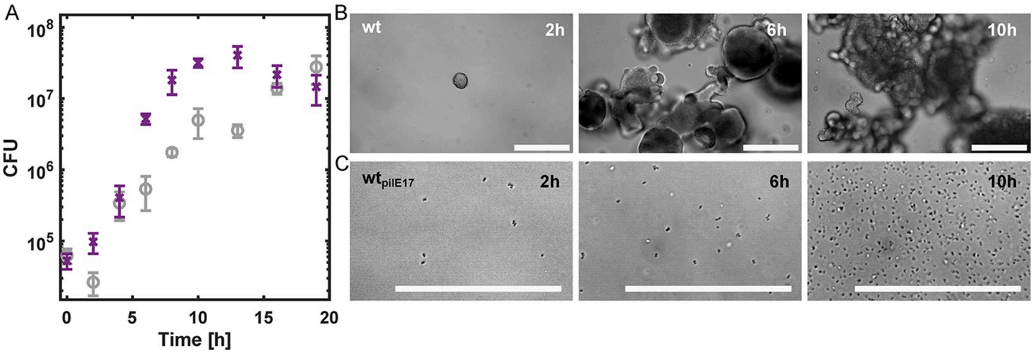

Fig 6. Growth kinetics of planktonic and aggregating strains. (A) CFU of the wt* strain (gray) and the wt$_{pilE17}$ strain (purple). Shown are mean values and standard errors of 3 to 4 biological culture replicates. Typical brightfield images of (B) wt* and (C) wt$_{pilE17}$ populations during growth in liquid culture. Samples were pipetted from the bottom of the microtiter plates and transferred to microscopy plates for imaging. Scale bar: 100 μm.

https://doi.org/10.1371/journal.pbio.3003022.g006

the exponential growth rate depends on the lifestyle, we determined the growth rates of aggregating strains (pooled for wt* and wt$_{pilE24}$) and planktonic strains (pooled for wt$_{pilE17}$ and wt$_{pilE32}$) (Fig xi in S1 Text). The aggregating strains grow at a rate of $r^{aggre.} = 0.67 \pm 0.05\ \mathrm{h}^{-1}$, which is significantly lower than the rate of planktonic strains $r^{plankt.} = 0.92 \pm 0.05\ \mathrm{h}^{-1}$.

It has been reported previously that loss of T4P enhances both the growth rate of *N. gonorrhoeae* [15] and transcription of metabolic genes [43]. This increase can be caused by the fact that pilin generation or pilus biogenesis consumes energy, reducing the growth rate [11] or by the fact that piliated gonococci form colonies in which central bacteria are growth arrested [44]. In this study, all strains are similar in their piliation levels, yet the aggregating wt and wt$_{pilE24}$ demonstrate very different growth behavior from the planktonic wt$_{pilE17}$ and wt$_{pilE32}$. These data indicate that aggregation strongly affects growth.

Antigenic variants of pilin affect antibiotic tolerance but not resistance

Next, we assessed whether variation of *pilE* affects antibiotic susceptibility, i.e., the ability to grow at elevated levels of antibiotics. We determined the minimal inhibitory concentrations (MICs) of antibiotics with different targets, in particular cell wall synthesis (ceftriaxone), DNA gyrase/topoisomerase (ciprofloxacin), and the ribosome (kanamycin) (Fig 7A). Despite the differences in aggregative behavior, there is no significant difference in MICs between the variant strains.

To characterize antibiotic tolerance, i.e., the ability to survive antibiotic concentrations higher than the MIC for extended periods of time, we examined the killing kinetics during treatment with lethal doses of antibiotics. Ceftriaxone is currently recommended for treatment of gonorrhea [45] and, therefore, we started by investigating its effects on survival during the planktonic and microcolony lifestyles. We let gonococci grow for 10 h in liquid media as described above and then added ceftriaxone at 4.8 μg/ml, which is 600× the MIC. The corresponding growth and survival curves in the absence of antibiotic treatment are shown in Fig 6. We found that the planktonic strain wt$_{pilE17}$ was killed significantly faster than the aggregating strain wt* (Fig 7B). To determine whether this difference was caused uniquely by aggregation or whether the T4P per se played a role in tolerance, we characterized the killing kinetics in a *pilE* deletion strain. *ΔpilE* cells were killed slightly but significantly faster than the wt$_{pilE17}$ strain, indicating that T4P or pilin have a protective role against ceftriaxone mediated killing. The killing kinetics of strain wt$_{pilE24}$ was comparable to wt* and that of wt$_{pilE32}$ and was comparable to wt$_{pilE17}$ (Fig 7B).

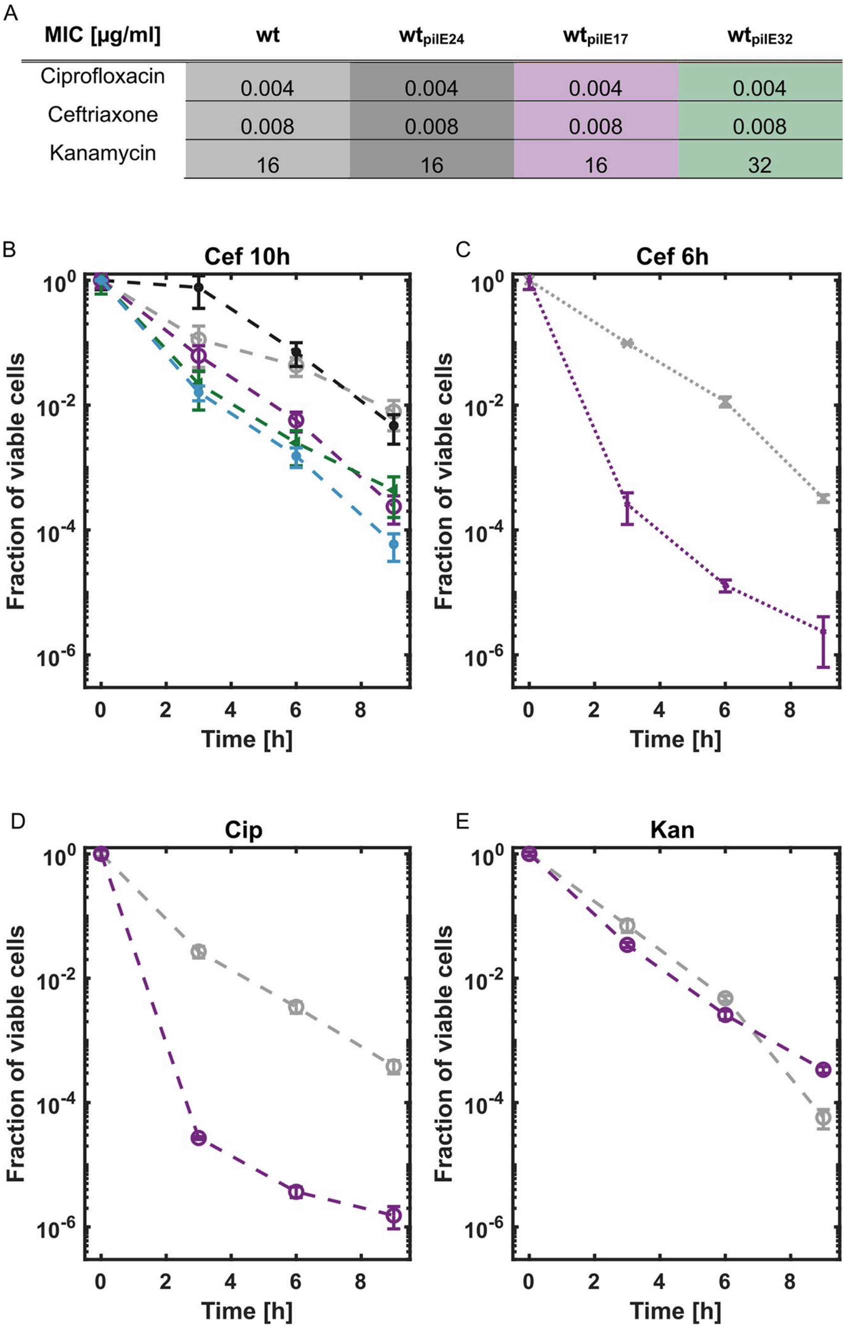

A

MIC [μg/ml]	wt	wt_{pilE24}	wt_{pilE17}	wt_{pilE32}
Ciprofloxacin	0.004	0.004	0.004	0.004
Ceftriaxone	0.008	0.008	0.008	0.008
Kanamycin	16	16	16	32

Fig 7. Effects of microcolony formation on antibiotic resistance and tolerance. (A) MICs for all pilin variants and antibiotic treatments were determined as the modal value from 3 biological culture replicates. (B) Fraction of viable cells (CFU normalized to CFU at the start of treatment) as a function of time during treatment with ceftriaxone (4.8 μg/ml), starting at 10 h of growth. Combined *p*-values (see Methods): $p_{wt\text{-}wt\mathit{pilE24}} = 0.34$, $p_{wt\text{-}wt\mathit{pilE17}} = 8.8 \times 10^{-5}$, $p_{wt\text{-}wt\mathit{pilE32}} = 0.00035$, $p_{wt\text{-}\Delta pilE} = 5.3 \times 10^{-5}$. (C) Fraction of viable cells as a function of time during treatment with ceftriaxone (4.8 μg/ml), starting at 6 h of growth. $p_{wt\text{-}wt\mathit{pilE17}} = 0.00025$. (D) Fraction of viable cells during treatment with ciprofloxacin (2.4 μg/ml). $p_{wt\text{-}wt\mathit{pilE17}} = 8.28 \times 10^{-5}$. (E) Fraction of viable cells during treatment with kanamycin (240 μg/ml). $p_{wt\text{-}wt\mathit{pilE17}} = 0.69$. Gray: wt, dark gray: wt_{pilE24}, purple: wt_{pilE17}, green: wt_{pilE32}, blue: *ΔpilE*. For (B–E), mean and standard error over 3 to 5 biological culture replicates are shown. The data underlying this figure can be found in S1 Data. CFU, colony forming unit; MIC, minimal inhibitory concentration.

https://doi.org/10.1371/journal.pbio.3003022.g007

To verify that the antibiotic concentration is not a limiting factor for killing, we investigated the time-kill kinetics at 3 different ceftriaxone concentrations (2.4 μg/ml, 4.8 μg/ml, and 9.6 μg/ml) and found that the aggregating strains are more tolerant than the planktonic strains independent of the ceftriaxone concentration (Fig viiA–C in S1 Text). Concluding, tolerance is not due to the aggregating cells having a lower antibiotic dose per cell, as their cell density is in fact lower after 10 h of growth than that of the planktonic cells, meaning their antibiotic dose per cell is even higher (Fig 6A). This suggests that we might underestimate the protective effect of aggregation. Since the killing kinetics were qualitatively independent of the antibiotic concentration, we conclude that the antibiotic dose per cell plays a minor role in this assay. Next, we tested whether the growth phase affects the protective effect of aggregation (Fig 7C). We treated the planktonic strain, wt_{pilE17}, and the aggregating strains, wt*, at 6 h of growth, i.e., in the middle of exponential growth with ceftriaxone at 600× MIC (4.8 μg/ml). We observed that the protective effect of aggregation, observed for wt*, was even stronger compared to treatment after 10 h of growth. We conclude that aggregation makes gonococci more tolerant to ceftriaxone treatment while the presence of pilin has a minor effect.

Finally, we addressed tolerance against bactericidal antibiotics with different cellular targets, in particular DNA gyrase/topoisomerase (ciprofloxacin), and the ribosome (kanamycin) at 10 h of growth (Fig 7D and 7E) [46,47]. We tested ciprofloxacin at 600× MIC (2.4 μg/ml) and kanamycin at 15× MIC (240 μg/ml) as the latter is not soluble at concentrations corresponding to 600× MIC. For ciprofloxacin (Fig 7D), the difference between the aggregating and the planktonic strain is even more pronounced than for ceftriaxone, with aggregating wt* exhibiting substantially higher viability than planktonic wt_{pilE17} cells. Notably, the planktonic cells showed a bi-phasic killing curve reminiscent of persister cells [32]. Under kanamycin treatment, the killing kinetics of aggregating and planktonic strains were comparable (Fig 7E). Nonetheless, the observed differences in tolerance to ceftriaxone and ciprofloxacin show that survivability of *N. gonorrhoeae* depends on its pilin antigenic variants, because the variation modulates T4P-mediated aggregation.

Discussion

This study explored the effect of pilin antigenic variation on the biophysical characteristics of the Type 4 pili and its interplay with bacterial survival under antibiotic treatment. We reveal how pilin antigenic variants govern the bacterial lifestyle, as hypermutable pilin variants possess distinct aggregating or planktonic phenotypes. Explicitly, *pilE* aggregative gonococcal variants exhibit a fitness advantage when treated with bactericidal antibiotics ceftriaxone and ciprofloxacin. Our results highlight the close relationship between aggregation and tolerance and suggest that antigenic variation plays an important role in bacterial survival and persistence that extends beyond escaping immune surveillance.

By investigating the pilin sequences of clinical isolates, we found *pilE* variants with distinct pilus functionalities. For example, wt_{pilE17} shows more efficient motility and aggregates less efficiently than wt*. We demonstrate here that these differences are due to T4P stereochemistry and not to piliation levels, in contrast to previous findings [7]. How might stereochemistry support different T4P-mediated functions? We propose that the undulating surface of the pilus allows intimate interactions along its length via protruding knobs formed by the β-hairpins and C-terminal tails inserting into the holes between subunits in adjacent pili. For strong pilus:pilus interactions, these features would need to have stereochemical complementarity. From the structural models, it is clear that amino acid changes in these knobs or holes can profoundly affect their shape and chemistry and thus their complementarity. Thus, an amino acid change on one feature may require a compensatory change on the other for stereochemical complementarity to be maintained. PilE_{wt} and PilE_{24} are most similar in sequence. PilE_{24} differs from PilE_{wt} for a number of surface residues, both at the rim of the hole and on the knob, but since strain wt_{pilE24} is a microcolony former like wt*, these differences are likely compensatory. The knobs of PilE_{wt} and PilE_{24} are somewhat negatively charged, which would complement their positively charged holes, but this could also be said of PilE_{17} and PilE_{32}. Since the latter are not aggregating, it may be that while their knobs and holes are electrostatically complementary their shapes/structures are not. We show here that the C-terminal region, from the β-hairpin through C-terminal tail, defines pilus:pilus interactions, as insertion of this segment, T136, in the non-aggregating strains restores aggregation. A shorter segment corresponding to the C-terminal tail only, restores the high rupture force and aggregation for wt_{pilE32} but is less effective for wt_{pilE17}. Interestingly, PilE in the $\text{wt}_{pilE17\text{-}K155}$ has an exposed lysine, K137, on the β-hairpin, whereas wt* and $\text{wt}_{pilE17\text{-}T136}$, $\text{wt}_{pilE32\text{-}T136}$, and $\text{wt}_{pilE32\text{-}K155}$ all have a threonine at this position (Fig 5B). Kennouche and colleagues found that a charged patch centered on an exposed lysine (K140), which is located in the loop immediately following the β-hairpin, is crucial for aggregation of *N. meningitidis* [17]. By contrast, in our strain $\text{wt}_{pilE17\text{-}K155}$ a single exposed lysine on the β-hairpin is linked to poor aggregation. This comparison shows that it is difficult to ascribe pilus:pilus interaction to single amino acid residues, since pilin antigenic variation generates too much sequence diversity. Importantly, however, both studies show that the highly variable C-terminal region of the pilin is crucial for aggregation.

In this study, we replaced the *pilE* sequence with sequences from clinical isolates. While the *pilS* that determine these structures are similar between the strains (Fig i in S1 Text), we cannot exclude that epistatic effects select for integration of different *pilS* sequences in different strains. For example, multiple genes encoding for T4P related proteins and other surface structures are phase variable [48]. Depending on the presence (or absence) of T4P assembly components and other surface structures, different *pilE* sequences may be selected for during infection. Our study does not account for such epistatic effects, since the *pilE* sequences were exchanged between different strains with different phase varions. In future studies, it will be interesting to address such epistatic effects.

It is widely accepted that biofilm formation leads to higher tolerance against antibiotic treatment [49–51], but the mechanisms causing tolerance are poorly understood. *N. gonorrhoeae* form microcolonies in solution that have properties similar to bacterial biofilms, including a gradient of limited oxygen, of growth, and of tolerance against antibiotics [44,52], and thus allow a systematic characterization of the effects of bacterial aggregation on tolerance. Here, we established stable *N. gonorrhoeae* strains expressing non-aggregative T4P that are otherwise fully functional, thus serving as excellent planktonic control strains. We show that T4P-mediated aggregation has a strong effect on tolerance. For ceftriaxone, we found an order of magnitude increase in the fraction of viable cells when bacteria formed colonies. This effect was robust with respect to the antibiotic concentration and the growth phase. Ceftriaxone is a β-lactam and for this class of antibiotics it has been shown for *E. coli* that the killing rate is inversely correlated with growth rate [53]. Similarly, growth-rate dependent killing rates were reported for *E. coli* treated with ciprofloxacin [49]. Bacteria at the center of gonococcal microcolony are growth arrested [44], and the fraction of dead cells in this location is lower under ceftriaxone treatment compared to the edges of the colonies [27], suggesting that local growth arrest enhances tolerance. Moreover, we propose that the formation of oxygen gradients within gonococcal colonies [52] can protect bacteria residing at the microcolony center where the oxygen concentration is lower. There is evidence that bactericidal antibiotics including ciprofloxacin and ceftriaxone kill bacteria (at least partially) by producing reactive oxygen species [50,51]. Reduced antibiotic penetration is suggested to enhance tolerance [36]. We can exclude this mechanism for our system, since we showed previously that antibiotic treatment causes swelling of the cell body and this effect is homogenous throughout the colonies [27]. Unexpectedly, microcolony formation did not protect gonococci from kanamycin treatment. For early-stage colonies, we found that cells at the center of the colonies are more tolerant to kanamycin than peripheral cells, most likely because cells at the center have lower electrical membrane potential [52]. On the hand, central cells grow more slowly and it has been shown that antibiotics that irreversibly bind the ribosome (like kanamycin) are more effective for slow-growing bacteria [54]. It is unclear, however, whether a similar argument holds for the killing rate at kanamycin concentrations exceeding the MIC. We anticipate that the strains introduced in this study will be useful for studying tolerance against stresses other than antibiotics. For example, it has been shown that piliation protects gonococci from killing by hydrogen peroxide [55,56], antimicrobial peptides [56], and neutrophils [55]. The fully piliated strains with self-aggregating versus non-aggregating properties will allow us to distinguish between protection by self-aggregation and protection by other T4P-related functions.

Based on our results, we propose that pilin antigenic variation has various functions beyond its well-known role in escape from immune surveillance. Within a gonococcal population, antigenic variation rapidly generates a standing variation of different *pilE* sequences with phenotypes that support adhesion, aggregation, twitching motility, or DNA uptake. We have shown that different variants can form colonies comprising different variants that segregate in agreement with the differential strength of adhesion hypothesis [28]. This shows that pilin antigenic variation governs the structural organization within the colonies and we anticipate that it impacts the efficiency of horizontal gene transfer across different variants. While the generation of variations is likely random, variants with different phenotypes are selected for during infection by the host environment. Here, we showed that these phenotypic changes impact antibiotic tolerance and, therefore, antigenic variation plays a key role in microcolony diversification, infection, and treatment of gonorrhea.

Materials and methods

Growth conditions

We used the same growth conditions described in previous studies [27]. Gonococcal base agar was made from 10 g/l dehydrated agar (BD Biosciences, Bedford, MA), 5 g/l NaCl (Roth, Darmstadt, Germany), 4 g/l K_2HPO_4 (Roth), 1 g/l KH_2PO_4 (Roth), 15 g/l Proteose Peptone No. 3 (BD Biosciences), 0.5 g/l soluble starch (Sigma-Aldrich, St. Louis, MO), and supplemented with 1% IsoVitaleX (IVX): 1 g/l D-glucose (Roth), 0.1 g/l L-glutamine (Roth), 0.289 g/l L-cysteine-HCL x H_2O (Roth), 1 mg/l thiamine pyrophosphate (Sigma-Aldrich), 0.2 mg/l Fe $(NO_3)_3$ (Sigma-Aldrich), 0.03 mg/l thiamine HCl (Roth), 0.13 mg/l 4-aminobenzoic acid (Sigma-Aldrich), 2.5 mg/l β-nicotinamide adenine dinucleotide (Roth), and 0.1 mg/l vitamin B12 (Sigma-Aldrich). GC medium is identical to the base agar composition but lacks agar and starch.

Bacterial strains

All strains used in this study (Table i in S1 Text) were derived from the *opa*- selected VD300 strain [57] and carry a deletion of the G4 motif required for pilin antigenic variation [58]. Colonies were grown overnight on agar plates and each colony used for the experiments was inspected using a stereomicroscope to ensure that it maintained its *opa*- phenotype.

Clinical isolates NG17, NG24 were cultured from urethral swabs in 2016 and NG32 in 2017, from male patients presenting with urethritis. After identification and susceptibility testing, they were stored in glycerol at −80˚C. Isolates were recovered from the freezer by plating out on chocolate agar for the purpose of this study.

First, clinical isolates were transferred back into the piliated state as described in the following. We grew bacterial cells for 1 day in liquid medium (37˚C and 5% CO_2) without shaking. The next day, we transferred bacteria growing at the surface with a loop to fresh GC-media. This process was repeated until a pellicle at the surface was formed. Then, we plated the pellicle on GC agar plates. Piliated phenotypes were chosen according to the colony morphology and testing for twitching motility.

To determine the sequence of the *pilE* variants, we performed a PCR with primers sk5 and sk34 on the respective gDNA (isolated with the Blood and Tissue Kit, Qiagen). The PCR product was sequenced with primer $\text{pilE}_{\text{IWupstream}}$ (Eurofins).

Construction of *pilE* variant strains

In order to construct isogenic strains that differ solely in the *pilE* sequence, the *pilE* sequences of the clinical isolates were cloned into the ΔG4 background strain (Ng150, derivative of MS11, [59]) replacing the native *pilE* gene. To avoid further genetic modification, the *pilE* genes were introduced by *ermC-rpsL*$_s$ based clean insertion as described [18].

The process for the construction was identical for strains $\text{wt}_{\text{pilE17}}$, $\text{wt}_{\text{pilE24}}$, and $\text{wt}_{\text{pilE32}}$ except for the respective primers. First, the 5′ UTR region of *pilE* was amplified from gDNA of strain Ng150 using primers sk159 and sk160 (Table iii in S1 Text). Second, the *pilE* gene was amplified from gDNA of the different clinical isolates NG17, NG24, and NG32 with primers sk161 and sk175, sk161 and sk167, and sk161 and sk162, respectively. Third, the 3′ UTR of *pilE* including the *ermC-rpsL*$_s$ was amplified from gDNA of strain Ng225 using primers sk163 and sk158. The 3 PCR products were fused and the final product was spot transformed into strain Ng150. After selection on erythromycin, insertions were controlled via screening PCR with primers sk32 and sk45. The respective strains were named *ΔG4 pilE*NG17/24/32 clean insertion step 1 (Ng239, Ng241, Ng229, respectively).

Next, the fusion construct for the counter selection was generated. To this end, the 5′ UTR region including the newly introduced *pilE* genes was amplified from gDNA of strains *ΔG4 pilE*NG17/32/24 clean insertion step 1 (Ng239, Ng229, Ng241) with primers sk159 and sk176 (Table iii in S1 Text), sk159 and sk168, sk158 and sk165, respectively. The 3′ UTR of *pilE* was amplified from gDNA of strain Ng150 with primers sk164 and sk158. The 2 products were joined in a fusion PCR and transformed into the respective strain of the first step (Ng239, Ng241, Ng229). During selection on streptomycin, the *ermC-rpsL*$_s$ construct is spliced out and the mutants are isogenic to the parental strain (Ng150) except for the *pilE* sequences. Insertions were controlled via screening PCR with primers sk32 and sk45 and subsequently checked via sequencing with primer sk129 (Eurofins). The final strains are referred to as wt_{pilE24} (Ng242), wt_{pilE17} (Ng240), and wt_{pilE32} (Ng230).

Construction of *pilE* hybrid strains

$pilE_{T136}$ hybrids: The N-terminal part of the *pilE* gene of strain wt_{pilE17} (Ng240) and wt_{pilE32} (Ng230) was fused with the C-terminal part of *pilE* of the wt* (Ng150) starting at amino acid T136. In detail, amino acids K137-E160 of $pilE_{17}$ and T135-P158 of $pilE_{32}$ were replaced by T136-K160 of $pilE_{wt}$. To this end, the N-terminal part unil K137 of $pilE_{17}$ and T136 $pilE_{32}$ including 567 bp upstream were amplified from wt_{pilE17} (Ng240) or wt_{pilE32} (Ng230) using primers sk384 and sk385 or sk384 and sk388, respectively (Table iii in S1 Text). The T136 C-terminal part including the *ermC rpsL*$_s$ cassette and the downstream part of *pilE* were amplified from strain *T126C step1* (Ng225, [18]) using primers sk386 and sk390 ($pilE_{17}$) or sk389 and sk390 ($pilE_{32}$). Both PCR products were fused with the GXL-polymerase (TaKaRa). The final fusion product was transformed into either wt_{pilE17} (Ng240) or wt_{pilE32} (Ng230). Selection was achieved by plating transformants on agar plates containing erythromycin. Correct insertion was checked via screening PCR (sk5 and sk32) and sequencing (sk5 or sk32). The mutants were named $\mathrm{wt}_{\mathrm{pilE17\_T136}}$ step1 (Ng292) and $\mathrm{wt}_{\mathrm{pilE32\_T136}}$ step1 (Ng294).

For the second step of the clean replacement, the fused *pilE* gene ($pilE_{17\_T136}$ or $pilE_{32\_T136}$) was amplified from the respective first step, either $\mathrm{wt}_{\mathrm{pilE17\_T136}}$ step1 (Ng292) or $\mathrm{wt}_{\mathrm{pilE32\_T136}}$ step1(Ng294) using primers sk384 and sk131. The downstream region of *pilE* was amplified with primers sk132 and sk390 from wt* (Ng150). The PCR products were fused with the GXL-polymerase and the fusion product was transformed in either $\mathrm{wt}_{\mathrm{pilE17\_T136}}$ step1 (Ng292) or $\mathrm{wt}_{\mathrm{pilE32\_T136}}$ step1(Ng294). Afterwards, the strains were selected on streptomycin. Correct insertion was checked via screening PCR and sequencing with primers sk5 and sk32. The new strains were named $\mathrm{wt}_{\mathrm{pilE17\_T136}}$ (Ng293) or $\mathrm{wt}_{\mathrm{pilE32\_T136}}$ (Ng295).

$pilE_{K155}$ hybrids: The C-terminal tail of the *pilE* gene of strains wt_{pilE17} (Ng240) and wt_{pilE32} (Ng230) were replaced with the C-terminal tail starting at K155 of *pilE* of strain wt* (Ng150). The *ermC-rpsL*$_s$ cassette was amplified from strain *T126C* step1 [18] and fused with the corresponding *pilE* upstream and downstream regions. The fusion product was transformed into either wt_{pilE17} (Ng240) or wt_{pilE32} (Ng230) and selected on erythromycin.

The $pilE_{17/32}$ gene including 567 bp upstream were amplified from wt_{pilE17} (Ng240) or wt_{pilE32} (Ng230) using primers sk384 and sk391 or sk384 and sk393, respectively (Table iii in S1 Text). The K155 C-terminal tail including the *ermC rpsL*$_s$ cassette and the downstream part of *pilE* were amplified from strain *T126C* step1 (Ng225) using primers sk392 and sk390 (NG17) or sk394 and sk390 (NG32). Both PCR products were fused with the GXL-polymerase (TaKaRa). The final fusion product was transformed into wt_{pilE17} (Ng240) or wt_{pilE32} (Ng230) and after transformation selection was performed on plates containing erythromycin. Correct insertion was checked via screening PCR with primers sk5 and sk32 and sequencing (sk5 or sk32) resulting in strains $\mathrm{wt}_{\mathrm{pilE17\_K155}}$ step1 (Ng304) and $\mathrm{wt}_{\mathrm{pilE32\_K155}}$ step1(Ng306).

For the second step of the clean replacement, the hybrid *pilE*s were amplified from the respective first step $\mathrm{wt}_{\mathrm{pilE17\_K155}}$ (Ng304) or $\mathrm{wt}_{\mathrm{pilE32\_K155}}$ step1 (Ng306). Primers sk384 and sk131 ($\mathrm{wt}_{\mathrm{pilE17\_K155}}$) and primer sk384 and sk395 ($\mathrm{wt}_{\mathrm{pilE32\_K155}}$) were used. The downstream region of *pilE* was amplified with primers sk132 and sk390 from wt* (Ng150). The PCR products were fused with the GXL-polymerase (TaKaRa) and the fusion product was transformed in either $\mathrm{wt}_{\mathrm{pilE17\_K155}}$ step1 (Ng304) or $\mathrm{wt}_{\mathrm{pilE32\_K155}}$ step1 (Ng306). Then, the strains were selected on streptomycin. Correct insertion was checked via screening PCR and sequencing (sk5 or sk32) and the strains were named $\mathrm{wt}_{\mathrm{pilE17\_K155}}$ (Ng305) and $\mathrm{wt}_{\mathrm{pilE32\_K155}}$ (Ng307).

Construction of *ΔpglF* strains

Deletion of the flippase *pglF* strongly reduces pilin glycosylation by interrupting the membrane translocation of lipid-attached carbohydrates [42]. To delete *pglF*, the respective strains were transformed with genomic DNA of strain Ng156 and selected on kanamycin [11].

Construction of *gfp* expressing strains

Genomic DNA of strain Ng105 [11] was used for transformation to insert GFP into the chromosome of the respective strains, generating strains $\mathrm{wt}_{pilE24\ green}$ (Ng309), $\mathrm{wt}_{pilE17\ green}$ (Ng308), and $\mathrm{wt}_{pilE32\ green}$ (Ng310) (Table i in S1 Text). Transformants were selected on plates containing erythromycin.

Construction of *ΔpilE strain*

The *pilE* gene was interrupted with a kanamycin resistance cassette. Three individual DNA fragments were amplified via PCR and fused; 5′ *pilE* including the upstream *pilE* region was amplified with primers sk45 and sk46 from gDNA of strain Ng150. *kanR* was amplified with primers sk47 and sk48 from genomic DNA of strain Ng052 [60]; 3′ *pilE* and the downstream region of *pilE* was amplified using primers sk49 and sk50. The PCR products were fused and the fusion construct was transformed into wt* strain. Transformants were selected on kanamycin.

Identification of *pilS* copies in genomes of gonococcal clinical isolates

To verify that the *pilE* variants are products of pilin antigenic variation, we first determined the *pilS* copies in the genome of the clinical isolates. *pilS* were identified using annotated *pilS* copies of strain *N. gonorrhoeae* MS11 (NCBI, CP003909.1) as reference. End and start sites of *pilS* copies were determined either by matching blast results using the SnapGene software (www.snapgene.com) or blastn (BLAST, NCBI) of the respective MS11 orthologs. The blast results were verified manually by identifying the conserved cysteine regions *cys1* and *cys2* in each *pilS* copy. The sequence identity of *pilS* copies from clinical isolates to *pilS* copies from strain *N. gonorrhoeae* MS11 were obtained *via* blastn (BLAST, NCBI).

Twitching motility analysis

We let the strains grow for 12 to 16 h on GC agar plates. We picked a few colonies, resuspended them in liquid GC medium, transferred them to a BSA coated coverslip (1 mg/ml), and then sealed the sample with Valep (Vaseline, wool fat and paraplast in a ratio of 1:1:1). Subsequently, we recorded videos with a confocal Ti-E inverted microscope (Nikon) equipped with a thermobox at 37°C with a framerate of 10 Hz and 100× magnification over 30 s. We stopped each measurement after 15 min to ensure constant experimental conditions. All strains were characterized in biological culture replicates on at least 3 different days.

Next, we tracked each bacterium over the whole measurement time. From each track, we calculated the MSD from the displacements $\delta(\tau) = |\vec{r}(t+\tau) - \vec{r}(t)|$ [61]. As the bacteria follow a corrleated random walk, we fitted $< \delta^2(\tau) >= 2\tau_c v^2(\tau - \tau_c(1 - e^{(-\tau/\tau_C)}) + A$ for the first 5 s to determine the correlation time τ_c and velocity v to the data of a single track (Fig vi in S1 Text). The variable A accounts for the tracking error. We took the mean and standard variation of the fit parameters to determine the average correlation time τ and velocity v_{corr} for the *pilE* variants. Statistical analysis of the distributions of the fit parameters for single bacteria tracks was performed via the Mann–Whitney U test.

Transmission electron microscopy and determination of T4P number

Bacteria grown overnight on GC agar plates were resuspended in liquid medium and adjusted to an optical density (OD_{600}) of 0.1. For sample preparation, 10 μl of the bacterial solution was transferred on a 100 mesh formvar coated copper grid (Science Services) and incubated for 20 min at room temperature. For fixation, the grid was put upside down in a drop of 2% formaldehyde (Science Services) and incubated for 5 min, followed by 5 times washing in PBS. Next, the mesh was placed on a drop of 1% glutaraldehyde (Sigma) for 5 min and washed 8 times in Milli-Q water. The samples were blotted on filter paper. For negative staining, the cells were again incubated with 10 μl of uranyl acetate for 4 min and the spill-over was removed by filter paper. Then, they were imaged in a transmission electron microscope (JEM-2100Plus (JEOL)) in the imaging facility of the CECAD, Cologne. All images were taken at 6,000× magnification at 40 μm under the default focus at room temperature. Pili were counted manually. Only pili that could be assigned to a single cell were considered. If single pili were not distinguishable within T4P bundles, they were counted as one pilus. All strains were characterized in biological culture replicates on 1 to 3 different days.

Generation of PilE and pilus models

AlphaFold [39] was used to generate models of $\mathrm{PilE_{wt}}$ and the PilE varients. Models were superimposed upon Chain A of the *N. gonorrhoeae* T4P cryoEM reconstruction [40] in Chimera (Petterson and colleagues, PMID 15264254) and residues 1–48 of the model were replaced with that of Chain A to replace the continuous α1-helix of the AF models with the melted helix seen in the filament. The helical symmetry parameters of *N. gonorrhoeae* T4P (10.1 Å rise, 100.8˚ rotation) were imposed on the PilE models to generate 18-mer filament models. Electrostatic potential was generated using the APBS tool of PyMol [62].

Confocal microscopy

Bacteria grown overnight on GC agar plates were resuspended in GC liquid media to an optical density of $\mathrm{OD_{600}}$ 0.1. Then, cells were mixed in a 1:1 ratio and vortexed vigorously. Subsequently, the bacterial solution was incubated for 45 min in a shaking incubator (37˚C, 250 rpm, 5% CO_2) to let the cells aggregate. Next, 300 μl of the suspension was transferred into a Poly-L-lysine coated (Sigma, final concentration: 0.005%) Ibidi treat 8-well plate. All images were acquired using an inverted microscope (Ti-E, Nikon) equipped with a thermo box (37˚C) and a spinning disk unit (CSU-1, Yokogawa) with 100× magnification, 1.49 NA, oil immersion objective lens. The excitation wavelengths were 488 nm and 560 nm. Three-dimensional z-stacks with a plane-to-plane distance of 0.2 μm and an overall height of 10 to 12 μm were acquired for 3D images. All mixtures were characterized in biological culture replicates on at least 3 different days.

Acquisition of brightfield images

Brightfield images of cells were recorded with an inverted Nikon Eclipse Ti with an ORCA camera model (40× magnification). After different time periods, 300 μl of growing cell cultures were transferred into an Ibidi 8-well plate attached to cover glass and were imaged directly.

To verify microcolony formation in liquid culture, cells grown overnight on GC agar plates were adjusted to an optical density of 0.1 in GC media, and 100 μl of this culture was transferred into 200 μl GC media in an Ibidi 8-well plate attached to a cover glass. Then, the cells were incubated for up to 1.5 h (37˚C, 5% CO_2) before imaging.

Distribution of aggregate sizes

The distribution of aggregate sizes was determined by incubating the respective strains at an initial $\mathrm{OD_{600}}$ of 0.033 in an Ibidi 8-well plate attached to a cover glass for 1 h and imaging using brightfield imaging (Fig vii in S1 Text). Aggregates were segmented using the Fiji segmentation tool and the radius was determined from the area of the segments assuming that aggregates were spherical. Strains wt_{pilE17}, wt_{pilE32} did not form aggregates. Strain $\mathrm{wt}_{pilE17K155}$ had a stronger tendency to aggregate than wt_{pilE17}, but the aggregates did not show clearly defined colony shapes, and therefore, we did not attempt to determine the radii of these aggregates (Fig 5E). Therefore, these 3 strains were excluded from the analysis. All strains were characterized in biological culture replicates on at least 3 different days.

We estimated the number of cells per aggregate $N = \Phi V_{agg}/V_{bacterium}$ assuming that the aggregates are spherical and that the bacteria are spheres with a radius of 0.5 μm. The volume fraction of gonococci is $\Phi \approx 0.5$ [63].

Dual laser tweezers experiments

The interaction forces of *pilE* variants were determined via a dual laser trap. The experimental setup and analysis is already published [22]. In short, we resuspended a few bacterial colonies from overnight GC agar plates in liquid GC medium. We added 1:1,000 ascorbic acid (500 mM). Next, we inoculated the bacteria on a BSA coated cover slip (1 mg/ml) and sealed the slide with VALEP (Vaseline, wool fat and paraplast in a ratio of 1:1:1). The major building blocks of the laser tweezers setup consist of a microscope equipped with a thermo-box at 33˚C, an IR-laser (1,064 nm) and an acousto-optical deflector which creates 2 time-shared optical potentials. The trap distance was set to 2.64 μm. We acquired videos of interacting bacteria with a framerate of 50 Hz. After 15 min, we stopped the measurement as we observed decreased activity of the gonococci. All strains were characterized in different samples on at least 3 different days.

We detected the displacements d of the bacteria from the equilibrium positions via a Hough transformation algorithm. From the displacement tracks, we determined the forces ($F \sim d$) and identified the interaction states, as described earlier in [22]. The potential of each trap was approximated to be harmonic for forces up to 80 pN.

At 100% laser intensity, the traps showed a trap stiffness of $k_{100\%} = 0.1$ pN/nm, whereby the laser intensity I is proportional to the stiffness of the trap $k \sim I$. We note that it was not possible to conduct the experiments with the same laser intensities for all variants, since deflections of the wt_{pilE32} and wt_{pilE17} strains were infrequent. This indicated that these 2 strains have lower interaction forces as they could not overcome the trapping potential of the traps at 100% laser power. Therefore, we adjusted the intensities of the laser. The measurements for the wt* and wt_{pilE24} could be performed at 100% laser power while for the other variants, the laser intensity needed to be decreased to 10% for strain wt_{pilE32} and to 5% for strain wt_{pilE17}. Under these conditions, the probability of pilus:pilus binding (Fig ix in S1 Text) was high enough for characterizing T4P mediated attractive forces.

Bacterial growth curves

Bacterial growth and aggregation were monitored by measuring the OD600 with an Infinite M200 plate reader. After 12 to 14 h on GC-agar plates, bacteria were resuspended in liquid GC medium and adjusted to an optical density OD_{600} of 0.1. For each time point and each condition, a 48-well plate (Greiner), containing 1 ml liquid GC media, was inoculated with 10 μl of the bacterial suspension. We incubated the bacteria at 37˚C, 5% CO_2 with a shaking period of 2 min per OD cycle, and measured the OD every 10 min. All strains were characterized in biological culture replicates on at least 3 different days.

To determine the number of CFUs during 19 h of growth, we performed the same protocol as described above and additionally transferred a whole well to a 1.5 ml reaction tube every 1 to 3 h. Next, we harvested the bacteria by centrifugation (5,000 g, 3 min) and resuspended them in 500 μl GC media. Subsequently, we vortexed for 30 s and added 500 μl of MQ-water to initiate the disassembly of gonococcal aggregates. Then, we again vortexed the suspension for 2 min. The prolonged time of vortexing was already shown to be sufficient to shear pili [64]. Additionally, we ensured reproducibility for each strain and for strains showing the same lifestyle. We performed 1:10 dilution series with vortexing inbetween and plated 50 μl of different dilutions on non-selective GC agarplates. After 48 h of growth (37˚C with 5% CO_2), we counted the CFUs.

To determine the growth rates, we plotted the growth curves from 2 h to 8 h. Then, we performed a linear regression *fitlm* for the log-plotted data via *Matlab* [61]. The slopes are defined as the growth rates. The significance analysis was performed via a pairwise ANOVA test for the linear regression models which includes an interaction term for the different *pilE* variant strains [61].

MIC determination

The minimal inhibitory concentration of the different antibiotics (ceftriaxone, ciprofloxacin, and kanamycin) was determined for each strain, and 1 ml cultures supplemented with increasing antibiotic concentrations were inoculated with approximately $5{\cdot}10^5$ cells of the following strains, wt* (Ng150), wt_{pilE24} (Ng242), wt_{pilE17} (Ng240), and wt_{pilE32} (Ng230). Bacteria were grown in an Infinite M200 plate reader at 37˚C, 5% CO_2 with a shaking period of 2 min per OD cycle. The lowest concentration of an antibiotic without detectable growth (OD600 nm ≤ 0.1) after 24 h was determined as the MIC of the respective antibiotic. All strains were characterized in biological culture replicates on at least 3 different days.

Bacterial survival assay

To investigate how antigenic variation impacts bacterial survival under antibiotic treatments, we developed a survival assay. Isolates were initially grown as described for the bacterial growth curves. Following resuspension in GC media, we let the bacteria grow for 10 h in an Infinite M200 plate reader at 37˚C, 5% CO_2 with a shaking period of 2 min per OD cycle. If other pre-growth durations were used, we indicated this in the figure and description for the specific experiments. OD was measured every 10 min. Next, we added antibiotics to each well except the control wells, and the plate was further incubated. The final concentrations of ceftriaxone were 2.4/4.8/9.6 μg/ml corresponding to the 300× MIC/600× MIC/1,200× MIC, respectively. For ciprofloxacin treatment, we added antibiotics to a final concentration of 2.4 μg/ml, and for kanamycin, the concentration was 240 μg/ml, corresponding to 600× MIC and 15× MIC, respectively. The solubility of kanamycin was too low to increase the antibiotic concentration. To determine the number of viable bacteria, cells were plated at 0 h, 3 h, 6 h, and 9 h after antibiotic treatment as described before (Methods: Bacterial growth curves). All strains were characterized in biological culture replicates on at least 3 different days.

Statistical analysis of the killing kinetics was performed via a combined *p*-values method for discrete data [65]. We have used the Mann–Whitney U test to compare single time points followed by the combination of the *p*-values via Mudholkar and George combining method [66].

Supporting information

S1 Text. Supplementary Figures and Supplementary Tables. Fig i. Sequence identity of *pilS* copies from gonococcal clinical isolates to orthologs from *N. gonorrhoeae* MS11. The sequence identity of each *pilS* to the respective copy of strain MS11 was determined using blastn (BLAST, NCBI). gray: $pilS_{24}$, orange: $pilS_{17}$, red: $pilS_{32}$. **Fig ii. Mapping of different *pilS* to *pilE* variants.** Each *pilS* copy of the clinical isolate was aligned against the respective *pilE* variant (black: $pilE_{wt^*}$, dark gray: $pilE_{24}$, red: $pilE_{32}$, orange: $pilE_{17}$). *pilS* sequences with 100% identity and at least 6 bp in length are shown. The alignments are ordered by the length of the matching sequence, e.g., the longest matching alignment for each position within *pilE* is directly underneath the *pilE* sequence. Only the 3 best matches are shown for each *pilE* variant. The illustrations were created with SnapGene software (www.snapgene.com). pilS5_extended: extended *pilS5* sequence including the conserved *cys2* region. **Fig iii. Model of the charge densities**. The charge density was simulated via PyMol and the APBS tool [62,69]. Models of wt* and variant pilus filaments are shown from the top and side in surface representation with electrostatic surface potential. Blue: positive charge, red: negative charge. **Fig iv. Pilus number per cell for *pilE* variants**. The pili numbers were determined from TEM images. Box plots show the median (central mark), bottom and top patches show 25th and 75th percentiles, respectively. Outliers are plotted individually (red + symbol) and are defined as values which are larger than 1.5 times the interquartile range from the bottom or top of the box, which corresponds to 99.3 percent coverage if the data is normally distributed, according to the Matlab function *boxplot* [61] which was used here. The whiskers length is defined as the maximum and minimum excluding the outliers. *P*-values were determined via a rank-sum test: $p > 0.05$ for wt*, wt_{pilE24}, wt_{pilE17}, wt_{pilE17_K155}, and wt_{pilE32_K155}, $p < 0.05$ for wt_{pilE32}, wt_{pilE17_T136}, and wt_{pilE32_T136}. Number of analyzed bacteria: $N_{wt^*} = 37$, $N_{wtpilE24} = 33$, $N_{wtpilE17} = 16$, $N_{wtpilE32} = 25$, $N_{wtpilE17\_K155} = 18$, and $N_{wtpilE32\_K155} = 18$, $Nwt_{pilE17\_T136} = 27$, and $N_{wtpilE32\_T136} = 19$. The data underlying this figure can be found in S1 Data. **Fig v. Correlation time and velocity of twitching motility of *pilE* variant strains**. (A) Correlation time of motile cells on a BSA coated coverslide. (B) Velocity of twitching motility. Significance analysis via Mann–Whitney U test compared to the wt*, star: $p < 0.05$. Error bars: 95% confidence bounds from fit to correlated random walk model (Fig vi in S1 Data). The data underlying this figure can be found in S1 Data. **Fig vi. Mean squared displacement (MSD) for all tracks of single cells on a BSA-coated cover slide**. Strains (A) wt* (Ng150), (B) wt_{pilE24} (Ng242), (C) wt_{pilE17} (Ng240), (D) wt_{pilE32} (Ng230). The MSD was fitted for the time interval of the first 5 s. Gray: trajectories of individual cells, red line: MSD model with fit parameters averaged from single MSD fits to single tracks of bacteria. $N = 46$–200 trajectories per strain. The data underlying this figure can be found in S1 Data. **Fig vii. Distributions of aggregate size after 1 h of incubation with initial $\mathbf{OD_{600}}$ of 0.033**. (A) Cumulative probability distribution p of aggregate radius r_{agg} with $r_{agg} \geq 2\mu m$. (B) Estimated fraction of cells that reside within colonies comprising light gray: $N<100$ cells, gray: $10<N<1{,}000$ cells, black: $N>1{,}000$ cells. Shown are only the the strains that form aggregates with well-defined contours. The data underlying this figure can be found in S1 Data. **Fig viii. Sequence alignment and structure predictions for PilE hybrids**. (A) Sequence alignment of the C-terminal regions. (B) Pilin models were generated using AlphaFold. PilE_{17_T136} (green) and PilE_{32_T136} (orange) superimposed on PilE_{wt}. PilE_{17_K155} (green) and PilE_{32_K155} (orange) superimposed on PilE_{wt}. **Fig ix. Fraction of successful attempts in dual trap assay**. We counted the fraction of interacting bacteria pairs because not every pair of bacteria showed interaction. This fraction strongly depends on the trap stiffness which was set to (A) $k \approx 0.1$ pN/nm for wt*, wt_{pilE24}, wt_{pilE17_T136}, wt_{pilE32_T136}, and wt_{pilE32_K155}. Since interactions were nearly undetectable at $k = 0.1$ pN/nm for strains wt_{pilE32}, wt_{pilE17} and wt_{pilE17_K155}, the stiffnesses were reduced to $k = 0.005$ pN/nm (light red) and $k \approx 0.01$ pN/nm (10%), respectively. Number of trapped bacteria pairs: $N = (73$–$170)$. Error bars: standard error over different days. The data underlying this figure can be found in S1 Data. **Fig x. Pilin glycosylation does not impact the colony phenotype of PilE variants**. Representative images of PilE variants in a Δ*pglF* background. (A) wt* Δ*pglF* (Ng156), (B) wt_{pilE24} Δ*pglF* (Ng312), (C) wt_{pilE17} Δ*pglF* (Ng311), (D) wt_{pilE32} Δ*pglF* (Ng313). Scale bar: 50 μm. **Fig xi. Growth rates for strains wt* (Ng150), $\mathbf{wt}_{pilE24}$ (Ng242), $\mathbf{wt}_{pilE17}$ (Ng240), $\mathbf{wt}_{pilE32}$ (Ng230)**. (A) Growth curves for all *pilE* variants from counting colony forming units. $N = 3$–4. Error bars: standard errors. (B, D) Linear regression fits to logarithmic data of CFU counts of each strain or pooled data regarding the lifestyle: planktonic or aggregating. (C, D) Growth rates determined from fits in (B) and (D), respectively. Error bars: errors of the fits. ANOVA test of the linear regression model indicated no significant difference between the growth rates of the individual strains with $p_{wt\text{-}wtpilE24} = 0.995$, $p_{wt\text{-}wtpilE17} = 0.071$, $p_{wt\text{-}wtpilE32} = 0.074$ but significant differences for pooled data $p_{aggreg.\text{-}planktonic} = 0.0074$. The data underlying this figure can be found in S1 Data. **Fig xii. Survival assay with different concentrations of ceftriaxone after 10 h of growth**. Killing kinetics of all variants, gray: wt*, dark gray: wt_{pilE24}, purple: wt_{pilE17}, and green: wt_{pilE32}, for (A) 300× MIC, combined *p*-values (see Methods): $p_{wt\text{-}wtpilE24} = 0.63$, $p_{wt\text{-}wtpilE17} = 0.00029$, $p_{wt\text{-}wtpilE32} = 0.0011$; (B) 600× MIC, $p_{wt\text{-}wtpilE24} = 0.35$, $p_{wt\text{-}wtpilE17} = 8.8\times10^{-5}$, $p_{wt\text{-}wtpilE32} = 0.00035$; (C) 1,200× MIC. $p_{wt\text{-}wtpilE24} = 0.99$, $p_{wt\text{-}wtpilE17} = 0.0038$, $p_{wt\text{-}wtpilE32} = 0.0013$. Shown are mean and standard error over 3 to 4 biological culture replicates. The data underlying this figure can

be found in S1 Data. **Table i. Strains used in this study. Table ii. Amino acid sequence identities of complete and partial regions of *pilE* compared to the MS11 *pilE* amino acid sequence according to Fig 1. The amino acid sequences were compared using BLAST [70]. Table iii. Primers used in this study**.
(PDF)

S1 Data. Data used for generating the figures. The data sheet contains the data used for generating Figs 3B, 5C,D, 6A, 7, and Figs iv, v, vi, vii, ix, xi, and xii in S1 Text and additional micrographs for Figs 3C, 4, and 5E.
(XLSX)

Acknowledgments

We thank the CECAD Imaging Facility (and Felix Gaedke) for their support (in microscopy/technique/data analysis) and Rosalind Allen, Isabel Rathmann, Stephan Wimmi, Gerrit Ansmann, and the Maier group for helpful discussions.

Author Contributions

Conceptualization: Isabelle Wielert, Sebastian Kraus-Römer, Lisa Craig, Paul G. Higgins, Berenike Maier.

Formal analysis: Isabelle Wielert, Sebastian Kraus-Römer.

Funding acquisition: Paul G. Higgins, Berenike Maier.

Investigation: Isabelle Wielert, Sebastian Kraus-Römer, Thorsten E. Volkmann, Lisa Craig.

Methodology: Isabelle Wielert, Sebastian Kraus-Römer, Lisa Craig.

Project administration: Berenike Maier.

Resources: Paul G. Higgins.

Software: Isabelle Wielert, Lisa Craig.

Supervision: Berenike Maier.

Visualization: Isabelle Wielert.

Writing – original draft: Isabelle Wielert, Sebastian Kraus-Römer, Lisa Craig, Berenike Maier.

Writing – review & editing: Isabelle Wielert, Sebastian Kraus-Römer, Lisa Craig, Paul G. Higgins, Berenike Maier.

References

1. Burrows LL. Pseudomonas aeruginosa twitching motility: type IV pili in action. Annu Rev Microbiol. 2012; 66:493–520. https://doi.org/10.1146/annurev-micro-092611-150055 PMID: 22746331
2. Craig L, Forest KT, Maier B. Type IV pili: dynamics, biophysics and functional consequences. Nat Rev Microbiol. 2019; 17(7):429–440. https://doi.org/10.1038/s41579-019-0195-4 PMID: 30988511
3. Swanson J, Robbins K, Barrera O, Corwin D, Boslego J et al. Gonococcal pilin variants in experimental gonorrhea. J Exp Med. 1987; 165(5). Available from: https://pubmed.ncbi.nlm.nih.gov/3106555/. https://doi.org/10.1084/jem.165.5.1344 PMID: 3106555
4. Criss AK, Kline KA, Seifert HS. The frequency and rate of pilin antigenic variation in Neisseria gonorrhoeae. Mol Microbiol. 2005; 58(2):510–519. Available from: https://onlinelibrary.wiley.com/doi/10.1111/j.1365-2958.2005.04838.x. PMID: 16194236

5. Fernandez-Martinez D, Kong Y, Goussard S, Zavala A, Gastineau P et al. Cryo-EM structures of type IV pili complexed with nanobodies reveal immune escape mechanisms. Nat Commun. 2024; 15(1):1–15. Available from: https://www.nature.com/articles/s41467-024-46677-y.
6. James JF, Swanson J Studies on gonococcus infection. XIII. Occurrence of color/opacity colonial variants in clinical cultures. Infect Immun. 1978; 19(1). Available from: https://pubmed.ncbi.nlm.nih.gov/415007/. https://doi.org/10.1128/iai.19.1.332-340.1978 PMID: 415007
7. Swanson J, Kraus SJ, Gotschlich EC. Studies on gonococcus infection. I. Pili and zones of adhesion: their relation to gonococcal growth patterns. J Exp Med. 1971; 134(4):886–906. https://doi.org/10.1084/jem.134.4.886 PMID: 4106489
8. Nassif X, Lowy J, Stenberg P, O'Gaora P, Ganji A, et al. Antigenic variation of pilin regulates adhesion of Neisseria meningitidis to human epithelial cells. Mol Microbiol. 1993; 8(4):719–725. Available from: https://onlinelibrary.wiley.com/doi/10.1111/j.1365-2958.1993.tb01615.x. PMID: 8332064
9. Zöllner R, Oldewurtel ER, Kouzel N, Maier B. Phase and antigenic variation govern competition dynamics through positioning in bacterial colonies. Sci Rep. 2017; 7(1):12151. https://doi.org/10.1038/s41598-017-12472-7 PMID: 28939833
10. Obergfell KP, Seifert HS. The Pilin N-terminal Domain Maintains Neisseria gonorrhoeae Transformation Competence during Pilus Phase Variation. PLoS Genet. 2016; 12(5):e1006069. https://doi.org/10.1371/journal.pgen.1006069 PMID: 27213957
11. Oldewurtel ER, Kouzel N, Dewenter L, Henseler K, Maier B, et al. Differential interaction forces govern bacterial sorting in early biofilms. Elife. 2015; 4:e10811. https://doi.org/10.7554/eLife.10811 PMID: 26402455
12. Helm RA, Seifert HS. Pilin antigenic variation occurs independently of the RecBCD pathway in Neisseria gonorrhoeae. J Bacteriol. 2009; 191(18):5613–5621. https://doi.org/10.1128/JB.00535-09 PMID: 19592592
13. Rotman E, Seifert HS. The genetics of Neisseria species. Annu Rev Genet. 2014; 48:405–431. https://doi.org/10.1146/annurev-genet-120213-092007 PMID: 25251852
14. Vink C, Rudenko G, Seifert HS. Microbial antigenic variation mediated by homologous DNA recombination. FEMS Microbiol Rev. 2012; 36(5):917–948. Available from: https://academic.oup.com/femsre/article/36/5/917/660062. https://doi.org/10.1111/j.1574-6976.2011.00321.x PMID: 22212019
15. Ozer EA, Prister LL, Yin S, Ward BH, Ivanov S, et al. PacBio Amplicon Sequencing Method To Measure Pilin Antigenic Variation Frequencies of Neisseria gonorrhoeae. mSphere. 2019; 4(5). https://doi.org/10.1128/mSphere.00562-19 PMID: 31578246
16. Cahoon LA, Seifert HS. Focusing homologous recombination: pilin antigenic variation in the pathogenic Neisseria. Mol Microbiol. 2011; 81(5):1136–1143. Available from: https://onlinelibrary.wiley.com/doi/full/10.1111/j.1365-2958.2011.07773.x. PMID: 21812841
17. Kennouche P, Charles-Orszag A, Nishiguchi D, Goussard S, Imhaus A-F, et al. Deep mutational scanning of the Neisseria meningitidis major pilin reveals the importance of pilus tip-mediated adhesion. EMBO J. 2019; 38(22):e102145. https://doi.org/10.15252/embj.2019102145 PMID: 31609039
18. Kraus-Römer S, Wielert I, Rathmann I, Grossbach J, Maier B. External Stresses Affect Gonococcal Type 4 Pilus Dynamics. Front Microbiol. 2022; 13. https://doi.org/10.3389/fmicb.2022.839711 PMID: 35283813
19. Skerker JM, Berg HC. Direct observation of extension and retraction of type IV pili. Proc Natl Acad Sci U S A. 2001; 98(12):6901–6904. https://doi.org/10.1073/pnas.121171698 PMID: 11381130
20. Marathe R, Meel C, Schmidt NC, Dewenter L, Kurre R et al. Bacterial twitching motility is coordinated by a two-dimensional tug-of-war with directional memory. Nat Commun. 2014; 5(1):3759. https://doi.org/10.1038/ncomms4759 PMID: 24806757
21. Holz C, Opitz D, Greune L, Kurre R, Koomey M, et al. Multiple Pilus Motors Cooperate for Persistent Bacterial Movement in Two Dimensions. Phys Rev Lett. 2010; 104 (17):178104. https://doi.org/10.1103/PhysRevLett.104.178104 PMID: 20482147
22. Welker A, Cronenberg T, Zöllner R, Meel C, Siewering K, et al. Molecular Motors Govern Liquidlike Ordering and Fusion Dynamics of Bacterial Colonies. Phys Rev Lett. 2018; 121(11):118102. https://doi.org/10.1103/PhysRevLett.121.118102 PMID: 30265121
23. Bonazzi D, Lo Schiavo V, Machata S, Djafer-Cherif I, Nivoit P, et al. Intermittent Pili-Mediated Forces Fluidize Neisseria meningitidis Aggregates Promoting Vascular Colonization. Cell. 2018; 174(1):143–155.e16. https://doi.org/10.1016/j.cell.2018.04.010 PMID: 29779947
24. Pönisch W, Weber CA, Juckeland G, Biais N, Zaburdaev V. Multiscale modeling of bacterial colonies: how pili mediate the dynamics of single cells and cellular aggregates. New J Phys. 2017; 19(1):15003. Available from: https://iopscience.iop.org/article/10.1088/1367-2630/aa5483/meta. https://doi.org/10.1088/1367-2630/aa5483 PMID: 34017216

25. Zöllner R, Cronenberg T, Kouzel N, Welker A, Koomey M, et al. Type IV Pilin Post-Translational Modifications Modulate Material Properties of Bacterial Colonies. Biophys J. 2019; 116(5):938–947. https://doi.org/10.1016/j.bpj.2019.01.020 PMID: 30739725

26. Maier B. How Physical Interactions Shape Bacterial Biofilms. Annu Rev Biophys. 2021; 50:401–417. https://doi.org/10.1146/annurev-biophys-062920-063646 PMID: 33637007

27. Cronenberg T, Hennes M, Wielert I, Maier B. Antibiotics modulate attractive interactions in bacterial colonies affecting survivability under combined treatment. PLoS Pathog. 2021; 17 (2):e1009251. https://doi.org/10.1371/journal.ppat.1009251 PMID: 33524048

28. Harris AK. Is cell sorting caused by differences in the work of intercellular adhesion? A critique of the steinberg hypothesis. J Theor Biol. 1976; 61(2):267–285. Available from: https://www.sciencedirect.com/science/article/pii/0022519376900199. https://doi.org/10.1016/0022-5193(76)90019-9 PMID: 985668

29. WHO (2021) Hepatitis, Global Hiv; Sexually Transmitted Infections Programmes. Global progress report on HIV, viral hepatitis and sexually transmitted infections, 2021. World Health Organization. Available from: https://www.who.int/publications/i/item/9789240027077. Accessed 15 February 2023.389Z.

30. Grad YH, Harris SR, Kirkcaldy RD, Green AG, Marks DS, et al. Genomic Epidemiology of Gonococcal Resistance to Extended-Spectrum Cephalosporins, Macrolides, and Fluoroquinolones in the United States, 2000–2013. J Infect Dis. 2016; 214(10):1579–1587. https://doi.org/10.1093/infdis/jiw420 PMID: 27638945

31. Bristow CC, Mortimer TD, Morris S, Grad YH, Soge OO, et al. Whole-Genome Sequencing to Predict Antimicrobial Susceptibility Profiles in Neisseria gonorrhoeae. J Infect Dis. 2023; 227(7):917–925. https://doi.org/10.1093/infdis/jiad027 PMID: 36735316

32. Balaban NQ, Helaine S, Lewis K, Ackermann M, Aldridge B, et al. Definitions and guidelines for research on antibiotic persistence. Nat Rev Microbiol. 2019; 17(7):441–448. Available from: https://www.nature.com/articles/s41579-019-0196-3. https://doi.org/10.1038/s41579-019-0196-3 PMID: 30980069

33. Levin-Reisman I, Ronin I, Gefen O, Braniss I, Shoresh N et al. Antibiotic tolerance facilitates the evolution of resistance. Science (New York, NY). 2017; 355(6327): 826–830. https://doi.org/10.1126/science.aaj2191 PMID: 28183996

34. Hall CW, Mah T-F. Molecular mechanisms of biofilm-based antibiotic resistance and tolerance in pathogenic bacteria. FEMS Microbiol Rev. 2017; 41 (3):276–301. Available from: https://academic.oup.com/femsre/article/41/3/276/3089981. https://doi.org/10.1093/femsre/fux010 PMID: 28369412

35. Flemming H-C, Wingender J, Szewzyk U, Steinberg P, Rice SA, et al.Biofilms: an emergent form of bacterial life. Nat Rev Microbiol. 2016; 14(9): 563–575. Available from: https://www.nature.com/articles/nrmicro.2016.94. https://doi.org/10.1038/nrmicro.2016.94 PMID: 27510863

36. Wang L-C, Litwin M, Sahiholnasab Z, Song W, Stein DC. Neisseria gonorrhoeae Aggregation Reduces Its Ceftriaxone Susceptibility. Antibiotics (Basel, Switzerland). 2018; 7(2). https://doi.org/10.3390/antibiotics7020048 PMID: 29914058

37. Cahoon LA, Seifert HS An alternative DNA structure is necessary for pilin antigenic variation in Neisseria gonorrhoeae. Science (New York, NY). 2009; 325(5941):764–767.

38. Craig L, Volkmann N, Arvai AS, Pique ME, Yeager M, et al. Type IV Pilus Structure by Cryo-Electron Microscopy and Crystallography: Implications for Pilus Assembly and Functions. Mol Cell. 2006; 23 (5):651–662. Available from: https://www.sciencedirect.com/science/article/pii/S1097276506004813. https://doi.org/10.1016/j.molcel.2006.07.004 PMID: 16949362

39. Abramson J, Adler J, Dunger J, Evans R, Green T, et al. Accurate structure prediction of biomolecular interactions with AlphaFold 3. Nature. 2024; 630(8016):493–500. Available from: https://www.nature.com/articles/s41586-024-07487-w. https://doi.org/10.1038/s41586-024-07487-w PMID: 38718835

40. Wang F, Coureuil M, Osinski T, Orlova A, Altindal T et al. Cryoelectron Microscopy Reconstructions of the Pseudomonas aeruginosa and Neisseria gonorrhoeae Type IV Pili at Sub-nanometer Resolution. Structure. 2017; 25(9): 1423–1435.e4. Available from: https://www.sciencedirect.com/science/article/pii/S0969212617302502. https://doi.org/10.1016/j.str.2017.07.016 PMID: 28877506

41. Dewenter L, Volkmann TE, Maier B. Oxygen governs gonococcal microcolony stability by enhancing the interaction force between type IV pili. Integr Biol. 2015; 7(10):1161–1170. https://doi.org/10.1039/c5ib00018a PMID: 25892255

42. Aas FE, Vik A, Vedde J, Koomey M, Egge-Jacobsen W. Neisseria gonorrhoeae O-linked pilin glycosylation: functional analyses define both the biosynthetic pathway and glycan structure. Mol Microbiol. 2007; 65(3):607–624. https://doi.org/10.1111/j.1365-2958.2007.05806.x PMID: 17608667

43. Salgado-Pabón W, Du Y, Hackett KT, Lyons KM, Arvidson CG, et al. Increased expression of the type IV secretion system in piliated Neisseria gonorrhoeae variants. J Bacteriol. 2010; 192(7):1912–1920. https://doi.org/10.1128/JB.01357-09 PMID: 20139191

44. Welker A, Hennes M, Bender N, Cronenberg T, Schneider G, et al. Spatiotemporal dynamics of growth and death within spherical bacterial colonies. Biophys J. 2021; 120(16):3418–3428. Available from: https://www.sciencedirect.com/science/article/pii/S0006349521005099. https://doi.org/10.1016/j.bpj.2021.06.022 PMID: 34214531

45. St Cyr S, Barbee L, Workowski KA, Bachmann LH, Pham C, et al. Update to CDC's Treatment Guidelines for Gonococcal Infection, 2020. MMWR Morb Mortal Wkly Rep. 2020; 69(50):1911–1916. https://doi.org/10.15585/mmwr.mm6950a6 PMID: 33332296

46. PubChem (2023.000Z) Ciprofloxacin. Available from: https://pubchem.ncbi.nlm.nih.gov/compound/2764. Accessed 23 February 2023.869Z.

47. PubChem (2023.000Z) Kanamycin. Available from: https://pubchem.ncbi.nlm.nih.gov/compound/6032. Accessed 23 February 2023.334Z.

48. Marri PR, Paniscus M, Weyand NJ, Rendón MA, Calton CM, et al. Genome Sequencing Reveals Widespread Virulence Gene Exchange among Human Neisseria Species. PLoS ONE. 2010; 5(7):e11835. Available from: https://journals.plos.org/plosone/article?id=10.1371/journal.pone.0011835. https://doi.org/10.1371/journal.pone.0011835 PMID: 20676376

49. Smirnova GV, Oktyabrsky ON. Relationship between Escherichia coli growth rate and bacterial susceptibility to ciprofloxacin. FEMS Microbiol Lett. 2018; 365(1). https://doi.org/10.1093/femsle/fnx254 PMID: 29228224

50. Marshall WC, Frank R, Amandine B, Michael JF, Philip SS. Contributions of Antibiotic Penetration, Oxygen Limitation, and Low Metabolic Activity to Tolerance of Pseudomonas aeruginosa Biofilms to Ciprofloxacin and Tobramycin. Antimicrob Agents Chemother. 2003; 47(1):317–323. https://doi.org/10.1128/AAC.47.1.317-323.2003 PMID: 12499208

51. Dwyer DJ, Belenky PA, Yang JH, MacDonald IC, Martell JD, et al. Antibiotics induce redox-related physiological alterations as part of their lethality. Proc Natl Acad Sci U S A. 2014; 111(20):E2100–E2109. https://doi.org/10.1073/pnas.1401876111 PMID: 24803433

52. Hennes M, Bender N, Cronenberg T, Welker A, Maier B. Collective polarization dynamics in bacterial colonies signify the occurrence of distinct subpopulations. PLoS Biol. 2023; 21(1):e3001960. https://doi.org/10.1371/journal.pbio.3001960 PMID: 36652440

53. Lee AJ, Wang S, Meredith HR, Zhuang B, Dai Z, et al. Robust, linear correlations between growth rates and β-lactam-mediated lysis rates. Proc Natl Acad Sci U S A. 2018; 115(16):4069–4074.

54. Greulich P, Scott M, Evans MR, Allen RJ. Growth-dependent bacterial susceptibility to ribosome-targeting antibiotics. Mol Syst Biol. 2015; 11(3):796. https://doi.org/10.15252/msb.20145949 PMID: 26146675

55. Stohl EA, Dale EM, Criss AK, Seifert HS. Neisseria gonorrhoeae metalloprotease NGO1686 is required for full piliation, and piliation is required for resistance to H2O2- and neutrophil-mediated killing. MBio. 2013; 4(4). https://doi.org/10.1128/mBio.00399-13 PMID: 23839218

56. Hu LI, Stohl EA, Seifert HS. The Neisseria gonorrhoeae type IV pilus promotes resistance to hydrogen peroxide- and LL-37-mediated killing by modulating the availability of intracellular, labile iron. PLoS Pathog. 2022; 18(6):e1010561. https://doi.org/10.1371/journal.ppat.1010561 PMID: 35714158

57. Koomey JM, Falkow S. Cloning of the recA gene of Neisseria gonorrhoeae and construction of gonococcal recA mutants. J Bacteriol. 1987; 169(2):790–795. https://doi.org/10.1128/jb.169.2.790-795.1987 PMID: 3100504

58. Nadzeya K, Oldewurtel ER, Berenike M. Gene Transfer Efficiency in Gonococcal Biofilms: Role of Biofilm Age, Architecture, and Pilin Antigenic Variation. J Bacteriol. 2015; 197(14):2422–2431. https://doi.org/10.1128/JB.00171-15 PMID: 25962915

59. Higashi DL, Lee SW, Snyder A, Weyand NJ, Bakke A, et al. Dynamics of Neisseria gonorrhoeae attachment: microcolony development, cortical plaque formation, and cytoprotection. Infect Immun. 2007; 75(10):4743–4753. https://doi.org/10.1128/IAI.00687-07 PMID: 17682045

60. Hepp C, Maier B. Kinetics of DNA uptake during transformation provide evidence for a translocation ratchet mechanism. Proc Natl Acad Sci U S A. 2016; 113(44):12467–12472. https://doi.org/10.1073/pnas.1608110113 PMID: 27791096

61. The MathWorks Inc. MATLAB version: 9.7.0 (R2019b). Natick, Massachusetts, United States: The MathWorks Inc.

62. Jurrus E, Engel D, Star K, Monson K, Brandi J, et al. Improvements to the APBS biomolecular solvation software suite. Protein Sci. 2018; 27(1):112–128. Available from: https://onlinelibrary.wiley.com/doi/10.1002/pro.3280. PMID: 28836357

63. Hennes M, Cronenberg T, Maier B. Caging dynamics in bacterial colonies. Phys Rev Res. 2022; 4 (1):13187.

64. Gonzalez Rivera AK, Forest KT. Shearing and Enrichment of Extracellular Type IV Pili. Methods Mol Biol (Clifton, NJ). 2017; 1615:311–320. https://doi.org/10.1007/978-1-4939-7033-9_25 PMID: 28667623

65. Ansmann Gerrit (2023) BPSB/combine-p-values-discrete: Version 1.2.1: Zenodo.

66. George EO, Mudholkar GS. On the convolution of logistic random variables. Metrika. 1983; 30(1):1–13.

67. Jumper J, Evans R, Pritzel A, Green T, Figurnov M, et al. Highly accurate protein structure prediction with AlphaFold. Nature. 2021; 596(7873):583–589. https://doi.org/10.1038/s41586-021-03819-2 PMID: 34265844

68. Ershov D, Phan M-S, Pylvänäinen JW, Rigaud SU, Le Blanc L, et al. TrackMate 7: integrating state-of-the-art segmentation algorithms into tracking pipelines. Nat Methods. 2022; 19 (7): 829–832. Available from: https://www.nature.com/articles/s41592-022-01507-1. https://doi.org/10.1038/s41592-022-01507-1 PMID: 35654950

69. Schrödinger LLC. The PyMOL Molecular Graphics System, Version 1.8. 2015.

70. Camacho C, Coulouris G, Avagyan V, Ma N, Papadopoulos J, et al. BLAST+: architecture and applications. BMC Bioinformatics. 2009; 10(1):1–9. Available from: https://bmcbioinformatics.biomedcentral.com/articles/10.1186/1471-2105-10-421. https://doi.org/10.1186/1471-2105-10-421 PMID: 20003500

6 Gonococcal Aggregation Causes Upregulation of Genes Involved in Antibiotic Tolerance

6.1 Publication

The following work with the title *Gonococcal aggregation causes upregulation of genes involved in antibiotic tolerance* is published on bioRxiv [134]. The reprint can be found in this chapter.

6.1.1 Contributions to the Publication

Sebastian Kraus-Römer, Isabel Rathman and myself were contributing to this project. Sebastian Kraus-Römer and Isabel Rathman contributed to the experimental design of the RNA extraction and the analysis of the RNA sequencing data. Samples were collected by Sebastian Kraus-Römer. Additionally, he created the gene deletion mutants. I contributed by performing the survival assays to determine the killing kinetics of the deletion strains and by conducting the statistical analysis of the experiments.

Berenike Maier, Sebastian Kraus-Römer, Isabel Rathman and myself were contributing in project design, writing the manuscript and creating the figures.

Gonococcal aggregation causes upregulation of genes involved in antibiotic tolerance

Sebastian Kraus-Römer*[1], Isabelle Wielert*[1,2], Isabel Rathmann*[1,3], Thorsten E. Volkmann[1], Paul G. Higgins[2,4,5], Berenike Maier[1,2]

[1]Institute for Biological Physics, University of Cologne, Germany

[2]Center for Molecular Medicine, University of Cologne, Germany

[3]Institute for Biodiversity and Ecosystem Dynamics, University of Amsterdam, Netherlands

[4]Institute for Medical Microbiology, Immunology and Hygiene, Faculty of Medicine and University Hospital Cologne, University of Cologne, Cologne, Germany

[5]German Centre for Infection Research, Partner site Bonn-Cologne, Cologne, Germany

*equal contribution

Abstract

Aggregation and biofilm formation can increase the tolerance of bacteria to external stressors, including antibiotic treatment. While resistant bacteria grow at an elevated drug dose, tolerant bacteria survive longer-term treatment. The mechanisms by which aggregation confers tolerance are insufficiently characterized for most organisms, including the human pathogen *Neisseria gonorrhoeae*. We hypothesize that bacterial aggregation causes upregulation of genes involved in tolerance and that deletion of these genes increases killing rates during antibiotic treatment. To test this hypothesis and identify genes involved in gonococcal tolerance, we compared the transcriptome of aggregating and planktonic *N. gonorrhoeae* strains. In general, the transcriptome analysis shows that aggregation causes a strong upregulation of prophage-related genes and a shift towards anaerobic respiration. We generated deletion strains for the twenty most upregulated genes and measured their killing kinetics during treatment with the clinically relevant antibiotics ceftriaxone or ciprofloxacin. We identified five genes and one multigene segment that are involved in gonococcal antibiotic tolerance. These include prophage genes whose deletion affects tolerance differently in aggregating and planktonic strains. Furthermore, deletion of genes encoding a putative multi-drug efflux pump, an alcohol dehydrogenase, and a DNA repair protein reduces tolerance. In summary, we have identified multiple genes that affect antibiotic tolerance and are upregulated in response to aggregation.

Author summary

Often bacterial infections recur after antibiotic treatment because not all of the bacteria were killed. The ability to survive treatment by bactericidal drugs is termed tolerance. It is well established that aggregation can increase tolerance by reducing growth and metabolism. However, the genes involved in tolerance are not well characterized, especially in the human pathogen *Neisseria gonorrhoeae*. Here, we aim to identify such genes by following the hypothesis that aggregation upregulates genes that cross-protect *N. gonorrhoeae* from antibiotic treatment. We show that prophage-associated genes are strongly upregulated in aggregates and that deletion of various phage genes affects tolerance to the currently administered drug, ceftriaxone. We identify three additional genes belonging to different functional classes whose deletion reduces tolerance to ciprofloxacin. Our study is an important step towards understanding the molecular mechanisms of gonococcal antibiotic tolerance. In particular, we propose that prophages could serve as a target for the treatment of tolerant gonococcal infections.

Introduction

While antibiotic resistance has been intensively studied, antibiotic tolerance has emerged as a serious yet less studied factor contributing to treatment failures (1). When bacteria are intermittently treated with bactericidal antibiotics, often a small fraction of the population will survive the treatment. Since killing is a stochastic process that occurs at a specific rate, the fraction of survivors follows characteristic killing kinetics. The shallower the killing kinetics the more tolerant are the cells. Alternatively, a subpopulation of cells can enter a different physiological state, the persister state, which has a lower killing rate. Increased tolerance and persistence can evolve during repeated intermittent antibiotic treatment (2-4). Antibiotic tolerance is problematic for the treatment of infections because the surviving subpopulation can cause recurrent infections (1) and tolerance often precedes and allows for the development of antibiotic resistance (5). One of the factors influencing the killing rate is cell aggregation and subsequent biofilm formation (6, 7). Here, we investigate whether genes upregulated due to aggregation are involved in the antibiotic tolerance of *Neisseria gonorrhoeae*, the causative agent of gonorrhea, one of the most common sexually transmitted infections worldwide (8).

The development of antibiotic resistance in *N. gonorrhoeae* is well documented (9, 10) and many genetic determinants underlying resistance are known (11, 12). In contrast, little is known about antibiotic tolerance of *N. gonorrhoeae*. Recently, tolerant strains of *N. gonorrhoeae* have been isolated and detected from patients and in WHO reference strains (13, 14). In several studies, tolerance to antibiotics has been investigated in vitro (15-17), but the molecular mechanisms and genes involved in tolerance remain largely elusive (18).

In other bacterial species, several genes have been identified that contribute to antibiotic tolerance (1), most of which are related to slow growth and reduced metabolism. The corresponding metabolic pathways include purine synthesis, stringent response, the TCA cycle, as well as the electron transport chain, but we assume that these represent only a fraction of genes and molecular mechanisms that mediate tolerance (1). Slow growth and reduced metabolism are pronounced in bacterial biofilms and are therefore likely to contribute to the protective effect of biofilm formation (6, 7). Moreover, there is evidence that aggregation triggers stress responses that cross-protect the bacteria from antibiotic treatment, including the stringent response and SOS response (19, 20).

N. gonorrhoeae (gonococci) form biofilms in vitro (21) and there is evidence for in vivo formation of biofilms (22). In vitro and on epithelial cell layers, *N. gonorrhoeae* quickly forms spherical aggregates, also known as microcolonies (23-25). The aggregation process is mediated by retractile type 4 pili (T4P) (26), which are present in large numbers at the gonococcal cell surface (27). These dynamic polymers create an attractive force between neighbouring cells (28-30) and govern the mechanical properties of the aggregates (28, 31-33). We have shown previously that within hours, cells within a microcolony differentiate into two subpopulations: a proliferating and highly energized subpopulation at the periphery of the microcolony, and a slowly growing subpopulation with reduced membrane potential at the centre (17, 34). These subpopulations exhibit different levels of tolerance to antibiotics (16, 17). It is currently unclear how gene expression changes during the early stages of gonococcal biofilm development. However, previous studies have characterized longer-term differences in gene expression between planktonic and biofilm-attached cells of a clinical *N. gonorrhoeae* isolate. Cells were grown in a flow chamber for two days and transcription in adherent cells and cells of the supernatant were compared using RNA microarray analysis (35). Under these experimental conditions, 3.8 % of the genome was differentially expressed. Genes encoding enzymes belonging to the anaerobic respiratory metabolism (*aniA*, *norB*, *ccp*) were among those that were strongly upregulated, while genes of the *nuo* cluster involved in aerobic respiration were among those that were downregulated. Deletion of genes involved in anaerobic respiration attenuated biofilm formation, suggesting that gonococci assume an anaerobic metabolism within the biofilm (35). Proteins belonging to the nitrite reduction pathway were also detected as upregulated in a proteomics study (36). Apart from this class of proteins / genes, there was little overlap between the biofilm transcriptome and the proteome although the experimental setup for biofilm formation was similar between both studies. The proteome study showed additional differential regulation of proteins involved in energy metabolism, protein synthesis, and cell envelope proteins (36). In the experimental setup used in these studies, the planktonic cells were sampled from the supernatant. Therefore, it is unclear whether they had recently dispersed from the biofilm and how the prehistory of biofilm growth and subsequent release affects gene expression.

Aggregation enhances antibiotic tolerance of *N. gonorrhoeae* to ceftriaxone (15, 37) and ciprofloxacin (37). It is unclear, however, which genes are involved in tolerance and which of them are related to aggregation. Here, we aim at identifying genes that affect gonococcal tolerance. It has been shown for other bacterial species that differential gene regulation triggered by aggregation can provide cross-protection against antibiotic treatment (19, 20). With this knowledge in mind, we set out to investigate the effect of aggregation-induced upregulation on the antibiotic tolerance of *N. gonorrhoeae*. In the first step, we examined which genes are differentially transcribed between planktonic and aggregating cells of *N. gonorrhoeae* and identify the twenty most upregulated genes. We then investigate the effects of deletion of these genes on tolerance to ceftriaxone and ciprofloxacin. To find out whether these effects require aggregation, we compare the effects in the background of aggregating and planktonic cells. We show that deletion of various genes associated with prophages impact tolerance differently in aggregating and planktonic strains. In aggregating strains, genes involved in drug efflux, DNA repair, and metabolism affect tolerance. The identification of these genetic determinants of tolerance will help to build a picture of the molecular mechanisms of antibiotic tolerance in *N. gonorrhoeae*.

Results

Aggregation causes profound changes in transcription.

T4P can attractively interact and by this govern gonococcal aggregation (23, 28, 30). Here, we investigate how aggregation affects transcription by RNA sequencing of aggregating and planktonic strains. The two aggregating strains used in this study contain different variants of the gene encoding the major pilin *pilE*, wt_{agg} and wt_{agg2} (37) (S1 Table). Two of the planktonic strains (wt_{plank}, $\text{wt}_{\text{plank2}}$) generate type 4 pili which do not mediate aggregation, but are otherwise functional (37). Furthermore, we used a planktonic strain that lacks *pilE* and cannot form pili (*ΔpilE*). For transcriptome analysis, we allowed the gonococcal strains to grow for 10 h. wt_{agg} and wt_{agg2} formed colonies at this time point, while wt_{plank}, $\text{wt}_{\text{plank2}}$, and the *ΔpilE* strains are planktonic (37). For all strains, RNA was isolated and sequenced.

In the first step, we evaluated clustering of the RNA-seq reads using principal component analysis (PCA). We found that the two aggregating strains and the three planktonic strains cluster separately in the first principal component (PC1) (Fig. 1A), which encompasses 78 % of the total variance. This result indicates that aggregation strongly affects transcription of gonococci. Interestingly, $\text{wt}_{\text{plank2}}$ replicates cluster separately from all the other strains along the second principal component (PC2), suggesting that the $\text{wt}_{\text{plank2}}$ expression data across all genes differs significantly from the other samples. The genes that have the largest influence when calculating the principal components in the new basis include phage-associated genes (NGFG_01274, NGFG_01290), an ATP-dependent RNA helicase (NGFG_01150) and two opacity proteins (NGFG_02259, NGFG_02351). When the genes with the highest effect on the PCA are excluded from the analysis, the clustering of conditions remains stable and similar to Fig. 1A, indicating that the clustering is caused by global strain differences and not by individual genes.

In the next step, we compare the transcription of the aggregating wt_{agg} strain with each of the four T4P-replacement strains. We consider genes to be differentially regulated if $-0.5 \leq log_2\, fold\ change \leq 0.5$ and the adjusted p-value is $p < 0.05$. Between the two aggregating strains wt_{agg2} and wt_{agg}, we find small differences in their transcriptome (Fig. 1B) as only 0.1 % of all genes are upregulated and 0.4 % are downregulated significantly. Comparing wt_{agg} to the planktonic strains reveals considerable differences in expression, with between 16 % and 2.7 % of genes being upregulated and between 9.7 % and 18.9 % of genes being downregulated (Fig. 1C-E).

155 Overall, RNA-seq analysis shows strong differences in gene expression between the
156 aggregating and planktonic strains.

157

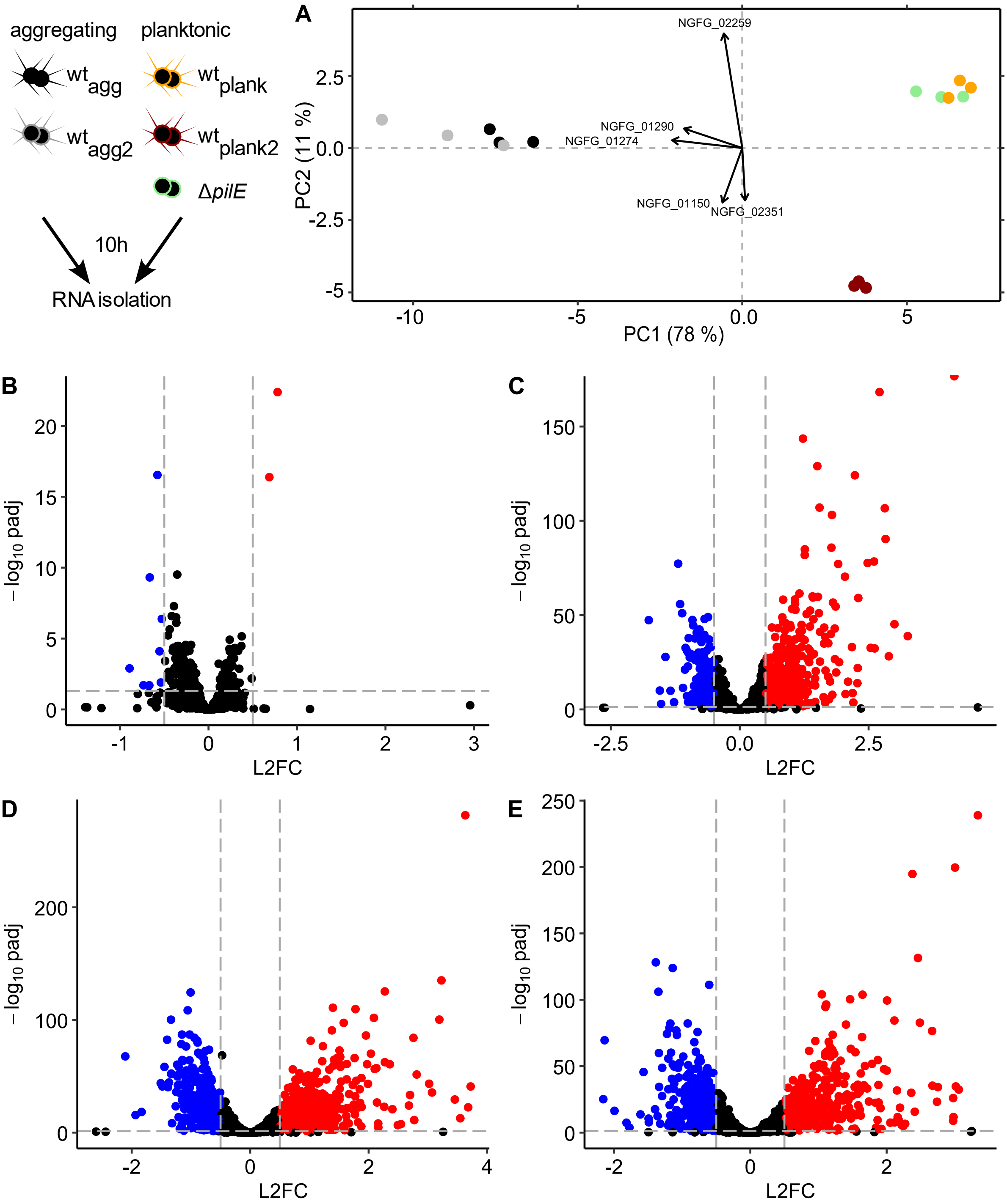

158

159 Fig. 1 Overview of the transcriptomes of aggregating and planktonic strains. A) PCA analysis.
160 wt_{agg} (black), wt_{agg2} (gray), wt_{plank} (orange), wt_{plank2} (red), and *ΔpilE* (green). Volcano-plots
161 showing the adjusted p-value as a function of the log_2-fold change (L2FC) for wt_{agg} versus B)
162 wt_{agg2}, C) wt_{plank2}, D) wt_{plank}, E) *ΔpilE*. Dashed lines depict the cut-offs for significant

differential transcription. Blue: significantly down-regulated genes, red: significantly up-regulated genes.

Transcription reveals upregulation of prophage-related genes and indicates a shift to anaerobic respiration

We assessed whether genes associated with specific biological functions were collectively upregulated or downregulated between the aggregating and planktonic strains. To this end, we performed a functional enrichment analysis for each strain using KEGG categories, as described previously (27, 38) (see Methods for details) (Fig. 2, S1 Fig.).

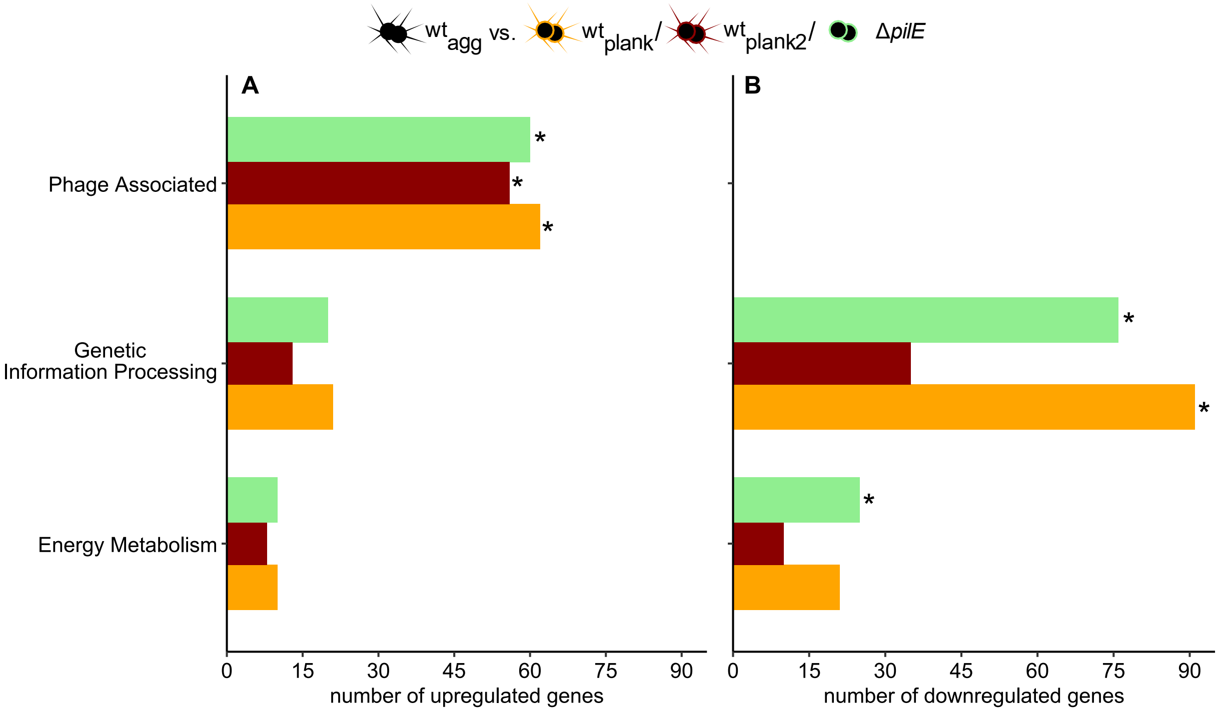

Fig. 2 Functional enrichment of up- and down-regulated genes in the wt_{agg} strain versus the *ΔpilE* (green), wt_{plank2} (red), and planktonic strains wt_{plank} (orange). Here, only significant KEGG categories are shown and the number of up- and down-regulated genes is computed and depicted as bar plots. Categories are analysed for enrichment with a Fisher's exact test and multiple testing correction is performed with the Bonferroni method. Significantly enriched categories are highlighted with * (p-value ≤ 0.01).

We find that the category of phage-associated genes is enriched among the upregulated genes when comparing wt_{agg} to all three planktonic strains (Fig. 2). The *N. gonorrhoeae* genome contains four tailed double-stranded prophages (39) (S2 Fig. A). In wt_{agg}, genes belonging to all of these prophages are significantly upregulated when compared to the planktonic strains (S2 Fig. B-E), indicating that aggregation causes upregulation of genes within the double-stranded prophages. Upregulation is most prominent for genes that belong to prophages Φ1 and Φ3.

The categories of genetic information processing and energy metabolism are enriched among the downregulated genes when comparing wt_{agg} to some of the planktonic strains (Fig. 2). Among the genes belonging to the energy metabolism category, genes involved in denitrification (*aniA* (NGFG_02154), *norB* (NGFG_02153), and *nos* genes) are upregulated, while genes involved in aerobic respiration (*nuo* genes) tend to be down-regulated. This indicates a shift from aerobic to anaerobic respiration in agreement with a previous report (35). For the category of genetic information processing, genes encoding ribosomal genes are among the most strongly downregulated genes within the aggregating strains. These genes include *rpl* and *rpm* genes encoding for the 50S subunit as well as *rps* genes encoding for the 30S subunit.

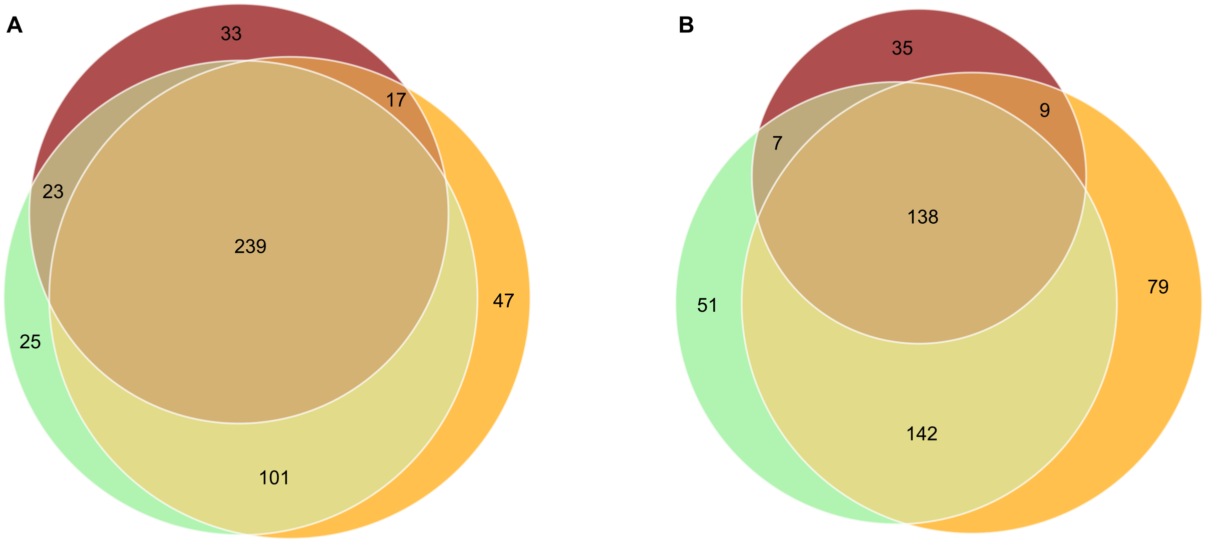

Fig. 3 Intersection of genes that are differentially transcribed by colony-forming strains compared to planktonic strains. A) upregulated genes, B) downregulated genes. wt_{agg} vs. wt_{plank} (orange), wt_{plank2} (red), and *ΔpilE* (green).

We define the aggregation transcriptome as the intersection of genes that are differentially regulated in all three planktonic strains compared to strain wt_{agg}. Within this intersection, 239 genes are consistently upregulated and 138 genes are consistently downregulated (Fig. 3). In terms of functional KEGG categories, only the category of phage-related genes is significantly overrepresented.

We conclude that 239 genes are upregulated and 138 genes are downregulated due to aggregation. The upregulated genes are functionally enriched in phage-associated genes.

Deletion of various genes upregulated in aggregates affects antibiotic tolerance to ciprofloxacin

To better understand the mechanisms causing increased tolerance, we scrutinized the effect of deleting the twenty most strongly upregulated genes of the aggregation transcriptome (Fig. 3) (S1 Table). First, we generated deletion strains within the wt_{agg} background. When consecutive genes on the genome belonged to these highly upregulated genes, they were deleted together in one strain. We have previously shown that the wt_{agg} strain multiplies nearly exponentially during the initial 10 h (37). To find out whether the gene deletions have a strong effect on the growth dynamics, we compared the number of cells after 10 h of growth between the different mutants. None of the deletion strains showed a significant growth defect (S3 Fig.). Furthermore, we assessed the minimal inhibitory concentrations of ciprofloxacin and ceftriaxone and found no significant changes except the *ΔrecN* strain that showed a two-fold reduction of the ciprofloxacin MIC (S2 Table).

For each deletion strain, we characterized the killing kinetics at its 600-fold MIC. This concentration was chosen for consistency with an earlier work in which we found strong effects of aggregation on the killing kinetics (37). By comparing killing kinetics over a time range of 9 h between the deletion strains and their parental strains, we determined deletions that altered the killing kinetics. We calculated the fraction of surviving cells (f) by dividing the CFU at the start of the antibiotic treatment by the CFU after treatment for either 3, 6 or 9 h $(f = CFU_{start}/CFU_{treatment})$ (S4 Fig.). Each condition was characterized in at least three independent experiments and we evaluated the significance by weighting with the number of replicates (40).

We discovered three gene deletions that significantly accelerated killing of wt_{agg} by ciprofloxacin (Fig. 4A). These deletions include the DNA repair gene *recN* (NGFG_00464), the gene encoding the putative *drug:*H^+ antiporter (NGFG_00826), and the alcohol dehydrogenase gene *adh* (NGFG_01080) (Fig. 4A). After the entire 9-hour treatment period, the deletion of each of the three genes reduces the fraction of surviving cells by a factor of 5 to 10.

We wondered whether a combinatorial deletion of genes significantly affecting the survival during ciprofloxacin treatment would have more severe effects. Therefore, we constructed a triple deletion strain *ΔrecN ΔNGFG_01080 ΔNGFG_00826*$_{agg}$ (3xΔ$_{agg}$). Compared to the single deletion strains (Fig. 4A), the triple deletion strain did not show accelerated killing (Fig. 4A). However, the number of cells was significantly reduced after 10 h of growth in that strain (Fig. S9A), suggesting that the cells grew more slowly. Since slow growth is often associated with increased tolerance (41), we cannot rule out that faster killing caused by the gene deletions and slower killing caused by reduced growth cancel each other out.

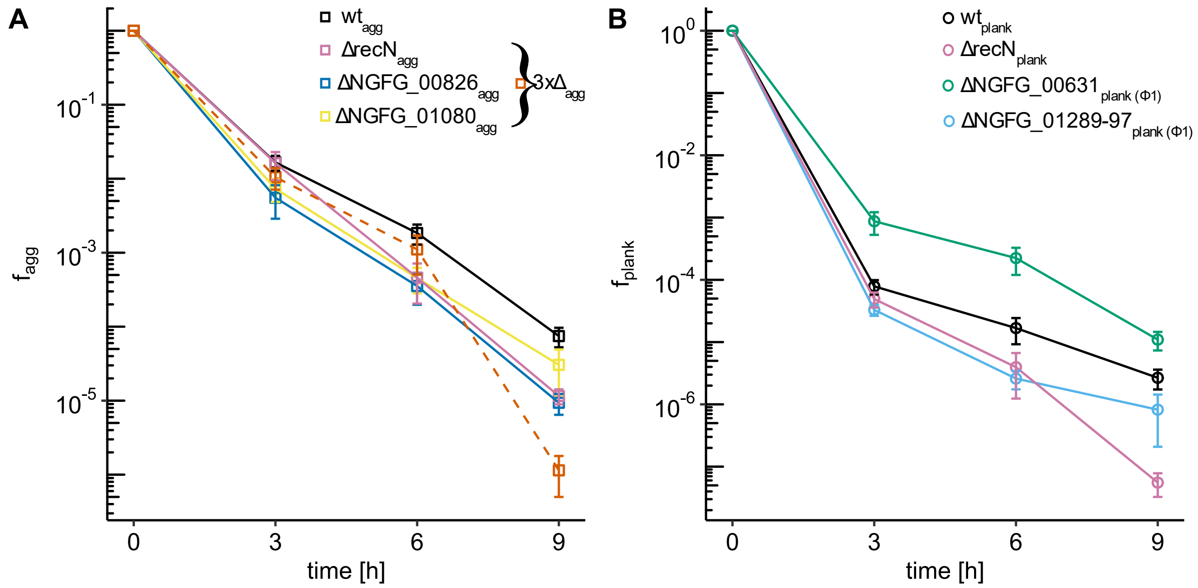

Fig. 4 Killing kinetics of deletion strains in aggregating (A, f_{agg}) and planktonic (B, f_{plank}) background under treatment with 2.4 µg/ml ciprofloxacin. Only strains for which the killing kinetics are significantly different from the kinetics of the parental strain are shown. Shown is the fraction of surviving cells $f = CFU_{start}/CFU_{treatment}$. A) Fractions of surviving aggregating cells (squares) with gene deletions and their respective parental strain. wt$_{agg}$ (Ng150, black), *ΔNGFG_01080*$_{agg}$ (Ng281, yellow), *ΔrecN*$_{agg}$ (Ng261, pink), *ΔNGFG_00826*$_{agg}$ (Ng262, blue), *3xΔ*$_{agg}$ (pooled data of Ng321 and Ng325, dashed orange). B) Fractions of surviving planktonic cells (circles) with gene deletions and their respective parental strain. wt$_{plank}$ (Ng240, black), *ΔrecN*$_{plank}$ (Ng275, pink), *ΔNGFG_00631*$_{plank}$ (Ng288, green), *ΔNGFG_01289-97*$_{plank}$ (Ng300, cyan).

Next, we addressed the question of which gene deletions affect tolerance in the planktonic strains. We deleted the same 20 genes (S1 Table) in the planktonic background (wt$_{\mathrm{plank}}$) and determined the killing kinetics of the deletion strains (S5 Fig.). Most deletions showed no strong growth effect after 10 h with the exceptions of strains *ΔNGFG_00631*$_{\mathrm{plank}}$ and *ΔNGFG_01491*$_{\mathrm{plank}}$ that had a slightly but significantly higher cell number at that growth stage (S3 Fig.). Again, we found that deletion of *recN* significantly accelerated killing (Fig. 4B), showing that this gene is important for tolerance to ciprofloxacin both in aggregates and for planktonic strains. Furthermore, we discovered that deletion of the multigene segment NGFG_01289-97 from prophage Φ1 accelerated the killing of planktonic strains. Interestingly, deletion of the phage related gene NGFG_00631 (Φ1) significantly slowed killing of the planktonic strain.

We conclude that deletion of genes encoding for a putative drug antiporter, a DNA repair protein, and an alcohol dehydrogenase reduce tolerance against ciprofloxacin.

Phage-related genes affect tolerance towards ceftriaxone

Next, we addressed the question of whether deletion of the 20 most upregulated genes of the aggregation transcriptome affects killing during the treatment with a different class of antibiotics. We treated the deletion strains with ceftriaxone at 600-fold MIC (4.8 µg/ml). Under ceftriaxone treatment, we did not identify deletions that significantly enhanced killing in the aggregating background (S6 Fig.). However, deletion of the phage-related genes NGFG_01289-97 significantly increased the fraction of surviving cells (Fig. 5A). Interestingly, the same deletion reduced the fraction of surviving bacteria in the planktonic background (Fig. 5B, S7 Fig.). This shows that the effects of these phage-related genes on ceftriaxone susceptibility depend on aggregation. Additionally, deletion of a putative terminase gene of prophage Φ1 (NGFG_01302) significantly reduced survival. Finally, deletion of the phage related gene NGFG_00631 (Φ1) significantly slowed killing under ceftriaxone treatment.

We conclude that the deletion of genes related to prophage Φ1 impacts the tolerance to ceftriaxone. In particular, deletion of a multigene segment affects the tolerance of aggregating and planktonic strains in opposite ways highlighting its lifestyle-specific effect.

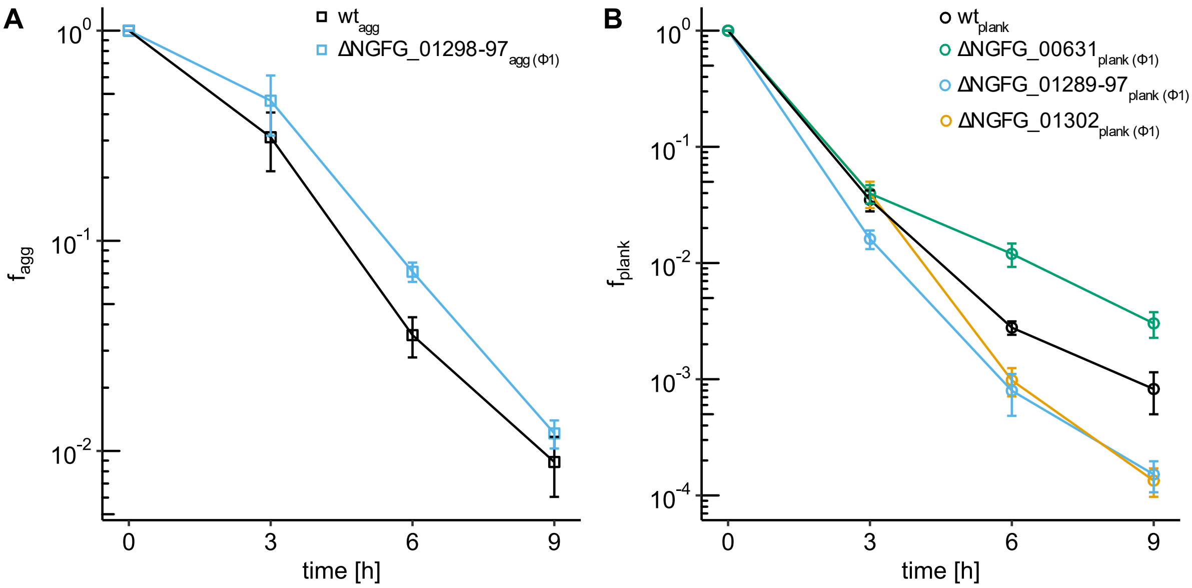

Fig. 5 Killing kinetics of deletion strains under treatment with 4.8 µg/ml ceftriaxone. Only strains whose killing kinetics is significantly different from the kinetics of the parental strain are shown. Shown are the fraction of surviving cells $f = CFU_{start}/CFU_{treatment}$. A) Fractions of surviving aggregating cells (squares) with gene deletions and their respective parental strain. wt$_{agg}$ (Ng150, black), *ΔNGFG_01289-97*$_{agg}$ (Ng273, cyan). B) Fractions of surviving planktonic cells (circles) with gene deletions and their respective parental strain. wt$_{plank}$ (Ng240, black), *ΔNGFG_01302*$_{plank}$ (Ng302, orange), *ΔNGFG_00631*$_{plank}$ (Ng288, green), *ΔNGFG_01289-97*$_{plank}$ (Ng300, cyan).

Discussion

In this study, we used transcriptomic data to identify genes involved in antimicrobial tolerance. We found five genes and one multigene segment that modify tolerance to ceftriaxone and/or ciprofloxacin. Genes influencing ciprofloxacin tolerance have different putative functions, whereas genes affecting ceftriaxone tolerance are associated with one of the prophages on the gonococcal genome. Our results point to tolerance mechanisms that differ from the reduction in cell growth and metabolism that has been demonstrated as a common theme in many studies as the cause of antibiotic tolerance (1, 7).

Differential expression in aggregates indicates anaerobic lifestyle

The transcriptome of the colony-forming isogenic strains differs significantly from that of the planktonic strains. The only genetic difference between the strains was the pilin variant that controls the attraction between cells (37). Thus, our results show that pilin antigenic variation strongly affects the transcriptional pattern of gonococci by regulating aggregation.

We found that genes involved in aerobic respiration showed a tendency to be downregulated in aggregating strains while genes involved in anaerobic respiration were more likely to be upregulated. Therefore, we compared our data with a study reporting on the anaerobic stimulon of *N. gonorrhoeae* F62 (42) and found a considerable overlap. Of the 196 differentially expressed genes during anaerobic conditions, we found 169 annotated orthologues in MS11. Up to 41 % of those genes were similarly regulated under our conditions. The gene categories that contain the most similar regulated genes belonged to regulation, phages, small molecules, and macromolecular biosynthesis. Genes that were strongly upregulated under both conditions include *aniA*, *nosR*, *recN*, *NGFG_01491*, and several genes encoding prophages Ngo Φ1-4. The observation that prophage genes were strongly upregulated under both conditions suggests a role for prophages in gonococcal biofilm development. There are interesting differences between the transcriptional responses to aggregation and oxygen limitation. For example, we show that various genes involved in iron and sulfate acquisition are upregulated in aggregates, while these genes tend to be downregulated during purely anaerobic conditions (42).

We compared our results with earlier works on gene expression in gonococcal biofilms, which used microarray and proteomic methods (35, 36). Those studies focused on mature biofilms and used a different method for comparing planktonic and biofilm-forming bacteria. Their studies compared cells living in biofilms to cells that had dispersed from the biofilm. PCA analysis of *P. aeruginosa* biofilms showed that dispersed cells cluster separately from the biofilm and planktonic cells, suggesting that dispersed cells represent a distinct stage in the transition from the biofilm to the planktonic lifestyle (43). Despite the different methods used in both studies (35, 36), their results were similar to our findings in terms of differential expression of genes involved in anaerobic respiration and the downregulation of genes involved in protein synthesis and energy metabolism. This shows that this transcriptional response to oxygen limitation as a consequence of aggregation is robust across experimental conditions of biofilm formation.

Genes with diverse functions affect tolerance of aggregating gonococci to ciprofloxacin

In this study, we started from the assumption that during aggregation, specific genes that also protect bacteria from antibiotic treatment are upregulated. Under ciprofloxacin treatment, we identified three genes from different functional classes whose deletion affected tolerance of gonococcal aggregates.

Deletion of *NGFG_00826* in the aggregating strain resulted in a less ciprofloxacin-tolerant phenotype. *NGFG_00826,* is annotated as the major facilitator superfamily (MFS) “drug:H+ antiporter”. The MFS transporters are secondary active transporters with a broad spectrum of substrates (44). In bacteria, these systems are used for nutrient uptake but also for export of toxic compounds such as antibiotics or heavy metals (45). MFS transporters contribute to antibiotic resistance in *E. coli* and *S. aureus* (46, 47). It is likely that this MFS transporter is also involved in extrusion of ciprofloxacin in *N. gonorrhoeae*. Similarly, an ABC transporter was described in *P. aeruginosa* that was upregulated in biofilms and increased tolerance to antibiotics, including ciprofloxacin (48). We propose that *NGFG_00826* drug transporter is upregulated in response to aggregation and cross-protects gonococci from ciprofloxacin treatment.

Moreover, deletion of a gene encoding an alcohol dehydrogenase (ADH), *NGFG_01080,* resulted in a less ciprofloxacin-tolerant phenotype in the aggregating strain. ADH are enzymes that convert alcohols to aldehydes and *vice versa*. Various studies showed that downregulating metabolic genes can increase tolerance (1). Here we observe the opposite: *adh*, a gene involved in carbon metabolism, is upregulated and its deletion reduces tolerance. ADH may be involved in maintaining redox balance and detoxifying reactive oxygen species, which often result from antibiotic treatment (49). Reduction equivalents such as NAD^+/NADH are converted during the oxidation of alcohols. Through the deletion of *NGFG_01080*, we might disturb the redox balance within the cells, thereby generating aggregates that are less resilient to antibiotic stress and reducing *N. gonorrhoeae*'s ability to deal with reactive oxygen species. It is tempting to speculate that *adh* is upregulated during aggregation to detoxify reactive oxygen species, and that this effect also protects the bacteria from antibiotic treatment.

The third gene whose deletion decreased tolerance to ciprofloxacin was *NGFG_00464,* which encodes the DNA repair protein RecN. Its deletion reduced tolerance in both aggregating and planktonic backgrounds even though the expression levels of *recN* were significantly lower in the planktonic strains. Since ciprofloxacin causes DNA damage, it was expected that deletion of a DNA repair gene would affect survival and growth under ciprofloxacin treatment.

In summary, we have identified three genes that influence the tolerance of aggregating gonococci to ciprofloxacin. Since these genes are among the most upregulated genes in aggregates compared to planktonic bacteria, it is reasonable to assume that their upregulation contributes to the protective effect of aggregation.

Prophage Φ1 genes influence tolerance in aggregating and planktonic bacteria

In our study, predominantly prophage-encoded genes were upregulated in the aggregated state. Recently, it was shown that prophage induction in other biofilm-forming species releases matrix components (50, 51). Activation of prophages may contribute to the stability of the aggregates by actively integrating phages into the matrix, as is the case in other pathogenic species (52, 53). We find that none of the gene deletions in the $\mathrm{wt}_{\mathrm{agg}}$ background affected its ability to form aggregates in liquid culture (S10 Fig.), suggesting that a different mechanism is at play in our system. Very little is known about the role of prophage activation of *N. gonorrhoeae*. In an early genomic study (54), five regions of strain FA1090 were assigned to dsDNA prophages Φ1- Φ5 and DNA from Φ1 was detected, suggesting that this phage is active. The latter region is also present in the derivatives of strain MS11 studied here. We used PHASTEST (39) and predicted four prophages on the genome (S2 Fig. A). The region corresponding to Φ1 is predicted by the software to be intact. All the genes we have identified as influencing tolerance belong to this prophage and many of them are upregulated in aggregates (S2 Fig. B). However, we show that in the planktonic strains, deletion of genes belonging to this prophage affects tolerance. The reason for this could be that some genes located in the prophage region affect bacterial physiology and thus tolerance. As discussed below, we consider it is more likely that the phage can be activated in the planktonic state, possibly by antibiotic treatment.

Deletion of *NGFG_00631* increased the tolerance of planktonic strains to ceftriaxone and ciprofloxacin. BLAST analysis of *NGFG_00631* revealed high sequence identity with *cro*, a transcriptional regulator of the Cro/CI family. It has been shown that an λcro$^-$ mutant cannot induce the lytic cycle of phage λ (55). The adjacent gene *NGFG_00630*, which is expressed in the opposite direction (but is not significantly upregulated or downregulated in our transcriptional analysis), shows high similarity to the gene encoding the repressor protein CI which is crucial for maintaining the lysogenic cycle of phage λ. We hypothesize that these proteins resemble the two regulatory proteins responsible for the bistable switch of temperate bacteriophages. Assuming that phage Φ1 can actively enter the lytic cycle, deletion of *NGFG_00631* would prevent the transition to the lytic cycle and explain the enhanced survival of planktonic mutants during antibiotic treatment. This is consistent with the increased cell number after ten hours of growth (S3 Fig.). However, we do not observe an enhanced survival of the corresponding aggregating *NGFG_00631* deletion strain. We hypothesize that lytic cycle-induced cell lysis provides a source of extracellular DNA that can be integrated into the extracellular matrix (22, 56). Thus, lysis in a subpopulation of gonococcal aggregates could enhance the structural integrity of aggregates and subsequently impact survival during antibiotic treatment.

The deletion of the genes *NGFG_01289-97* showed the most ubiquitous effect on gonococcal tolerance. In the planktonic strain, this deletion led to reduced tolerance to ciprofloxacin and ceftriaxone. When the same stretch of genes was deleted in the aggregating strain, the mutants showed a higher tolerance to ceftriaxone than the wt_{agg}. According to BLAST analyses, these genes encode a variety of phage tail and connector proteins. These proteins are essential for phage assembly (57), but their deletion may not prevent cell lysis once the lytic cycle has been activated. Lack of these components could lead to conditions similar to those of an abortive infection during a phage infection, in which the cell harbouring the unassembled phage dies before phage maturation (58). This effect could prove detrimental to planktonic cells, especially under antibiotic stress. However, the aggregated counterpart might benefit from cell lysis prior to phage assembly, as more cell debris could be integrated into the extracellular matrix, especially free unpackaged DNA. Deletion of *NGFG_01302* may have similar effects, as it encodes the small terminase subunit TerS. The absence of this essential subunit for DNA recognition and the initiation of the packaging process could interfere with virus assembly, which would have the same effect as deletion of *NGFG_01289-97*.

We conclude that multiple genes related to prophages influence antibiotic tolerance. Importantly, deletion of a stretch of genes which is most likely essential for phage assembly leads to opposite results in aggregating and planktonic strains when treated with ceftriaxone. This suggests that the role of prophage genes in tolerance depends on bacterial aggregation.

Conclusion

Gonococcal aggregation increases antibiotic tolerance (15, 37). Therefore, genes that affect aggregation, including *pilE*, *pptA*, *pilT*, *opa*, and *lgtE*, modulate tolerance (15, 16, 37). Most mechanisms that cause bacterial tolerance are based on reducing growth rates or the slowing down of metabolic pathways (1, 7). We have previously shown that aggregation decelerates the growth rate of gonococci (37), and it is conceivable that growth rate reduction directly increases tolerance. Also, consistent with a slowed metabolism, there is evidence that point mutations in the gene encoding phosphopyruvate hydrase *eno* may be involved in tolerance (18). In this study, we identify multiple genes that affect antibiotic tolerance but not growth, of gonococci. Three genes with putative functions in drug efflux, DNA repair, and carbon metabolism and/or ROS detoxification are strongly upregulated in aggregates and involved in increasing the tolerance of those aggregates to ciprofloxacin. In addition, two genes and one multigene segment related to prophage Φ1 affect tolerance to ceftriaxone and ciprofloxacin. Although gonococcal phages are poorly characterized (54), our results are most consistent with the interpretation that phage induced lysis is detrimental to planktonic cells and, simultaneously reduces antibiotic tolerance. In contrast, our data suggest that prophages could be activated by aggregation and aggregated gonococci are less sensitive to phage activation. Overall, the mechanisms of gonococcal antibiotic tolerance are diverse and we propose that multiple mechanisms act together in gonococcal aggregates and biofilms. It will be particularly interesting to study the interplay between aggregation, prophage activation, and antibiotic tolerance in future studies.

Materials and Methods

Growth conditions

N. gonorrhoeae was grown at 37 °C and 5 % CO_2. Gonococcal base agar was made from 10 g/l dehydrated agar (BD Biosciences, Bedford, MA), 5 g/l NaCl (Roth, Darmstadt, Germany), 4 g/l K_2HPO_4 (Roth), 1 g/l KH_2PO_4 (Roth), 15 g/l Proteose Peptone No. 3 (BD Biosciences), 0.5

g/l soluble starch (Sigma-Aldrich, St. Louis, MO), and supplemented with 1% IsoVitaleX (IVX): 1 g/l D-glucose (Roth), 0.1 g/l L-glutamine (Roth), 0.289 g/l L-cysteine-HCL x H_2O (Roth), 1 mg/l thiamine pyrophosphate (Sigma-Aldrich), 0.2 mg/l $Fe(NO_3)_3$ (Sigma-Aldrich), 0.03 mg/l thiamine HCl (Roth), 0.13 mg/l 4-aminobenzoic acid (Sigma-Aldrich), 2.5 mg/l β-nicotinamide adenine dinucleotide (Roth), and 0.1 mg/l vitamin B12 (Sigma-Aldrich). Liquid GC media is identical to the base agar composition but lacks agar and starch.

Antibiotics

Antibiotics were purchased from Roth, Merck, Thermo Fisher, or Hello Bio. Stock solutions of antibiotics were prepared as follows. Ceftriaxone was dissolved in DMSO and adjusted to a final concentration of 1 mg/ml. Ciprofloxacin was dissolved in 0.1 M HCl (10 mg/ml). Erythromycin was dissolved in ethanol (10 mg/ml). Streptomycin (100 mg/ml) and kanamycin (50 mg/ml) were dissolved in milliQ water. For selective plates, the final concentration of erythromycin, streptomycin and kanamycin were 5-10 µg/ml, 100 µg/ml and 50 µg/ml, respectively.

Bacterial strains

All strains used in this study (S3 Table) were derived from the *opa*- selected VD300 strain (59). To suppress antigenic variation, the G4 motif upstream of *pilE* was deleted in all strains (60). The *pilE* variant strains from Wielert et al (37) were used and named according to their planktonic ($_{\text{plank}}$) or aggregative ($_{\text{agg}}$) phenotype.

Construction of single knock-out strains

We generated deletion strains of the twenty most upregulated genes of the aggregation transcriptome (S1 Table) within the wt_{agg} background. When consecutive genes on the genome belonged to these highly upregulated genes, they were deleted together in one strain. The deletion strains were generated by replacing the gene of interest by a kanamycin resistance cassette including a promoter. Therefore, all genes residing downstream of the gene of interest within the same operon are affected by the deletion. In general, we expected genes in the same operon to have a comparable differential regulation and in such cases deleted the entire operon. In addition, we used the transcriptome study by Remmele et al. (61) to assess potential downstream effects of the gene deletions. In this study, the only deletion likely to affect a downstream gene is that of *ΔNGFG_00631*, which may affect another phage-related gene. Therefore, for most genes located in operons, our study cannot distinguish which specific gene of the operon is responsible for the effect.

Single genes or multiple consecutive genes were replaced by a kanamycin resistance cassette (aminoglycoside phosphotransferase AHM36341.1). The procedure for this replacement was the same for all mutants. In brief, the up- and downstream regions of the gene of interest were fused with a kanamycin resistance cassette and used to transform *N. gonorrhoeae*. By homologous recombination the gene of interest is replaced by the *kanR* construct.

Primers A & B and primers C & D were used to amplify the upstream and downstream region of the genes of interest from gDNA of strain $\mathrm{wt}_{\mathrm{agg}}$ (Ng150). Primer E & F were used to amplify the kanamycin resistance cassette from genomic DNA of strain Ng052. The corresponding primer combinations are listed in S4 Table and the primer sequences are found in S6 Table. All amplified PCR products were purified with the PCR purification KIT (Qiagen) and then fused with the GXL-polymerase (TaKaRa). Then $\mathrm{wt}_{\mathrm{agg}}$ (Ng150) or $\mathrm{wt}_{\mathrm{plank}}$ (Ng240) were transformed with the fusion products. Selection was achieved by plating transformants on agar plates containing kanamycin. Correct replacement was checked via screening PCR with primers A & D and sequencing (A or D).

The gene deletions generated based on the twenty most upregulated genes in the aggregation transcriptome are listed in S1 Table. The deletion of genes may affect the expression of genes residing downstream of the deleted genes (62). We expect that genes residing within the same operon show similar patterns of differential gene expression within the gonococcal aggregates compared to planktonic cells. Therefore, we deleted all consecutive genes in a single strain if all of them were strongly upregulated. Nevertheless, in some strains we cannot exclude that the expression of genes downstream of the deleted gene are affected by the replacement of the gene of interest with the antibiotic resistance cassette which has its own promoter. Following the operon analysis of Remmele et al (61), we find only one gene that most likely resides within an operon with a downstream gene among the deleted genes (S1 Table).

Construction of triple knock-out strain

Triple deletion strains (S3 Table) were generated by clean deletion of two genes in the background of deletion strains carrying the *kanR* resistance cassette as described above. The upstream and downstream regions of the gene of interest (each ~1000 bp) were amplified from genomic DNA of $\mathrm{wt}_{\mathrm{agg}}$ using primers cdA & cdB and cdC & cdD, respectively. The *ermC* *rpsL*$_s$ cassette was amplified from strain *T126C* step1 (Ng225) using primers cdE & cdF. The PCR products were purified with the PCR purification KIT (Qiagen) and subsequently fused with the GXL-polymerase (TaKaRa). The final fusion product was used for transformation. Selection was performed on plates containing 10 mg/ml erythromycin. Correct insertion was verified via screening PCR with primers cdA & cdD and sequencing (cdA or cdD). For the second step of the clean replacement, the upstream and downstream regions of the gene of interest (each ~1000 bp) were amplified from genomic DNA of $\mathrm{wt}_{\mathrm{agg}}$ using primers cdG & cdH and cdI & cdJ, respectively. Both PCR products were purified with the PCR purification KIT (Qiagen) and subsequently fused with the GXL-polymerase (TaKaRa). The fusion product was transformed and the strains were selected on 100 mg/ml streptomycin. Correct deletion was verified via screening PCR (cdG & cdJ) and sequencing (cdG or cdJ). All primer combinations and primer sequences are listed in S5 and S6 table, respectively.

Determination of MIC

The minimal inhibitory concentrations (MIC) of the antibiotics ceftriaxone and ciprofloxacin were determined for each strain (S2 Table). 10 µl $OD_{600}= 0.1$ cells were inoculated into 1 ml GC-medium in 48 well plates (Greiner Bio-One) and supplemented with doubling dilutions of antibiotics. Bacteria were grown in an Infinite M200 plate reader (Tecan) at 37°C, 5% CO_2 with a shaking period of 2 min per OD measurement cycle. The lowest concentration of an antibiotic without detectable growth ($OD_{600} \leq 0.1$) after 24 h was determined as the MIC of the respective antibiotic.

Bacterial survival assay

Cultures were inoculated as described for the characterization of the MIC, and grown for 10 h in an Infinite M200 plate reader (Tecan) (37°C, 5% CO_2 with a shaking period of 2 min per OD measurement cycle). After 10 h, we added antibiotics to each well except the control wells. We incubated the bacteria with 2.4 µg/ml ciprofloxacin or 4.8 µg/ml ceftriaxone for 0 h, 3 h, 6 h, or 9 h. Subsequently, the complete culture was transferred into a 1.5 ml reaction tube and cells were pelleted by centrifugation. The supernatant was discarded and 500 µl GC media and 500 µl milliQ water were added. The mixture was vortexed for 2 min. Before plating and each dilution step cells were vortexed rigorously to dissolve aggregates. Then serial dilutions were plated and incubated for 48 h (37°C, 5% CO_2). To determine the fraction of surviving cells colony forming units (CFU) of the different treatment periods (3 h, 6 h, 9 h) were divided by the CFU of the control (0 h).

Statistical analysis of the killing kinetics was performed via a combined p-values method for discrete data (40). We have used the Mann-Whitney U test to compare single time-points followed by the combination of the p-values via Mudholkar and George combining method (63).

For both antibiotic treatments, we assessed whether the introduced kanamycin allele might affect survival. We found that in the planktonic background, which is more susceptible to antibiotic treatment, the introduction of the kanamycin resistance gene in the intergenic *aspC-lctP* locus did not affect the survival compared to wt_{plank} (S8 Fig. B, C). Furthermore, we show that neither the carrying capacity of $lctP{:}kanR{:}aspC_{plank}$ nor *ΔpilE* is significantly different from wt_{plank} (S8 Fig. A)

Aggregation assay in liquid media

To check whether mutants in the wt_{agg} background maintain the ability to form aggregates in liquid media we imaged the cultures (S10 Fig.). We adjusted the OD_{600} to 0.1 and added 100 µl of cells to 200 µl of fresh GC media in an ibidi 8-well. Cells were grown for 5 h (37°C, 5% CO_2) prior to imaging. Images were recorded with an inverted Nikon Eclipse Ti with an ORCA camera model (40x magnification).

RNA isolation and sequencing

To compare the transcriptional changes between the planktonic and the biofilm lifestyle of *N. gonorrhoeae*, different strains were grown in 1 ml GC medium in a 24-well plate (Greiner Bio-One). The initial concentrations of each of the strains wt_{agg}, wt_{agg2}*ΔpilE*, wt_{plank}, wt_{plank2} were approximately 3×10^6 cells ml^{-1}. Cells were grown for 10 h at 37°C, 5% $C0_2$ in an Infinite M200 plate reader with a shaking period of 2 min per OD cycle (OD was measured every 10 min). Microscopy samples were taken to assess aggregation of each culture at this time point. Batch effects were minimized by using three replicates of each culture from the same day.

Total RNA was isolated from liquid gonococcal cultures with the RNeasy Mini Kit (Qiagen) according to the manufacturer's instructions. Prior to RNA isolation, the bacterial cultures were mixed with the RNA protect Bacteria Reagent (Qiagen) according to the manufacturer's instructions and the pellets were stored at -80 °C.

Next-generation sequencing, in particular the Illumina HiSeq system (NEB), was used to obtain gonococcal transcriptomes. mRNA sequencing was carried out by the Cologne Center for Genomics (University of Cologne, Germany) with 100 bp paired-end reads and on average 10 million reads per sample. For sample submission, the final RNA concentration was adjusted to 50-200 ng/µl in at least 10 µl volume.

Raw read analysis pipeline and differential gene expression

As a reference, the MS11 genome sequence (Ngo MS11) was obtained from NCBI with the accession number CP003909.1. This was used as a reference for all strains in the fasta format and the annotation was downloaded in the gff3 format. For improving the MS11 annotation, the orthologs of all genes were detected in *N. gonorrhoeae* FA1090 (Ngo FA1090) with the accession number NC_002946.2 and *N. meningitidis* MC85 (Nmen) NC_003112.2 via blastn (64).

The sequencing reads from each data set were trimmed and paired using Trimmomatic (version 0.36) (65). The reads were then mapped against the reference genome of Neisseria gonorrhoeae MS11 (NCBI, CP003909.1) using STAR (2.5.3a) (66). Subsequently, read counts were called for each gene of the reference with featureCounts from the subread package (version: 2.0.1) (67). The package DESeq2 implemented in R was used to perform the principal component analysis with the plotPCA function and raw count data was transformed with the regularized logarithm function. We calculated the differential gene expression with the DESeq2 package implemented in R. For each gene, we obtained the log2-fold change of the biofilm-forming strain wt_{agg} with respect to each planktonic strain ΔpilE, wt_{pilE17}, wt_{pilE24}, wt_{pilE32} as well as the associated adjusted *p*-value. A gene is regarded as differentially regulated if the (adjusted) *p*-value is ≤ 0.05 and the $|\text{log2-fold change}| \geq 0.5$.

Genes with redundant regions across the genome were excluded from the analysis. These genes were detected by blasting single gene sequences against the Ngo MS11 genome and detecting regions where blast coverage was at least at 30% with an identity of 99% or higher. For Ngo

MS11, we find 130 multi-mapping genes, which are excluded from the further analysis. As the *pilS* loci and *pilE* share similar regions among each other, we excluded all of these loci from the analysis of the global transcriptome.

Functional annotation with KEGG categories

As Ngo MS11 is not functionally annotated well, we use the Ngo FA1090 strain and its KEGG annotation (38). Each gene is sorted into one of 17 categories. Large categories containing more than 60 genes include: phage associated, metabolism of co-factors and vitamins, hypothetical, genetic information processing, energy metabolism, cellular processes/ human disease, carbohydrate metabolism, and amino acid metabolism. Genes collected in the category 'hypothetical' are not assumed to share any biological function. In the enrichment analysis, the genes that have no orthologue in Ngo FA1090 or that are not connected to any gene category in Ngo FA1090 are excluded. We test for the significance of functional enrichment in each category by performing a one-sided Fisher's exact test and Bonferroni correction to mitigate the multiple testing problem. Categories were condensed such that each gene is associated with one category.

Manuscript editing

DeepL was used for editing the grammar and formulations of the manuscript.

Acknowledgements

We thank Gerrit Ansmann, Tobias Bollenbach, Natalie Balaban, and the Maier group for helpful discussions. This work has been supported by the Center for Molecular Medicine Cologne, the Deutsche Forschungsgemeinschaft through grant MA3898 and CRC1310, and the IHRS BioSoft.

References

1. A. T. Deventer, C. E. Stevens, A. Stewart, J. K. Hobbs, Antibiotic tolerance among clinical isolates: mechanisms, detection, prevalence, and significance. *Clin Microbiol Rev* 10.1128/cmr.00106-24, e0010624 (2024).

2. N. Q. Balaban *et al.*, Definitions and guidelines for research on antibiotic persistence. *Nat Rev Microbiol* 10.1038/s41579-019-0196-3, 441–448 (2019).

3. O. Fridman, A. Goldberg, I. Ronin, N. Shoresh, N. Q. Balaban, Optimization of lag time underlies antibiotic tolerance in evolved bacterial populations. *Nature* **513**, 418-+ (2014).

4. E. J. Zheng *et al.*, Modulating the evolutionary trajectory of tolerance using antibiotics with different metabolic dependencies. *Nat Commun* **13**, 2525 (2022).

5. I. Levin-Reisman *et al.*, Antibiotic tolerance facilitates the evolution of resistance. *Science* **355**, 826-830 (2017).

6. J. Yan, B. L. Bassler, Surviving as a Community: Antibiotic Tolerance and Persistence in Bacterial Biofilms. *Cell Host & Microbe* **26**, 15-21 (2019).

7. O. Ciofu, C. Moser, P. O. Jensen, N. Hoiby, Tolerance and resistance of microbial biofilms. *Nat Rev Microbiol* **20**, 621-635 (2022).

8. R. D. Kirkcaldy *et al.*, Neisseria gonorrhoeae Antimicrobial Susceptibility Surveillance - The Gonococcal Isolate Surveillance Project, 27 Sites, United States, 2014. *MMWR Surveill Summ* **65**, 1-19 (2016).

9. C. U.S. Department of Health and Human Services (2019) CDC. Antibiotic Resistance Threats in the United States. (Atlanta, GA: U.S. Department of Health and Human Services, CDC).

10. B. Suay-Garcia, M. T. Perez-Gracia, Drug-resistant Neisseria gonorrhoeae: latest developments. *Eur J Clin Microbiol Infect Dis* **36**, 1065-1071 (2017).

11. T. D. Mortimer, J. J. Zhang, K. C. Ma, Y. H. Grad, Loci for prediction of penicillin and tetracycline susceptibility in : a genome-wide association study. *Lancet Microbe* **3**, E376-E381 (2022).

12. C. C. Bristow *et al.*, Whole-Genome Sequencing to Predict Antimicrobial Susceptibility Profiles in Neisseria gonorrhoeae. *J Infect Dis* **227**, 917-925 (2023).

13. M. Balduck *et al.*, Tolerance to Ceftriaxone in Neisseria gonorrhoeae: Rapid Induction in WHO P Reference Strain and Detection in Clinical Isolates. *Antibiotics (Basel)* **11** (2022).

14. M. Balduck *et al.*, The Prevalence of Antibiotic Tolerance in Neisseria gonorrhoeae Varies by Anatomical Site. *Pathogens* **13** (2024).

15. L. C. Wang, M. Litwin, Z. Sahiholnasab, W. Song, D. C. Stein, Neisseria gonorrhoeae Aggregation Reduces Its Ceftriaxone Susceptibility. *Antibiotics (Basel)* **7** (2018).

16. T. Cronenberg, M. Hennes, I. Wielert, B. Maier, Antibiotics modulate attractive interactions in bacterial colonies affecting survivability under combined treatment. *PLoS Pathog* **17**, e1009251 (2021).

17. M. Hennes, N. Bender, T. Cronenberg, A. Welker, B. Maier, Collective polarization dynamics in bacterial colonies signify the occurrence of distinct subpopulations. *PLoS Biol* **21**, e3001960 (2023).

18. S. S. Manoharan-Basil *et al.*, Enolase Is Implicated in the Emergence of Gonococcal Tolerance to Ceftriaxone. *Antibiotics-Basel* **12** (2023).

19. P. R. Secor, L. A. Michaels, A. Ratjen, L. K. Jennings, P. K. Singh, Entropically driven aggregation of bacteria by host polymers promotes antibiotic tolerance in Pseudomonas aeruginosa. *Proc Natl Acad Sci U S A* **115**, 10780-10785 (2018).

20. S. P. Bernier *et al.*, Starvation, together with the SOS response, mediates high biofilm-specific tolerance to the fluoroquinolone ofloxacin. *PLoS Genet* **9**, e1003144 (2013).

21. L. L. Greiner *et al.*, Biofilm Formation by Neisseria gonorrhoeae. *Infect Immun* **73**, 1964-1970 (2005).

22. M. L. Falsetta *et al.*, The Composition and Metabolic Phenotype of Neisseria gonorrhoeae Biofilms. *Front Microbiol* **2**, 75 (2011).

23. D. L. Higashi *et al.*, Dynamics of Neisseria gonorrhoeae attachment: microcolony development, cortical plaque formation, and cytoprotection. *Infect Immun* **75**, 4743-4753 (2007).

24. L. Dewenter, T. E. Volkmann, B. Maier, Oxygen governs gonococcal microcolony stability by enhancing the interaction force between type IV pili. *Integr Biol-Uk* **7**, 1161-1170 (2015).

25. H. S. Kuan, W. Ponisch, F. Julicher, V. Zaburdaev, Continuum Theory of Active Phase Separation in Cellular Aggregates. *Phys Rev Lett* **126**, 018102 (2021).

26. L. Craig, K. T. Forest, B. Maier, Type IV pili: dynamics, biophysics and functional consequences. *Nat Rev Microbiol* 10.1038/s41579-019-0195-4 (2019).

27. S. Kraus-Romer, I. Wielert, I. Rathmann, J. Grossbach, B. Maier, External Stresses Affect Gonococcal Type 4 Pilus Dynamics. *Front Microbiol* **13**, 839711 (2022).

28. A. Welker *et al.*, Molecular Motors Govern Liquidlike Ordering and Fusion Dynamics of Bacterial Colonies. *Phys Rev Lett* **121**, 118102 (2018).

29. R. Zöllner *et al.*, Type IV Pilin Post-Translational Modifications Modulate Material Properties of Bacterial Colonies. *Biophys J* **116**, 938-947 (2019).

30. A. J. Merz, M. So, M. P. Sheetz, Pilus retraction powers bacterial twitching motility. *Nature* **407**, 98-102 (2000).

31. B. Maier, How Physical Interactions Shape Bacterial Biofilms. *Annual Review of Biophysics, Vol 50, 2021* **50**, 401-417 (2021).

32. E. R. Oldewurtel, N. Kouzel, L. Dewenter, K. Henseler, B. Maier, Differential interaction forces govern bacterial sorting in early biofilms. *Elife* **4** (2015).

33. W. Ponisch, C. A. Weber, G. Juckeland, N. Biais, V. Zaburdaev, Multiscale modeling of bacterial colonies: how pili mediate the dynamics of single cells and cellular aggregates. *New Journal of Physics* **19** (2017).

34. A. Welker *et al.*, Spatiotemporal dynamics of growth and death within spherical bacterial colonies. *Biophys J* **120**, 3418-3428 (2021).

35. M. L. Falsetta *et al.*, Transcriptional profiling identifies the metabolic phenotype of gonococcal biofilms. *Infect Immun* **77**, 3522-3532 (2009).

36. N. J. Phillips *et al.*, Proteomic analysis of Neisseria gonorrhoeae biofilms shows shift to anaerobic respiration and changes in nutrient transport and outermembrane proteins. *PLoS One* **7**, e38303 (2012).

37. I. Wielert *et al.*, Antigenic variation impacts gonococcal lifestyle and antibiotic tolerance by modulating interbacterial forces. *bioRxiv* 10.1101/2023.07.06.548055 (2023).

38. R. McClure *et al.*, Global Network Analysis of Neisseria gonorrhoeae Identifies Coordination between Pathways, Processes, and Regulators Expressed during Human Infection. *Msystems* **5** (2020).

39. D. S. Wishart *et al.*, PHASTEST: faster than PHASTER, better than PHAST. *Nucleic Acids Res* **51**, W443-W450 (2023).

40. G. Ansmann, BPSB/combine-p-values-discrete: Version 1.2.1: Zenodo. (2023).

41. G. V. Smirnova, O. N. Oktyabrsky, Relationship between growth rate and bacterial susceptibility to ciprofloxacin. *Fems Microbiol Lett* **365** (2018).

42. V. M. Isabella, V. L. Clark, Deep sequencing-based analysis of the anaerobic stimulon in Neisseria gonorrhoeae. *BMC Genomics* **12**, 51 (2011).

43. S. L. Chua *et al.*, Dispersed cells represent a distinct stage in the transition from bacterial biofilm to planktonic lifestyles. *Nat Commun* **5**, 4462 (2014).

44. D. Drew, R. A. North, K. Nagarathinam, M. Tanabe, Structures and General Transport Mechanisms by the Major Facilitator Superfamily (MFS). *Chem Rev* **121**, 5289-5335 (2021).

45. M. Pasqua *et al.*, The Varied Role of Efflux Pumps of the MFS Family in the Interplay of Bacteria with Animal and Plant Cells. *Microorganisms* **7** (2019).

46. K. Nishino, A. Yamaguchi, Analysis of a complete library of putative drug transporter genes in Escherichia coli. *J Bacteriol* **183**, 5803-5812 (2001).

47. H. Yoshida, M. Bogaki, S. Nakamura, K. Ubukata, M. Konno, Nucleotide sequence and characterization of the Staphylococcus aureus norA gene, which confers resistance to quinolones. *J Bacteriol* **172**, 6942-6949 (1990).

48. B. Poudyal, K. Sauer, The PA3177 Gene Encodes an Active Diguanylate Cyclase That Contributes to Biofilm Antimicrobial Tolerance but Not Biofilm Formation by Pseudomonas aeruginosa. *Antimicrob Agents Chemother* **62** (2018).

49. P. Echave, J. Tamarit, E. Cabiscol, J. Ros, Novel antioxidant role of alcohol dehydrogenase E from Escherichia coli. *J Biol Chem* **278**, 30193-30198 (2003).

50. M. Carrolo, M. J. Frias, F. R. Pinto, J. Melo-Cristino, M. Ramirez, Prophage spontaneous activation promotes DNA release enhancing biofilm formation in Streptococcus pneumoniae. *PLoS One* **5**, e15678 (2010).

51. O. E. Petrova, J. R. Schurr, M. J. Schurr, K. Sauer, The novel Pseudomonas aeruginosa two-component regulator BfmR controls bacteriophage-mediated lysis and DNA release during biofilm development through PhdA. *Mol Microbiol* **81**, 767-783 (2011).

52. E. Bille *et al.*, A virulence-associated filamentous bacteriophage of Neisseria meningitidis increases host-cell colonisation. *PLoS Pathog* **13**, e1006495 (2017).

53. P. R. Secor *et al.*, Filamentous Bacteriophage Promote Biofilm Assembly and Function. *Cell Host Microbe* **18**, 549-559 (2015).

54. A. Piekarowicz *et al.*, Characterization of the dsDNA prophage sequences in the genome of Neisseria gonorrhoeae and visualization of productive bacteriophage. *Bmc Microbiology* **7** (2007).

55. H. Eisen, P. Brachet, L. Pereira da Silva, F. Jacob, Regulation of repressor expression in lambda. *Proc Natl Acad Sci U S A* **66**, 855-862 (1970).

56. M. Zweig *et al.*, Secreted single-stranded DNA is involved in the initial phase of biofilm formation by Neisseria gonorrhoeae. *Environ Microbiol* **16**, 1040-1052 (2014).

57. A. A. Aksyuk, M. G. Rossmann, Bacteriophage assembly. *Viruses* **3**, 172-203 (2011).

58. A. Lopatina, N. Tal, R. Sorek, Abortive Infection: Bacterial Suicide as an Antiviral Immune Strategy. *Annu Rev Virol* **7**, 371-384 (2020).

59. J. M. Koomey, S. Falkow, Cloning of the recA gene of Neisseria gonorrhoeae and construction of gonococcal recA mutants. *J Bacteriol* **169**, 790-795 (1987).

60. R. Zollner, E. R. Oldewurtel, N. Kouzel, B. Maier, Phase and antigenic variation govern competition dynamics through positioning in bacterial colonies. *Sci Rep* **7**, 12151 (2017).

61. C. W. Remmele *et al.*, Transcriptional landscape and essential genes of. *Nucleic Acids Res* **42**, 10579-10595 (2014).

62. A. Mateus *et al.*, Transcriptional and Post-Transcriptional Polar Effects in Bacterial Gene Deletion Libraries. *mSystems* **6**, e0081321 (2021).

63. G. O. George, G. S. Mudholkar, On the convolution of logistic random variables. *Metrika* **30**, 1-13 (1983).

64. C. Camacho *et al.*, BLAST+: architecture and applications. *BMC Bioinformatics* **10**, 421 (2009).

65. A. M. Bolger, M. Lohse, B. Usadel, Trimmomatic: a flexible trimmer for Illumina sequence data. *Bioinformatics* **30**, 2114-2120 (2014).

66. A. Dobin *et al.*, STAR: ultrafast universal RNA-seq aligner. *Bioinformatics* **29**, 15-21 (2013).

67. Y. Liao, G. K. Smyth, W. Shi, featureCounts: an efficient general purpose program for assigning sequence reads to genomic features. *Bioinformatics* **30**, 923-930 (2014).

68. C. Hepp, B. Maier, Kinetics of DNA uptake during transformation provide evidence for a translocation ratchet mechanism. *Proc Natl Acad Sci U S A* **113**, 12467-12472 (2016).

7 Eversion of Gonococcal Colonies is Triggered by Differential Pilus Interactions

The single-cell interaction forces shape bacterial biofilms [17]. Especially for *N. gonorrhoeae*, it was found that the attractive interactions mediated by T4P of single cells lead to spherically shaped microcolonies [16]. The phenotypic characteristics of the colonies are determined by the interactions between the individual cells, as the colonies undergo phase transitions from liquid-like to solid-like depending on the interactions between the cells [16].

As the colonies grow, chemical gradients, including oxygen, are likely to be established towards the centre of the colonies [77]. At the single cell level, we know that piliation levels depend on the external stress applied [132] and that oxygen concentration affects pilus-pilus interactions [60]. In *N. gonorrhoeae*, a spatio-temporal gradient of growth has been observed, accompanied by the emergence of a hyperpolarisation ring that expands over time due to oxygen limitation [103, 105].

How nutrient and oxygen gradients affect phenotypic behaviour over time remain unclear. To assess the spatio-temporal dynamics of cell motility within the colony during the establishment of oxygen gradients, we tracked individual cells in the colony and analysed the within-colony dynamics over time.

This work was performed in close collaboration with Stephan Wimmi (from our group) and Marc Hennes (from our group), Kai Zhou (Institute for Infectious Diseases and Zoonoses, Ludwig-Maximilians-Universität Munich) and Benedikt Sabass (Institute for Infectious Diseases and Zoonoses, Ludwig-Maximilians-Universität Munich). The initial work was done by Marc Hennes. Stephan Wimmi performed the experiments and Kai Zhou and Benedikt Sabass have worked on the theoretical simulations of gonococcal colonies. I developed the tools for image analysis and analysed all movies to quantify single-cell motility and cellular fluxes during colony development.

7.1 Gonococcal Colonies Evert and Disperse Single Cells

In order to study the dynamics of maturing gonococcal colonies, we performed flow chamber experiments with the wt* strain to follow the growth of gonococcal colonies under a constant nutrient supply. Using bright-field imaging, we revealed an unexpected behaviour: the colonies evert. Phenotypic characterisation shows that in the first hours, the colony radii increased due to growth. After approximately 6 h, eversion occurs and we observed a rapid morphological transformation (Fig. 7.1A). The cells, initially located at the centre of the colony, gradually move towards the periphery until the colony's surface ruptures. Subsequently, most of the cells that were previously residing at the colony centre spread across the colony surface. This process causes an eversion of the colony. Additionally, a fraction of cells disperse.

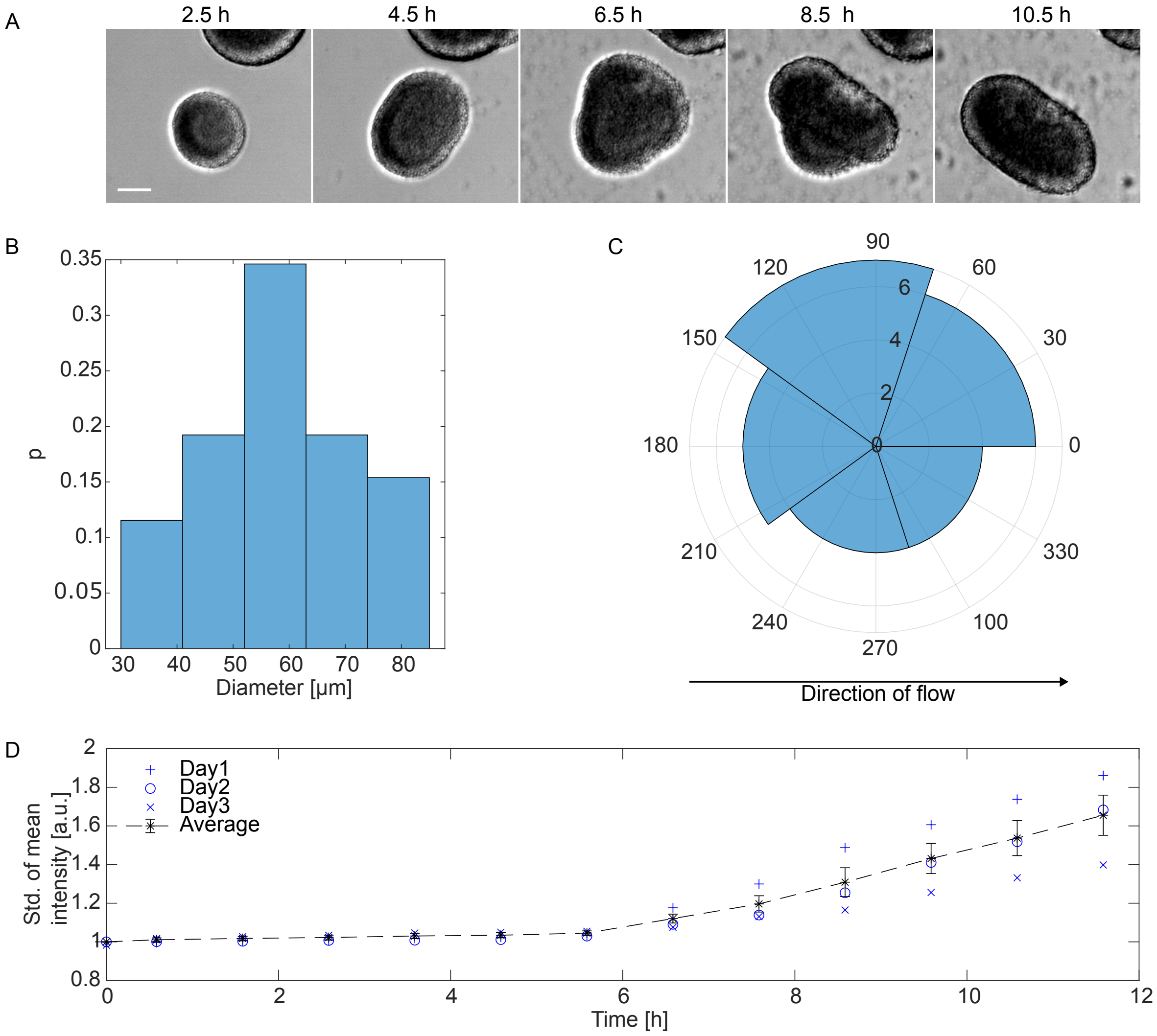

Figure 7.1: A) Time-lapse of colony during flow-chamber experiment. Scale bar = 20 µm. B) Distribution of size of colonies prior to eversion. C) Direction of eversion with regard to the flow direction. D) Standard deviation of the mean intensity of the empty area of the flow chamber. N = 3.

The analysis of the brightfield images revealed that approximately 25% of colonies exhibited this phenomenon, with the entire process taking approximately 2.5 h. The average diameter of colonies undergoing eversion was found to be $D_{eversion}$ = 58.28±13.02 µm (standard deviation) (Fig. 7.1B). As we performed the experiments under flow, we also tested if the eversion direction is correlating with the direction of the flow. To this end, the eversion direction measured from bright-field images was analysed regarding the flow direction. The results showed a distribution of the eversion direction (Fig. 7.1C), which was independent of the flow direction. When eversion began, we also noticed an increase in single cells around the colonies. The time point at which single cells emerge – indicated by an increase in the standard deviation of the mean in an previously empty ROI of 253.9 x 139.9 μm – was consistent across the experiments at ≈ 6 h (Fig. 7.1D). These single cells subsequently generated new colonies (Supplementary 9.5, Fig. 9.1). By visual inspection of the brightfield movies, the inner core of the colonies seemed to become more motile. We characterised motility systematically by single-cell tracking within the colonies. To this end, the fluorescent strain wt_{green} was utilised, and flow chamber experiments were performed with enhanced temporal and imaging resolution. The results obtained from tracking the single cells demonstrated that cells migrate from the centre to the periphery, and at the edges, cells flow back outwards (Fig. 7.2A).

We characterised the single cell motility in the inner core of the colony at different time points prior to eversion and during eversion. In particular, we were interested whether the behaviour showed characteristics of diffusive or ballistic behaviour. The MSDs of the bacteria at the centre were determined (Methods 2.3.4), revealing the scaling behaviours for the different time points (Fig. 7.2B). At early time points, the scaling exponent of $0.29 < 1$ indicates sub-diffusive behaviour in agreement with caged dynamics [102]. Directly before eversion, the scaling exponent increased, suggesting that the behaviour becomes more diffusive. During eversion, the motility transitions to a super-diffusive scaling behaviour with a scaling exponent of $1.36 > 1$.

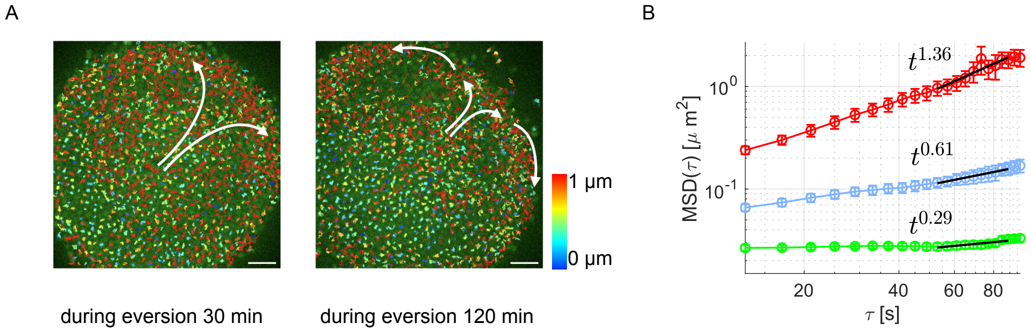

Figure 7.2: A) Overlay between gfp-fluorescence intensity and single-cell trajectories over 4 min at the start of colony eversion (left) and during colony eversion (right). The white arrows are drawn to guide the eye and indicate the direction of the ballistic movement of the cells. Scale bar = 5 μm. Color bar = track displacement. B) MSDs of cells at the centre of the colony (spherical ROI with R=10 μm). Red: during eversion; Blue: 30 min prior to eversion; Green: 2-3 h prior to eversion. The black lines are linear fits to the curves in the time interval of 50-90 s, indicating the scaling behaviour. N = 7.

The higher motility right before eversion indicated that the cells in the centre show reduced interactions. One idea why there might be decreased interaction was an increasing number of dead cells due to nutrient or oxygen limitation towards the centre of the colony. We investigated the dynamics of external DNA and dead cells during eversion via labelling of external DNA and dead cells with SytoX (Fig. 7.3A). Their flow was analysed via PIV (Methods 2.3.4). In the early hours of the experiment, dead cells and DNA accumulated in the colony's centre (Fig. 7.3B). During the eversion process, these cells and the external DNA moved towards the periphery. The results obtained demonstrate that colonies reaching a specific size after six hours of growth tend to undergo eversion. During this process, central cells showed super-diffusive movement towards the periphery, resulting in the dispersion of individual cells, dead cells and external DNA from the colony.

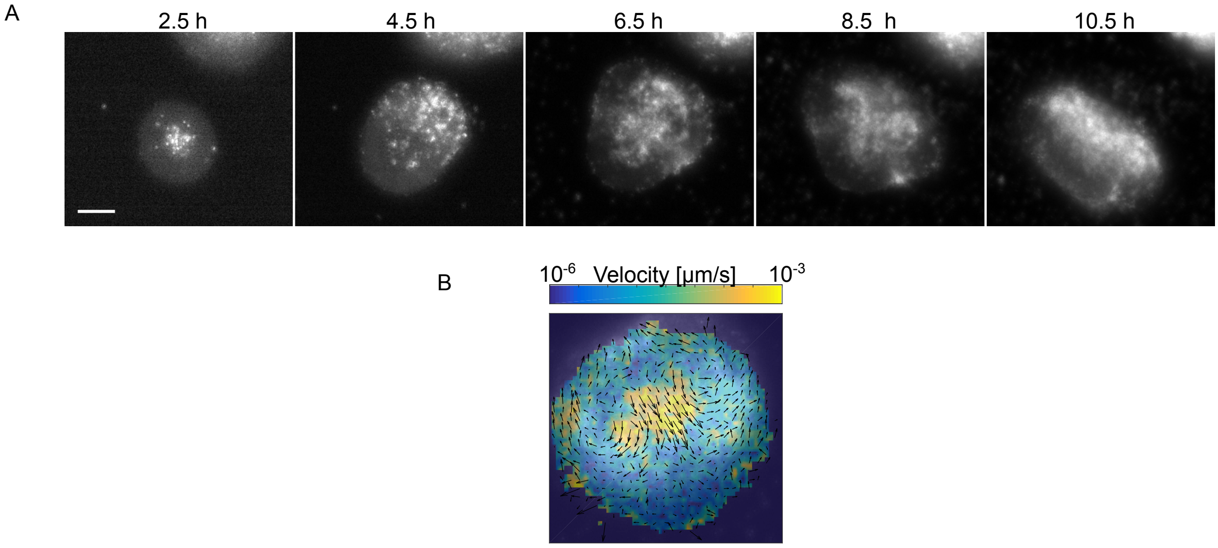

Figure 7.3: A) Time-lapse microscopy of *N. gonorrhoeae* colony with external DNA and dead cells stained with SytoX. Passed time is indicated above each micrograph. Scale bar: 20 µm. B) Example of PIV analysis of SytoX signal over 1 h. Color bar: velocity of flow.

7.2 Analysis of Single-Cell Motility Reveals a Travelling Wave of Hyper-Motile Cells

Since, we have observed the super-diffusive movement of the cells in the centre and the outward flow during eversion, we aimed in understanding what the trigger for eversion and the more motile inner core is.

It is known that oxygen depletion occurs in the centre of the colony [105]. In addition, Stephan Wimmi performed pilus labelling experiments in air-tight chambers and showed that oxygen depletion reduces piliation, which leads to decreased single-cell interaction. Moreover, it was shown that reduced oxygen concentration decreases pilus-pilus interaction [60]. These findings suggest that an oxygen gradient towards the centre of the colony leads to decreased cohesion of the cells and by this to increased motility.

To test whether reduced cohesion in the centre of the colony is sufficient to explain eversion, Benedikt Sabass and Kai Zhou performed simulation experiments of a colony of total size r_t and an inner less interacting shell of radius r_i. They found that eversion depends on the ratio of the colony size r_t and the width of the strongly interacting outer shell $d = r_t - r_i$ [158].

To correlate this prediction with the experiments, we analysed the spatio-temporal dynamics of the entire gonococcal colonies prior to eversion. The within-colony motility was monitored every 30 min prior to eversion (Fig. 7.4A). From single-cell tracks we determined the effective diffusion constant D (Methods 2.3.4). Initially, we observed homogeneous motility, characterised by caging dynamics within the colony (Fig. 7.2B) [102]. Notably, cells located at the colony's surface exhibited larger track displacements due to their enhanced degrees of freedom, as not all pili were bound. These cells were excluded for further analysis. Subsequent observation over time revealed the emergence of a motile shell within the colony centre, which expanded over time until the outer shell, exhibiting reduced motility, ruptured and the colony everted (Fig. 7.4B). Other examples, also including the edge of the colony, can be found in the supplementary material (Supp. 9.5, Fig. 9.2A-F). Furthermore, the analysis of the radii of the inner shell (Methods 2.3.4) prior to eversion revealed an increase over time (Fig. 7.4C) in accordance with the theoretical predictions.

These findings indicate that prior to eversion, a highly motile shell, which is triggered by reduced cohesion forces of the cells, expands until the less-motile outer shell ruptures and the colony everts.

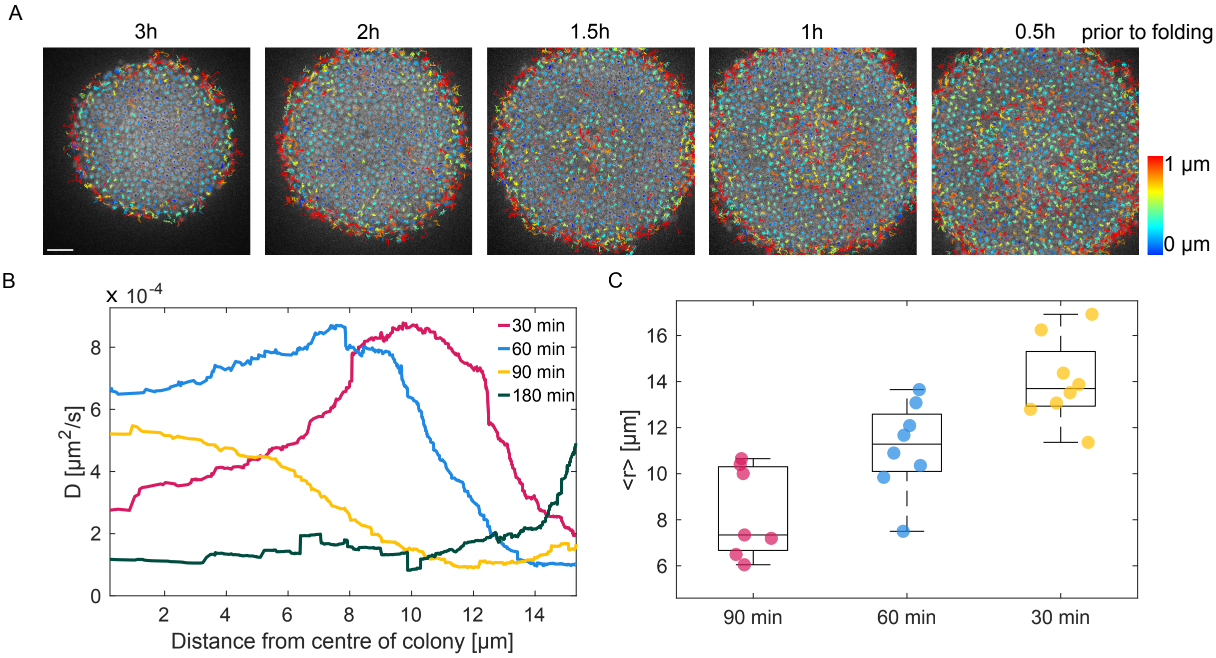

Figure 7.4: A) Overlay between gfp-fluorescence intensity of the cells and single-cell trajectories at different times prior to colony eversion. Scale bar: 5 µm. Color bar = track displacements. B) Radially averaged effective diffusion constant *D* as a function of the distance from the centre of the colony for the times series shown in A. The hyper-motile surface is removed for clarity. C) Radius of hyper-motile inner shell as a function of time prior to colony eversion. N = 7.

7.3 Discussion

This study investigated the phenomenon of gonococcal colony eversion during maturation. The process of eversion was first characterised, followed by the analysis of the spatio-temporal dynamics of gonococcal colonies prior to eversion.

We found that an expanding, highly motile inner shell is formed prior to eversion. We hypothesise that the trigger for less attractive interactions of the bacteria in the centre is a reduced oxygen concentration, which leads to weaker interaction strength of the bacteria, resulting in the more motile inner core (Fig. 7.5). This hypothesis is based on the observation that oxygen depletion occurs in the centre of the colony [105] and that reduced oxygen concentrations lead to strongly reduced pilus-pilus interactions [60]. This is also in agreement with the finding of Stephan Wimmi, who demonstrated that piliation is reduced by oxygen reduction by directly visualising T4P during oxygen depletion.

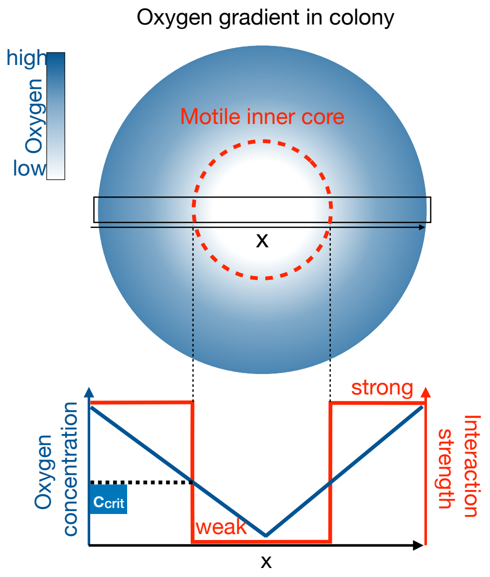

Figure 7.5: Hypothetical correlation between oxygen concentration and interaction strength in gonococcal colony. Slicing through the colony (marked with black rectangle) reveals decreasing oxygen levels towards the centre and increasing levels towards the periphery. Interaction strength is dependent on the local oxygen concentration: when the concentration exceeds a critical threshold ($c > c_{\text{crit}}$), bacteria exhibit strong interactions. Below this threshold, the interaction strength is weak, leading to the formation of a motile inner core (marked with red dashed line) within the colony.

As a consequence, cohesion at the centre is reduced, which shifts the system away from its free energy minimum according to the differential strength of adhesion theory [100]. To minimise its free energy again, the system then undergoes eversion.

The role of external DNA and dead cells during the eversion process is not entirely clear and needs further investigation. Increased levels of external DNA could be a byproduct of oxygen depletion which could lead to cell death and the subsequent release of DNA. Since DNA is a stabilising factor during colony formation [20], it could influence in which direction the colony everts. If the accumulation of DNA stochastically stabilises regions in the colony, these would be less prone to rupture as the motile shell is built and the direction of eversion would not be determined, which is consistent with our experimental results.

Another open question is which biological function colony eversion has, and whether this process confers a selective advantage in terms of survival or infection. Eversion could facilitate bacterial dispersal under nutrient- or oxygen-limited conditions, where remaining within the dense biofilm structure would be disadvantageous. Supporting this hypothesis, we observed that cells released during eversion are able to form new colonies in the surroundings, suggesting that eversion acts as an effective mechanism for spatial expansion.

In conclusion, we have shown that bacterial colonies undergo eversion during maturation. The formation of a hyper-motile shell suggests that cells in the centre exhibit reduced attractive interactions. We hypothesise that an oxygen gradient leads to reduced cohesion at the centre, which consequently results in colony eversion. In addition, we observed that cells were expelled during this process, which may be beneficial for the bacterial population under nutrient-limited conditions by facilitating spatial expansion. Further research is needed to investigate the role of external DNA accumulation and to elucidate the biological function of the eversion process.

8 Conclusion and Outlook

In this work we investigated how T4P properties affect cell-to-cell interactions and how these affect the physical properties of bacterial colonies in *N. gonorrhoeae*. We further show that aggregation and colony mechanics influences antibiotic tolerance (Fig. 8.1).
At the single-cell level, we used two complementary techniques to study T4P-mediated interactions: fluorescence-based live-cell imaging to visualise T4P dynamics, and dual optical laser tweezers to determine the forces between attractively interacting cells. Following antibiotic treatment, fluorescence microscopy revealed a significant reduction in T4P dynamics, while laser tweezers measurements showed altered cell-to-cell interactions. To study the effect of antigenic variation, we analysed different PilE variants and found that changes in the stereochemistry of the major pilin modulate the attractive forces between cells, as confirmed by the laser tweezers experiments.
At the multicellular level, we found that the strength of attractive interactions determines the bacterial lifestyle, with weak interactions promoting planktonic growth and strong interactions leading to aggregation into gonococcal colonies. Upon antibiotic treatment, both the degree of aggregation and colony viscosity influenced bacterial susceptibility as evidenced by altered killing kinetics: stronger interactions conferred increased antibiotic tolerance.

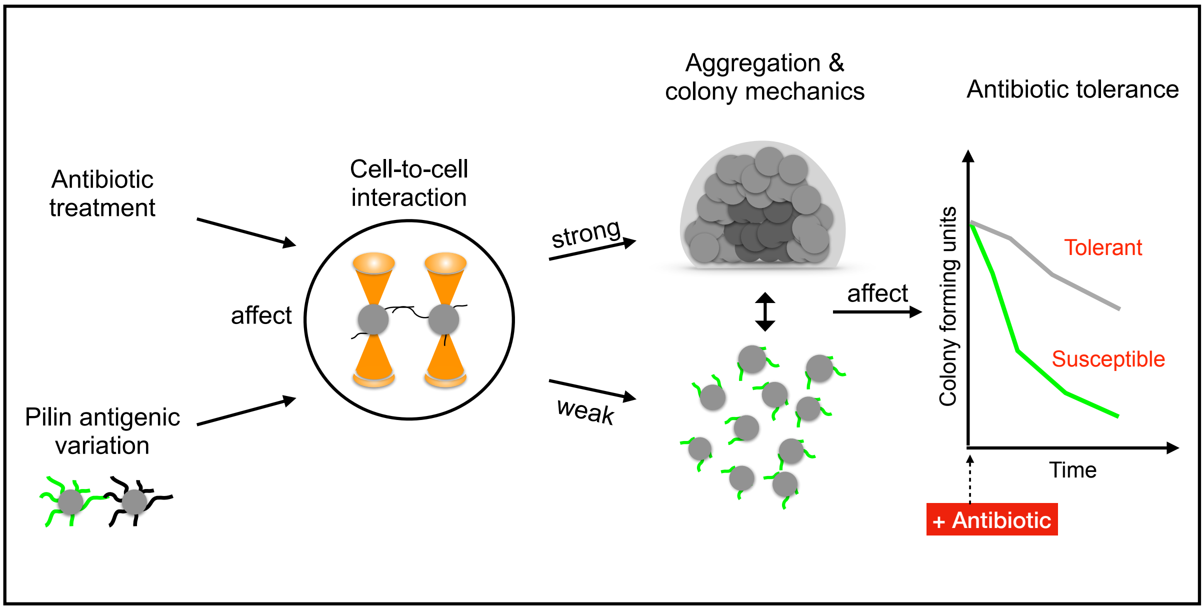

Figure 8.1: Graphical abstract of this work. We showed that antibiotic treatment and pilin antigenic variation affect single-cell interactions. The altered cell-to-cell attractions led to changes in aggregation and colony mechanics. The resulting bacterial lifestyle, aggregating or planktonic, directly influence antibiotic tolerance.

The Interplay of Extracellular DNA, Prophages and Antibiotic Tolerance

In this study, we have shown that aggregating *N. gonorrhoeae* are protected from ceftriaxone and ciprofloxacin treatment. In addition, by comparing the transcriptomes of bacteria with either a planktonic or an aggregating lifestyle, and by examining deletion strains of genes that were highly upregulated in the biofilm, we found that prophage genes influence tolerance differently in planktonic and aggregating strains.

The prophage Φ_1 was found to be upregulated in the aggregating strain. We assign this to a stress response due to nutrient and oxygen limitation for cells in depth of the colonies, as phages can be activated by external stresses [159]. We also observed an effect of phage gene deletions in the planktonic strains, which we attributed to phage activity due to stress during antibiotic treatment. Lytic activity of phages in planktonic cells may reduce survival, but could provide matrix material in the form of extracellular DNA for aggregating cells, potentially affecting the biophysical properties of the colonies. It was already demonstrated that extracellular DNA affects colony dynamics and the formation of biofilms for *S. aureus*. DNase treatment was shown to result in reduced biomass and clumping of bacteria [160]. Furthermore, in *Shewanella oneidensis* biofilms, iron-induced prophage activation has been shown to result in an increase in external DNA [161] and in *Streptococcus pneumoniae*, prophage activation promotes DNA release, thereby enhancing biofilm formation [162].

In this work, an accumulation of dead cells and extracellular DNA in the centre of mature colonies was observed, supporting the hypothesis that extracellular DNA and dead cells may influence colony structure and dynamics (Section 7.1). More solid colonies, promoted by a stronger DNA network, would result in better protection, as we have shown that reduced motility leads to higher antibiotic tolerance (Chapter 4).

So far, extracellular DNA has been shown to stabilise early biofilms [20, 60] and is a major component of the extracellular matrix of gonococcal biofilms [19], for *N. gonorrhoeae*. However, the impact of prophage activity, which might promote external DNA release, on antibiotic tolerance in gonococcal biofilms remains to be elucidated. Furthermore, it would be interesting to test whether gonococci have evolved a symbiotic interaction with the phage during biofilm formation. One approach to investigate this would be to examine the live/dead cell ratio during phage activity using live cell imaging with labelled dead cells. It would also be interesting to specifically fluorescently label the phage in biofilms, examine its level of activity and correlate this with the number of dead cells to demonstrate lytic activity under external stress. A subsequent step would be to investigate how colony dynamics are affected when the phage is deleted – is motility within the colony enhanced or does the colony still grow? Direct visualisation of the DNA network combined with analysis of the local order could reveal whether increased external DNA results in more densely packed colonies.

How does Standing Variation of PilE Affect Pathogenicity and Antibiotic Tolerance During Infection?

T4P play a central role in host colonisation by mediating initial adhesion [24] and enabling infection, as unpiliated bacteria were shown to be unable to cause infections in males [163]. The high rate of antigenic variation [43] suggests that a bacterial population carries multiple antigenic variants during infection. Our research revealed that pilin variants exhibit a planktonic or aggregating lifestyle and that aggregating variants are protected from antibiotic treatment. One possibility is that pilin antigenic variation acts as a bet-hedging strategy during infection. Based on the hypothesis that planktonic strains may facilitate spreading, while aggregating strains offer protection from external stress, it could be advantageous for a bacterial population to carry both variants simultaneously – enabling rapid adaptation to changing environmental conditions. To explore this hypothesis, two key aspects need to be tested, the first being whether planktonic variants indeed promote spreading. This could be addressed using cervical epithelial cells [78] to determine if specific pilin variants enhance spatial colonisation using direct imaging of the infected tissue. However, the eversion process observed in bacterial colonies could also facilitate spatial expansion, which would challenge this hypothesis. Second, the potential protective role of aggregation during infection should be tested by comparing infection outcomes in the presence and absence of antibiotic treatment. Here, a co-culture tissue model representing different cell types, could be used [164] and combined with direct imaging. Another infection model would be provided by endometrium organoids, recently developed by Borretto et al. [165], as *N. gonorrhoeae* is often associated with the pelvic inflammatory disease [166]. For other pathogenic bacteria, such as *P. aeruginosa* and *S. aureus*, biofilm formation has been shown to be a response to antibiotic treatment [167, 168]. In contrast, gonococci exhibit a constant variation of different lifestyles, which may influence the rate at which persistent infections develop, as the biofilm lifestyle is often found in persistent infections [8]. These experiments could also clarify the broader biological function of colony formation, which remains poorly understood in *N. gonorrhoeae* infections [169]. A deeper understanding of the infection process and its connection to antibiotic tolerance could contribute to the development of new treatment strategies for *N. gonorrhoeae* infections.

How does Anaerobic Respiration Affect Single-Cell Interactions and Colony Dynamics?

Oxygen limitation plays a crucial role during infection. *N. gonorrhoeae* colonises anatomical sites such as the urogenital tract, pharynx, and rectum [170, 171], where oxygen levels are significantly lower than in ambient air. For example, in the female reproductive tract, oxygen concentrations decrease from approximately 5% in the fallopian tubes to 2% in the uterus [172, 173], and to about 0.4% in the oral cavity [174], compared to 20% in the atmosphere [175]. Under these oxygen limited conditions, gonococci have been observed to switch from aerobic respiration to anaerobic denitrification to survive [79, 176]. In this work, we demonstrated that aggregating bacteria also showed increased expression of genes associated with anaerobic respiration compared to planktonic cells. Additionally, we observed that gonococcal colonies undergo eversion, a process we propose is triggered by oxygen depletion towards the centre of the colony and the resulting reduction in cell-cell cohesion. Dewenter et al. demonstrated that gonococcal colonies disassemble under anaerobic conditions [60]. Moreover, recently, a study reported collective membrane hyperpolarisation in the centre of gonococcal colonies, driven by oxygen depletion, which could be suppressed by nitrite supplementation [105]. These findings indicate that oxygen limitation plays a critical role in biofilm formation and raise the question of whether providing nitrite as an alternative electron acceptor can restore piliation and aggregation under anaerobic conditions and potentially preventing eversion. It also remains unclear how colony structure and motility are affected under oxygen limitation and nitrite supplementation.

A possible experimental approach would be to characterise single-cell interactions, twitching motility, and colony formation under anaerobic conditions with nitrite supplementation. Anaerobic conditions could be achieved by introducing an oxygen scavenging system or by working with air-tight systems. These experiments would also provide insights whether biofilms can be formed during infections and which role aggregation plays under anaerobic conditions.

9 Supplementary Information

9.1 Supplementary Information for Chapter 3

Here, supplementary information of the reprinted publication from chapter 3 will be reprinted [132].

Supplementary information for

External stresses affect gonococcal type 4 pilus dynamics

Sebastian Kraus-Römer[1]*, Isabelle Wielert[1]*, Isabel Rathmann[1], Jan Grossbach[2], Berenike Maier[1, 3, #]

*equal contribution

[1] University of Cologne, Institute for Biological Physics

[2] University of Cologne, Faculty of Mathematics and Natural Sciences, CECAD

[3] Center for Molecular Medicine Cologne

berenike.maier@uni-koeln.de

Supplementary Figures

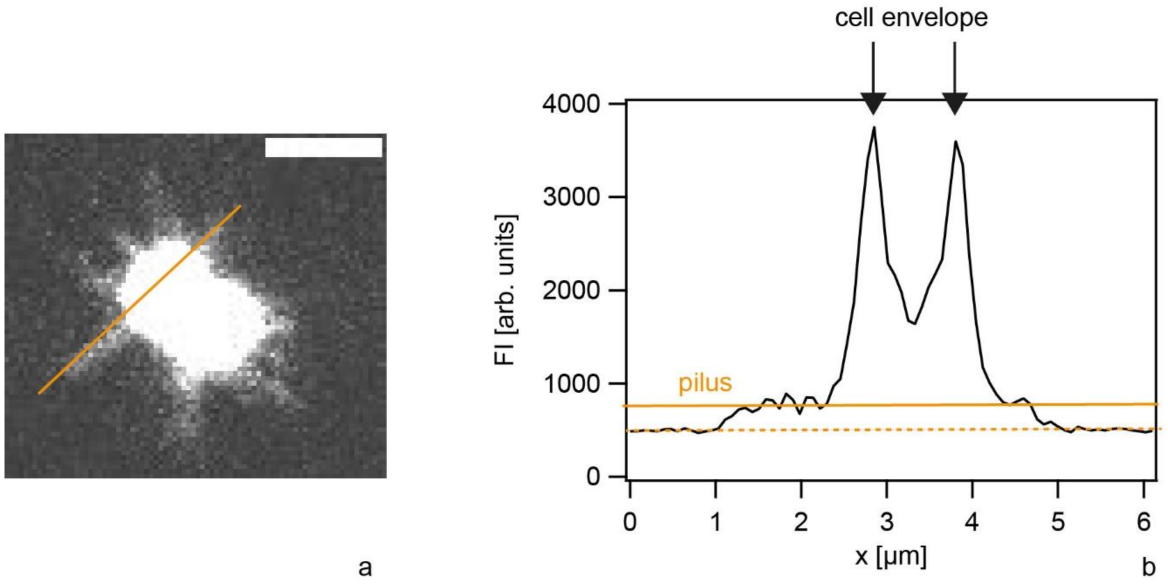

Fig. S1. The fluorescence intensity of the cell contour exceeds the intensity of labeled T4P. a) Labeled gonococcus. The intensity profile is measured along the orange line. Scale bar: 2 µm. b) The intensity profile along the orange line of a). The background intensity is identified (dashed orange line at 500 a.u). The labelled T4P intensity was 750 a.u. (solid orange line). The cell body was found to have an intensity maximum of 3800 a.u.

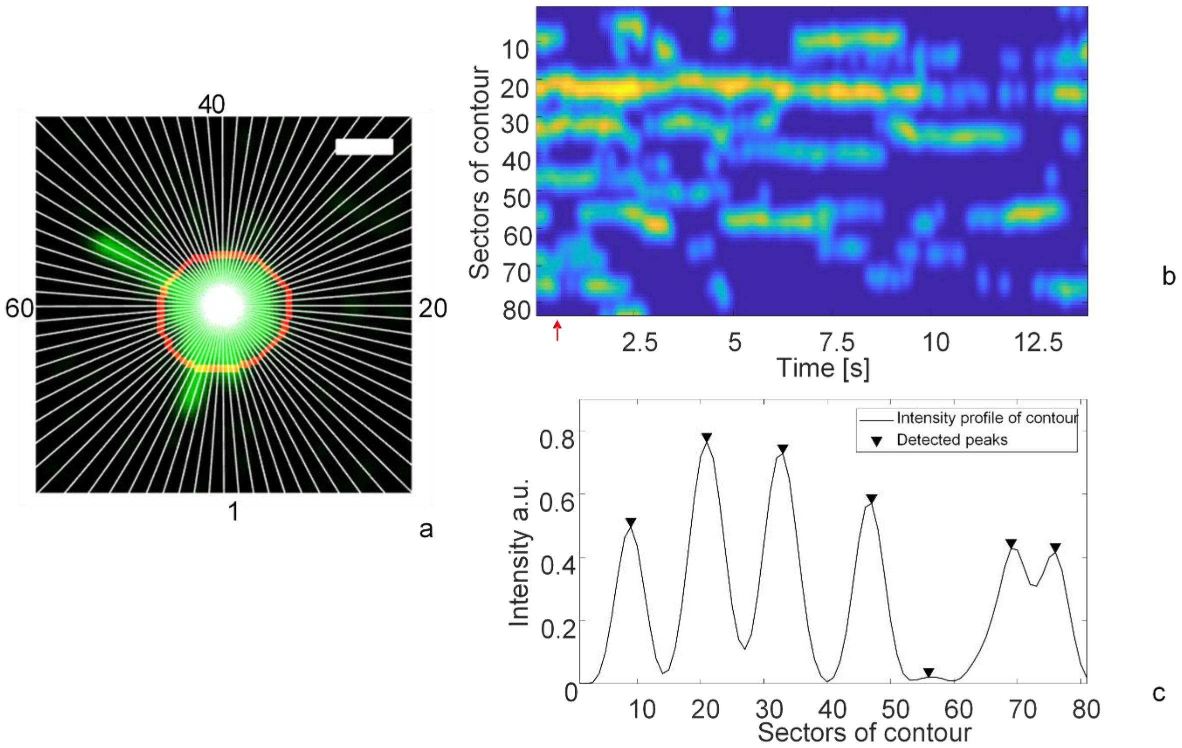

Fig. S2 Determination of the T4P production rate, r_P. a) Labeled gonococcus with T4P (green) and its contour (red). The white lines represent the division of the contour in 80 parts. Scale bar: 1 µm. b) Kymograph of contour. Frame 10 marked with red arrow. c) Intensity profile from contour for frame 10 of the kymograph with detected peaks (black arrows) representing the present T4P.

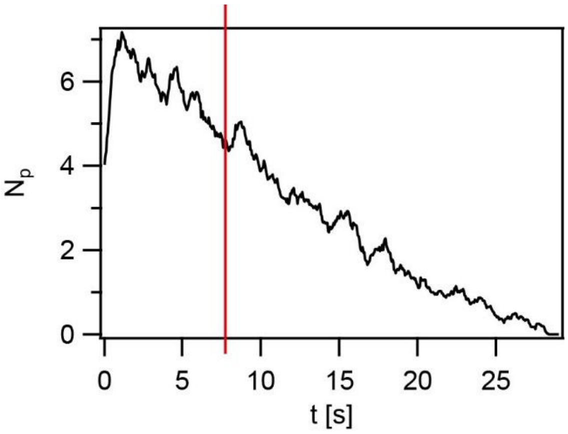

Fig. S3 The detected number of T4P per cell, N_p, decreases rapidly. N_p as a function of time averaged for 40 gonococci. At time t = 0, image acquisition starts. The red line marks the initial 7.5 s.

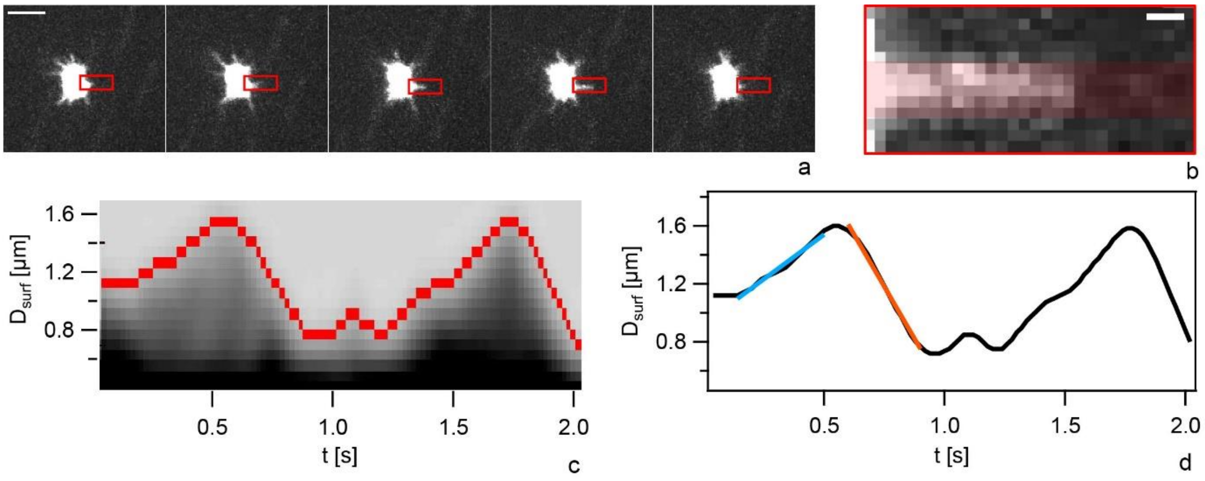

Fig. S4 Determination of the velocities of T4P elongation, v_{elo}, and retraction, v_{ret}. a) Time lapse of T4P elongation and retraction. Time between each image: 0.5 s, Scale bar: 3 µm. b) ROI shown in a). The red shaded area represents area used to create the intensity profiles for the kymograph. Scale bar: 0.3 µm. c) Kymograph and edge detection. Distance of the cell surface, D_{surf}, as a function of time. d) Example track of the pilus tips' distance to the cell surface D_{surf} with time. Blue line: slope used to determine the elongation velocities. Orange line: slope used to to determine the retraction velocities.

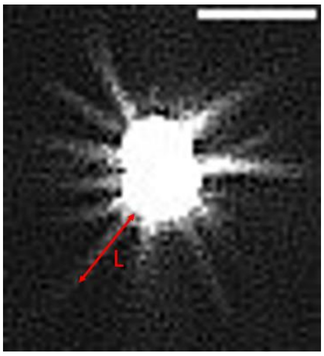

Fig. S5 Determination of the maximum T4P length, l_p. The sum of all intensity values for the first 100 frames of the acquired videos. The red line represents how the length L of the T4P are determined. Scale bar: 2 µm.

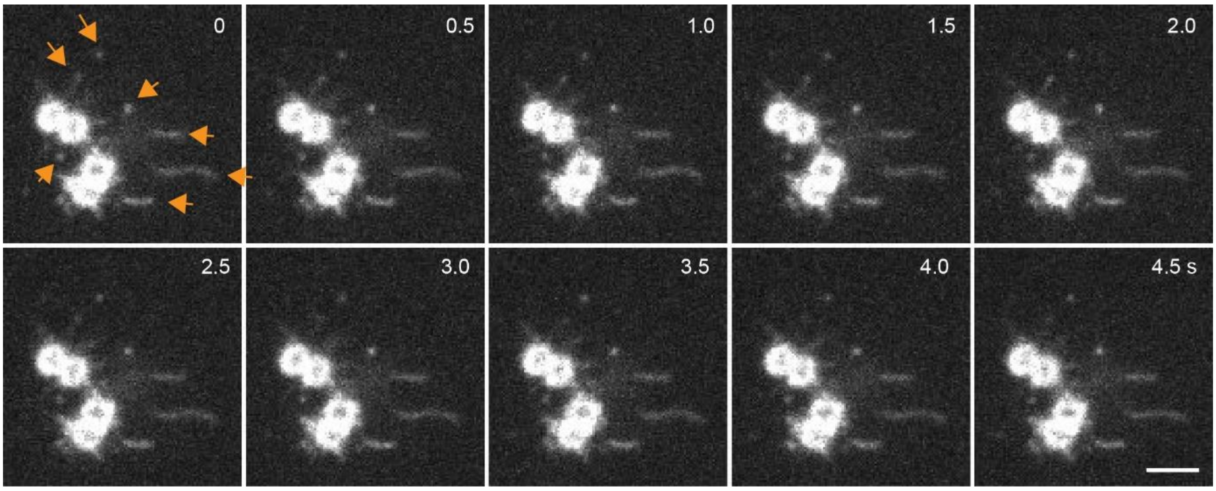

Fig. S6 Time lapse of *ΔpilT* mutant gonococci (Ng250). Orange arrows depict typical fluorescent foci observed around *ΔpilT* bacteria, indicating that mostly the tips of T4P are fluorescent. We suggest that fluorescent pilin is integrated into the T4P during and shortly after incubation with the fluorescent dye. After removal of AF488 molecules, new (unlabeled) pilin is synthesized and integrated into existing T4P.

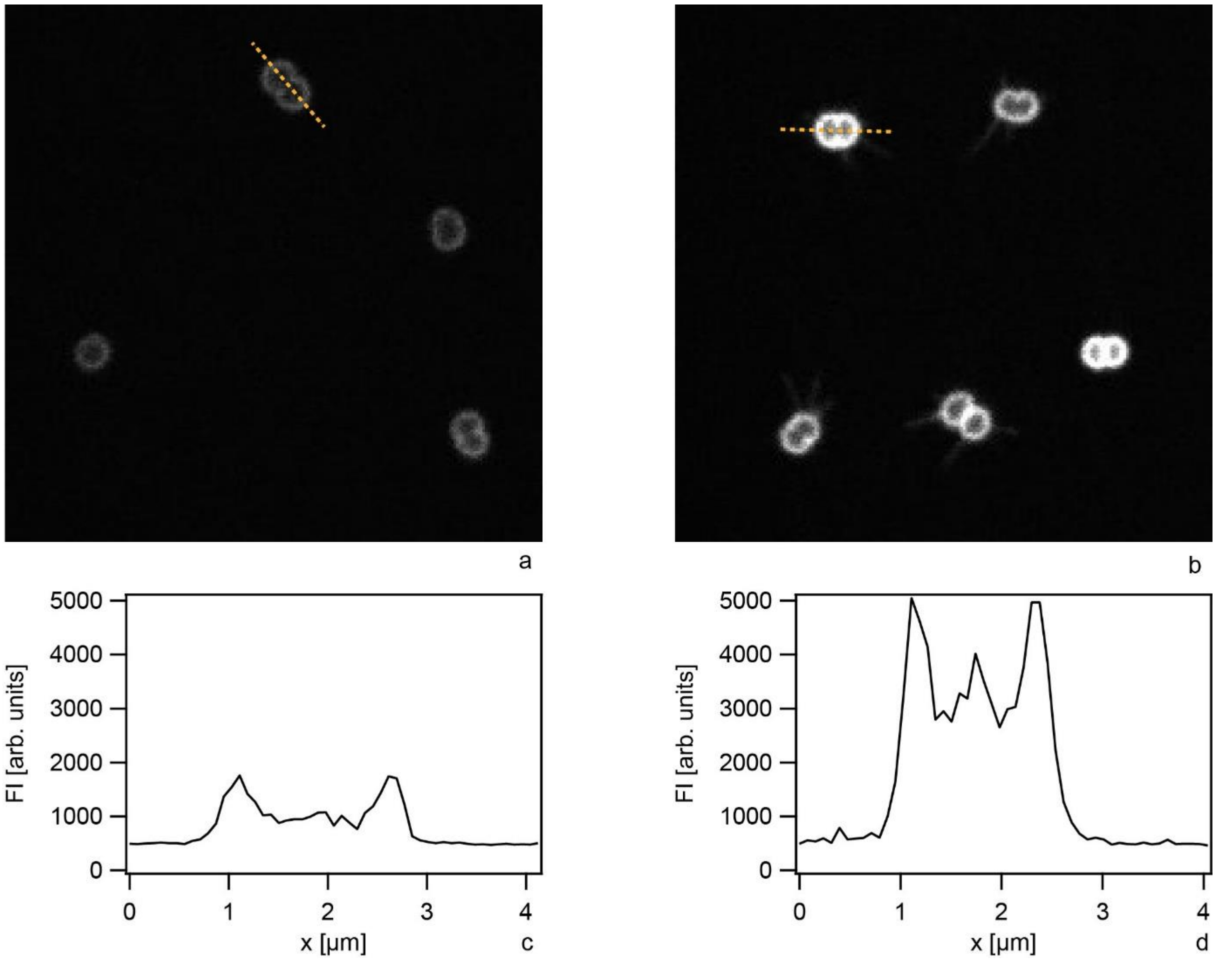

Fig. S7 Staining of the cell envelope. Bacteria were incubated with Flour 488 C_5 maleimide dye as described in the Methods. a) Parental strain NG150 lacking the T126C modification and b) NG226 carrying the T126C modification in the major pilin. c) Intensity profile through the dotted lines shown in a). d) Intensity profile through the dotted lines shown in b).

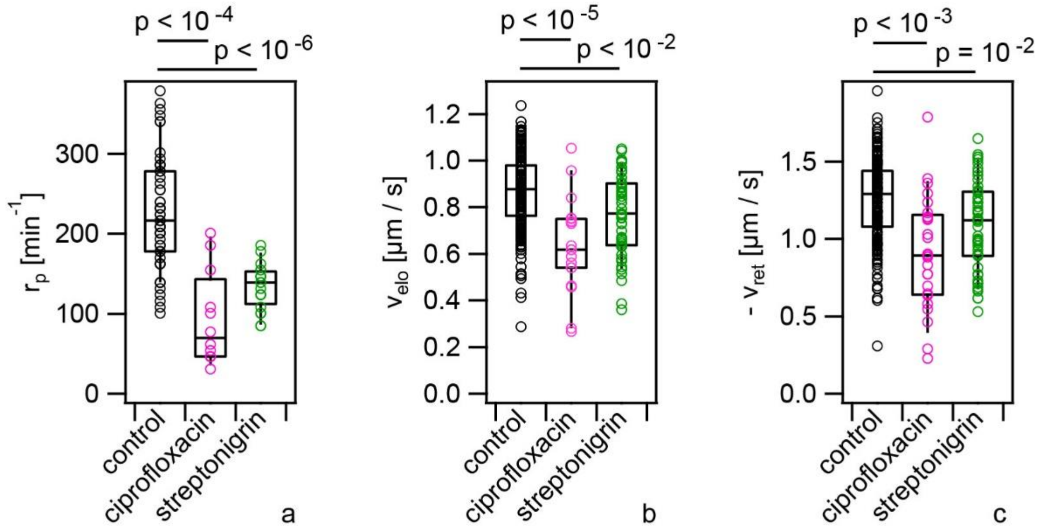

Fig. S8 Antibiotics that interfere with DNA replication reduce T4P production rate. Cells were treated with ciprofloxacin or streptonigrin, respectively at 2-fold MIC for 3 h. a) Rate of T4P production, r_p. (> 12 cells for each condition) b) T4P elongation velocities, v_{elo} (> 18 T4P for each condition). c) T4P retraction velocities, v_{ret} (> 24 T4P for each condition). Shown are circles: single T4P data, box: 25 / 75 percentiles, and median for 171 T4P. p-values obtained from KS test.

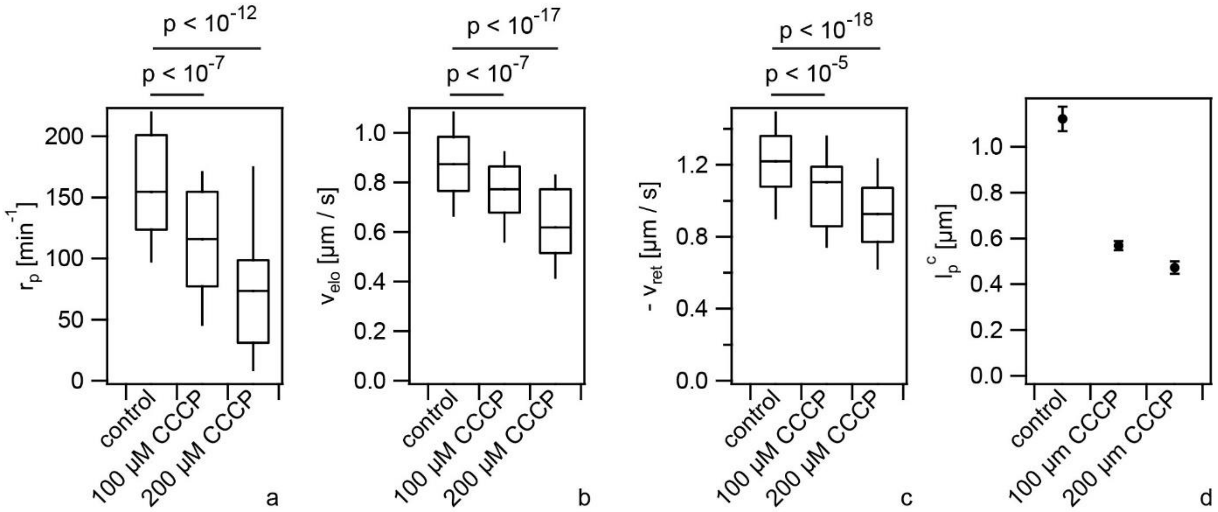

Fig. S9 CCCP reduces T4P production rate and T4P dynamics. Cells were treated with CCCP for 10 min. a) Rate of T4P production, r_p. (> 30 cells for each condition) c) T4P elongation velocities, v_{elo} (> 87 T4P for each condition). d) T4P retraction velocities, v_{ret} (> 100 T4P for each condition). Shown are box: 25 / 75 percentiles, and median for 171 T4P. p-values obtained from KS test. d) Characteristic maximal T4P length. (> 156 T4P for each condition)

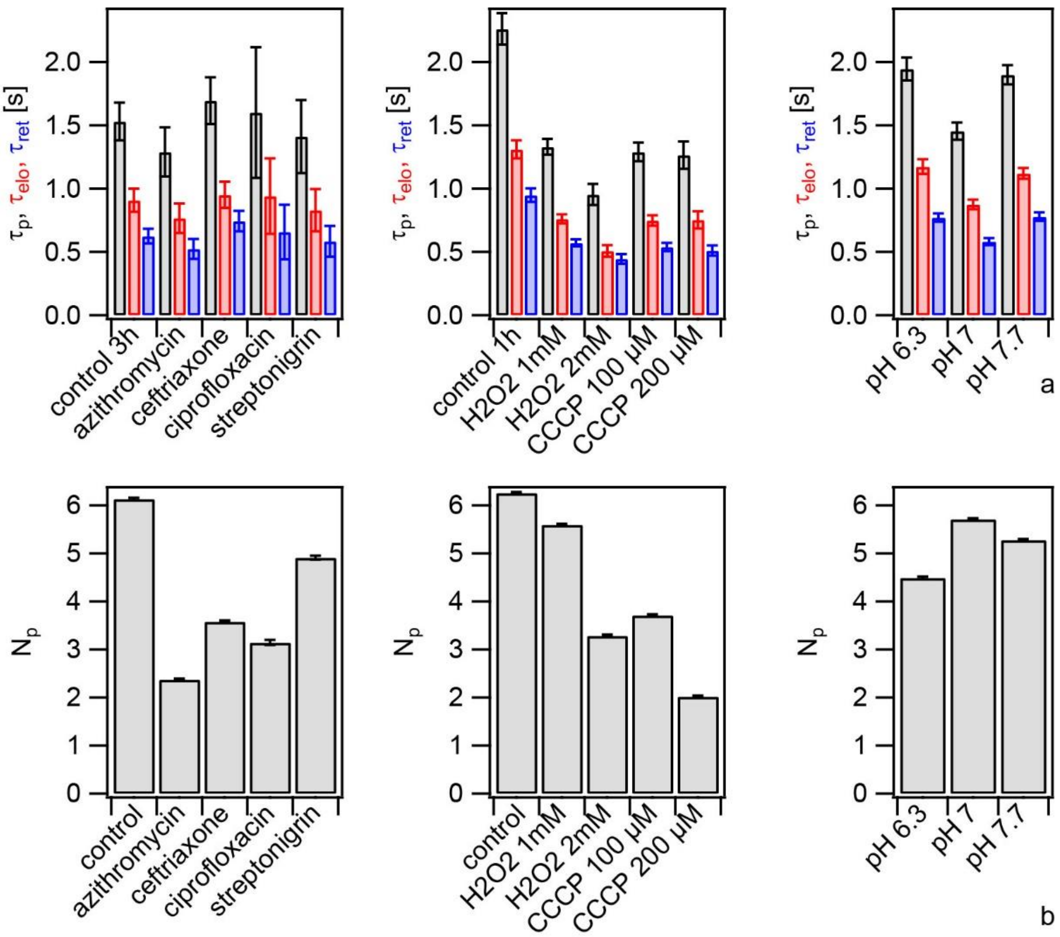

Fig. S10 T4P lifetimes, τ_p, and number of T4P, N_p, under the different conditions studied. a) Mean T4P lifetimes calculated as $\tau_p = l_p/v_{elo} + l_p/v_{ret}$ (grey), mean durations of T4P elongation calculated as $\tau_{elo} = l_p/v_{elo}$ (red), and mean durations of T4P elongation calculated as $\tau_{ret} = l_p/v_{ret}$ (blue). Error bars: standard error of the mean. b) Mean number of T4P per cell, N_p, and standard error. Please note that the incubation times in the different subpanels are different (see Methods).

Supplementary Tables

***Neisseria gonorrhoeae* strains**	**relevant genotype**	**source**
ΔG4 (Ng150)	*G4::aac*	(1)
pilE^{T126C}(Ng226)	*G4::aac* *pilE::pilE*^{T126C}	this study
pilE^{T126C} Δ*pilT* (Ng250)	*G4::aac* *pilE:: pilE*^{T126C} *pilT::m-Tn3cm*	this study, (2)

Table S1 Strains used in this study

name	5'→3' sequence
sk5	CCGCTCGAGCGGTTCCGACCCAATCAACACACC
sk9	TATAACCCTCTTTATTTTTTCCTCC
sk10	AGCTTTGGCTAACACACACG
sk32	GGGCCTTGAAGCGCAATCGATATA
sk40	AATATCTATACTTAAGTCATTTGGCATCAGATGCCTTA
sk43	AAAATGGTTCTGCGGACAGCCGGTT**TGC**CGCGCCGCCAAAGACGACGACGCCG
sk44	ACCGAACCGTTTTCACGCTTGGCCCACAGGGAGAG
sk45	CAACCCTTAAAGGAAAAACCATGCAATAC
sk129	TTCCGACCCAATCAACACA
sk131	TTTAAGGCCTAATTTGCCTCATTTGGCATCAGATGCCTTAT
sk132	ATCTGATGCCAAATGAGGCAAATTAGGCCTTAAATTTTA
sk135	GATTTATTTAAAATTTAAGGCCTAATTTGCCAATTCCCGACTGATTGTGAGG
sk143	GTCGGGAATTGGCAAATTAGGCCTTAAATTTTAAATAAATC
sk145	ATGCCGTCTGAATAGTCGAATCGATGCTGTG
sk146	ATCTGATGCCAAATGACCCGGTGCTTCATCACC
sk147	CACCGGGTCATTTGGCATCAGATGCCTTA
sk158	GTATCGGCAATGACGGTTCG

Table S2 Primers used in this study

Substance	MIC		Source
	Δ*G4* *(Ng150)*	ΔG4 *pilE*^{T126C} (Ng226)	
azithromycin[µg/mL]	0.128	not determined	(3)
ceftriaxone[µg/mL]	0.008	not determined	(3)
cirpofloxacin[µg/mL]	0.004	0.004	this study
streptonigrin[µg/mL]	0.064	0.064	this study
H_2O_2 [mM]	2	1	this study

Table S3 Minimal inhibitory concentrations

9.2 Supplementary Information for Chapter 4

Here, supplementary information of the reprinted publication from chapter 4 will be reprinted [131].

Supporting figures, tables, and movies

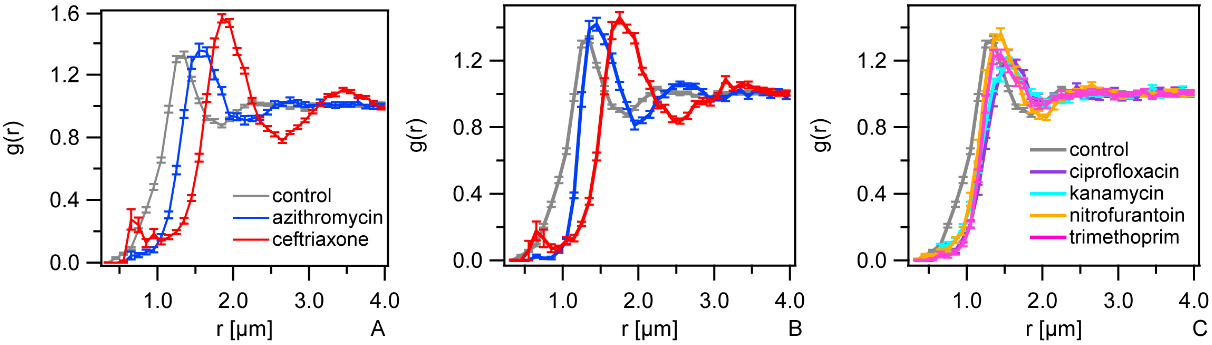

Fig. S1 Radial distribution functions. Bacteria (wt*, Ng150) were inoculated into flow chambers and colonies were allowed to assemble for 1 h. Subsequently, they were treated with antibiotics for 3 h at a) 100x MIC, or b, c) 1x MIC. The values for r_0 shown in Fig. 2d, f are obtained from fits to eq. 1 to these distributions.

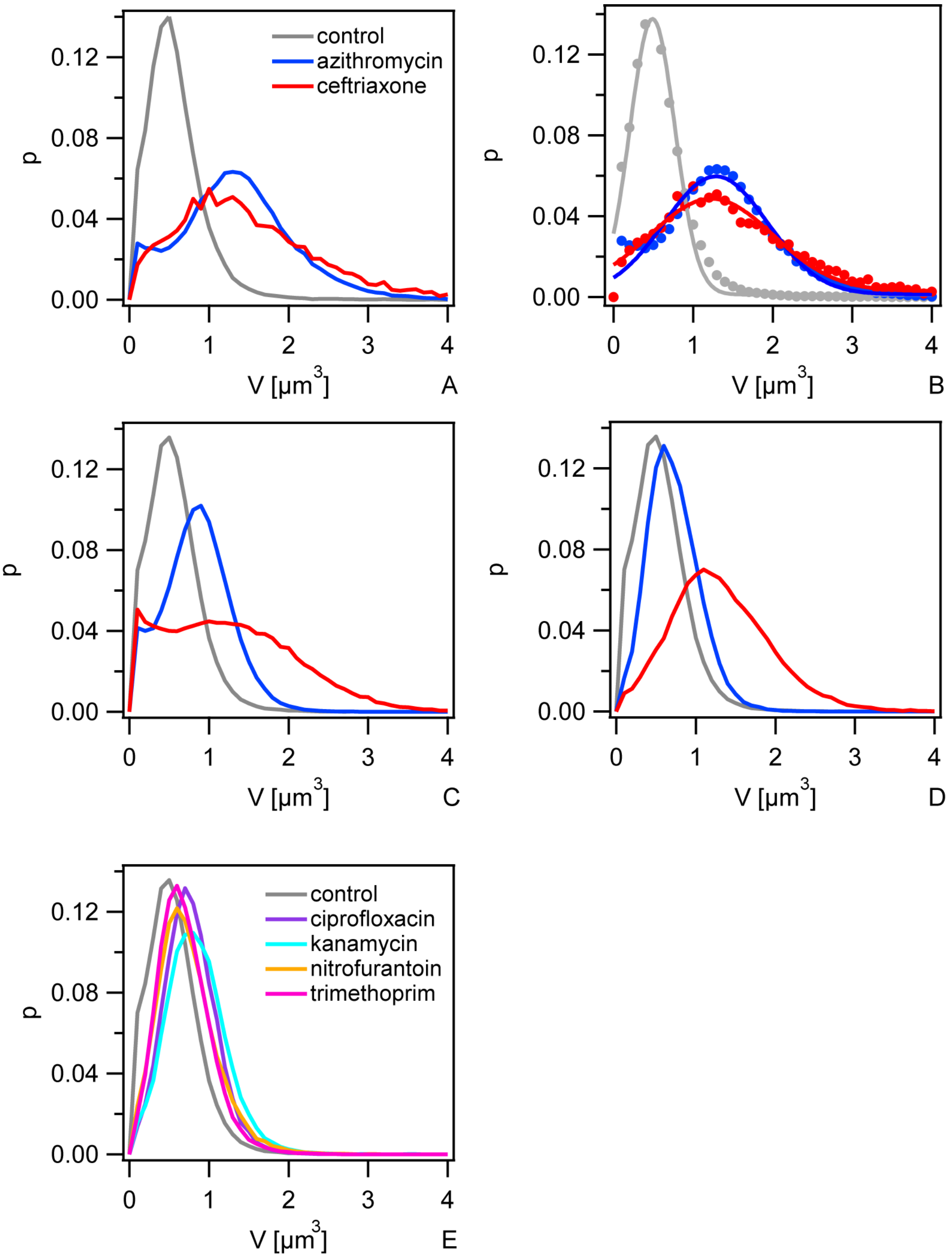

Fig. S2 Distributions of cell volumes. Bacteria (wt*, Ng150) were inoculated into flow chambers and colonies were allowed to assemble for 1 h. Subsequently, they were treated with antibiotics for a, b) 5 h at 100x MIC, c) 3 h at 100x MIC, d - e) 3 h at 1x MIC. The mean values shown in Fig. 2e, g are obtained from Gaussian fits to these distributions. b) Markers: data points, full lines: fits to Gaussian function.

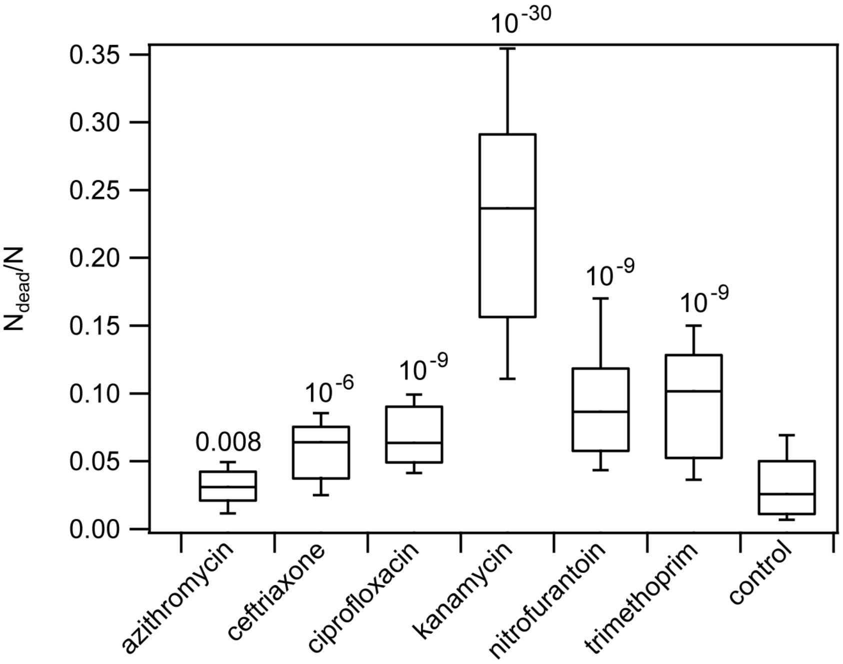

Fig. S3 Fractions of dead cells $f_{dead} = N_{dead}/N$ after 3 h of treatment at 1x MIC. Numbers: p-values from two sample KS-test against the control.

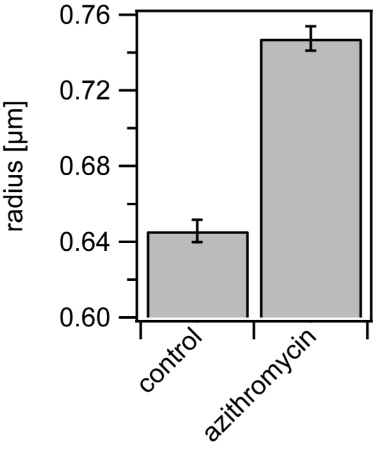

Fig. S4 Control for cell radius increase under azithromycin treatment. wt* cells (Ng150) were incubated for 1 h in liquid medium and subsequently treated with azithromycin at 100x MIC for 2 h. Radii of individual cells were determined using phase contrast microscopy. Mean ± standard error of radii of N = 75 cells. $p < 10^{-16}$ (KS test).

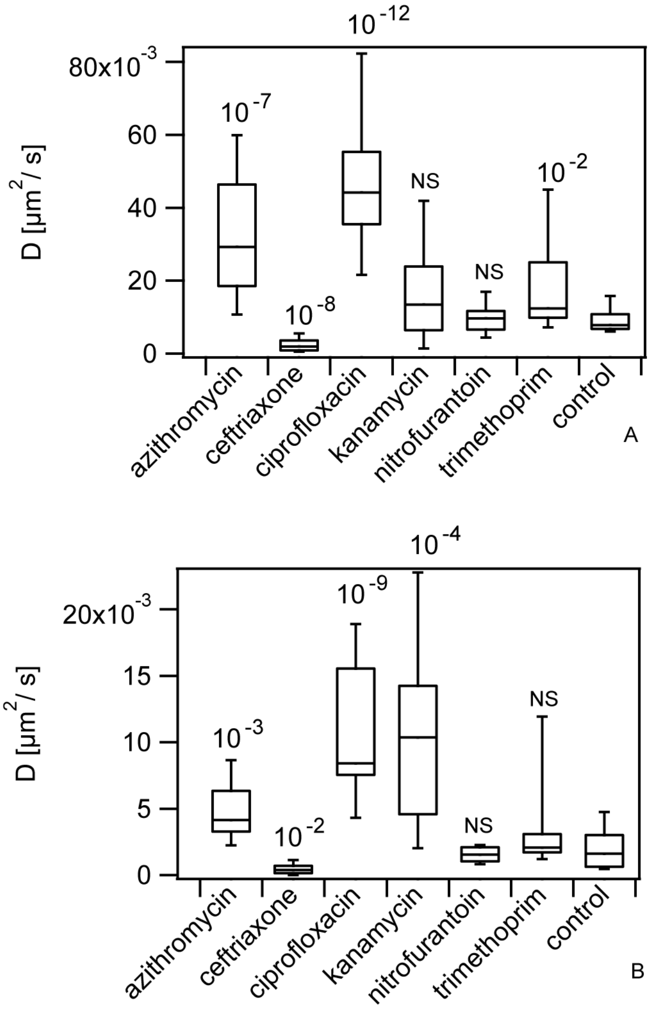

Fig. S5 Antibiotic treatment strongly affects bacterial motility within colonies. wt* gonococci (Ng150) were inoculated into flow chambers and colonies were allowed to assemble for 1 h. Subsequently, they were treated with different antibiotics at their respective MICs for 3 h (0.064 µg / ml azithromycin, 0.004 µg / ml ceftriaxone, 0.002 µg / ml ciprofloxacin, 20 µg / ml kanamycin, 0.48 µg / ml nitrofurantoin, 32 µg / ml trimethoprim). Effective diffusion constant was measured at a) the edge and b) at R = 5 µm into the colony. N = 12 - 20 colonies. Numbers are p-values from two sample KS-test against the respective controls.

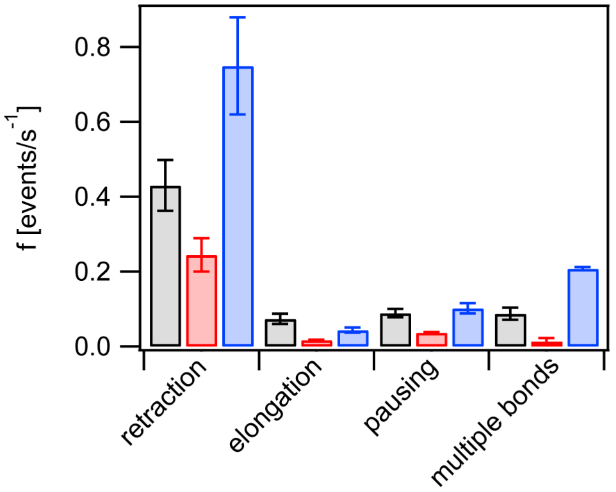

Fig. S6 Frequencies of T4P retraction, elongation, pausing, and multiple T4P-T4P bonds. Grey: control, red: with 6.4 µg / ml azithromycin for (2 - 3) h, blue: with 0.4 µg / ml ceftriaxone for (2 - 3) h. Error bars: bootstrapping.

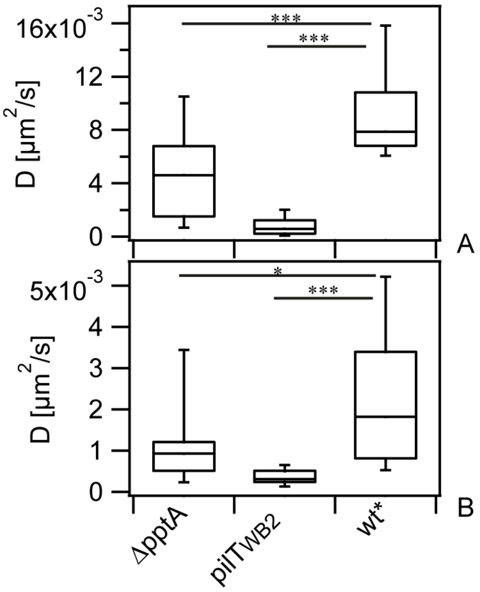

Fig. S7 Mean effective diffusion constant *D* of untreated cells at a) the edge of the colony and b) within the colony at *R = 5* µm after 6 h of growth for strains *ΔpptA* (Ng142), *pilT*$_{WB2}$ (Ng176), and wt* (Ng150). Box: 25/75 percentile, whiskers: 10/90 percentile. N = 13 - 20. All statistical comparisons were made by two-sample KS-test: *P 0.05; ***P 0.001.

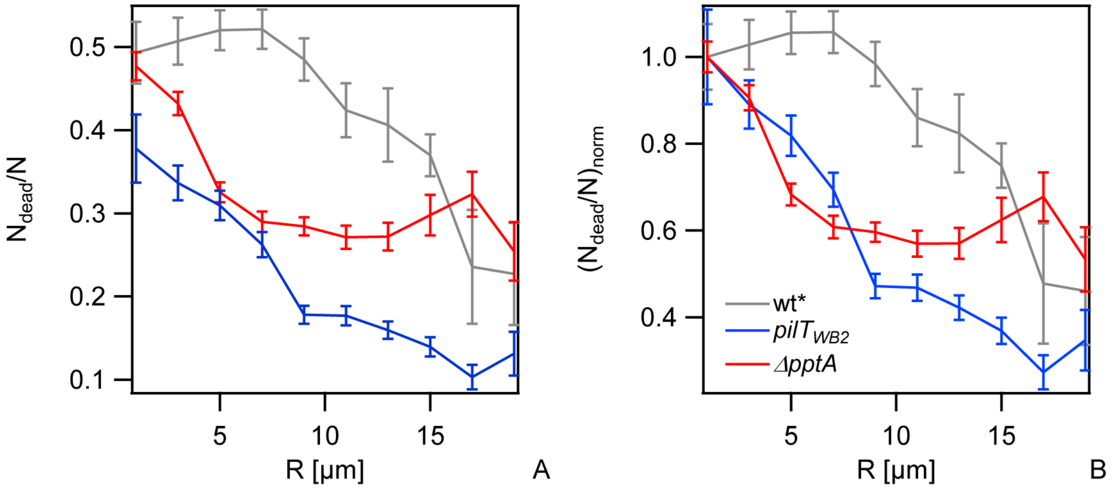

Fig. S8 Fraction of dead cells $f_{dead} = N_{dead}/N$ in colonies as a function of distance from the edge of the colony at R = 0. Bacteria were inoculated into flow chambers and colonies were allowed to assemble for 1 h. Subsequently, they were treated with with 0.4 µg / ml ceftriaxone for 5 h. a) Fractions of dead cells. b) Fractions of dead cells normalized to fraction at the edge. Grey: wt* (Ng150), blue: *pilT*$_{WB2}$ (Ng176), red: *ΔpptA* (Ng142). Error bars: standard error of the mean. N = (9 - 46) colonies per data point.

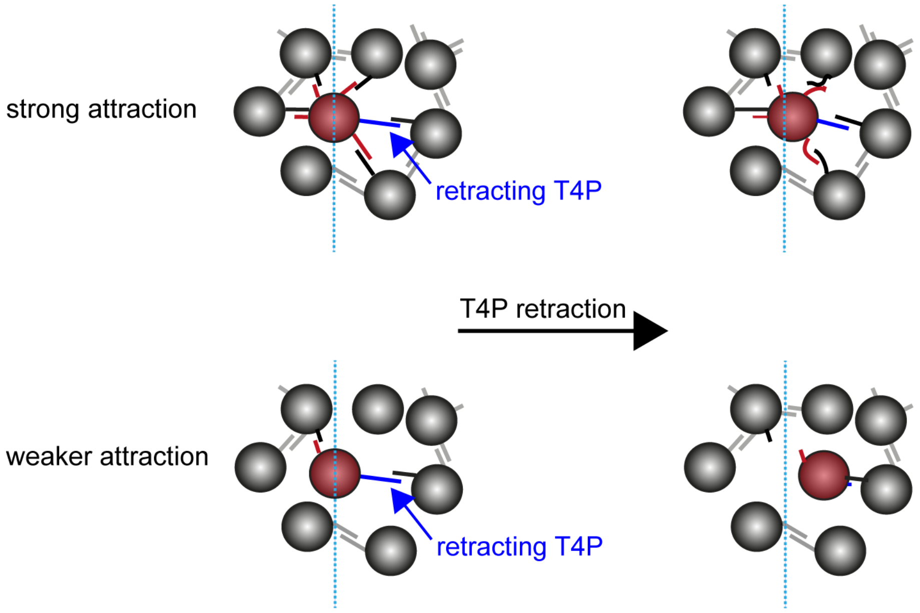

Fig. S9 Tug-of-war model for motility within colony. In the absence of azithromycin, a bacterium within the colony simultaneously forms multiple bonds with adjacent bacteria (top). When a T4P retracts, movement of the cell body is hindered by T4P-T4P bonds at the opposite side of the retracting pilus. In the presence of azithromycin, the probability that a T4P-T4P bond is formed is reduced (bottom). Thus the probability that a retracting T4P has opposing T4P-T4P bonds is lower. As a consequence, the bacterium is more motile.

Strain	**Relevant genotype**	**Source/Reference**
*wt** (Ng150)	*G4::aac*	[17]
pilT$_{WB2}$ (Ng176)	*iga::P*$_{pilE}$ *pilTWB ermC* *G4::aac*	[16]
ΔpptA (Ng142)	*pptA::kan* *G4::aac*	[17]
ΔpilE (Ng196)	*pilE::cat* *G4::aac*	This study, [16]

Table S1 Bacterial strains used in this study

antibiotic	**MIC [µg / ml]** *ΔpilE*	**MIC [µg / ml]** wt*
azithromycin	0.064	0.128
ceftriaxone	0.004	0.008
ciprofloxacin	0.48	
kanamycin	32	
nitrofurantoin	0.002	
trimethoprim	20	

Table S2 Minimal inhibitory concentrations (MICs) of antibiotics. MICs were determined from bacteria that cannot form colonies (Δ*pilE*, Ng196) and from colony-forming *wt** (Ng150) by testing for the ability to grow overnight.

Movie S1. Typical movie of a single confocal plane of untreated wt* cells. Purple circles denote the positions of individual cells. When individual circles disappear transiently, the tracking algorithm has lost the position this bacterium. Scale bar: 10 µm, Δt = 0.03 s.

https://doi.org/10.1371/journal.ppat.1009251.s013

Movie S2. Typical movie of a single confocal plane of azithromycin-treated wt* cells (100 MIC, 5 h). Purple circles denote the positions of individual cells. When individual circles disappear transiently, the tracking algorithm has lost the position this bacterium. Scale bar: 10 µm, Δt= 0.03 s.

https://doi.org/10.1371/journal.ppat.1009251.s014

9.3 Supplementary Information for Chapter 5

Here, supplementary information of the reprinted publication from chapter 5 will be reprinted [133].

Supporting Information for

Pilin antigenic variants impact gonococcal lifestyle and antibiotic tolerance by modulating interbacterial forces

Isabelle Wielert[1,2,§], Sebastian Kraus-Römer[1,2,§], Thorsten E. Volkmann[1,2], Lisa Craig[3], Paul G. Higgins[2,4,5], Berenike Maier[1,2, *]

[1]Institute for Biological Physics, University of Cologne, Germany

[2]Center for Molecular Medicine Cologne

[3]Department of Molecular Biology and Biochemistry, Simon Fraser University, Burnaby, British Columbia, Canada

[4]Institute for Medical Microbiology, Immunology and Hygiene, Faculty of Medicine and University Hospital Cologne, University of Cologne, Cologne, Germany

[5]German Centre for Infection Research, Partner site Bonn-Cologne, Cologne, Germany

[§] equal contribution

***** corresponding

Supporting Figures

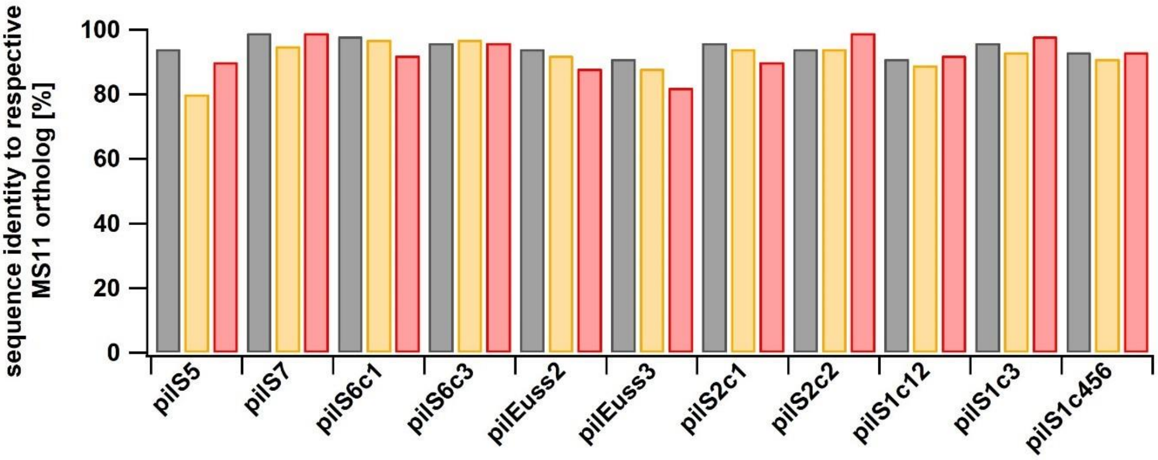

Figure i. Sequence identity of *pilS* copies from gonococcal clinical isolates to orthologs from *N. gonorrhoeae* MS11. The sequence identity of each *pilS* to the respective copy of strain MS11 was determined using blastn (BLAST®, NCBI). grey: *pilS*$_{24}$, orange: *pilS*$_{17}$, red: *pilS*$_{32}$.

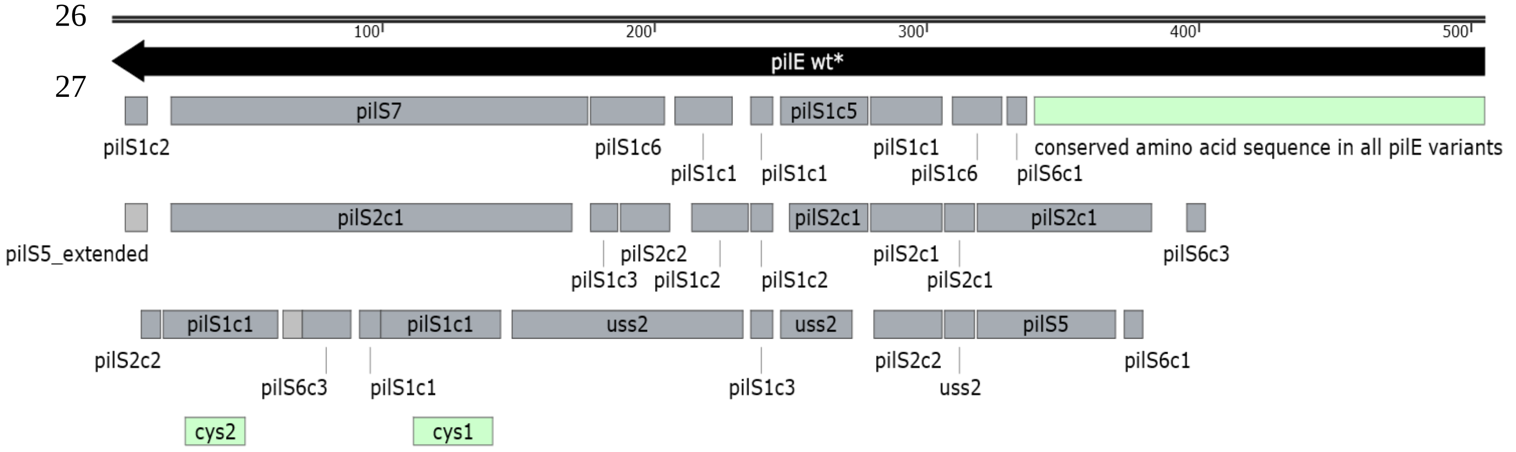
100
200
300
400
500
pilE wt*
pilS7
pilS1c5
pilS1c2
pilS1c6
pilS1c1
pilS1c1
pilS1c1
pilS1c6
conserved amino acid sequence in all pilE variants
pilS6c1
pilS2c1
pilS2c1
pilS2c1
pilS5_extended
pilS2c2
pilS1c3
pilS1c2
pilS1c2
pilS2c1
pilS2c1
pilS6c3
pilS1c1
pilS1c1
uss2
uss2
pilS5
pilS2c2
pilS6c3
pilS1c1
pilS1c3
pilS2c2
uss2
pilS6c1
cys2
cys1

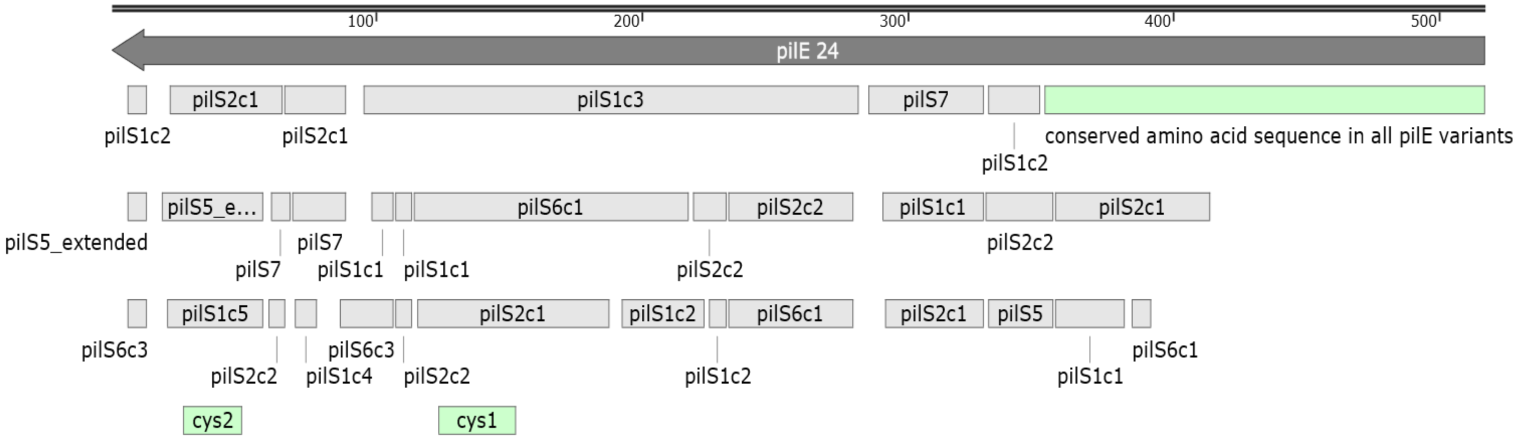
100
200
300
400
500
pilE 24
pilS2c1
pilS1c3
pilS7
pilS1c2
pilS2c1
conserved amino acid sequence in all pilE variants
pilS1c2
pilS5_e...
pilS6c1
pilS2c2
pilS1c1
pilS2c1
pilS5_extended
pilS7
pilS7
pilS1c1
pilS1c1
pilS2c2
pilS2c2
pilS1c5
pilS2c1
pilS1c2
pilS6c1
pilS2c1
pilS5
pilS6c3
pilS6c3
pilS6c1
pilS2c2
pilS1c4
pilS2c2
pilS1c2
pilS1c1
cys2
cys1

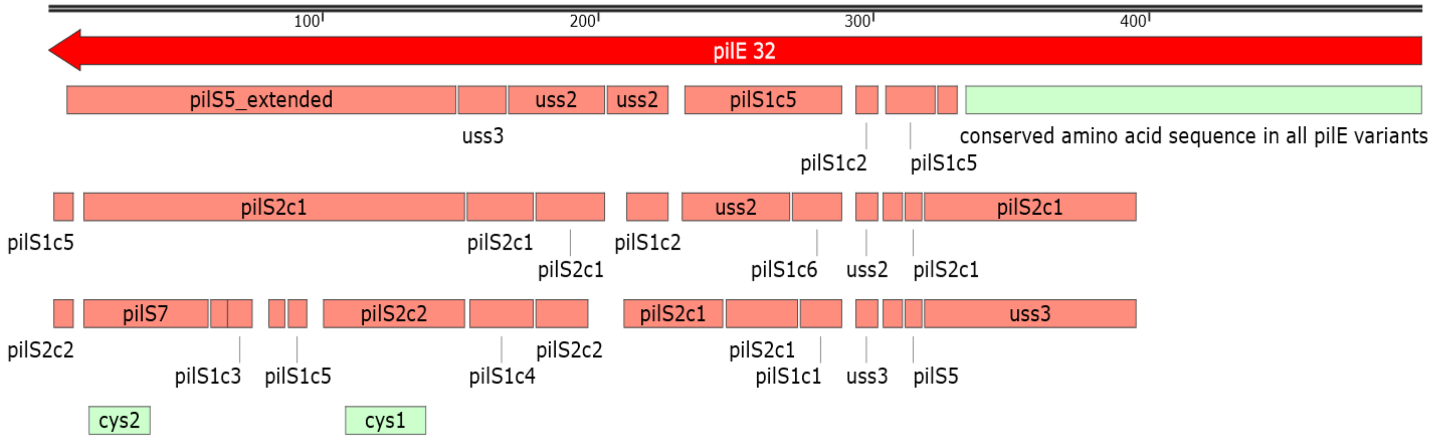
100
200
300
400
pilE 32
pilS5_extended
uss2
uss2
pilS1c5
uss3
conserved amino acid sequence in all pilE variants
pilS1c2
pilS1c5
pilS2c1
uss2
pilS2c1
pilS1c5
pilS2c1
pilS1c2
pilS2c1
pilS1c6
uss2
pilS2c1
pilS7
pilS2c2
pilS2c1
uss3
pilS2c2
pilS2c2
pilS2c1
pilS1c3
pilS1c5
pilS1c4
pilS1c1
uss3
pilS5
cys2
cys1

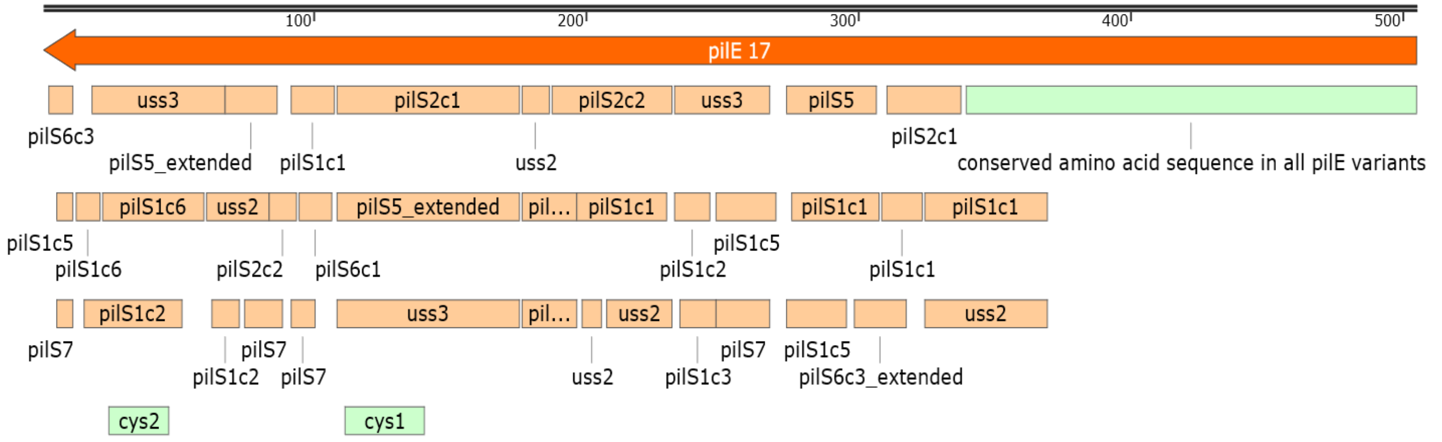
100
200
300
400
500
pilE 17
uss3
pilS2c1
pilS2c2
uss3
pilS5
pilS6c3
pilS2c1
pilS5_extended
pilS1c1
uss2
conserved amino acid sequence in all pilE variants
pilS1c6
uss2
pilS5_extended
pil...
pilS1c1
pilS1c1
pilS1c1
pilS1c5
pilS1c5
pilS1c6
pilS2c2
pilS6c1
pilS1c2
pilS1c1
pilS1c2
uss3
pil...
uss2
uss2
pilS7
pilS7
pilS7
pilS1c5
pilS1c2
pilS7
uss2
pilS1c3
pilS6c3_extended
cys2
cys1

Figure ii. Mapping of different *pilS* to *pilE* variants. Each *pilS* copy of the clinical isolate was aligned against the respective *pilE* variant (black: *pilE*$_{wt*}$, dark grey: *pilE*$_{24,}$ red: *pilE*$_{32,}$ orange: *pilE*$_{17}$). *pilS* sequences with 100 % identity and at least 6 bp in length are shown. The alignments are ordered by the length of the matching sequence, e.g. the longest matching alignment for each position within *pilE* is directly underneath the *pilE* sequence. Only the three best matches are shown for each *pilE* variant. The illustrations were created with SnapGene software (www.snapgene.com). pilS5_extended: extended *pilS5* sequence including the conserved *cys2* region.

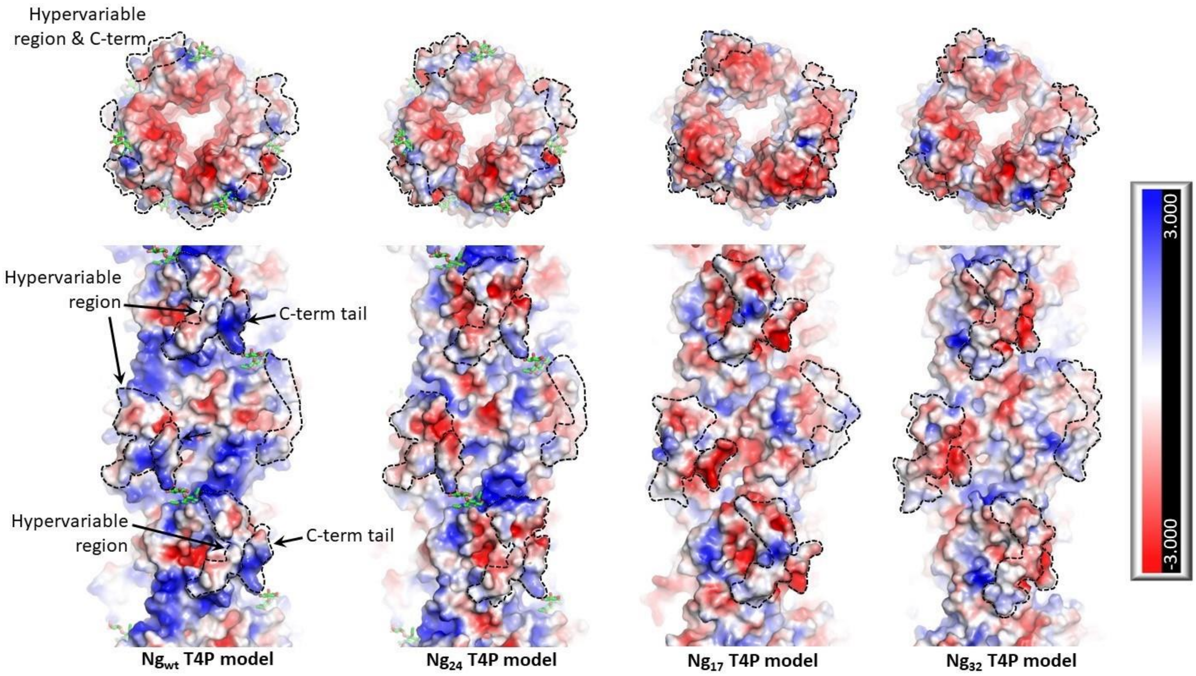

Figure iii. Model of the charge densities. The charge density was simulated via PyMol and the APBS tool [65,69]. Models of wt* and variant pilus filaments are shown from the top and side in surface representation with electrostatic surface potential. Blue: positive charge, red: negative charge.

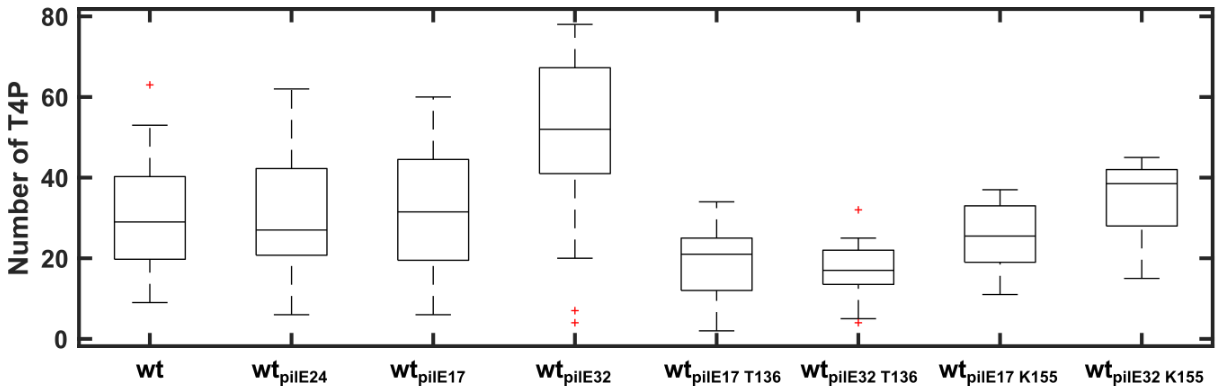

Figure iv. Pilus number per cell for *pilE* variants. The pili numbers were determined from TEM images. Box plots show the median (central mark), bottom and top patches show 25th and 75th percentiles, respectively. Outliers are plotted individually (red + symbol) and are defined as values which are larger than 1.5 times the interquartile range from the bottom or top of the box, which corresponds to 99.3 percent coverage if the data is normally distributed, according to the Matlab function *boxplot* [64] which was used here. The whiskers length is defined as the maximum and minimum excluduing the outliers. P-values were determined via a rank-sum test: $p > 0.05$ for wt*, wt_{pilE24}, wt_{pilE17}, $\mathrm{wt}_{pilE17\_K155}$, and $\mathrm{wt}_{pilE32\_K155}$, $p < 0.05$ for wt_{pilE32}, $\mathrm{wt}_{pilE17\_T136}$, and $\mathrm{wt}_{pilE32\_T136}$. Number of analysed bacteria: $N_{\mathrm{wt}*} = 37$,$N_{\mathrm{wt}pilE24} = 33$,$N_{\mathrm{wt}pilE17} = 16$, $N_{\mathrm{wt}pilE32} = 25$, $N_{\mathrm{wt}pilE17\_K155} = 18$, and $N_{\mathrm{wt}pilE32\_K155} = 18$, $\mathrm{Nwt}_{pilE17\_T136} = 27$, and $N_{\mathrm{wt}pilE32\_T136} = 19$. The data underlying this figure can be found in S1 Data.

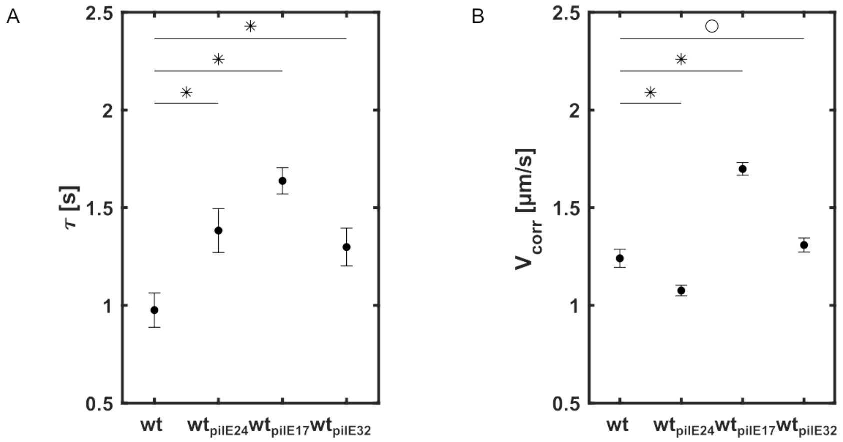

Figure v. Correlation time and velocity of twitching motility of *pilE* variant strains. A) Correlation time of motile cells on a BSA coated coverslide. B) Velocity of twitching motility. Significance analysis via Mann-Whitney U test compared to the wt*, star: $p < 0.05$. Error bars: 95% confidence bounds from fit to corrrelated random walk model (Fig. S6). Error bars: 95% confidence bounds from fit to correlated random walk model (Fig. vi in S1 Data). The data underlying this figure can be found in S1 Data.

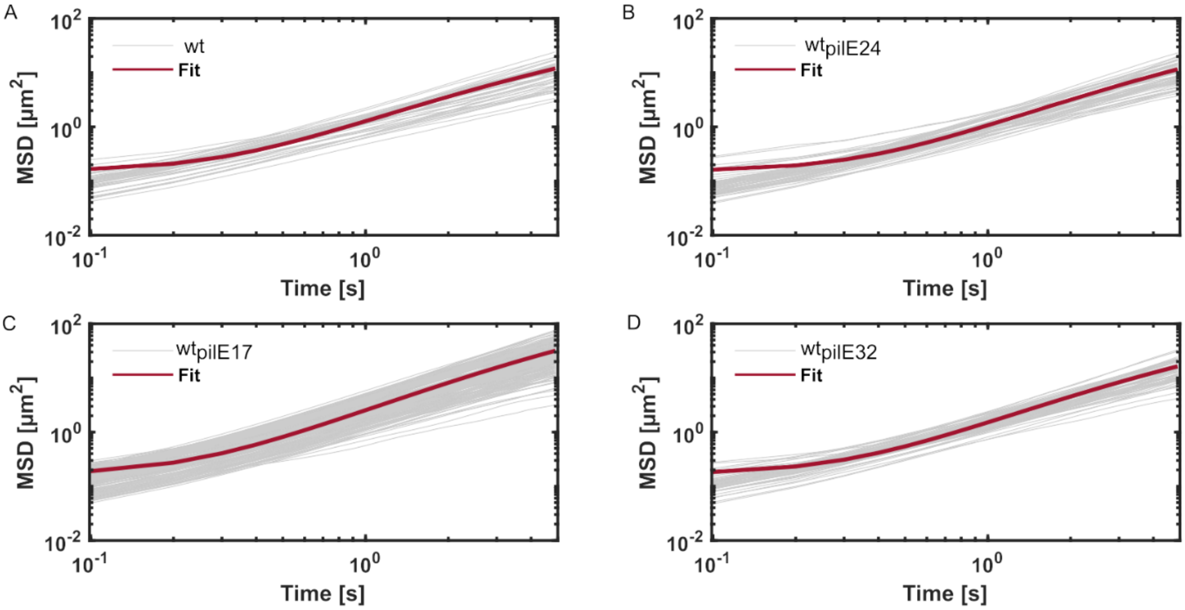

Figure vi. Mean squared displacement (MSD) for all tracks of single cells on a BSA-coated cover slide. Strains A) wt* (Ng150), B) wt$_{pilE24}$ (Ng242), C) wt$_{pilE17}$ (Ng240), D) wt$_{pilE32}$ (Ng230). The MSD was fitted for the time interval of the first 5 s. Grey: trajectories of individual cells, red line: MSD model with fit parameters averaged from single MSD fits to single tracks of bacteria. N = 46-200 trajectories per strain. The data underlying this figure can be found in S1 Data.

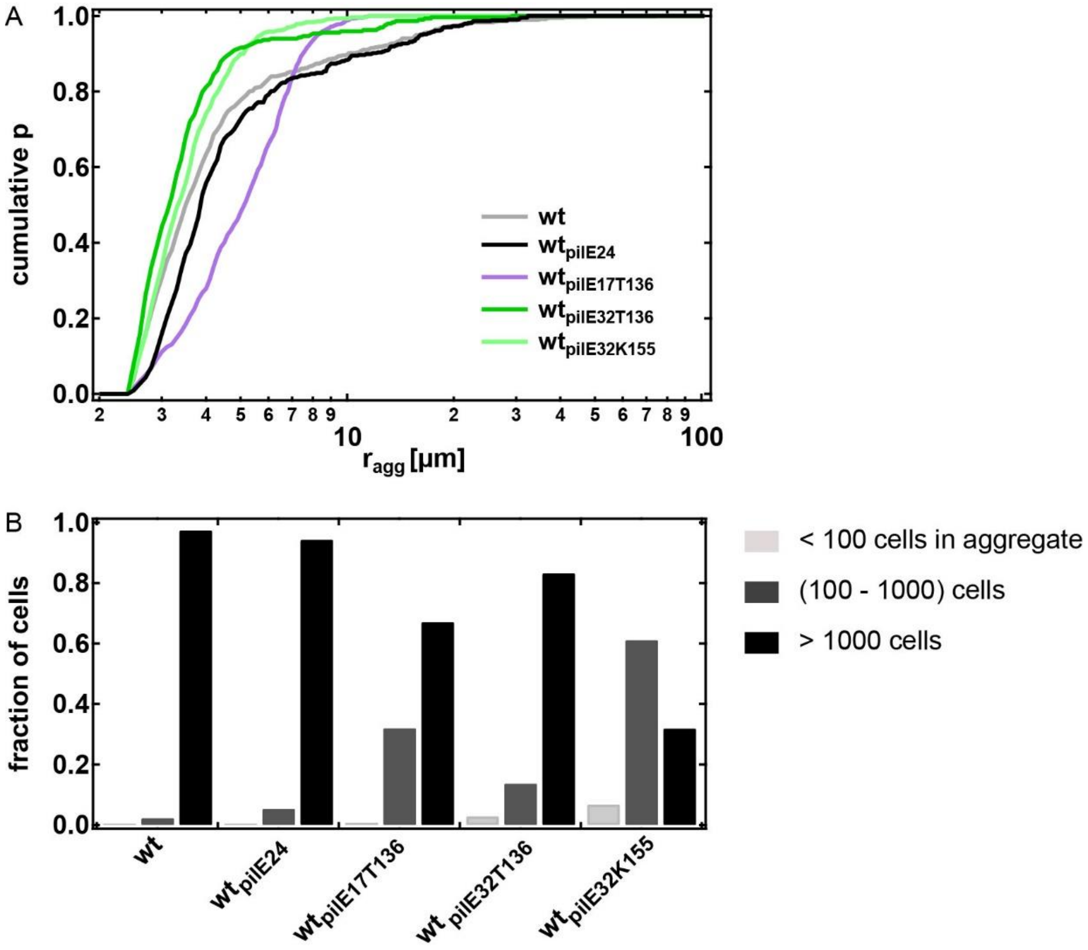

Figure vii. Distributions of aggregate size after 1 h of incubation with initial OD_{600} of 0.033. A) Cumulative probability distribution p of aggregate radius r_{agg} with $r_{agg} \geq 2\mu m$. B) Estimated fraction of cells that reside within colonies comprising light gray: $N < 100$ cells, gray: $10 < N < 1000$ cells, black: $N > 1000$ cells. Shown are only the the strains that form aggregates with well defined contours. The data underlying this figure can be found in S1 Data.

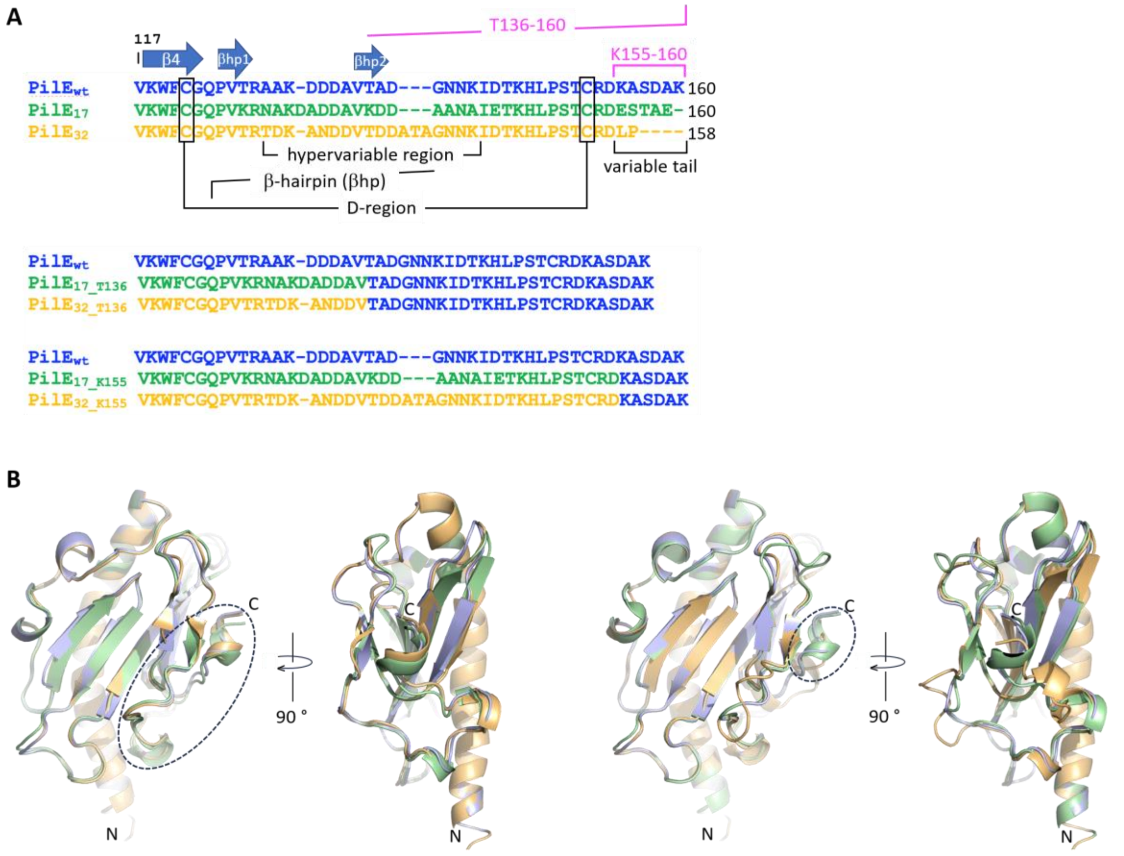

PilE$_{17\_T136}$ (green) and PilE$_{32\_T136}$ (orange) superimposed on PilE$_{wt}$ PilE$_{17\_K155}$ (green) and PilE$_{32\_K155}$ (orange) superimposed on PilE$_{wt}$

Figure viii. Sequence alignment and structure predictions for PilE hybrids. A) Sequence alignment of the C-terminal regions. B) Pilin models were generated using AlphaFold. PilE$_{17\_T136}$ (green) and PilE$_{32\_T136}$ (orange) superimposed on PilE$_{wt}$. PilE$_{17\_K155}$ (green) and PilE$_{32\_K155}$ (orange) superimposed on PilE$_{wt}$.

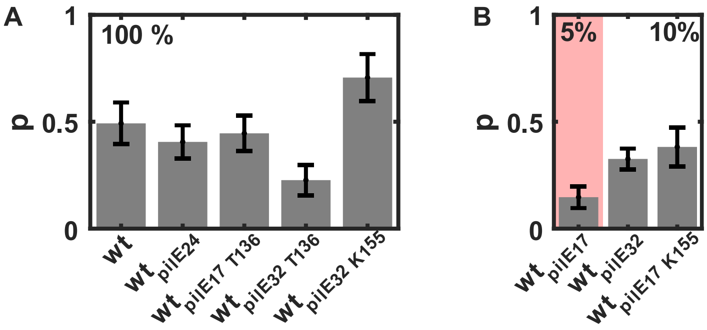

Figure ix. Fraction of successful attempts in dual trap assay. We counted the fraction of interacting bacteria pairs because not every pair of bacteria showed interaction. This fraction strongly depends on the trap stiffness which was set to A) $k \approx 0.1$ pN/nm for wt*, wt_{pilE24}, $\mathrm{wt}_{pilE17\_T136}$, $\mathrm{wt}_{pilE32\_T136}$, and $\mathrm{wt}_{pilE32\_K155}$. Since interactions were nearly undetectable at $k = 0.1$ pN/nm for strains wt_{pilE32}, wt_{pilE17} and $\mathrm{wt}_{pilE17\_K155}$, the stiffnesses were reduced to $k = 0.005$ pN/nm (light red) and $k \approx 0.01$ pN/nm (10%), respectively. Number of trapped bacteria pairs: N = (73 – 170). Error bars: standard error over different days. The data underlying this figure can be found in S1 Data.

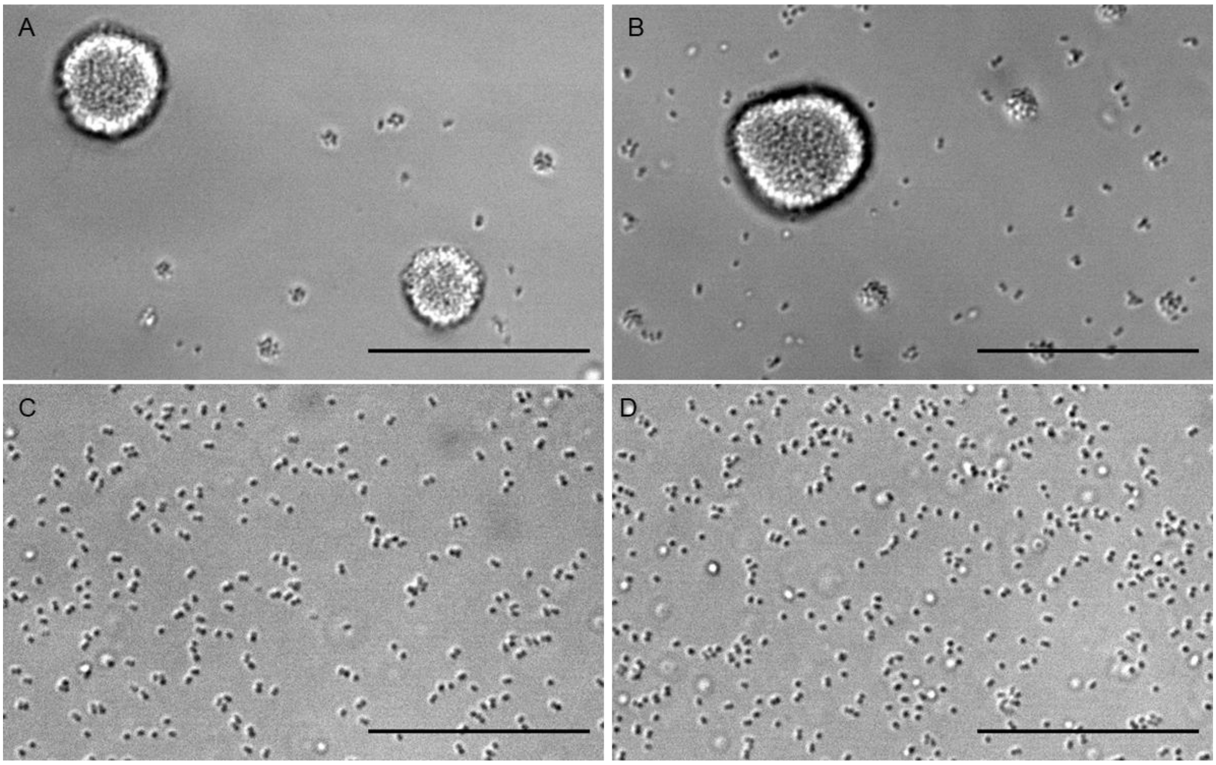

Figure x. Pilin glycosylation does not impact the colony phenotype of PilE variants. Representative images of PilE variants in a Δ*pglF* background. A) wt* Δ*pglF* (Ng156), B) wt$_{pilE24}$ Δ*pglF* (Ng312), C) wt$_{pilE17}$ Δ*pglF* (Ng311), D) wt$_{pilE32}$ Δ*pglF* (Ng313). Scale bar: 50 μm.

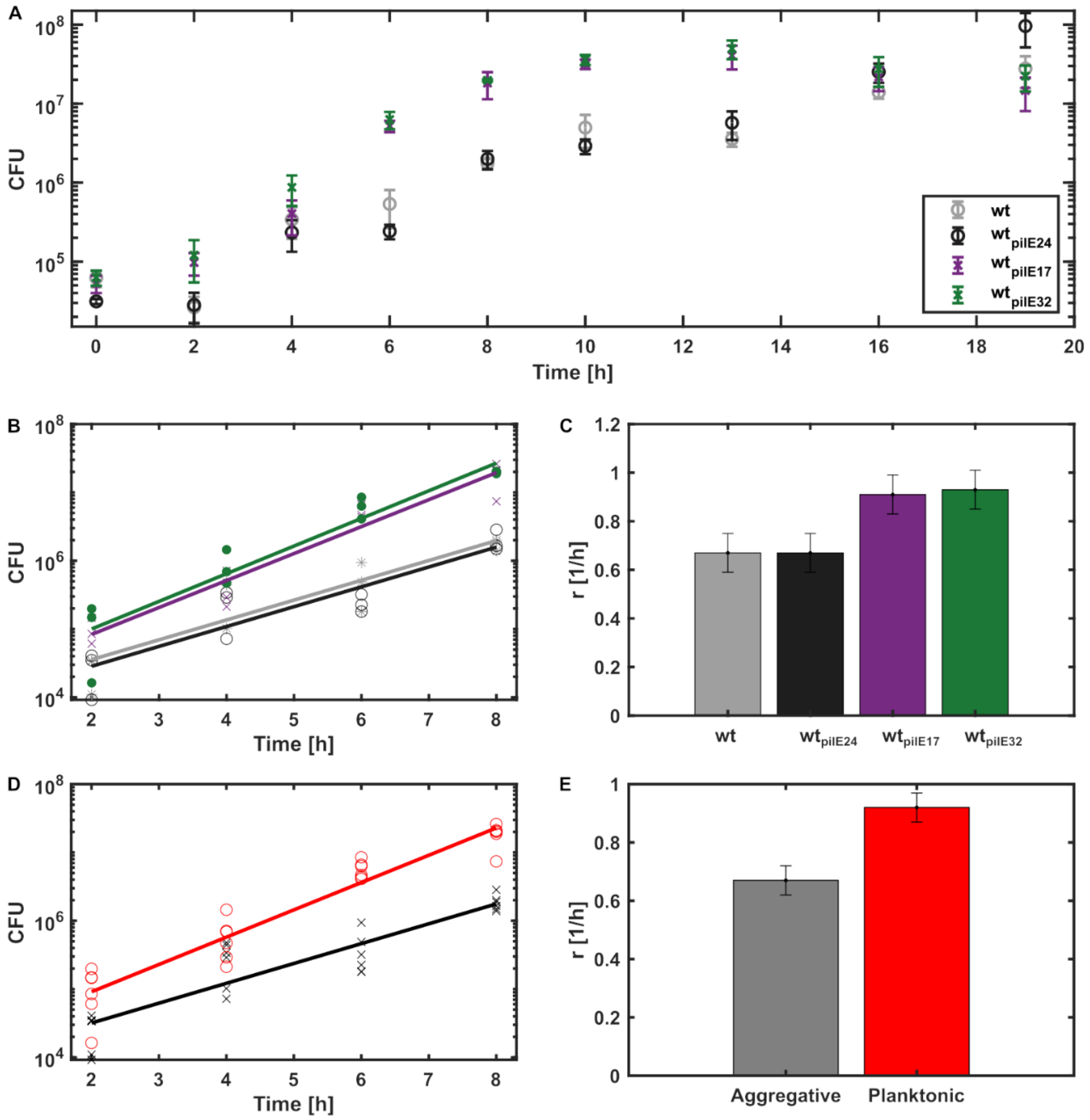

Figure xi. Growth rates for strains wt* (Ng150), wt$_{pilE24}$ (Ng242), wt$_{pilE17}$ (Ng240), wt$_{pilE32}$ (Ng230). A) Growth curves for all *pilE* variants from counting colony forming units. N=3-4. Error bars: standard errors. B), D) Linear regression fits to logarithmic data of CFU counts of each strain or pooled data regarding the lifestyle: planktonic or aggregating. C), D) Growth rates determined from fits in B) and D), respectively. Error bars: errors of the fits. Anova-test of the linear regression model indicated no significant difference between the growth rates of the individual strains with $p_{wt\text{-}wt\mathit{pilE24}} = 0.995$, $p_{wt\text{-}wt\mathit{pilE17}} = 0.071$, $p_{wt\text{-}wt\mathit{pilE32}} = 0.074$ but significant differences for pooled data $p_{aggreg.\text{-}planktonic} = 0.0074$.

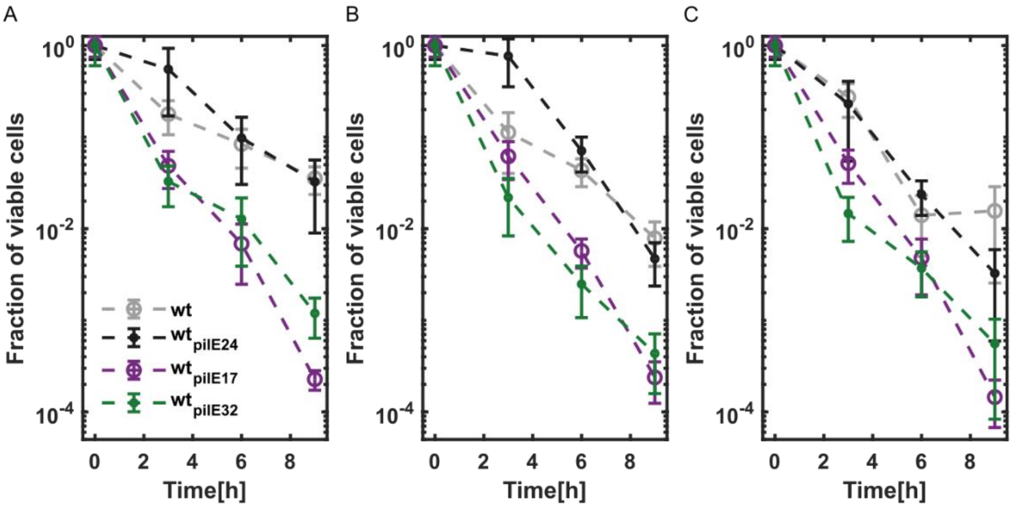

Figure xii. Survival assay with different concentrations of ceftriaxone after 10 h of growth. Killing kinetics of all variants, grey: wt*, dark grey: $\text{wt}_{\mathit{pilE24}}$, purple: $\text{wt}_{\mathit{pilE17}}$, and green: $\text{wt}_{\mathit{pilE32}}$, for A) 300x MIC, combined p-values (see Methods): $p_{\text{wt-wt}\mathit{pilE24}} = 0.63$, $p_{\text{wt-wt}\mathit{pilE17}} = 0.00029$, $p_{\text{wt-wt}\mathit{pilE32}} = 0.0011$; B) 600x MIC, $p_{\text{wt-wt}\mathit{pilE24}} = 0.35$, $p_{\text{wt-wt}\mathit{pilE17}} = 8.8\times10^{-5}$, $p_{\text{wt-wt}\mathit{pilE32}} = 0.00035$; C) 1200x MIC. $p_{\text{wt-wt}\mathit{pilE24}} = 0.99$, $p_{\text{wt-wt}\mathit{pilE17}} = 0.0038$, $p_{\text{wt-wt}\mathit{pilE32}} = 0.0013$. Error bars: standard errors over 3-4 independent experiments. Shown are mean and standard error over 3-4 biological culture replicates. The data underlying this figure can be found in S1 Data.

Supplementary Tables

strain	**relevant genotype**	**reference**	**strain data base entry**
N. gonorrhoeae NG32	-	clinical isolate	Ngc001
N. gonorrhoeae NG17	-	clinical isolate	Ngc004
N. gonorrhoeae NG24	-	clinical isolate	Ngc007
$\Delta G4$ *(wt*)*	*G4::apraR*	[26]	Ng150
T126C step1	*G4::apraR, pilE::*$pilE^{T126C}$ *ermC* $rpsL_s$	[19]	Ng225
$\Delta comE_{234}\Delta pilV$	*comE4::Kan, comE3::Clm, comE2::Erm, recA6ind(tetM) pilVfs*	[63]	Ng052
wt_{pilE32} step1	*G4::apraR, pilE::*$pilE_{clinicalisolateNG32}$ *ermC* $rpsL_s$	this study	Ng229
wt_{pilE32}	*G4::apraR,* $pilE_{clinicalisolateNG32}$	this study	Ng230
wt_{pilE17} step1	*G4::apraR, pilE::*$pilE_{clinicalisolateNG17}$ *ermC* $rpsL_s$	this study	Ng239
wt_{pilE17}	*G4::apraR,* $pilE_{clinicalisolateNG17}$	this study	Ng240
wt_{pilE24} step1	*G4::apraR, pilE::*$pilE_{clinicalisolateNG24}$ *ermC* $rpsL_s$	this study	Ng241
wt_{pilE24}	*G4::apraR,* $pilE_{clinicalisolateNG24}$	this study	Ng242
wt* $_{\text{green}}$	*G4::apraR, iga::*P_{pilE}*gfp-ermC*	[11]	Ng105
wt*$_{\text{red}}$	*G4::apraR, lctp:*P_{pilE}*mcherry aadA:aspC*	[9]	Ng170
wt* Δ*pglF*	*G4::apraR, pglF::*P_{pilE}*gfp-kanR*	[11]	Ng156
$\text{wt}_{pilE17\text{green}}$	*G4::apraR,* $pilE_{clinicalisolateNG17}$ *iga::*P_{pilE}*gfp-ermC*	this study	Ng308
$\text{wt}_{pilE24\text{green}}$	*G4::apraR, pilE::*$pilE_{clinicalisolateNG24}$ *iga::*P_{pilE}*gfp-ermC*	this study	Ng309
$\text{wt}_{pilE32\text{green}}$	*G4::apraR,* $pilE_{clinicalisolateNG32}$ *iga::*P_{pilE}*gfp-ermC*	this study	Ng310
wt_{pilE17_T136} step1	*G4::apraR,* $pilE_{clinicalisolateNG17}{}^{K137\text{-}E160}$ ::$pilE_{wt}{}^{T136\text{-}K160}$ *ermC* $rpsL_s$	this study	Ng292

$\mathrm{wt}_{pilE17\_T136}$	*G4::apraR,* $pilE_{clinicalisolateNG17}^{K137-E160}$ $::pilE_{wt}^{T136-K160}$	this study	Ng293
$\mathrm{wt}_{pilE32\_T136}$ step1	*G4::apraR,* $pilE_{clinicalisolateNG32}^{T135-P158}$ $::pilE_{wt}^{T136-K160}$ *ermC* $rpsL_{s}$	this study	Ng294
$\mathrm{wt}_{pilE32\_T136}$	*G4::apraR,* $pilE_{clinicalisolateNG32}^{T135-P158}$ $::pilE_{wt}^{T136-K160}$	this study	Ng295
$\mathrm{wt}_{pilE17\_K155}$ step1	*G4::apraR,* $pilE_{clinicalisolateNG17}^{E156-P158}$ $::pilE_{wt}^{K155-K160}$ *ermC* $rpsL_{s}$	this study	Ng304
$\mathrm{wt}_{pilE17\_K155}$	*G4::apraR,* $pilE_{clinicalisolateNG17}^{E156-P158}$ $::pilE_{wt}^{K155-K160}$	this study	Ng305
$\mathrm{wt}_{pilE32\_K155}$ step1	*G4::apraR,* $pilE_{clinicalisolateNG32}^{L157-P158}$ $::pilE_{wt}^{K155-K160}$ *ermC* $rpsL_{s}$	this study	Ng306
$\mathrm{wt}_{pilE32\_K155}$	*G4::apraR,* $pilE_{clinicalisolateNG32}^{L157-P158}$ $::pilE_{wt}^{K155-K160}$	this study	Ng307
$\Delta pilE_{green}$	*pilE::gfp-kanR*	[61,11]	Ng081
wt_{pilE17} $\Delta pglF$	$pglF::P_{pilE}gfp\text{-}kanR$	this study	Ng311
wt_{pilE24} $\Delta pglF$	$pglF::P_{pilE}gfp\text{-}kanR$	this study	Ng312
wt_{pilE32} $\Delta pglF$	$pglF::P_{pilE}gfp\text{-}kanR$	this study	Ng313
$\Delta pilE$	*pilE::kanR*	this study	Ng253

Table i Strains used in this study.

Region	PilE variant	Query Cover [%]	Identity [%]	e-value	length
complete	NG17	98.0	80.6	4e-85	167
	NG32	96.0	86.6	5e-95	165
	NG24	99.0	90.0	3e-104	171
without conserved	NG17	94.0	73.6	5e-48	115
	NG32	94.0	80.4	3e-57	113
	NG24	99.0	85.6	2e-66	119
Semi-variable	NG17	100.0	76.1	1e-43	67
	NG32	100.0	80.6	2e-37	66
	NG24	100.0	89.6	2e-36	67
cys1	NG17	100.0	84.6	3e-13	13
	NG32	100.0	100.0	2e-15	13
	NG24	100.0	100.0	2e-15	13
Hypervariable loop	NG17	94.0	57.9	5e-06	20
	NG32	100.0	59.1	1e-09	22
	NG24	100.0	56.5	2e-08	23
cys2	NG17	100.0	100.0	5e-12	10
	NG32	100.0	100.0	5e-12	10
	NG24	100.0	100.0	5e-12	10
Hypervariable tail	NG17	-	-	-	5
	NG32	-	-	-	2
	NG24	83.0	100.0	5e-05	6

Table ii. Amino acid sequence identities of complete and partial regions of *pilE* compared to the MS11 *pilE* amino acid sequence according to Fig. 1. The amino acid sequences were compared using BLAST [70].

Primer	**5’ →3’**
sk5	CCGCTCGAGCGGTTCCGACCCAATCAACACACC
sk32	GGGCCTTGAAGCGCAATCGATATA
sk45	CAACCCTTAAAGGAAAAACCATGCAATAC
sk46	TTGTATTCAGACGGCCAGTGACTTTTTGAAGGGTATTCATAAAATTACTCCTAATTG
sk47	TAATTTTATGAATACCCTTCAAAAAGTCACTGGCCGTCTGAATACAAC
sk48	GGGTAAAGCTTAGAAAAACTCATCGAGCATCAAATGAAAC
sk49	AATAAATTGCAGTTTCATTTGATGCTCGATGAGTTTTTCTAAGCTTTACCCTTATCGAGCTGATGATTGT
sk50	CATTTTCGGCTCCTTATTCGGTTTGAC
sk129	TTCCGACCCAATCAACACA
sk131	TTTAAGGCCTAATTTGCCTCATTTGGCATCAGATGCCTTAT
sk132	ATCTGATGCCAAATGAGGCAAATTAGGCCTTAAATTTTA
sk158	GTATCGGCAATGACGGTTCG
sk159	GAGTTGTCTCTGACACATTCTGG
sk159	GAGTTGTCTCTGACACATTCTGG
sk160	GAAGGGTATTCATAAAATTACTCCTAATTGAAAGGGG
sk161	CAATTAGGAGTAATTTTATGAATACCCTTCAAAAAGGCTTTACCC
sk162	GGTGATGAAGCACCGGGTCACGGCAGGTCACGG
sk163	TGACCCGGTGCTTCATCACC
sk164	TGAGGCAAATTAGGCCTTAAATTTTAAATAAATC
sk165	GATTTATTTAAAATTTAAGGCCTAATTTGCCTCACGGCAGGTCACGG
sk167	GGTGATGAAGCACCGGGTCAGGCGGCATCAGATGC
sk168	GATTTATTTAAAATTTAAGGCCTAATTTGCCTCAGGCGGCATCAGATG
sk175	GGTGATGAAGCACCGGGTCATTCGGCAGTTGATTCATCACG
sk176	GATTTATTTAAAATTTAAGGCCTAATTTGCCTCATTCGGCAGTTGATTCATCACG
sk384	ACCACTGCTGTGAGCGC
sk385	GCGGTGACGGCGTCGTCGGCGTCTTTGGCGTTGCG
sk386	CAAAGACGCCGACGACGCCGTCAC
sk388	GCCGTCGGCGGTAACGTCGTCGTTGGCTTTGTC
sk389	GCCAACGACGACGTTACCGCCGACGGCAAC
sk390	GTTACCAAACTCGACGGCACG
sk391	GTCATTTGGCATCAGATGCCTTATCACGGCAGGTTGACGG
sk392	CGTCAACCTGCCGTGATAAGGCATCTGATGCCAAATGACC
sk393	CATTTGGCATCAGATGCCTTGTCACGGCAGGTTGACGG
sk394	CGTCAACCTGCCGTGACAAGGCATCTGATGCCAAATGACC
sk395	TTTAAGGCCTAATTTGCCTCATTTGGCATCAGATGCCTTGTC

Table iii: Primers used in this study.

9.4 Supplementary Information for Chapter 6

Here, supplementary information of the reprinted publication from chapter 6.

Supplementary Figures

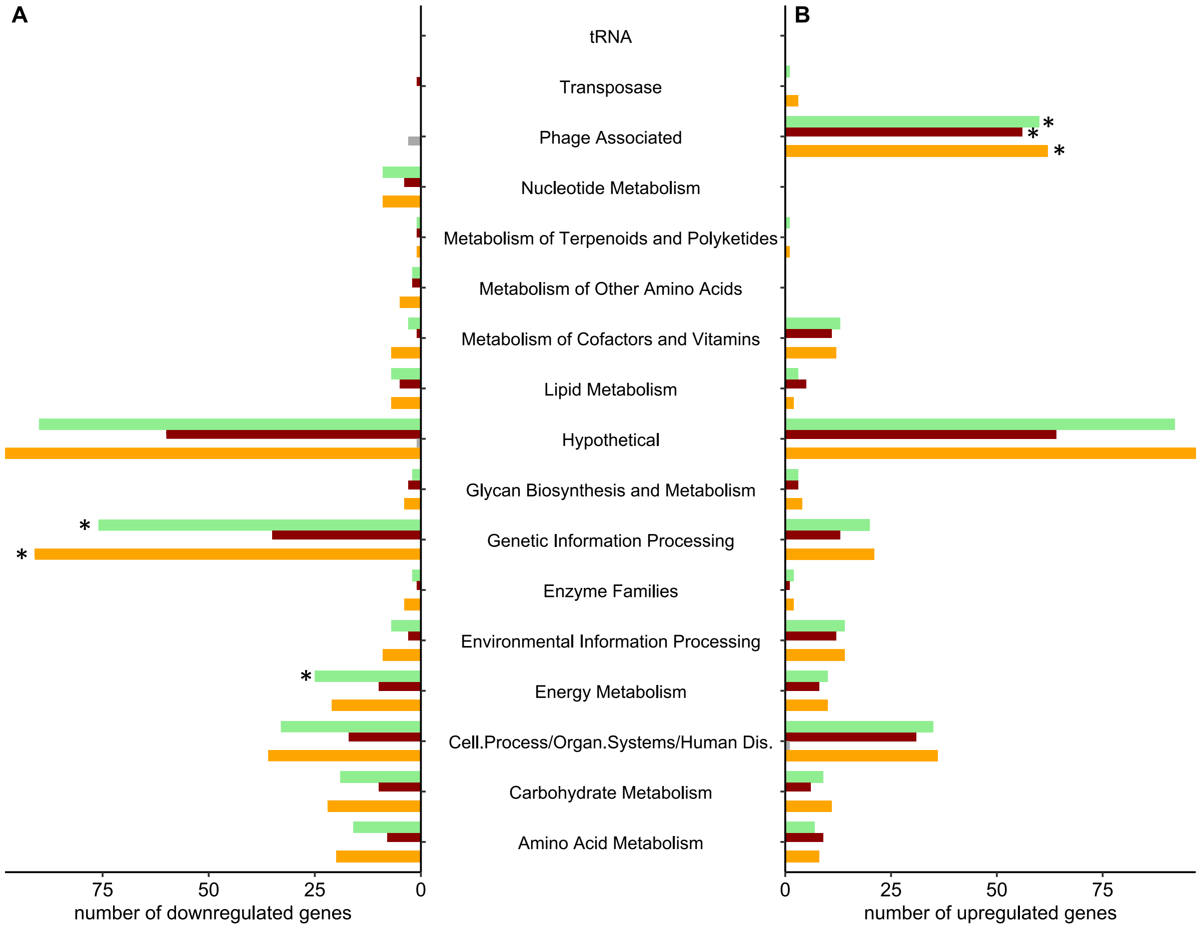

S1 Fig.: Functional enrichment of differentially expressed genes, wt_{agg} vs. wt_{plank} (orange), $\text{wt}_{\text{plank2}}$ (red), and *ΔpilE* (green). Genes that belonged to neither KEGG category nor had an FA1090 ortholog are excluded. Only significantly differentially expressed genes are shown. A) Number of downregulated genes. B) Number of upregulated genes. Significantly enriched categories are highlighted with * ($p\text{-value} \leq 0.01$).

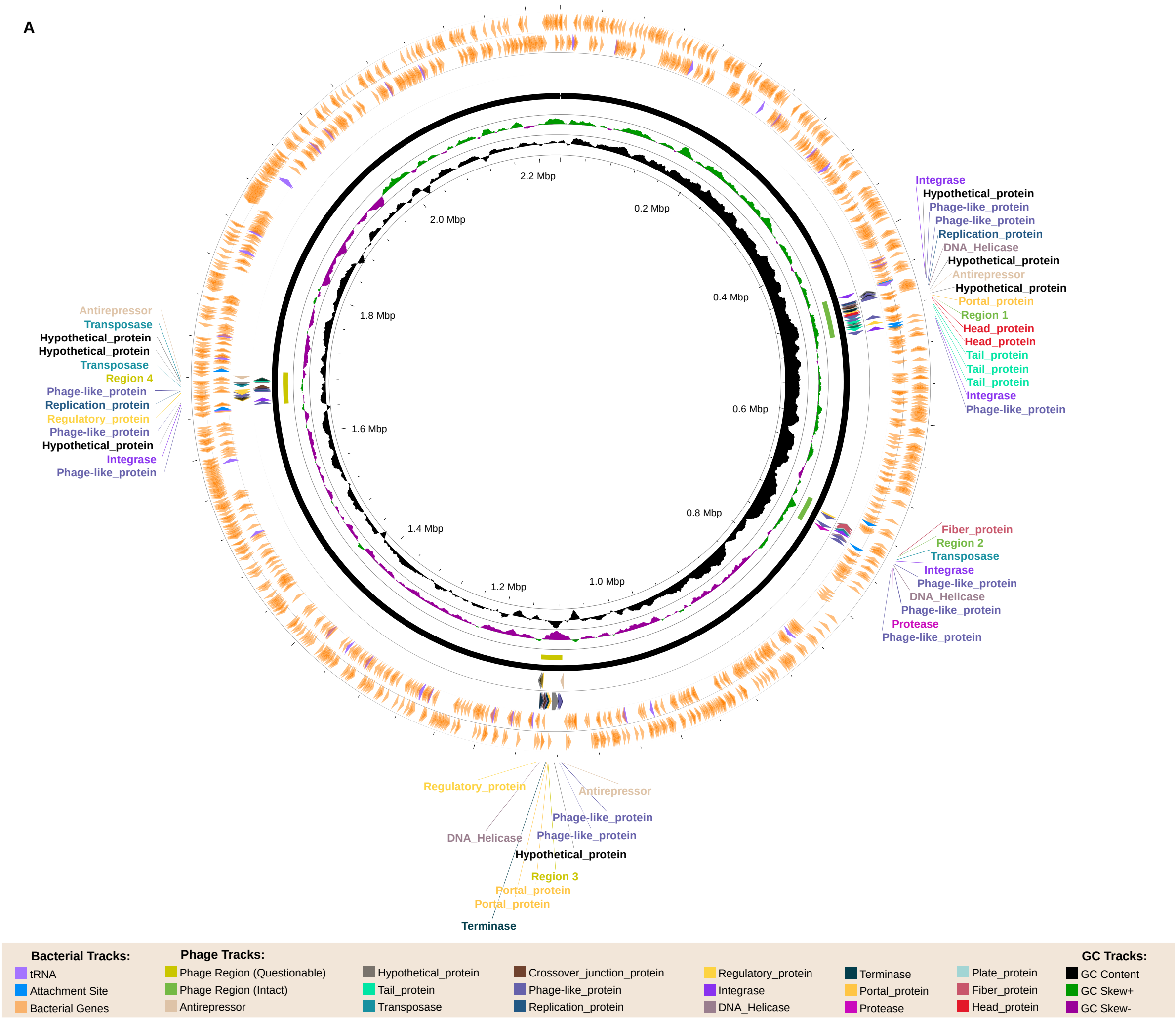
A
2.2 Mbp
0.2 Mbp
0.4 Mbp
0.6 Mbp
0.8 Mbp
1.0 Mbp
1.2 Mbp
1.4 Mbp
1.6 Mbp
1.8 Mbp
2.0 Mbp
Integrase
Hypothetical_protein
Phage-like_protein
Phage-like_protein
Replication_protein
DNA_Helicase
Hypothetical_protein
Antirepressor
Hypothetical_protein
Portal_protein
Region 1
Head_protein
Head_protein
Tail_protein
Tail_protein
Tail_protein
Integrase
Phage-like_protein
Fiber_protein
Region 2
Transposase
Integrase
Phage-like_protein
DNA_Helicase
Phage-like_protein
Protease
Phage-like_protein
Regulatory_protein
Antirepressor
Phage-like_protein
DNA_Helicase
Phage-like_protein
Hypothetical_protein
Region 3
Portal_protein
Portal_protein
Terminase
Antirepressor
Transposase
Hypothetical_protein
Hypothetical_protein
Transposase
Region 4
Phage-like_protein
Replication_protein
Regulatory_protein
Phage-like_protein
Hypothetical_protein
Integrase
Phage-like_protein
Bacterial Tracks:
tRNA
Attachment Site
Bacterial Genes
Phage Tracks:
Phage Region (Questionable)
Phage Region (Intact)
Antirepressor
Hypothetical_protein
Tail_protein
Transposase
Crossover_junction_protein
Phage-like_protein
Replication_protein
Regulatory_protein
Integrase
DNA_Helicase
Terminase
Portal_protein
Protease
Plate_protein
Fiber_protein
Head_protein
GC Tracks:
GC Content
GC Skew+
GC Skew-

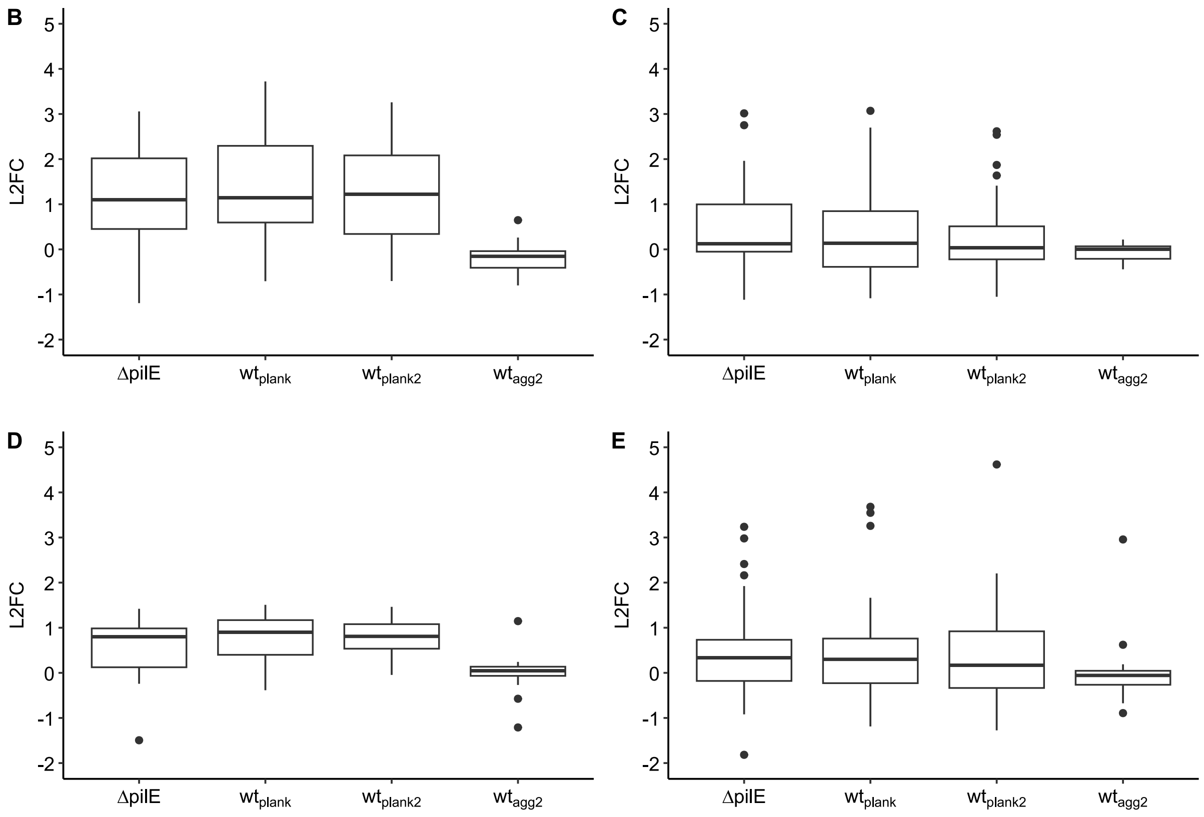

S2 Fig.: Prophages of *N. gonorrhoeae* MS11 (CP003909.1) as predicted with PHASTEST (39) and their differential expression. L2FC were obtained by comparing the expression of *pilE* variant strains to wt$_{agg}$. Genes were categorized according to the four predicted prophages of *N. gonorrhoeae* MS11 by PHASTEST. All genes between the respective genome range were assigned as part of the corresponding phage. A) Circular map of the *N. gonorrhoeae* MS11 (CP003909.1) genome with positions of predicted prophages. Differential expression of B) Φ1, C) Φ2, D) Φ3, and E) Φ4.

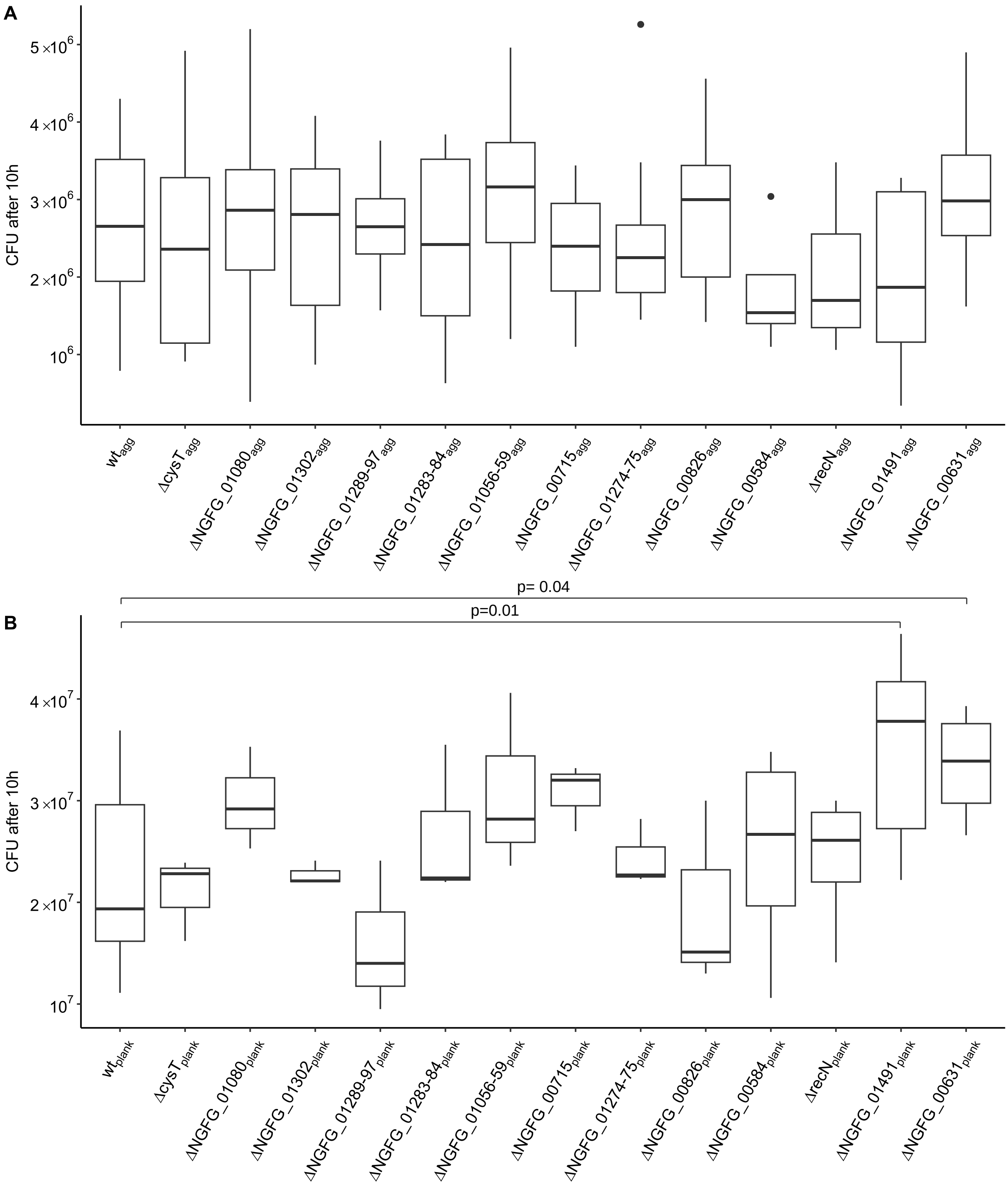

S3 Fig.: CFU of A) aggregating and B) planktonic strains after 10 h of growth in liquid.

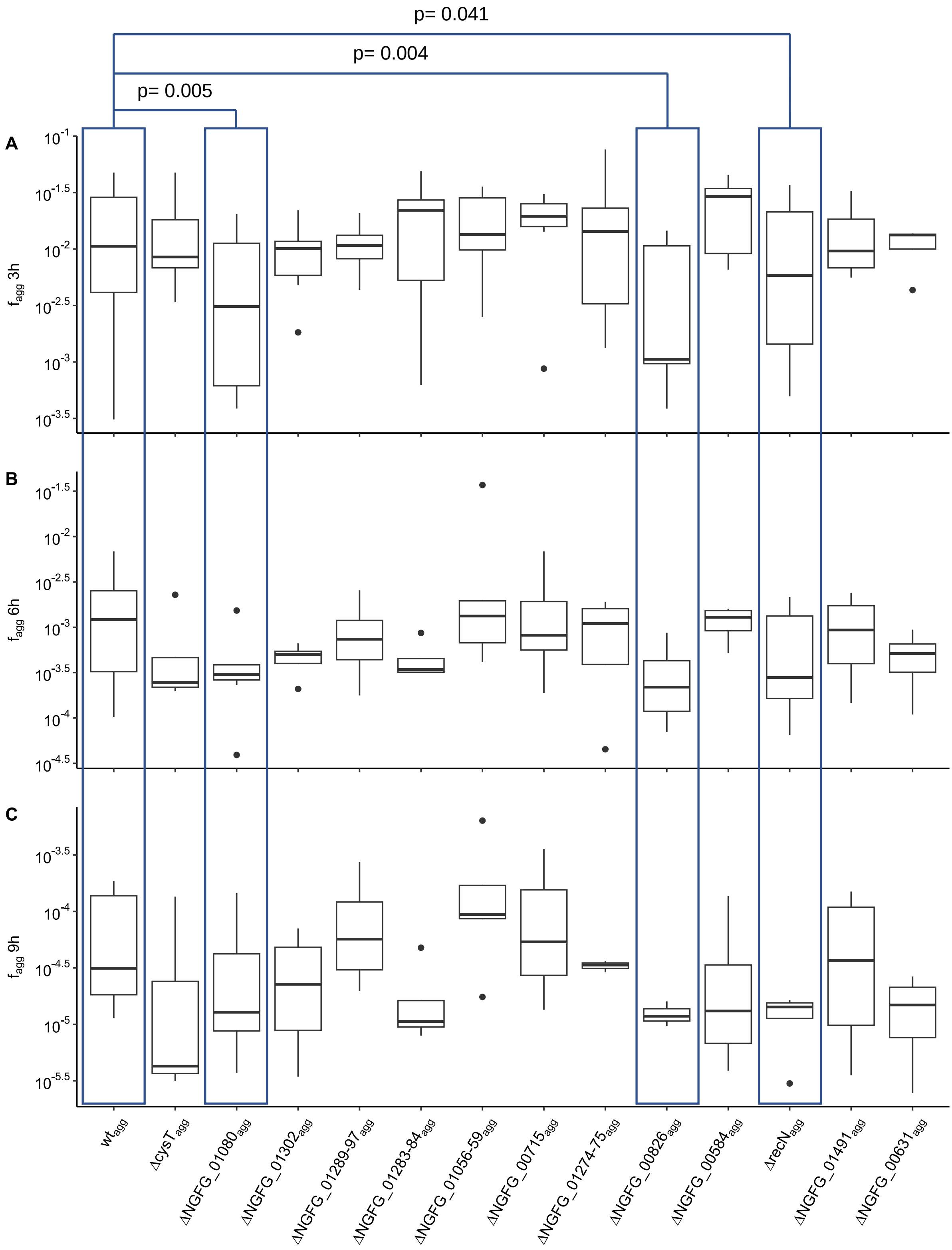

822

823 S4 Fig.: Fractions of surviving aggregating cells under ciprofloxacin treatment for A) 3 h, B)
824 6 h and C) 9 h.

825

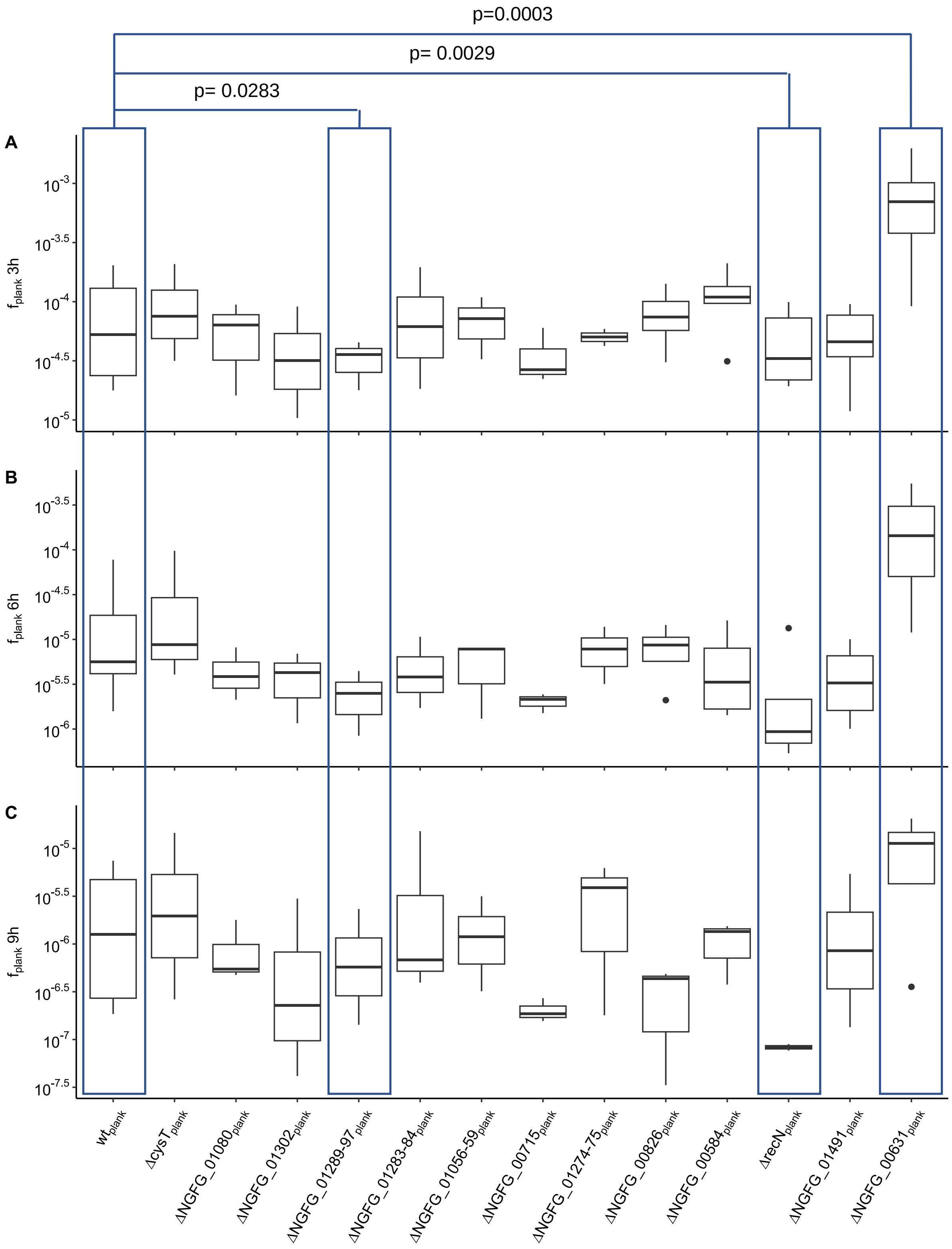

826 S5 Fig.: Fractions of surviving planktonic strains under ciprofloxacin treatment for A) 3 h, B)
827 6 h and C) 9 h.

828

829

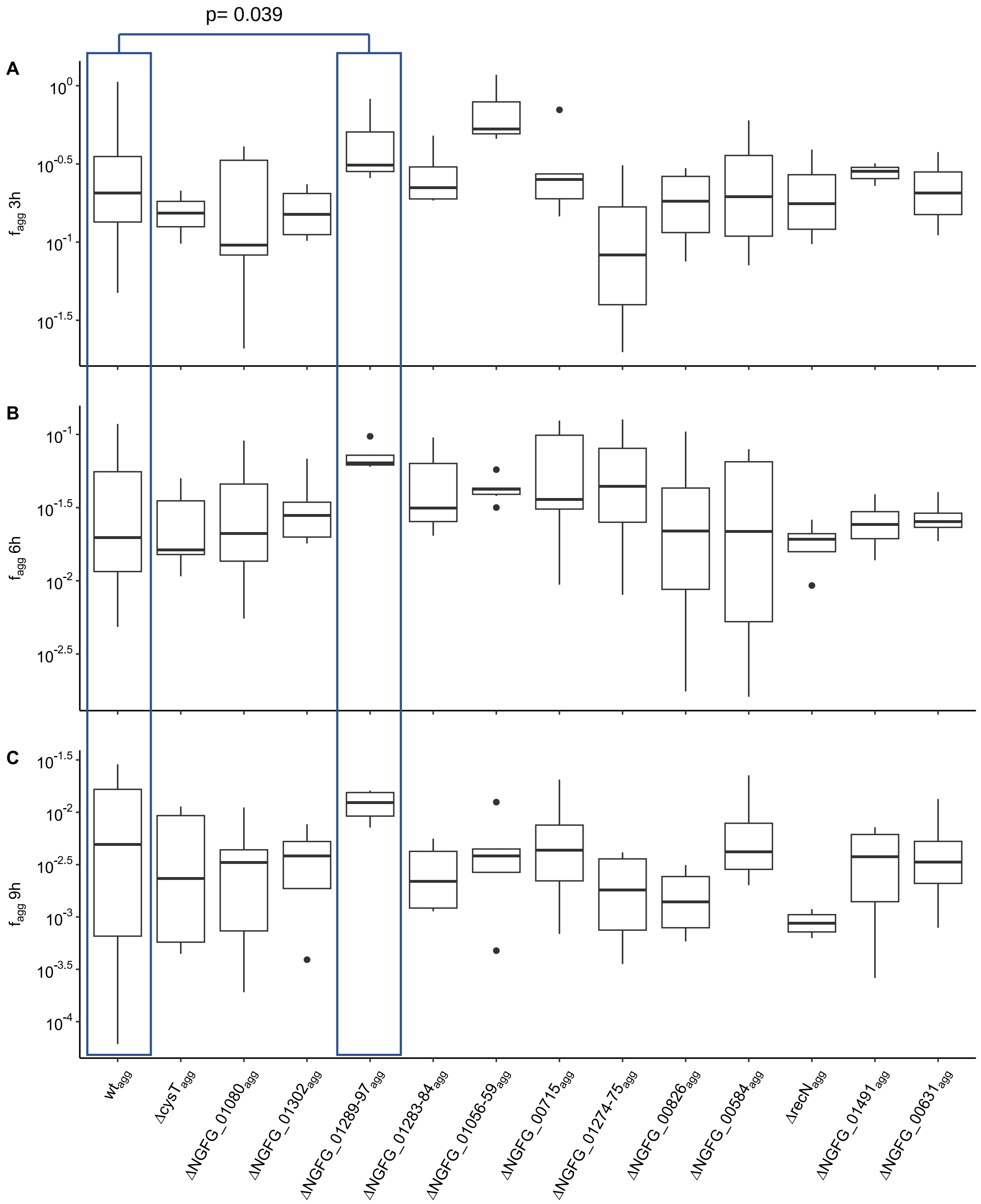

S6 Fig.: Fractions of surviving aggregating cells under ceftriaxone treatment for A) 3 h, B) 6 h and C) 9 h.

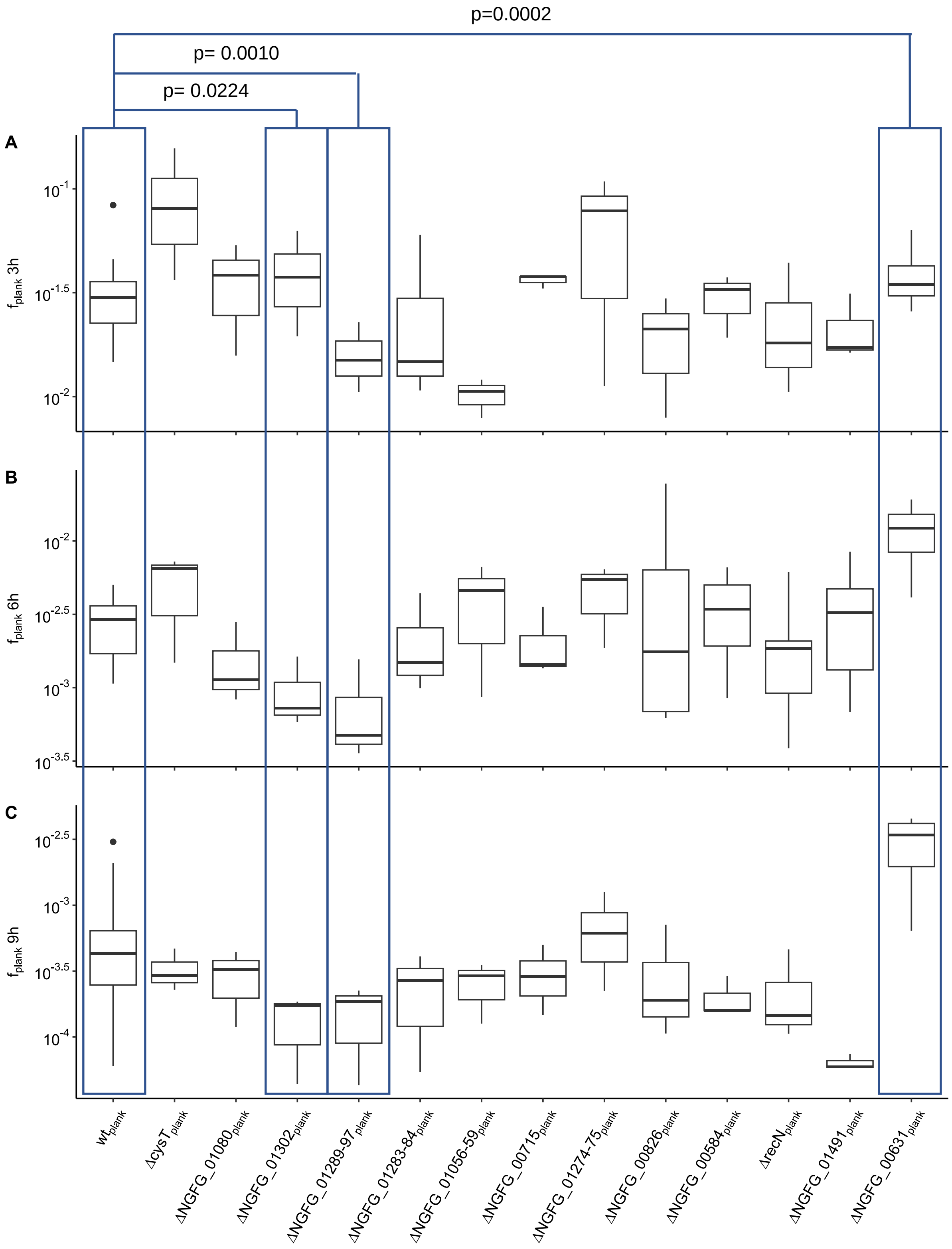

834 S7 Fig.: Fractions of surviving planktonic cells under ceftriaxone treatment for A) 3 h, B) 6 h
835 and C) 9 h.

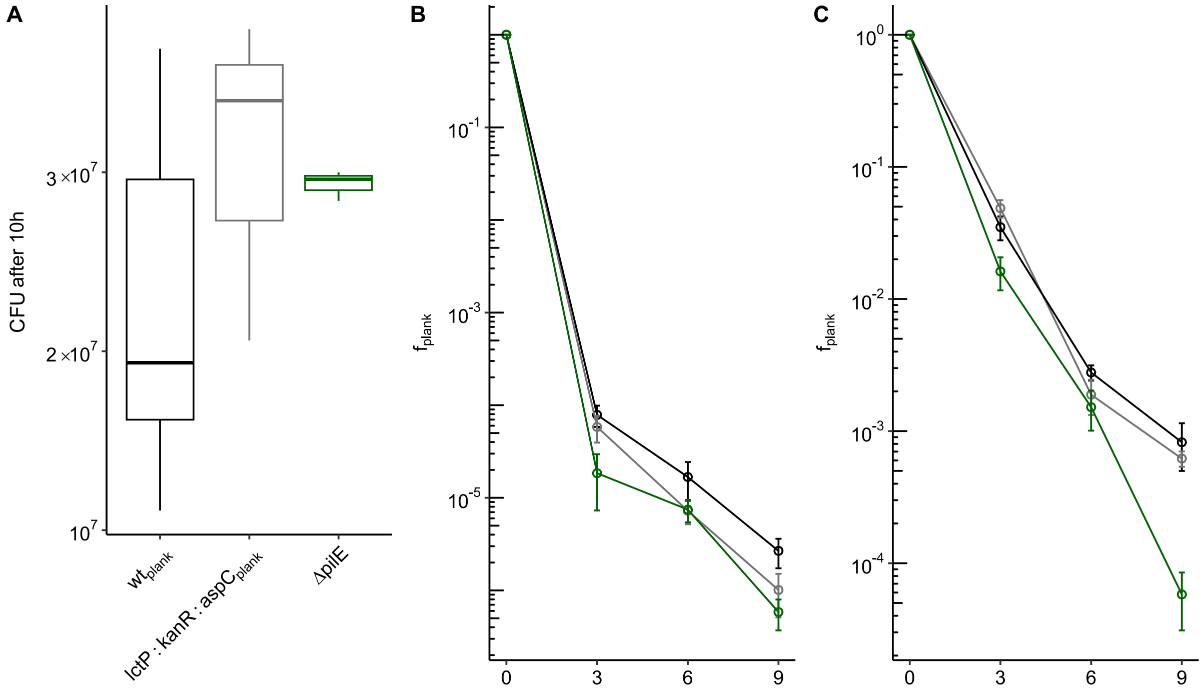

S8 Fig.: The impact of *pilE* deletion and the kanamycin resistance cassette on cell survival during ciprofloxacin and ceftriaxone treatment compared to wt$_{plank}$. *kanR* was introduced into the intergenic *lctP::aspC* locus. A) CFU after 10 h of strains wt$_{plank}$ (Ng240, black), *ΔpilE* (Ng253, green), lctP:kanR:aspC$_{plank}$ (Ng290, grey). B, C) Fractions of surviving planktonic control strains and their respective parental strain. wt$_{plank}$ (Ng240, black), *ΔpilE* (Ng253, green), lctP:kanR:aspC$_{plank}$ (Ng290, grey) under B) ciprofloxacin ($p_{wtplank-\ \Delta pilE}$= 0.12, $p_{wtplank-lctP:kanR:aspCplank}$= 0.87) and C) ceftriaxone treatment ($p_{wtplank-\Delta pilE}$= 9.8×10^{-4}, $p_{wtplank-lctP:kanR:aspCplank}$= 0.76).

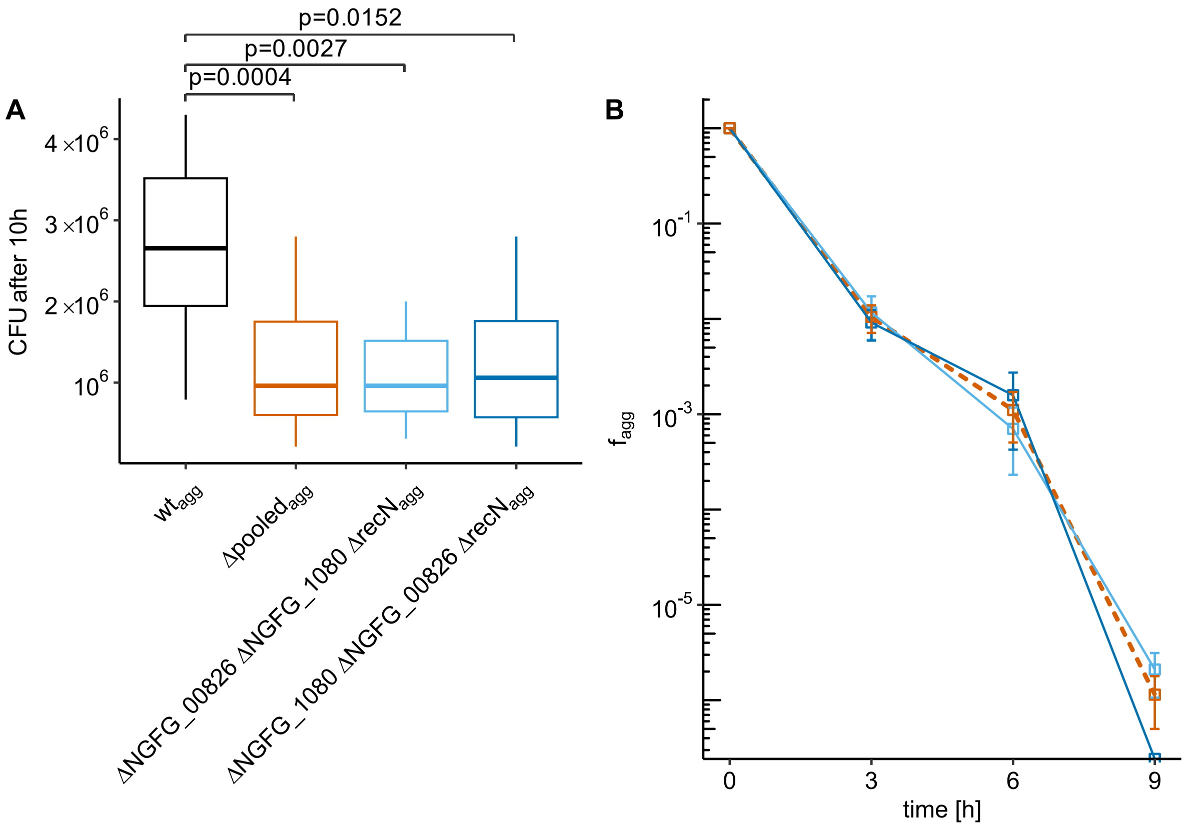

S9 Fig.: Triple knock out strains. The order of the deletion does not significantly impact the triple knock out phenotype. Therefore, we pooled the data of both genotypes for better statistics. A) CFU after 10 h. B) Fractions of surviving aggregating triple KO strains ΔNGFG_00826 ΔNGFG_01080 Δ*recN*$_{\mathrm{agg}}$ (Ng321, cyan) and ΔNGFG_01080 ΔNGFG_00826 Δ*recN*$_{\mathrm{agg}}$ (Ng325, blue) compared to the pooled data (dashed, orange). p-value between ΔNGFG_01080 Δ*recN*$_{\mathrm{agg}}$ (Ng321) and ΔNGFG_01080 ΔNGFG_00826 Δ*recN*$_{\mathrm{agg}}$ (Ng325) = 0.14.

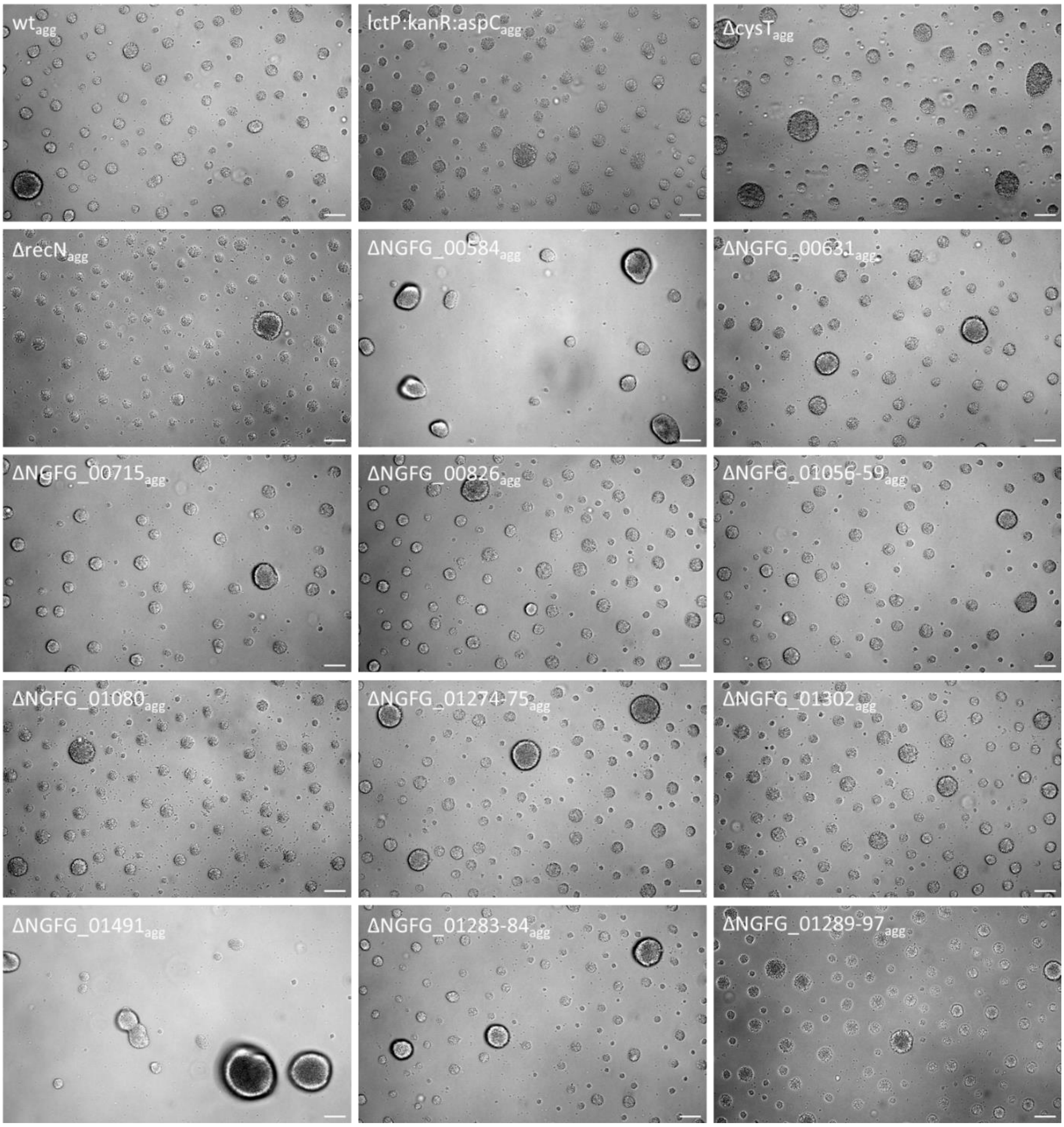

S10 Fig.: All mutants in the wt$_{agg}$ background maintain the ability to form aggregates in liquid media. Cells were grown for 5 h without shaking (37°C, 5% CO_2). Scale bar: 25 µm.

Supplementary tables and data sheets

Deletion	**Gene**	**Annotated function**	**Putative function acc. to protein BLAST analysis***[1]	**KEGG category**	**Potential operon with***[2]
ΔrecN	NGFG_00464 (*recN*)	DNA repair protein	DNA repair protein	Hypothetical	-
ΔNGFG_00584	NGFG_00584	hypothetical protein	hypothetical protein	Hypothetical	-
ΔcysT	NGFG_00600 (*cysT*)	sulfate ABC transporter permease	sulfate ABC transporter permease subunit CysT	-	-
ΔNGFG_00631	NGFG_00631	hypothetical protein	YdaS family protein/ DNA-binding transcriptional regulator/Cro-CI family transcriptional regulator	-	NGFG_02290 (L2FC 1.54, phage protein, phage associated, x)
ΔNGFG_00715	NGFG_00715	phage protein	transposase	Phage Associated	-
ΔNGFG_00826	NGFG_00826	drug:H+ antiporter-2 (14 Spanner) (DHA2) family drug resistance MFS transporter	MFS transporter/DHA2 family efflux permease subunit	Cellular Processes/ Organismal Systems/ Human Disease	-
ΔNGFG_01056-59	NGFG_01056	phage protein	antitoxin/putative zinc finger/helix-turn-helix protein	Phage Associated	-
	NGFG_01058	phage protein	baseplate wedge subunit	-	-
	NGFG_01059	phage baseplate assembly protein	x	Phage Associated	-
ΔNGFG_01080	NGFG_01080	alcohol dehydrogenase	zinc-dependent alcohol dehydrogenase family protein	Carbohydrate Metabolism	-
ΔNGFG_01274-75	NGFG_01274	phage tape measure protein	tail tape measure	Phage Associated	-
	NGFG_01275	hypothetical protein	hypothetical protein/ ParD-like antitoxin of type II bacterial toxin-antitoxin system	Phage Associated	-

ΔNGFG_01283-84	NGFG_01283	phage protein	hypothetical protein	Phage Associated	-
	NGFG_01284	phage protein	hypothetical protein	Phage Associated	-
ΔNGFG_01289-97	NGFG_01289	phage protein	minor tail protein	Phage Associated	-
	NGFG_01290	phage protein	x	Phage Associated	-
	NGFG_01291	phage protein	SNF2 helicase protein	Phage Associated	-
	NGFG_01292	phage protein	tail tube protein	Phage Associated	-
	NGFG_01293	phage protein	hypothetical protein	Phage Associated	-
	NGFG_01294	phage protein	minor tail protein	Phage Associated	-
	NGFG_01295	phage protein	virion morphogenesis protein	-	-
	NGFG_01296	phage protein	head tail connector protein	Phage Associated	-
	NGFG_01297	phage protein	hypothetical	-	-
ΔNGFG_01302	NGFG_01302	phage protein	small terminase subunit, terS	Phage Associated	-

*[1] protein BLAST excluding *'Neisseriales'*

*[2] according to Remmele *et al.* (61)

x= no significant similarity found

S1 Table: Overview of gene deletion strains.

Strain	**MIC [µg/ml]**	
	ceftriaxone	**ciprofloxacin**
wt$_{agg}$	0.008	0.004
ΔcysT$_{agg}$	0.008	0.004
ΔNGFG_01080$_{agg}$	0.008	0.004
ΔNGFG_01302$_{agg}$	0.008	0.004
ΔNGFG_01289-97$_{agg}$	0.008	0.004
ΔNGFG_01283-84$_{agg}$	0.008	0.004
ΔNGFG_01056-59$_{agg}$	0.008	0.004
ΔNGFG_00715$_{agg}$	0.008	0.004
ΔNGFG_01274-75$_{agg}$	0.008	0.004
ΔNGFG_00826$_{agg}$	0.008	0.004
ΔNGFG_00584$_{agg}$	0.008	0.004
ΔrecN$_{agg}$	0.008	0.002
ΔNGFG_01491$_{agg}$	0.008	0.004
ΔNGFG_00631$_{agg}$	0.008	0.004
lctP:kanR:aspC$_{agg}$	0.008	0.004
3xΔ$_{agg}$	not determined	0.004

S2 Table: MIC of aggregating strains.

Abbreviation	**Strain number**	**Strain**	**Relevant genotype**	**Reference**
wt$_{agg}$	Ng150	ΔG4 (wt*)	*G4::apraR*	(29)
-	Ng225	T126C step1	*G4::apraR,* *pilE::pilE*^{T126C} *ermC* *rpsL*$_{S}$	(27)
-	Ng052	*ΔcomE*$_{234}$*ΔpilV*	*comE4::Kan,* *comE3::Clm,* *comE2::Erm,* *recA6ind(tetM) pilVfs*	(68)
wt$_{plank2}$	Ng230	wt$_{pilE32}$	*G4::apraR,* *pilE*$_{clinicalisolateNG32}$	(37)
wt$_{plank}$	Ng240	wt$_{pilE17}$	*G4::apraR,* *pilE*$_{clinicalisolateNG17}$	(37)
wt$_{agg2}$	Ng242	wt$_{pilE24}$	*G4::apraR,* *pilE*$_{clinicalisolateNG24}$	(37)
Δ*pilE*	Ng253	Δ*pilE*	*pilE::kanR*	(37)
ΔrecN$_{agg}$	Ng261	ΔG4 ΔrecN	*recN::kanR*	this study
ΔNGFG_00826$_{agg}$	Ng262	ΔG4 ΔNGFG_00826	*NGFG_00826::kanR*	this study
ΔNGFG_01491$_{agg}$	Ng263	ΔG4 ΔNGFG_01491	*NGFG_01491::kanR*	this study
ΔNGFG_00584$_{agg}$	Ng264	ΔG4 ΔNGFG_00584	*NGFG_00584::kanR*	this study
ΔNGFG_01283-84$_{agg}$	Ng269	ΔG4 ΔNGFG_01283-1284	*NGFG_01283-1284::kanR*	this study
ΔNGFG_01274-1275$_{agg}$	Ng270	ΔG4 ΔNGFG_01274-1275	*NGFG_01274-1275::kanR*	this study
ΔNGFG_01056-1059$_{agg}$	Ng271	ΔG4 ΔNGFG_01056-1059	*NGFG_01056-1059::kanR*	this study
ΔNGFG_00715$_{agg}$	Ng272	ΔG4 ΔNGFG_00715	*NGFG_00715::kanR*	this study
ΔNGFG_01289-97$_{agg}$	Ng273	ΔG4 ΔNGFG_01289-1297	*NGFG_01289-1297::kanR*	this study
ΔrecN$_{plank}$	Ng275	NG17 ΔrecN	*recN::kanR*	this study
ΔNGFG_00826$_{plank}$	Ng276	NG17 ΔNGFG_00826	*NGFG_00826::kanR*	this study
ΔNGFG_01491$_{plank}$	Ng277	NG17 ΔNGFG_01491	*NGFG_01491::kanR*	this study
ΔNGFG_00584$_{plank}$	Ng278	NG17 ΔNGFG_00584	*NGFG_00584::kanR*	this study
ΔcysT$_{agg}$	Ng279	ΔG4 ΔcysT	*cysT::kanR*	this study

ΔNGFG_01302$_{\text{agg}}$	Ng280	ΔG4 ΔNGFG_01302	*NGFG_01302::kanR*	this study
ΔNGFG_01080$_{\text{agg}}$	Ng281	ΔG4 ΔNGFG_01080	*NGFG_01080::kanR*	this study
ΔNGFG_00631$_{\text{plank}}$	Ng288	NG17 ΔNGFG_00631	*NGFG_00631::kanR*	this study
ΔNGFG_00631$_{\text{agg}}$	Ng289	ΔG4 ΔNGFG_00631	*NGFG_00631::kanR*	this study
lctP:kanR:aspC$_{\text{plank}}$	Ng290	NG17 lctP:kanR:aspC	*lctP:kanR:aspC*	this study
lctP:kanR:aspC$_{\text{agg}}$	Ng291	ΔG4 lctP:kanR:aspC	*lctP:kanR:aspC*	this study
ΔNGFG_01284-83$_{\text{plank}}$	Ng296	NG17 ΔNGFG_01284-1283	*NGFG_01284-1283::kanR*	this study
ΔNGFG_01274-75$_{\text{plank}}$	Ng297	NG17 ΔNGFG_01274-1275	*NGFG_01274-1275::kanR*	this study
ΔNGFG_01056-59$_{\text{plank}}$	Ng298	NG17 ΔNGFG_01056-1059	*NGFG_01056-1059::kanR*	this study
ΔNGFG_00715$_{\text{plank}}$	Ng299	NG17 ΔNGFG_00715	*NGFG_00715::kanR*	this study
ΔNGFG_01289-97$_{\text{plank}}$	Ng300	NG17 ΔNGFG_01289-1297	*NGFG_01289-1297::kanR*	this study
ΔcysT$_{\text{plank}}$	Ng301	NG17 ΔcysT	*cysT::kanR*	this study
ΔNGFG_01302$_{\text{plank}}$	Ng302	NG17 ΔNGFG_01302	*NGFG_01302::kanR*	this study
ΔNGFG_01080$_{\text{plank}}$	Ng303	NG17 ΔNGFG_01080	*NGFG_01080::kanR*	this study
ΔNGFG_00826 ΔNGFG_01080 Δ*recN*$_{\text{agg}}$	Ng321	ΔG4 ΔNGFG_00826 ΔNGFG_01080 Δ*recN*	*NGFG_00826::kanR* ΔNGFG_01080 Δ*recN*	this study
ΔNGFG_01080 ΔNGFG_00826 Δ*recN*$_{\text{agg}}$	Ng325	ΔG4 ΔNGFG_01080 ΔNGFG_00826 Δ*recN*	*NGFG_01080::kanR ΔNGFG_00826 ΔrecN*	this study

S3 Table: Strains used in this study.

885

Gene	**Primer A**	**Primer B**	**Primer C**	**Primer D**	**Primer E**	**Primer F**
NGFG_00464	sk260	sk261	sk262	sk263	sk264	sk265
NGFG_00826	sk248	sk249	sk250	sk251	sk252	sk253
NGFG_01491	sk266	sk267	sk268	sk269	sk270	sk271
NGFG_00584	sk254	sk255	sk256	sk257	sk258	sk259
NGFG_01284, 1283	sk288	sk289	sw28	sw29	sk290	sk291
NGFG_01275, 1274	sk292	sk293	sw28	sw29	sk294	sk295
NGFG_01059, 1058, 1056	sk296	sk297	sw28	sw29	sk298	sk299
NGFG_00715	sk304	sk305	sw28	sw29	sk306	sk307
NGFG_01289-1297	sk308	sk309	sw28	sw29	sk310	sk311
NGFG_00600	sk344	sk345	sw28	sw29	sk346	sk347
NGFG_01302	sk340	sk341	sw28	sw29	sk342	sk343
NGFG_01080	sk348	sk349	sw28	sw29	sk350	sk351
NGFG_00631	sk370	sk371	sw28	sw29	sk372	sk373
lctP:aspC	tc14	sk381	sw28	sw29	sk382	sk383

886 S4 Table: Primer combinations used for *kanR* replacements.

887

888

Gene	**Primer cdA**	**Primer cdB**	**Primer cdC**	**Primer cdD**	**Primer cdE**	**Primer cdF**	**Primer cdG**	**Primer cdH**	**Primer cdI**	**Primer cdJ**
NGFG_00826	sk248	sk402	sk403	sk404	sk405	sk253	sk248	sk406	sk407	sk253
NGFG_01080	sk348	sk349	sk403	sk404	sk350	sk351	sk348	sk408	sk409	sk351
NGFG_00464	sk260	sk410	sk403	sk404	sk411	sk265	sk260	sk414	sk415	sk265

889 S5 Table: Primer combinations used for clean deletions.

890

Name	**Sequence 5’ → 3’**
sk248	GTCCTTTTGCAGGGTTGTC
sk249	CGACGTTGTATTCAGACGGCCAGTGACCCCGCATCCCGACAAAA
sk250	GTCACTGGCCGTCTGAATAC
sk251	CTTACTGTACCTTACTCTGTTAGAAAAACTCATCGAGCATCAAATG
sk252	GCTCGATGAGTTTTTCTAACAGAGTAAGGTACAGTAAGCGTTATG
sk253	GCCCTTTTCGCGGTAATAATC
sk254	CTACACCTCGCATACCATTAATC
sk255	CAGACGGCCAGTGAAAATGAAATAGTTGCTTTAATTTCTAAAAAAATTGATG
sk256	GAAATTAAAGCAACTATTTCATTTTCACTGGCCGTCTGAATAC
sk257	GAATTAATATCAATAAGAGAAAATTTAGAAAAACTCATCGAGCATCAAATG
sk258	GCTCGATGAGTTTTTCTAAATTTTCTCTTATTGATATTAATTCTTATTTAAGAATAGTAATG
sk259	GTCATTCAACAGCGGCATAC
sk260	GCTTAAAAAAGCACGTCAGAAAGAAG
sk261	CCAGTGATGTGAGGATTCCTTAGCAATTCTAC
sk262	GTAGAATTGCTAAGGAATCCTCACATCACTGGCCGTCTGAATAC
sk263	GTTATTTTTGTAACTGATTGATTTTAGAAAAACTCATCGAGCATCAAATG
sk264	GCTCGATGAGTTTTTCTAAAATCAATCAGTTACAAAAATAACTGAAAATAGAAG
sk265	CATCTCTTTTCACAACGCCTG
sk266	CGTCCGACATGGTGTTATTC
sk267	GGCCAGTGATTTTCTATCCTTTTTCTGTCAATTCGG
sk268	GAATTGACAGAAAAAGGATAGAAAATCACTGGCCGTCTGAATAC
sk269	GCAGGTTTAGAAAAACTCATCGAGCATCAAATG
sk270	CATTTGATGCTCGATGAGTTTTTCTAAACCTGCCTGCCATTTGAAA
sk271	CAGAGCCATTACGTCTTGTTTC
sk288	GTTGTCGCTCGCTTCCCA
sk289	CCCGGGCCCGGGCCCACCCGTCACACACCCC
sk290	CCCCCGGGGGCCCCCTTTCGAGCGGTATCGCGG
sk291	CAAAATCCGTTTCAGGCGGCATAAT
sk292	CGGCAATCAGGGCAATATGGT
sk293	CCCGGGCCCGGGCCCCTCTGCACCCTGTCAAAATAAAAGGC

sk294	CCCCCGGGGGCCCCCGAAAATGCCGTCCGAAAGGTTCG
sk295	CTATCAAAAAAAGTGCCTGTGGAGGTC
sk296	CTTTGGGCAAGGCTGCC
sk297	CCCGGGCCCGGGCCCCCTATGGCGGCAAAACGC
sk298	CCCCCGGGGGCCCCCATTTTTTGTGGCTGTACTAGATTATCCCTAAATTCC
sk299	GAACAGAGCCGCACTATTCAACC
sk304	CAACTACGCCTACGGCATCAAAAC
sk305	CCCGGGCCCGGGCCCCGCCTTCTCCCGTTTCACC
sk306	CCCCCGGGGGCCCCCGTTTCAACCGAAAACAGCTTTTATAGTGG
sk307	GAGGTTGCGGCTTTGTTGG
sk308	CACCTTGTCTGTAATCTGTGTGGC
sk309	CCCGGGCCCGGGCCCCTCAAAATCTCCAAAAGAAAAAGCCGTCTG
sk310	CCCCCGGGGGCCCCCTATGCCGTCCGAAACGGATTTGAG
sk311	GCAGATGTAACGGTTGACGATTTACC
sk340	CATAGGGCGGTCTGAAATTCACG
sk341	CCCGGGCCCGGGCCCAAACCCTCCTCAAAAAAGAAACCGTC
sk342	CCCCCGGGGGCCCCCCATAAAACGCTAATCATAAGAGGGGCTG
sk343	GCAACGCCTTGACAAATTGCAG
sk344	CTAAAAGTGCCAATACGCCGGAG
sk345	CCCGGGCCCGGGCCCGGTCGTCTGAAAACGAATCCGC
sk346	CCCCCGGGGGCCCCCGGTCGGTAAGGGTGGAAAATAAAGG
sk347	CCAAATAATAAAGCGTATGAACTGCCGC
sk348	GTTTGGCGGCAAAGTCGG
sk349	CCCGGGCCCGGGCCCGCTGATACTCCTTGCTTGTTGATAAATAATTTCAATACC
sk350	CCCCCGGGGGCCCCCTCGCCGTTGAATCAGTTGTTTTTTAAGC
sk351	GTAACCAATCCCGAACAGCTCAAAG
sk370	CGCAATGACATTCTCGAGATAACCG
sk371	CCCGGGCCCGGGCCCAGCCAGTTACTCAATTAAATAGCTTCATTATAGC
sk372	CCCCCGGGGGCCCCCAAAGCCCGTCGGGTCAGAT
sk373	CCCAAAGGCTTTGCCAATTTCG
sk381	CCCGGGCCCGGGCCCATGTTCTTCAAGCACATCGAAGCC
sk382	CCCCCGGGGGCCCCCCTAGAGGAAGAAAATCATTGCCGCG

sk383	CTTCATCGTGCCTTGGTCTGAAATC
sw28	GGGCCCGGGCCCGGGTCACTGGCCGTCTGAATACAA
sw29	GGGGGCCCCCGGGGGTTAGAAAAACTCATCGAGCATCAAATGAAAC
tc14	TGGCGATGATTTCGTGGTCTT

S6 Table: Primers used in this study.

9.5 Supplementary Information for Chapter 7

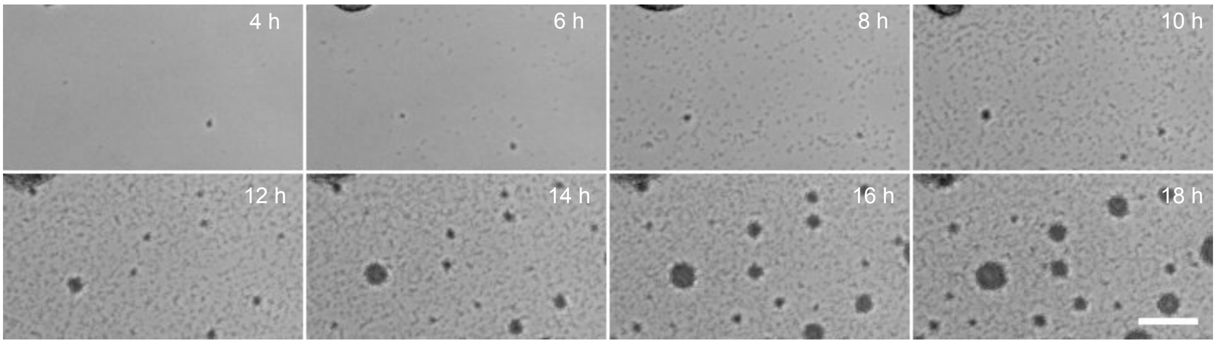

Figure 9.1: A) Time-lapse of empty ROI of flow-chamber experiment. After 6 h single cells appear leading to new colonies over time. Scale bar = 50 µm.

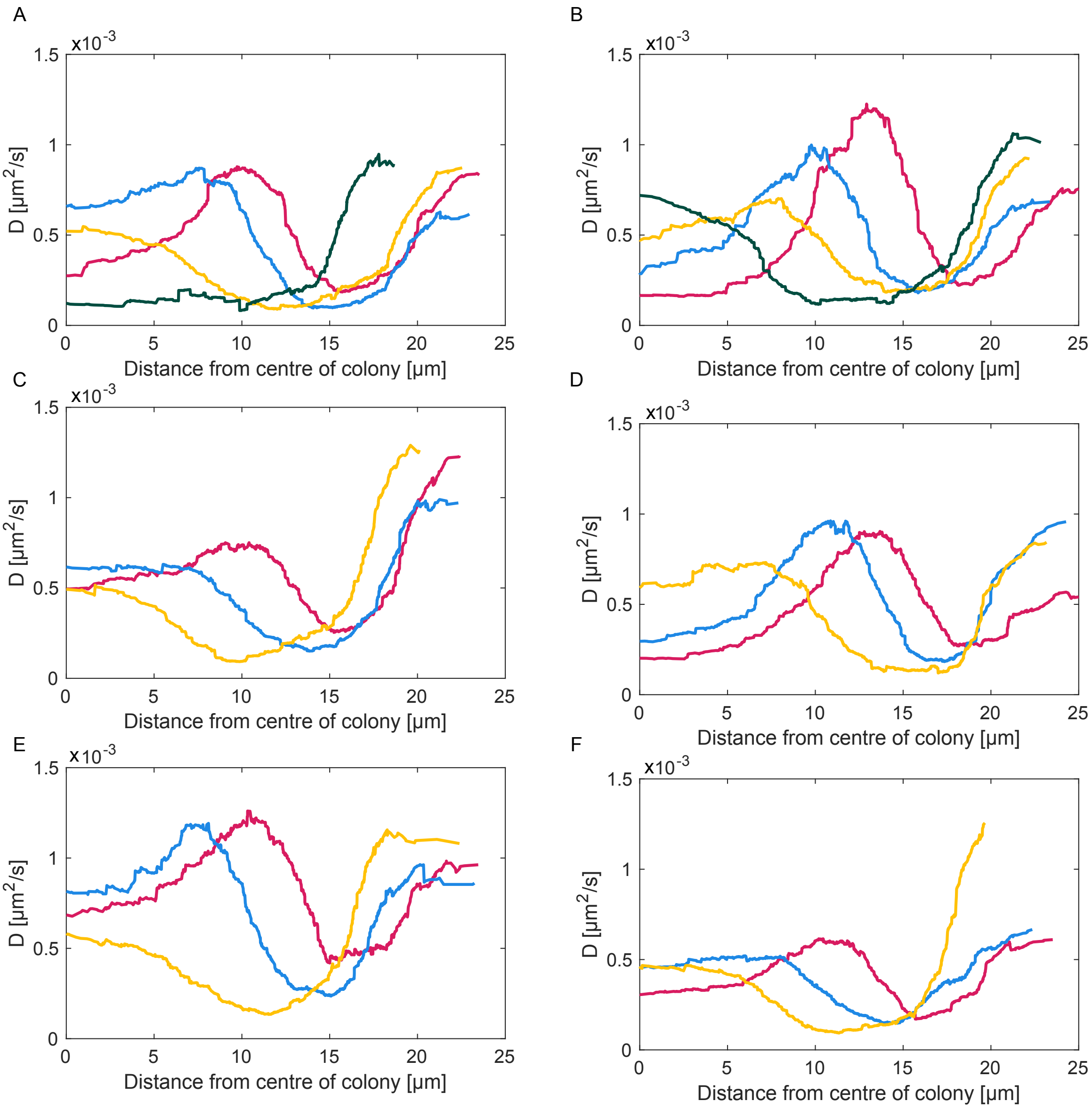

Figure 9.2: A) Example from main text of effective diffusion constant including the hyper-motile edges. green: 180 min; yellow: 90 min; blue: 60 min; magenta: 30 min prior to eversion. B-F) Examples of averaged effective diffusion constants *D* plotted from the centre of the colony towards the edge for the specific times prior to eversion. green: 120 min; yellow: 90 min; blue: 60 min; magenta: 30 min prior to eversion.

List of Figures

List of Tables

Bibliography

1. Flemming H.-C., Wingender J., Szewzyk U., Steinberg P., Rice S. A. & Kjelleberg S. “Biofilms: an emergent form of bacterial life”. *Nature Reviews Microbiology* **14**(9), 563–575, (2016). doi: `10.1038/nrmicro.2016.94`. (Cited on pages 1, 10, 11, 13).
2. Flemming H.-C. & Wuertz S. “Bacteria and archaea on earth and their abundance in biofilms”. *Nature Reviews Microbiology* **17**(4), 247–260, (2019). doi: `10.1038/s41579-019-0158-9`. (Cited on pages 1, 8, 10).
3. Spoering A. L. & Lewis K. “Biofilms and planktonic cells of Pseudomonas aeruginosa have similar resistance to killing by antimicrobials”. *Journal of Bacteriology* **183**(23), 6746–6751, (2001). doi: `10.1128/jb.183.23.6746-6751.2001`. (Cited on pages 1, 15).
4. Hobley L., Harkins C., MacPhee C. E. & Stanley-Wall N. R. “Giving structure to the biofilm matrix: an overview of individual strategies and emerging common themes”. *FEMS Microbiology Reviews* **39**(5), 649–669, (2015). doi: `10.1093/femsre/fuv015`. (Cited on page 1).
5. Perry E. K. & Tan M.-W. “Bacterial biofilms in the human body: prevalence and impacts on health and disease”. *Frontiers in Cellular and Infection Microbiology* **13**, (2023). doi: `10.3389/fcimb.2023.1237164`. (Cited on page 1).
6. Tamayo R., Patimalla B. & Camilli A. “Growth in a biofilm induces a hyperinfectious phenotype in Vibrio cholerae”. *Infection and Immunity* **78**(8), 3560–3569, (2010). doi: `10.1128/iai.00048-10`. (Cited on page 1).
7. Koo H., Allan R. N., Howlin R. P., Stoodley P. & Hall-Stoodley L. “Targeting microbial biofilms: current and prospective therapeutic strategies”. *Nature Reviews Microbiology* **15**(12), 740–755, (2017). doi: `10.1038/nrmicro.2017.99`. (Cited on page 1).
8. Meredith H. R., Srimani J. K., Lee A. J., Lopatkin A. J. & You L. “Collective antibiotic tolerance: mechanisms, dynamics and intervention”. *Nature Chemical Biology* **11**(3), 182–188, (2015). doi: `10.1038/nchembio.1754`. (Cited on pages 1, 15, 17, 147).
9. Meirelles L. A., Vayena E., Debache A., Schmidt E., Rossy T., Distler T., Hatzimanikatis V. & Persat A. “Pseudomonas aeruginosa faces a fitness trade-off between mucosal colonization and antibiotic tolerance during airway infection”. *Nature Microbiology* **9**(12), 3284–3303, (2024). doi: `10.1038/s41564-024-01842-3`. (Cited on page 1).
10. last checked: 01.03.2025. `https://www.cdc.gov/sti-statistics/annual/summary.html`. (Cited on page 1).

11. last checked: 01.03.2025. `https://www.ecdc.europa.eu/en/publications-data/gonorrhoea-annual-epidemiological-report-2023`. (Cited on page 1).

12. "Enhanced gonococcal antimicrobial surveillance programme (EGASP): surveillance report 2023". WHO. (Cited on page 1).

13. Balduck M., Strikker A., Gestels Z., Abdellati S., Van den Bossche D., De Baetselier I., Kenyon C. & Manoharan-Basil S. S. "The prevalence of antibiotic tolerance in Neisseria gonorrhoeae varies by anatomical site". *Pathogens* **13**(7), (2024). doi: `10.3390/pathogens13070538`. (Cited on pages 1, 16).

14. Levin-Reisman I., Ronin I., Gefen O., Braniss I., Shoresh N. & Balaban N. Q. "Antibiotic tolerance facilitates the evolution of resistance". *Science (New York, N.Y.)* **355**(6327), 826–830, (2017). doi: `10.1126/science.aaj2191`. (Cited on page 1).

15. Apicella M. A., Steichen C. T., McEwan A. G., Cho C., Falsetta M. L., Ketterer M., Shao J., Hunt J. & Jennings M. P. "The composition and metabolic phenotype of Neisseria gonorrhoeae biofilms". *Frontiers in Microbiology* **2**, (2011). doi: `10.3389/fmicb.2011.00075`. (Cited on page 1).

16. Welker A., Cronenberg T., Zöllner R., Meel C., Siewering K., Bender N., Hennes M., Oldewurtel E. R. & Maier B. "Molecular motors govern liquidlike ordering and fusion dynamics of bacterial colonies". *Physical Review Letters* **121**(11), 118102, (2018). doi: `10.1103/PhysRevLett.121.118102`. (Cited on pages 1, 7, 12, 13, 19, 137).

17. Maier B. "How physical interactions shape bacterial biofilms". *Annual review of biophysics* **50**, 401–417, (2021). doi: `10.1146/annurev-biophys-062920-063646`. (Cited on pages 1, 11, 13, 137).

18. Nahum Y., Gross N., Cerrone A., Matous K. & Nerenberg R. "Effect of biofilm physical characteristics on their susceptibility to antibiotics: impacts of low-frequency ultrasound". *npj Biofilms and Microbiomes* **10**(1), 70, (2024). doi: `10.1038/s41522-024-00544-2`. (Cited on page 1).

19. Steichen C. T., Cho C., Shao J. Q. & Apicella M. A. "The Neisseria gonorrhoeae biofilm matrix contains DNA, and an endogenous nuclease controls its incorporation". *Infection and immunity* **79**(4), 1504–1511, (2011). doi: `10.1128/IAI.01162-10`. (Cited on pages 1, 146).

20. Zweig M., Schork S., Koerdt A., Siewering K., Sternberg C., Thormann K., Albers S.-V., Molin S. & van der Does C. "Secreted single-stranded DNA is involved in the initial phase of biofilm formation by Neisseria gonorrhoeae". *Environmental Microbiology* **16**(4), 1040–1052, (2014). doi: `10.1111/1462-2920.12291`. (Cited on pages 1, 142, 146).

21. Heikens E., Bonten M. J. M. & Willems R. J. L. "Enterococcal Surface Protein Esp Is Important for Biofilm Formation of Enterococcus faecium E1162". *Journal of Bacteriology* **189**(22), 8233–8240, (2007). doi: `10.1128/jb.01205-07`. (Cited on page 2).

22. Boyd A. & Chakrabarty A. M. "Pseudomonas aeruginosa biofilms: role of the alginate exopolysaccharide". *Journal of Industrial Microbiology* **15**(3), 162–168, (1995). doi: `10.1007/BF01569821`. (Cited on pages 2, 12).

23. Ronish L. A., Lillehoj E., Fields J. K., Sundberg E. J. & Piepenbrink K. H. "The structure of PilA from Acinetobacter baumannii AB5075 suggests a mechanism for functional specialization in Acinetobacter type IV pili". *Journal of Biological Chemistry* **294**(1), 218–230, (2019). doi: `10.1074/jbc.RA118.005814`. (Cited on page 2).

24. Burrows L. L. "Pseudomonas aeruginosa twitching motility: type IV pili in action". *Annual review of microbiology* **66**, 493–520, (2012). doi: `10.1146/annurev-micro-092611-150055`. (Cited on pages 2, 9, 147).

25. Pelicic V. "Type IV pili: e pluribus unum?" *Molecular Microbiology* **68**(4), 827–837, (2008). doi: `10.1111/j.1365-2958.2008.06197.x`. (Cited on page 2).

26. Rotman E. & Seifert H. S. "The genetics of Neisseria species". *Annual review of genetics* **48**, 405–431, (2014). doi: `10.1146/annurev-genet-120213-092007`. (Cited on pages 2, 4, 5, 17).

27. Craig L., Pique M. E. & Tainer J. A. "Type IV pilus structure and bacterial pathogenicity". *Nature Reviews Microbiology* **2**(5), 363–378, (2004). doi: `10.1038/nrmicro885`. (Cited on pages 2, 8).

28. Taktikos J., Lin Y. T., Stark H., Biais N. & Zaburdaev V. "Pili-induced clustering of N. gonorrhoeae bacteria". *PLOS ONE* **10**(9), (2015). doi: `10.1371/journal.pone.0137661`. (Cited on page 2).

29. Maier B., Potter L., So M., Long C. D., Seifert H. S. & Sheetz M. P. "Single pilus motor forces exceed 100 pN". *Proceedings of the National Academy of Sciences of the United States of America* **99**(25), (2002). doi: `10.1073/pnas.242523299`. (Cited on pages 2, 6, 27).

30. Bieber D., Ramer S. W., Wu C. Y., Murray W. J., Tobe T., Fernandez R. & Schoolnik G. K. "Type IV pili, transient bacterial aggregates, and virulence of enteropathogenic Escherichia coli". *Science (New York, N.Y.)* **280**(5372), 2114–2118, (1998). doi: `10.1126/science.280.5372.2114`. (Cited on page 2).

31. Tacket C. O., Taylor R. K., Losonsky G., Lim Y., Nataro J. P., Kaper J. B. & Levine M. M. "Investigation of the roles of toxin-coregulated pili and mannose-sensitive hemagglutinin pili in the pathogenesis of Vibrio cholerae O139 infection". *Infection and immunity* **66**(2), 692–695, (1998). doi: `10.1128/IAI.66.2.692-695.1998`. (Cited on page 2).

32. Biais N., Higashi D. L., Brujić J., So M. & Sheetz M. P. "Force-dependent polymorphism in type IV pili reveals hidden epitopes". *Proceedings of the National Academy of Sciences* **107**(25), 11358–11363, (2010). doi: `10.1073/pnas.0911328107`. (Cited on page 2).

33. Craig L., Volkmann N., Arvai A. S., Pique M. E., Yeager M., Egelman E. H. & Tainer J. A. "Type IV pilus structure by cryo-electron microscopy and crystallography: implications for pilus assembly and functions". *Molecular Cell* **23**(5), 651–662, (2006). doi: `10.1016/j.molcel.2006.07.004`. (Cited on pages 2–4).

34. Parge H. E., Forest K. T., Hickey M. J., Christensen D. A., Getzoff E. D. & Tainer J. A. "Structure of the fibre-forming protein pilin at 2.6 Å resolution". *Nature* **378**(6552), 32–38, (1995). doi: `10.1038/378032a0`. (Cited on pages 2, 3).

35. Craig L., Forest K. T. & Maier B. "Type IV pili: dynamics, biophysics and functional consequences". *Nature reviews. Microbiology* **17**(7), 429–440, (2019). doi: `10.1038/s41579-019-0195-4`. (Cited on pages 2, 3).

36. Helaine S., Dyer D. H., Nassif X., Pelicic V. & Forest K. T. "3D structure/function analysis of PilX reveals how minor pilins can modulate the virulence properties of type IV pili". *Proceedings of the National Academy of Sciences of the United States of America* **104**(40), 15888–15893, (2007). doi: `10.1073/pnas.0707581104`. (Cited on page 2).

37. Kirchner M. & Meyer T. F. "The PilC adhesin of the Neisseria type IV pilus – binding specificities and new insights into the nature of the host cell receptor". *Molecular Microbiology* **56**(4), 945–957, (2005). doi: `10.1111/j.1365-2958.2005.04600.x`. (Cited on page 2).

38. Ayers M., Howell P. L. & Burrows L. L. "Architecture of the type II secretion and type IV pilus machineries". *Future microbiology* **5**(8), 1203–1218, (2010). doi: `10.2217/fmb.10.76`. (Cited on page 3).

39. Chang Y.-W., Rettberg L. A., Treuner-Lange A., Iwasa J., Søgaard-Andersen L. & Jensen G. J. "Architecture of the type IVa pilus machine". *Science (New York, N.Y.)* **351**(6278), (2016). doi: `10.1126/science.aad2001`. (Cited on page 3).

40. Kolappan S., Coureuil M., Yu X., Nassif X., Egelman E. H. & Craig L. "Structure of the Neisseria meningitidis Type IV pilus". *Nature Communications* **7**, 13015, (2016). doi: `10.1038/ncomms13015`. (Cited on pages 3, 4).

41. Hung M.-C. & Christodoulides M. "The biology of Neisseria adhesins". *Biology* **2**(3), 1054–1109, (2013). doi: `10.3390/biology2031054`. (Cited on page 4).

42. Wachter J., Masters T. L., Wachter S., Mason J. & Hill S. A. "pilS loci in Neisseria gonorrhoeae are transcriptionally active". *Microbiology* **161**(5), 1124–1135, (2015). doi: `10.1099/mic.0.000061`. (Cited on page 4).

43. Helm R. A. & Seifert H. S. "Pilin antigenic variation occurs independently of the RecBCD pathway in Neisseria gonorrhoeae". *Journal of bacteriology* **191**(18), 5613–5621, (2009). doi: `10.1128/JB.00535-09`. (Cited on pages 4, 147).

44. Vink C., Rudenko G. & Seifert H. S. "Microbial antigenic variation mediated by homologous DNA recombination". *FEMS Microbiology Reviews* **36**(5), 917–948, (2012). doi: `10.1111/j.1574-6976.2011.00321.x`. (Cited on page 4).

45. Cahoon L. A. & Seifert H. S. “Focusing homologous recombination: pilin antigenic variation in the pathogenic Neisseria”. *Molecular Microbiology* **81**(5), 1136–1143, (2011). doi: `10.1111/j.1365-2958.2011.07773.x`. (Cited on page 4).

46. Kennouche P., Charles-Orszag A., Nishiguchi D., Goussard S., Imhaus A.-F., Dupré M., Chamot-Rooke J. & Duménil G. “Deep mutational scanning of the Neisseria meningitidis major pilin reveals the importance of pilus tip-mediated adhesion”. *The EMBO Journal* **38**(22), (2019). doi: `10.15252/embj.2019102145`. (Cited on page 5).

47. Zöllner R., Oldewurtel E. R., Kouzel N. & Maier B. “Phase and antigenic variation govern competition dynamics through positioning in bacterial colonies”. *Scientific reports* **7**(1), 12151, (2017). doi: `10.1038/s41598-017-12472-7`. (Cited on pages 5, 13, 19).

48. Rotman E. & Seifert H. S. “Neisseria gonorrhoeae MutS affects pilin antigenic variation through mismatch correction and not by pilE guanine quartet binding”. *Journal of bacteriology* **197**(10), 1828–1838, (2015). doi: `10.1128/JB.02594-14`. (Cited on page 5).

49. Phillips R., Kondev J. & Theriot J. “Physical Biology of the Cell” (Garland Science, 2009) (cited on pages 5, 9).

50. Freitag N. E., Seifert H. S. & Koomey M. “Characterization of the pilF-pilD pilus-assembly locus of Neisseria gonorrhoeae”. *Mol Microbiol* **16**(3), 575–586, (1995). doi: `10.1111/j.1365-2958.1995.tb02420.x`. (Cited on page 5).

51. Wolfgang M., Lauer P., Park H. S., Brossay L., Hébert J. & Koomey M. “PilT mutations lead to simultaneous defects in competence for natural transformation and twitching motility in piliated Neisseria gonorrhoeae.” *Mol Microbiol* **29**(1), 321–330, (1998). doi: `10.1046/j.1365-2958.1998.00935.x`. (Cited on page 5).

52. Clausen M., Koomey M. & Maier B. “Dynamics of type IV pili is controlled by switching between multiple states”. *Biophysical journal* **96**(3), 1169–1177, (2009). doi: `10.1016/j.bpj.2008.10.017`. (Cited on pages 6–8).

53. Merz A. J., So M. & Sheetz M. P. “Pilus retraction powers bacterial twitching motility”. *Nature* **407**(6800), 98–102, (2000). doi: `10.1038/35024105`. (Cited on page 6).

54. Biais N., Ladoux B., Higashi D., So M. & Sheetz M. “Cooperative retraction of bundled type IV pili enables nanonewton force generation”. *PLOS Biology* **6**(4), 1–7, (2008). doi: `10.1371/journal.pbio.0060087`. (Cited on page 6).

55. Sabass B., Koch M. D., Liu G., Stone H. A. & Shaevitz J. W. “Force generation by groups of migrating bacteria”. *Proceedings of the National Academy of Sciences* **114**(28), 7266–7271, (2017). doi: `10.1073/pnas.1621469114`. (Cited on page 6).

56. Jaumouillé V. in *Fluorescent Microscopy* 125–139 (Springer US, New York, NY, 2022). ISBN: 978-1-0716-2051-9 (cited on page 6).

57. Maier B. & Wong G. C. L. “How bacteria use type IV Pili machinery on surfaces”. *Trends in Microbiology* **23**(12), 775–788, (2015). doi: `10.1016/j.tim.2015.09.002`. (Cited on pages 6, 8).

58. Maier B., Koomey M. & Sheetz M. P. “A force-dependent switch reverses type IV pilus retraction”. *Proceedings of the National Academy of Sciences* **101**(30), 10961–10966, (2004). doi: `10.1073/pnas.0402305101`. (Cited on page 6).

59. Zöllner R., Cronenberg T., Kouzel N., Welker A., Koomey M. & Maier B. “Type IV pilin post-translational modifications modulate material properties of bacterial colonies”. *Biophysical Journal* **116**(5), 938–947, (2019). doi: `10.1016/j.bpj.2019.01.020`. (Cited on pages 7, 13, 19).

60. Dewenter L., Volkmann T. E. & Maier B. “Oxygen governs gonococcal microcolony stability by enhancing the interaction force between type IV pili”. *Integrative biology : quantitative biosciences from nano to macro* **7**(10), 1161–1170, (2015). doi: `10.1039/c5ib00018a`. (Cited on pages 7, 13, 137, 140, 142, 146, 148).

61. Zöllner R., Cronenberg T., Maier B. & O’Toole G. “Motor properties of PilT-independent type 4 pilus retraction in gonococci”. *Journal of Bacteriology* **201**(18), e00778–18, (2019). doi: `10.1128/JB.00778-18`. (Cited on page 7).

62. Oldewurtel E. R., Kouzel N., Dewenter L., Henseler K., Maier B. & Kolter R. “Differential interaction forces govern bacterial sorting in early biofilms”. *eLife* **4**, e10811, (2015). doi: `10.7554/eLife.10811`. (Cited on pages 7, 13, 19, 20).

63. Skerker J. M. & Berg H. C. “Direct observation of extension and retraction of type IV pili”. *Proceedings of the National Academy of Sciences of the United States of America* **98**(12), 6901–6904, (2001). doi: `10.1073/pnas.121171698`. (Cited on page 8).

64. Koch M. D., Fei C., Wingreen N. S., Shaevitz J. W. & Gitai Z. “Competitive binding of independent extension and retraction motors explains the quantitative dynamics of type IV pili”. *Proceedings of the National Academy of Sciences* **118**(8), e2014926118, (2021). doi: `10.1073/pnas.2014926118`. (Cited on page 8).

65. Talà L., Fineberg A., Kukura P. & Persat A. “Pseudomonas aeruginosa orchestrates twitching motility by sequential control of type IV pili movements”. *Nature Microbiology* **4**(5), 774–780, (2019). doi: `10.1038/s41564-019-0378-9`. (Cited on page 8).

66. Ellison C. K., Dalia T. N., Dalia A. B. & Brun Y. V. “Real-time microscopy and physical perturbation of bacterial pili using maleimide-conjugated molecules”. eng. *Nat Protoc* **14**(6), 1803–1819, (2019). doi: `10.1038/s41596-019-0162-6`. (Cited on pages 8, 17).

67. Ellison C. K., Dalia T. N., Vidal Ceballos A., Wang J. C.-Y., Biais N., Brun Y. V. & Dalia A. B. “Retraction of DNA-bound type IV competence pili initiates DNA uptake during natural transformation in Vibrio cholerae” **3**(7), 773–780, (2018). doi: `10.1038/s41564-018-0174-y`. (Cited on page 8).

68. Ellison C. K., Kan J., Dillard R. S., Kysela D. T., Ducret A., Berne C., Hampton C. M., Ke Z., Wright E. R., Biais N., Dalia A. B. & Brun Y. V. “Obstruction of pilus retraction stimulates bacterial surface sensing”. *Science* **358**(6362), 535–538, (2017). doi: `10.1126/science.aan5706`. (Cited on page 8).

69. Vlamakis H. C., Kirby J. R. & Zusman D. R. “The Che4 pathway of Myxococcus xanthus regulates type IV pilus-mediated motility”. *Molecular Microbiology* **52**(6), 1799–1811, (2004). doi: `10.1111/j.1365-2958.2004.04098.x`. (Cited on page 8).

70. Jarrell K. F. & McBride M. J. “The surprisingly diverse ways that prokaryotes move”. *Nature Reviews Microbiology* **6**(6), 466–476, (2008). doi: `10.1038/nrmicro1900`. (Cited on page 8).

71. Holz C., Opitz D., Greune L., Kurre R., Koomey M., Schmidt M. A. & Maier B. “Multiple Pilus Motors Cooperate for Persistent Bacterial Movement in Two Dimensions”. *Physical Review Letters* **104**(17), 178104, (2010). doi: `10.1103/PhysRevLett.104.178104`. (Cited on pages 9, 10, 36).

72. Zaburdaev V., Biais N., Schmiedeberg M., Eriksson J., Jonsson A.-B., Sheetz M. P. & Weitz D. A. “Uncovering the mechanism of trapping and cell orientation during Neisseria gonorrhoeae twitching motility”. *Biophysical Journal* **107**(7), 1523–1531, (2014). doi: `https://doi.org/10.1016/j.bpj.2014.07.061`. (Cited on page 9).

73. Marathe R., Meel C., Schmidt N. C., Dewenter L., Kurre R., Greune L., Alexander Schmidt M., Müller M. J., Lipowsky R., Maier B. & Klumpp S. “Bacterial twitching motility is coordinated by a two-dimensional tug-of-war with directional memory”. *Nature Communications* **5**(1), 3759, (2014). doi: `10.1038/ncomms4759`. (Cited on pages 9, 36).

74. Kurre R. & Maier B. “Oxygen depletion triggers switching between discrete speed modes of gonococcal type IV pili”. *Biophysical journal* **102**(11), 2556–2563, (2012). doi: `10.1016/j.bpj.2012.04.020`. (Cited on page 10).

75. Sauer K., Camper A. K., Ehrlich G. D., Costerton J. W. & Davies D. G. “Pseudomonas aeruginosa displays multiple phenotypes during development as a biofilm”. *J Bacteriol* **184**(4), 1140–1154, (2002). doi: `10.1128/jb.184.4.1140-1154.2002`. (Cited on page 10).

76. Singer S. W., Erickson B. K., VerBerkmoes N. C., Hwang M., Shah M. B., Hettich R. L., Banfield J. F. & Thelen M. P. “Posttranslational modification and sequence variation of redox-active proteins correlate with biofilm life cycle in natural microbial communities”. *The ISME Journal* **4**(11), 1398–1409, (2010). doi: `10.1038/ismej.2010.64`. (Cited on page 10).

77. Serra D. O. & Hengge R. “Stress responses go three dimensional - the spatial order of physiological differentiation in bacterial macrocolony biofilms”. *Environ Microbiol* **16**(6), 1455–1471, (2014). doi: `10.1111/1462-2920.12483`. (Cited on pages 11, 137).

78. Falsetta M. L., Bair T. B., Ku S. C., vanden Hoven R. N., Steichen C. T., McEwan A. G., Jennings M. P. & Apicella M. A. “Transcriptional profiling identifies the metabolic phenotype of gonococcal biofilms”. *Infection and Immunity* **77**(9), 3522–3532, (2009). doi: `10.1128/iai.00036-09`. (Cited on pages 11, 147).

79. Phillips N. J., Steichen C. T., Schilling B., Post D. M. B., Niles R. K., Bair T. B., Falsetta M. L., Apicella M. A. & Gibson B. W. “Proteomic Analysis of Neisseria gonorrhoeae Biofilms Shows Shift to Anaerobic Respiration and Changes in Nutrient Transport and Outermembrane Proteins”. *PLOS ONE* **7**(6), 1–18, (2012). doi: `10.1371/journal.pone.0038303`. (Cited on pages 11, 147).

80. Falsetta M. L., McEwan A. G., Jennings M. P. & Apicella M. A. “Anaerobic metabolism occurs in the substratum of gonococcal biofilms and may be sustained in part by nitric oxide”. *Infection and Immunity* **78**(5), 2320–2328, (2010). doi: `10.1128/iai.01312-09`. (Cited on page 11).

81. Flemming H.-C. & Wingender J. “The biofilm matrix”. *Nature Reviews Microbiology* **8**(9), 623–633, (2010). doi: `10.1038/nrmicro2415`. (Cited on page 11).

82. Roilides E., Simitsopoulou M., Katragkou A. & Walsh T. J. “How biofilms evade host defenses”. *Microbiology Spectrum* **3**(3), 10.1128/microbiolspec.mb-0012–2014, (2015). doi: `10.1128/microbiolspec.mb-0012-2014`. (Cited on page 11).

83. Vidakovic L., Singh P. K., Hartmann R., Nadell C. D. & Drescher K. “Dynamic biofilm architecture confers individual and collective mechanisms of viral protection”. *Nat Microbiol* **3**(1), 26–31, (2018). doi: `10.1038/s41564-017-0050-1`. (Cited on page 11).

84. Abe K., Nomura N. & Suzuki S. “Biofilms: hot spots of horizontal gene transfer (HGT) in aquatic environments, with a focus on a new HGT mechanism”. *FEMS Microbiol Ecol* **96**(5), (2020). doi: `10.1093/femsec/fiaa031`. (Cited on page 11).

85. Iskratsch T., Wolfenson H. & Sheetz M. P. “Appreciating force and shape —the rise of mechanotransduction in cell biology”. *Nature Reviews Molecular Cell Biology* **15**(12), 825–833, (2014). doi: `10.1038/nrm3903`. (Cited on page 11).

86. Mann E. E. & Wozniak D. J. “Pseudomonas biofilm matrix composition and niche biology”. *FEMS Microbiology Reviews* **36**(4), 893–916, (2012). doi: `10.1111/j.1574-6976.2011.00322.x`. (Cited on page 12).

87. Drescher K., Dunkel J., Nadell C. D., van Teeffelen S., Grnja I., Wingreen N. S., Stone H. A. & Bassler B. L. “Architectural transitions in Vibrio cholerae biofilms at single-cell resolution”. *Proceedings of the National Academy of Sciences* **113**(14), E2066–E2072, (2016). doi: `10.1073/pnas.1601702113`. (Cited on page 12).

88. Yan J., Nadell C. D., Stone H. A., Wingreen N. S. & Bassler B. L. “Extracellular-matrix-mediated osmotic pressure drives Vibrio cholerae biofilm expansion and cheater exclusion”. *Nature Communications* **8**(1), 327, (2017). doi: `10.1038/s41467-017-00401-1`. (Cited on page 12).

89. Seminara A., Angelini T. E., Wilking J. N., Vlamakis H., Ebrahim S., Kolter R., Weitz D. A. & Brenner M. P. “Osmotic spreading of Bacillus subtilis biofilms driven by an extracellular matrix”. *Proceedings of the National Academy of Sciences* **109**(4), 1116–1121, (2012). doi: `10.1073/pnas.1109261108`. (Cited on page 12).

90. Smith W. P. J., Davit Y., Osborne J. M., Kim W., Foster K. R. & Pitt-Francis J. M. “Cell morphology drives spatial patterning in microbial communities”. *Proceedings of the National Academy of Sciences* **114**(3), E280–E286, (2017). doi: `10.1073/pnas.1613007114`. (Cited on page 12).

91. You Z., Pearce D. J. G., Sengupta A. & Giomi L. “Geometry and mechanics of microdomains in growing bacterial colonies”. *Phys. Rev. X* **8**, 031065, (2018). doi: `10.1103/PhysRevX.8.031065`. (Cited on page 12).

92. Beroz F., Yan J., Meir Y., Sabass B., Stone H. A., Bassler B. L. & Wingreen N. S. “Verticalization of bacterial biofilms”. *Nature Physics* **14**(9), 954–960, (2018). doi: `10.1038/s41567-018-0170-4`. (Cited on page 12).

93. Yan J., Sharo A. G., Stone H. A., Wingreen N. S. & Bassler B. L. “Vibrio cholerae biofilm growth program and architecture revealed by single-cell live imaging”. *Proceedings of the National Academy of Sciences* **113**(36), E5337–E5343, (2016). doi: `10.1073/pnas.1611494113`. (Cited on page 12).

94. Hartmann R., Singh P. K., Pearce P., Mok R., Song B., Díaz-Pascual F., Dunkel J. & Drescher K. “Emergence of three-dimensional order and structure in growing biofilms”. *Nature Physics* **15**(3), 251–256, (2019). doi: `10.1038/s41567-018-0356-9`. (Cited on pages 12, 13).

95. Nijjer J., Li C., Zhang Q., Lu H., Zhang S. & Yan J. “Mechanical forces drive a reorientation cascade leading to biofilm self-patterning”. *Nature Communications* **12**(1), 6632, (2021). doi: `10.1038/s41467-021-26869-6`. (Cited on page 13).

96. Copenhagen K., Alert R., Wingreen N. S. & Shaevitz J. W. “Topological defects promote layer formation in Myxococcus xanthus colonies”. *Nature Physics* **17**(2), 211–215, (2021). doi: `10.1038/s41567-020-01056-4`. (Cited on page 13).

97. Bonazzi D., Lo Schiavo V., Machata S., Djafer-Cherif I., Nivoit P., Manriquez V., Tanimoto H., Husson J., Henry N., Chaté H., Voituriez R. & Duménil G. “Intermittent Pili-Mediated Forces Fluidize Neisseria meningitidis Aggregates Promoting Vascular Colonization”. *Cell* **174**(1), 143–155.e16, (2018). doi: `10.1016/j.cell.2018.04.010`. (Cited on page 13).

98. Pönisch W., Weber C. A., Juckeland G., Biais N. & Zaburdaev V. “Multiscale modeling of bacterial colonies: how pili mediate the dynamics of single cells and cellular aggregates”. *New Journal of Physics* **19**(1), 015003, (2017). doi: `10.1088/1367-2630/aa5483`. (Cited on page 13).

99. Steinberg M. S. “Reconstruction of tissues by dissociated cells”. *Science* **141**(3579), 401–408, (1963). doi: `10.1126/science.141.3579.401`. (Cited on page 13).

100. Harris A. K. “Is cell sorting caused by differences in the work of intercellular adhesion? A critique of the steinberg hypothesis”. *Journal of Theoretical Biology* **61**(2), 267–285, (1976). doi: `10.1016/0022-5193(76)90019-9`. (Cited on pages 13, 142).

101. Pönisch W., Eckenrode K. B., Alzurqa K., Nasrollahi H., Weber C., Zaburdaev V. & Biais N. “Pili mediated intercellular forces shape heterogeneous bacterial microcolonies prior to multicellular differentiation”. *Scientific reports* **8**(1), 16567–16567, (2018). doi: `10.1038/s41598-018-34754-4`. (Cited on page 13).

102. Hennes M, Cronenberg T & Maier B. “Caging dynamics in bacterial colonies”. *Physical Review Research* **4**(1), 013187, (2022). doi: `10.1103/PhysRevResearch.4.013187`. (Cited on pages 13, 139, 140).

103. Welker A., Hennes M., Bender N., Cronenberg T., Schneider G. & Maier B. “Spatiotemporal dynamics of growth and death within spherical bacterial colonies”. *Biophysical Journal* **120**(16), 3418–3428, (2021). doi: `10.1016/j.bpj.2021.06.022`. (Cited on pages 13, 16, 19, 137).

104. Stewart P. S. & Franklin M. J. “Physiological heterogeneity in biofilms”. *Nature Reviews Microbiology* **6**(3), 199–210, (2008). doi: `10.1038/nrmicro1838`. (Cited on page 13).

105. Hennes M., Bender N., Cronenberg T., Welker A. & Maier B. “Collective polarization dynamics in bacterial colonies signify the occurrence of distinct subpopulations”. *PLOS Biology* **21**(1), e3001960, (2023). doi: `10.1371/journal.pbio.3001960`. (Cited on pages 13, 16, 137, 140, 142, 148).

106. Fleming A. “On the antibacterial action of cultures of a penicillium, with special reference to their use in the isolation of B. influenzae”. *Br J Exp Pathol.* **10**(3), 226–236, (1929). (Cited on page 13).

107. Aminov R. I. “A brief history of the antibiotic era: Lessons learned and challenges for the future”. *Frontiers in Microbiology* **1**, (2010). doi: `10.3389/fmicb.2010.00134`. (Cited on page 13).

108. Darby E. M., Trampari E., Siasat P., Gaya M. S., Alav I., Webber M. A. & Blair J. M. A. “Molecular mechanisms of antibiotic resistance revisited”. *Nature Reviews Microbiology* **21**(5), 280–295, (2023). doi: `10.1038/s41579-022-00820-y`. (Cited on pages 14, 15).

109. Miller W. R. & Arias C. A. “ESKAPE pathogens: antimicrobial resistance, epidemiology, clinical impact and therapeutics”. *Nature Reviews Microbiology* **22**(10), 598–616, (2024). doi: `10.1038/s41579-024-01054-w`. (Cited on page 14).

110. Balaban N. Q., Helaine S., Lewis K., Ackermann M., Aldridge B., Andersson D. I., Brynildsen M. P., Bumann D., Camilli A., Collins J. J., Dehio C., Fortune S., Ghigo J.-M., Hardt W.-D., Harms A., Heinemann M., Hung D. T., Jenal U., Levin B. R., Michiels J., Storz G., Tan M.-W., Tenson T., van Melderen L. & Zinkernagel A. "Definitions and guidelines for research on antibiotic persistence". *Nature Reviews Microbiology* **17**(7), 441–448, (2019). doi: `10.1038/s41579-019-0196-3`. (Cited on page 14).

111. Brauner A., Fridman O., Gefen O. & Balaban N. Q. "Distinguishing between resistance, tolerance and persistence to antibiotic treatment". *Nature Reviews Microbiology* **14**(5), 320–330, (2016). doi: `10.1038/nrmicro.2016.34`. (Cited on page 14).

112. Brauner A., Shoresh N., Fridman O. & Balaban N. Q. "An experimental framework for quantifying bacterial tolerance". *Biophysical Journal* **112**(12), 2664–2671, (2017). doi: `10.1016/j.bpj.2017.05.014`. (Cited on page 14).

113. Levin-Reisman I., Ronin I., Gefen O., Braniss I., Shoresh N. & Balaban N. Q. "Antibiotic tolerance facilitates the evolution of resistance". *Science* **355**(6327), 826–830, (2017). doi: `10.1126/science.aaj2191`. (Cited on page 14).

114. Gefen O., Chekol B., Strahilevitz J. & Balaban N. Q. "TDtest: easy detection of bacterial tolerance and persistence in clinical isolates by a modified disk-diffusion assay". *Scientific Reports* **7**(1), 41284, (2017). doi: `10.1038/srep41284`. (Cited on page 15).

115. Fanous J., Claudi B., Tripathi V., Li J., Goormaghtigh F. & Bumann D. "Limited impact of Salmonella stress and persisters on antibiotic clearance". *Nature* **639**(8053), 181–189, (2025). doi: `10.1038/s41586-024-08506-6`. (Cited on page 15).

116. Mok W. W. K. & Brynildsen M. P. "Timing of DNA damage responses impacts persistence to fluoroquinolones". *Proceedings of the National Academy of Sciences* **115**(27), E6301–E6309, (2018). doi: `10.1073/pnas.1804218115`. (Cited on page 15).

117. Davies J. & Davies D. "Origins and evolution of antibiotic resistance". *Microbiol Mol Biol Rev* **74**, (2010). doi: `10.1128/MMBR.00016-10`. (Cited on page 15).

118. Allison K. R., Brynildsen M. P. & Collins J. J. "Metabolite-enabled eradication of bacterial persisters by aminoglycosides". *Nature* **473**(7346), 216–220, (2011). doi: `10.1038/nature10069`. (Cited on page 15).

119. Lewis K. "Persister cells, dormancy and infectious disease". *Nature Reviews Microbiology* **5**(1), 48–56, (2007). doi: `10.1038/nrmicro1557`. (Cited on page 15).

120. Vázquez-Laslop N., Lee H. & Neyfakh A. A. "Increased persistence in Escherichia coli caused by controlled expression of toxins or other unrelated proteins". *Journal of Bacteriology* **188**(10), 3494–3497, (2006). doi: `10.1128/jb.188.10.3494-3497.2006`. (Cited on page 15).

121. Yang Q. E. & Walsh T. R. "Toxin–antitoxin systems and their role in disseminating and maintaining antimicrobial resistance". *FEMS Microbiology Reviews* **41**(3), 343–353, (2017). doi: `10.1093/femsre/fux006`. (Cited on page 15).

122. Fridman O., Goldberg A., Ronin I., Shoresh N. & Balaban N. Q. "Optimization of lag time underlies antibiotic tolerance in evolved bacterial populations". *Nature* **513**(7518), 418–421, (2014). doi: `10.1038/nature13469`. (Cited on page 15).

123. Sulaiman J. E. & Lam H. "Evolution of bacterial tolerance under antibiotic treatment and its implications on the development of resistance". *Frontiers in microbiology* **12**, 617412, (2021). doi: `10.3389/fmicb.2021.617412`. (Cited on page 15).

124. Ciofu O., Moser C., Jensen P. Ø. & Høiby N. "Tolerance and resistance of microbial biofilms". *Nature Reviews Microbiology* **20**(10), 621–635, (2022). doi: `10.1038/s41579-022-00682-4`. (Cited on page 16).

125. Unemo M. & Shafer W. M. "Antimicrobial resistance in Neisseria gonorrhoeae in the 21st century: past, evolution, and future". *Clinical microbiology reviews* **27**(3), 587–613, (2014). doi: `10.1128/CMR.00010-14`. (Cited on page 16).

126. Shafer W. M., Datta A., Kumar Kolli V. S., Mahbubur Rahman M., Balthazar J. T., Martin L. E., Veal W. L., Stephens D. S. & Carlson R. "Phase variable changes in genes lgtA and lgtC within the lgtABCDE operon of Neisseria gonorrhoeae can modulate gonococcal susceptibility to normal human serum". *Journal of Endotoxin Research* **8**(1), 47–58, (2002). doi: `10.1177/09680519020080010501`. (Cited on page 16).

127. Bristow C. C., Mortimer T. D., Morris S., Grad Y. H., Soge O. O., Wakatake E., Pascual R., Murphy S. M., Fryling K. E., Adamson P. C., Dillon J.-A., Parmar N. R., Le H. H. L., van Le H., Ovalles Ureña R. M., Mitchev N., Mlisana K., Wi T., Dickson S. P. & Klausner J. D. "Whole-genome sequencing to predict antimicrobial susceptibility profiles in Neisseria gonorrhoeae". *The Journal of Infectious Diseases* **227**(7), 917–925, (2023). doi: `10.1093/infdis/jiad027`. (Cited on page 16).

128. Balduck M., Laumen J. G. E., Abdellati S., De Baetselier I., de Block T., Manoharan-Basil S. S. & Kenyon C. "Tolerance to ceftriaxone in Neisseria gonorrhoeae: Rapid induction in WHO P reference strain and detection in clinical isolates". *Antibiotics* **11**(11), (2022). doi: `10.3390/antibiotics11111480`. (Cited on page 16).

129. Wang L.-C., Litwin M., Sahiholnasab Z., Song W. & Stein D. C. "Neisseria gonorrhoeae aggregation reduces its ceftriaxone susceptibility". *Antibiotics (Basel, Switzerland)* **7**(2), (2018). doi: `10.3390/antibiotics7020048`. (Cited on page 16).

130. Manoharan-Basil S. S., Balduck M., Abdellati S., Gestels Z., de Block T. & Kenyon C. "Enolase is implicated in the emergence of gonococcal tolerance to ceftriaxone". *Antibiotics* **12**(3), (2023). doi: `10.3390/antibiotics12030534`. (Cited on page 16).

131. Cronenberg T., Hennes M., Wielert I. & Maier B. "Antibiotics modulate attractive interactions in bacterial colonies affecting survivability under combined treatment". *PLOS Pathogens* **17**(2), e1009251, (2021). doi: `10.1371/journal.ppat.1009251`. (Cited on pages 19, 57, 164).

132. Kraus-Römer S., Wielert I., Rathmann I., Grossbach J. & Maier B. "External stresses affect gonococcal type 4 pilus dynamics". *Frontiers in microbiology* **13**, (2022). doi: `10.3389/fmicb.2022.839711`. (Cited on pages 19, 32, 34, 41, 137, 149).

133. Wielert I., Kraus-Römer S., Volkmann T. E., Craig L., Higgins P. G. & Maier B. "Pilin antigenic variants impact gonococcal lifestyle and antibiotic tolerance by modulating interbacterial forces". *PLOS Biology* **23**(1), e3003022, (2025). doi: `10.1371/journal.pbio.3003022`. (Cited on pages 19, 20, 23, 36, 79, 173).

134. Kraus-Römer S., Wielert I., Rathmann I., Volkmann T. E., Higgins P. G. & Maier B. "Gonococcal aggregation causes upregulation of genes involved in antibiotic tolerance". *bioRxiv*, (2025). doi: `10.1101/2025.01.17.633513`. (Cited on pages 20, 21, 107).

135. Zöllner R. "Linking intercellular forces to colony dynamics and fitness in bacterial populations". PhD thesis (2019) (cited on pages 23, 26, 28, 30).

136. Wielert I. "GitHub Repository of this study". `https://github.com/IsabelleWielert/PhDThesisIW`. (Cited on pages 23, 24, 29–32, 34, 36, 37, 41).

137. Ansmann G. "BPSB/combine-p-values-discrete: Version 1.2.1". (Cited on page 24).

138. George, E. O., & G. S. Mudholkar. "On the convolution of logistic random variables". *Metrika 30.1* **1983**, 1–13, (1983). (Cited on page 24).

139. Tych K., Hechtl V. K. & Mandal S. "The Power of Light: Nobel Prize in Physics 2018". *IEEE Pulse* **10**(2), 14–19, (2019). doi: `10.1109/MPULS.2019.2899703`. (Cited on page 25).

140. Ashkin A. "Forces of a single-beam gradient laser trap on a dielectric sphere in the ray optics regime". *Biophysical Journal* **61**(2), 569–582, (1992). doi: `https://doi.org/10.1016/S0006-3495(92)81860-X`. (Cited on pages 25, 26).

141. Neuman K. C. & Block S. M. "Optical trapping." eng. *Rev Sci Instrum* **75**(9), 2787–2809, (2004). doi: `10.1063/1.1785844`. (Cited on pages 26, 27, 29).

142. Opitz D. "Mechanical forces during the infection of human ephitelial cells with Neisseria gonorrhoeae." PhD thesis (Westfälische Wilhelm-Universität Münster, 2011) (cited on page 26).

143. Berg-Sørensen K. & Flyvbjerg H. "Power spectrum analysis for optical tweezers". *Review of Scientific Instruments* **75**(3), 594–612, (2004). doi: `10.1063/1.1645654`. (Cited on pages 28, 29).

144. Duda R. O. & Hart P. E. "Use of the Hough Transformation to detect lines and curves in pictures". *Commun. ACM* **15**(1), 11–15, (1972). doi: `10.1145/361237.361242`. (Cited on page 28).

145. Kubo R., Toda M. & Hashitsume N. "Statistical Physics II" (Springer-Verlag Berlin Heidelberg, 1991) (cited on page 29).

146. Hooke R. "Lectures de potentia restitutiva, or of spring explaining the power of springing bodies". **6** (John Martyn, 2016) (cited on page 31).

147. Kurre R., Kouzel N., Ramakrishnan N., Oldewurtel E. R. & Maier B. “Speed switching of gonococcal surface motility correlates with proton motive force”. *PLOS ONE* **8**(6), e67718, (2013). doi: `10.1371/journal.pone.0067718`. (Cited on page 36).

148. Crocker J. C. & Grier D. G. “When like charges attract: The effects of geometrical confinement on long-range colloidal interactions”. *Phys. Rev. Lett.* **77**, 1897–1900, (1996). doi: `10.1103/PhysRevLett.77.1897`. (Cited on page 36).

149. Schindelin J., Arganda-Carreras I., Frise E., Kaynig V., Longair M., Pietzsch T., Preibisch S., Rueden C., Saalfeld S., Schmid B., Tinevez J.-Y., White D. J., Hartenstein V., Eliceiri K., Tomancak P. & Cardona A. “Fiji: an open-source platform for biological-image analysis”. *Nature Methods* **9**(7), 676–682, (2012). doi: `10.1038/nmeth.2019`. (Cited on page 37).

150. Thévenaz P., Ruttimann U. E. & Unser M. “A pyramid approach to subpixel registration based on intensity”. *IEEE transactions on image processing : a publication of the IEEE Signal Processing Society* **7**(1), 27–41, (1998). doi: `10.1109/83.650848`. (Cited on page 37).

151. Ershov D., Phan M.-S., Pylvänäinen J. W., Rigaud S. U., Le Blanc L., Charles-Orszag A., Conway J. R. W., Laine R. F., Roy N. H., Bonazzi D., Duménil G., Jacquemet G. & Tinevez J.-Y. “TrackMate 7: integrating state-of-the-art segmentation algorithms into tracking pipelines”. *Nature Methods* **19**(7), 829–832, (2022). doi: `10.1038/s41592-022-01507-1`. (Cited on page 37).

152. Thielicke W. & Stamhuis E. J. “Towards user-friendly, affordable and accurate Digital Particle Image Velocimetry in MATLAB”. *Journal of Open Research Software*, (2014). doi: `10.5334/jors.bl`. (Cited on page 40).

153. Thielicke W. & Sonntag R. “Particle Image Velocimetry for MATLAB: Accuracy and enhanced algorithms in PIVlab”. *Journal of Open Research Software* **9(1)**, 12, (2020). doi: `10.5334/jors.334`. (Cited on page 40).

154. Thielicke W. “The flapping flight of birds: Analysis and application”. PhD thesis (2014) (cited on page 40).

155. Raffel M., Willert C. E., Scarano F., Kähler C. J., Wereley S. T. & Kompenhans J. “Particle image velocimetry” 3rd ed. 2018. eng, 1 Online–Ressource (XXVI, 669 p. 434 illus., 164 illus. in color). ISBN: 9783319688527 (Springer International Publishing Imprint: Springer, Cham, 2018) (cited on page 40).

156. Abramson J., Adler J., Dunger J., Evans R., Green T., Pritzel A., Ronneberger O., Willmore L., Ballard A. J., Bambrick J., Bodenstein S. W., Evans D. A., Hung C.-C., O’Neill M., Reiman D., Tunyasuvunakool K., Wu Z., Žemgulytė A., Arvaniti E., Beattie C., Bertolli O., Bridgland A., Cherepanov A., Congreve M., Cowen-Rivers A. I., Cowie A., Figurnov M., Fuchs F. B., Gladman H., Jain R., Khan Y. A., Low C. M. R., Perlin K., Potapenko A., Savy P., Singh S., Stecula A., Thillaisundaram A., Tong C., Yakneen S., Zhong E. D., Zielinski M., Žídek A., Bapst V., Kohli P., Jaderberg M., Hassabis D. & Jumper J. M. “Accurate structure

prediction of biomolecular interactions with AlphaFold 3". *Nature* **630**(8016), 493–500, (2024). doi: `10.1038/s41586-024-07487-w`. (Cited on page 79).

157. Jurrus E, Engel D, Star K, Monson K, Brandi J, Felberg L. E, Brookes D. H, Wilson L, Chen J, Liles K, Chun M, Li P, Gohara D. W, Dolinsky T, Konecny R, Koes D. R, Nielsen J. E, Head-Gordon T, Geng W, Krasny R, Wei G, J. Holst M. J, McCammon A. J & Baker N. A. "Improvements to the APBS biomolecular solvation software suite". *Protein Science* **27**(1), 112–128, (2018). doi: `10.1002/pro.3280`. (Cited on page 79).

158. Zhou K. "Non-equilibrium dynamics of bacterial colonies". PhD thesis (2023) (cited on page 140).

159. Kamal F. & Dennis J. J. "Burkholderia cepacia complex phage-antibiotic synergy (PAS): Antibiotics stimulate lytic phage activity". *Applied and Environmental Microbiology* **81**(3), 1132–1138, (2015). doi: `10.1128/AEM.02850-14`. (Cited on page 146).

160. DeFrancesco A. S., Masloboeva N., Syed A. K., DeLoughery A., Bradshaw N., Li G.-W., Gilmore M. S., Walker S. & Losick R. "Genome-wide screen for genes involved in eDNA release during biofilm formation by Staphylococcus aureus". *Proceedings of the National Academy of Sciences* **114**(29), E5969–E5978, (2017). doi: `10.1073/pnas.1704544114`. (Cited on page 146).

161. Binnenkade L., Teichmann L. & Thormann K. M. "Iron triggers LSo prophage induction and release of extracellular DNA in Shewanella oneidensis MR-1 biofilms." *Appl Environ Microbiol* **80**(17), 5304–5316, (2014). doi: `10.1128/AEM.01480-14`. (Cited on page 146).

162. Carrolo M., Frias M. J., Pinto F. R., Melo-Cristino J. & Ramirez M. "Prophage spontaneous activation promotes DNA release enhancing biofilm formation in Streptococcus pneumoniae". *PLOS ONE* **5**(12), 1–10, (2010). doi: `10.1371/journal.pone.0015678`. (Cited on page 146).

163. Swanson J., Robbins K., Barrera O., Corwin D., Boslego J., Ciak J., Blake M. & Koomey J. M. "Gonococcal pilin variants in experimental gonorrhea". *The Journal of experimental medicine* **165**(5), (1987). doi: `10.1084/jem.165.5.1344`. (Cited on page 147).

164. Heydarian M., Schweinlin M., Schwarz T., Rawal R., Walles H., Metzger M., Rudel T. & Kozjak-Pavlovic V. "Triple co-culture and perfusion bioreactor for studying the interaction between Neisseria gonorrhoeae and neutrophils: A novel 3D tissue model for bacterial infection and immunity". *Journal of Tissue Engineering* **12**, 2041731420988802, (2021). doi: `10.1177/2041731420988802`. (Cited on page 147).

165. Boretto M., Cox B., Noben M., Hendriks N., Fassbender A., Roose H., Amant F., Timmerman D., Tomassetti C., Vanhie A., Meuleman C., Ferrante M. & Vankelecom H. "Development of organoids from mouse and human endometrium showing endometrial epithelium physiology and long-term expandability". *Development* **144**(10), 1775–1786, (2017). doi: `10.1242/dev.148478`. (Cited on page 147).

166. McCormack W. M. “Pelvic inflammatory disease”. *New England Journal of Medicine* **330**(2), 115–119, (1994). doi: `10.1056/NEJM199401133300207`. (Cited on page 147).

167. Kaplan J. B., Izano E. A., Gopal P., Karwacki M. T., Kim S., Bose J. L., Bayles K. W. & Horswill A. R. “Low levels of beta-lactam antibiotics induce extracellular DNA release and biofilm formation in Staphylococcus aureus”. *mBio* **3**(4), 10.1128/mbio.00198–12, (2012). doi: `10.1128/mbio.00198-12`. (Cited on page 147).

168. Elliott D., Burns J. L. & Hoffman L. R. “Exploratory study of the prevalence and clinical significance of tobramycin-mediated biofilm induction in Pseudomonas aeruginosa isolates from cystic fibrosis patients”. *Antimicrobial Agents and Chemotherapy* **54**(7), 3024–3026, (2010). doi: `10.1128/aac.00102-10`. (Cited on page 147).

169. Quillin S. J. & Seifert H. S. “Neisseria gonorrhoeae host adaptation and pathogenesis”. *Nature Reviews Microbiology* **16**(4), 226–240, (2018). doi: `10.1038/nrmicro.2017.169`. (Cited on page 147).

170. Unemo M., Seifert H. S., Hook E. W., Hawkes S., Ndowa F. & Dillon J.-A. R. “Gonorrhoea”. *Nature reviews. Disease primers* **5**(1), 79, (2019). doi: `10.1038/s41572-019-0128-6`. (Cited on page 147).

171. Escobar A., Rodas P. I. & Acuña-Castillo C. “Macrophage-Neisseria gonorrhoeae interactions: A better understanding of pathogen mechanisms of immunomodulation”. *Frontiers in immunology* **9**, 3044, (2018). doi: `10.3389/fimmu.2018.03044`. (Cited on page 147).

172. De Munck N., Janssens R., Segers I., Tournaye H., Van de Velde H. & Verheyen G. “Influence of ultra-low oxygen (2%) tension on in-vitro human embryo development”. *Human Reproduction* **34**(2), 228–234, (2018). doi: `10.1093/humrep/dey370`. (Cited on page 147).

173. Fischer B. & Bavister B. D. “Oxygen tension in the oviduct and uterus of rhesus monkeys, hamsters and rabbits”. *Reproduction* **99**(2), 673–679, (1993). doi: `10.1530/jrf.0.0990673`. (Cited on page 147).

174. Eskow R. & Loesche W. “Oxygen tensions in the human oral cavity”. *Archives of Oral Biology* **16**(9), 1127–1128, (1971). doi: `10.1016/0003-9969(71)90218-4`. (Cited on page 147).

175. Schlesinger W. H. & Bernhardt E. S. “Chapter 3 - The Atmosphere”, 51–97, (2020). doi: `10.1016/B978-0-12-814608-8.00003-7`. (Cited on page 147).

176. Knapp J. S. & Clark V. L. “Anaerobic growth of Neisseria gonorrhoeae coupled to nitrite reduction”. *Infection and Immunity* **46**(1), 176–181, (1984). doi: `10.1128/iai.46.1.176-181.1984`. (Cited on page 147).